

# Human Heme Dioxygenases

Thesis submitted for the degree of Doctor of  
Philosophy  
at the University of Leicester

by



Nishma Chauhan, B.Sc. (Hons) Chemistry

Department of Chemistry  
Faculty of Science  
University of Leicester

February 2009

UMI Number: U594483

All rights reserved

INFORMATION TO ALL USERS

The quality of this reproduction is dependent upon the quality of the copy submitted.

In the unlikely event that the author did not send a complete manuscript and there are missing pages, these will be noted. Also, if material had to be removed, a note will indicate the deletion.



UMI U594483

Published by ProQuest LLC 2013. Copyright in the Dissertation held by the Author.  
Microform Edition © ProQuest LLC.

All rights reserved. This work is protected against  
unauthorized copying under Title 17, United States Code.



ProQuest LLC  
789 East Eisenhower Parkway  
P.O. Box 1346  
Ann Arbor, MI 48106-1346

*To Mum*

# Statement

Unless otherwise acknowledged, the experimental work described in this thesis has been carried out by the author in the Henry Wellcome laboratories for Structural Biology, at the University of Leicester between October 2005 and February 2009. The work has not been submitted, and is not presently being submitted for any other degree at this or any other university.

Signed:

Date:

Department of Chemistry

University of Leicester

University Road

Leicester

LE1 7RH

UK

# Human Heme Dioxygenases

Nishma Chauhan

## Abstract

The L-kynurenine pathway, which leads to the formation of NAD, is the major catabolic route of L-tryptophan metabolism in biology. The initial step in this pathway is oxidation of L-tryptophan to *N*-formyl-kynurenine. In all biological systems examined to date, this is catalysed by one of two heme enzymes, indoleamine 2,3-dioxygenase (IDO) or tryptophan 2,3-dioxygenase (TDO). In this thesis the reaction mechanism, the reactive catalytic intermediates involved in this reaction and the nature of substrate (L-tryptophan and dioxygen)-protein interactions, if any, present within the active site of rhIDO have been examined.

In Chapter 2, we addressed the role of S167 in rhIDO (S167A and S167H), which is replaced with a histidine residue in TDO enzymes. Kinetic and spectroscopic data for S167A indicate that this residue is not essential for O<sub>2</sub> or substrate binding. The data for S167H show that the ferrous-oxy complex is dramatically destabilised, which is similar to the behaviour observed in rhTDO. The implications of these results are discussed in terms of our current understanding of IDO and TDO catalysis.

In Chapter 3, it was shown that 1-methyl-tryptophan is a substrate for rhIDO and S167A. However, no activity was observed for rhTDO. Substitution of an active site histidine residue in rhTDO (H76S) allows accommodation of the additional methyl group and 1-methyl-tryptophan turnover to occur. These observations suggest that deprotonation of the indole N<sup>1</sup> is not essential for catalysis, and an alternative reaction mechanism is presented. Additional experiments using EPR and <sup>1</sup>H ENDOR spectroscopy were used to examine the surrounding environment of the heme iron. The results reveal important information on the surrounding environment of the heme-bound dioxygen and the interactions present in the ternary complex. The mechanistic implications of such interactions are discussed in this work.

In Chapter 5, we undertook site-directed mutagenesis of several active site residues and the role of each residue on dioxygen, substrate binding and in catalysis was examined. We found the conserved residue R231 plays a key role in substrate binding and is likely to do so in all heme dioxygenase enzymes. The F227A variant was found to be catalytically competent for L-tryptophan turnover and suggests that this residue is not involved in substrate recognition like previously proposed.

In Chapter 6, we have shown that rhTDO and rhIDO can utilise hydrogen peroxide as an alternative oxygen source to dioxygen. For rhTDO, approximately two equivalents of H<sub>2</sub>O<sub>2</sub> were consumed in the production of one molecule of *N*-formyl-kynurenine, suggesting that an alternative mechanistic pathway is used with hydrogen peroxide.

# Acknowledgements

I would like to thank my supervisor Prof Emma L. Raven for giving me the opportunity to work in her laboratory and for her guidance, support and help throughout the three years of my PhD. I am extremely grateful to Dr Jaswir Basran for her ever willingness to pass on practical and theoretical knowledge, especially for kinetic and molecular biology aspects of the work; I would also like to thank Jaswir for being a great friend throughout the course of my PhD.

I would also like to thank Dr Igor Efimov for his expertise in redox potentiometry, Dr Graham Eaton for his assistance in obtaining mass spectra, Dr Roman Davydov (Department of Chemistry, Northwestern University) for collecting EPR and ENDOR spectra and Dr Paul Jenkins for helpful discussions. I am grateful to Prof Steve Chapman (Department of Chemistry, University of Edinburgh) for allowing me to work within his laboratory. In particular, I would like to thank Dr Sarah Thackray and Dr Chris Mowat for their assistance and useful discussions.

For financial support I am indebted to the EPSRC and the University of Leicester.

I am also grateful to Dr Zoi Pipirou, Dr Sandip Badyal, Dr Emma Murphy, Miss Sara Rafice, Mr Andrea Gumiero, Mrs Zimna Wazeer and Mrs Nina Bhanji for their encouragement and assistance in the lab.

Most of all I would like to thank my Mum for the never-ending support and encouragement she has given me.

# Contents

<b>Statement</b>	<b>i</b>
<b>Abstract</b>	<b>ii</b>
<b>Acknowledgements</b>	<b>iii</b>
<b>Table of Contents</b>	<b>iv</b>
<b>Abbreviations</b>	<b>xi</b>

## Chapter 1 Introduction

1.1	Chemical properties of dioxygen	2
1.2	Oxygen activation by metal ions	3
1.3	Oxygen activation by heme	4
1.4	Oxygenases	6
1.5	Monooxygenases	6
	1.5.1 Cytochrome P450s	7
1.6	Dioxygenases	8
	1.6.1 Indoleamine 2,3-dioxygenase and tryptophan 2,3-dioxygenase	9
1.7	Discovery of IDO and TDO	10
1.8	Occurrence	13
1.9	The effect of IDO and TDO in biological systems	14
	1.9.1 The kynurenine pathway	14
	1.9.2 The physiological role of IDO	14
1.10	Bacterial expression of IDO and TDO enzymes	15
1.11	The catalytic cycle of IDO and TDO	16
1.12	Crystallographic studies	17
	1.12.1 The X-ray crystal structure of rhIDO	17
	1.12.2 The X-ray crystal structures of bacterial TDO	20
	1.12.3 Comparison of IDO and TDO crystal structures	23

1.13	Properties of IDO and TDO	25
1.13.1	Heme iron coordination structures	25
1.13.2	O <sub>2</sub> and CO binding	27
1.13.3	Catalytic activity	27
1.13.4	IDO and TDO inhibition	29
1.13.5	Redox properties of IDO and TDO	31
1.14	Proposed reaction mechanisms	31
1.15	Unanswered questions	36
1.16	Thesis aims	37
1.17	References	38

## **Chapter 2 The role of serine 167 rhIDO: a comparison with TDO**

2.1	Introduction	50
2.2	Results	52
2.2.1	Expression and purification	52
2.2.1.1	Expression system	52
2.2.1.2	SDS-PAGE analysis	52
2.2.2	Electronic absorption spectra	53
2.2.3	EPR spectroscopy	54
2.2.4	Binding of non-catalytic ligands	55
2.2.5	Substrate binding	57
2.2.6	Crystal screens	60
2.2.7	Redox measurements	60
2.2.8	Steady-state kinetics	62
2.2.9	The catalytic ferrous-oxy complex	63
2.2.9.1	rhIDO and its variants	63
2.2.9.2	Reaction of O <sub>2</sub> with rhIDO in the presence of 1-methyl-tryptophan	66

2.2.10	Expression, purification and spectroscopic characterisation of rhTDO	67
2.2.11	Reaction of O <sub>2</sub> with rhTDO	67
2.2.12	Detection of intermediate species during reaction of reduced enzyme with L-Trp and O <sub>2</sub>	69
2.3	Discussion	74
2.4	References	79

## **Chapter 3 Reassessment of the reaction mechanism in heme dioxygenases**

3.1	Introduction	83
3.2	Results	85
3.2.1	Purification of 1-methyl-tryptophan	85
3.2.2	Expression, purification and spectroscopic characterisation of rhIDO and S167A	86
3.2.3	Identification of reaction products catalysed by rhIDO & S167A	87
3.2.3.1	UV-visible spectroscopy	87
3.2.3.2	LC-MS analysis	88
3.2.4	Expression, purification and spectroscopic characterisation of rhTDO	89
3.2.5	LC-MS analysis of the reaction products catalysed by rhTDO	89
3.2.6	Expression, purification and spectroscopic characterisation of H76S	90
3.2.7	LC-MS analysis of the reaction products catalysed by H76S	90
3.2.8	Steady-state kinetics	91
3.3	Discussion	93
3.4	References	96

## **Chapter 4 Analysis of the heme center in the ferrous-oxy and ternary complexes of rhIDO as probed by EPR and ENDOR spectroscopy**

4.1	Introduction	99
4.2	Results	102
4.2.1	Ferrous rhIDO	102
4.2.2	Ferrous-oxy rhIDO	103
4.2.3	Ferrous-NO and ferrous-Trp-NO	105
4.2.4	Ternary complex – [rhIDO <sup>II</sup> -Trp-O <sub>2</sub> ]	106
4.2.4	Ternary complex – [rhIDO <sup>II</sup> -methylTrp-O <sub>2</sub> ]	108
4.3	Discussion	111
4.4	References	115

## **Chapter 5 Mutagenesis of active site residues in rhIDO**

5.1	Introduction	119
5.2	Results	121
5.2.1	Mutagenesis, expression, isolation and purification	121
5.2.2	Characterisation of the active site variants of rhIDO	121
5.2.2.1	Electronic absorption spectra	121
5.2.2.2	Binding of non-catalytic ligands	123
5.2.3	Equilibrium binding experiments	125
5.2.3.1	Cyanide binding	125
5.2.3.2	L-Trp binding	126
5.2.4	Steady-state kinetics	126
5.2.5	Kinetics of O <sub>2</sub> binding	128

5.2.6	Characterisation of the R231K variant of rhIDO	130
5.2.6.1	Electronic absorption spectra	130
5.2.6.2	Equilibrium binding experiments	131
5.2.6.3	Kinetics of O <sub>2</sub> binding	131
5.2.6.4	Steady-state kinetics	133
5.3	Discussion	134
5.4	References	137

## **Chapter 6 H<sub>2</sub>O<sub>2</sub>-mediated catalysis in the heme dioxygenases**

6.1	Introduction	140
6.2	Results	141
6.2.1	UV-visible spectroscopy	141
6.2.2	LC-MS analysis	142
6.2.3	Titration of H <sub>2</sub> O <sub>2</sub> with ferric enzyme and L-Trp	144
6.2.4	Detection of possible intermediate species	145
6.3	Discussion	146
6.4	References	149

## **Chapter 7 Forward perspectives**

7.1	References	155
-----	------------	-----

## **Chapter 8 Experimental**

8.1	Materials and stock solutions	158
8.2	Recombinant DNA techniques	158
8.2.1	Oligonucleotides	158

8.2.2	Site-directed mutagenesis	159
8.2.3	Isolation of DNA	160
8.2.4	Agarose gel electrophoresis	161
8.2.5	DNA sequencing	161
8.2.6	Transformation of the recombinant DNA into competent <i>E.coli</i> cells	161
8.3	Protein expression of rhIDO and variants	162
8.4	Isolation and purification of rhIDO and variants	163
8.4.1	Preparation of <i>E. coli</i> lysate	163
8.4.2	Ni-NTA metal-affinity chromatography	163
8.4.3	Reconstitution of rhIDO variants	164
8.4.4	Fast Protein Liquid Chromatography	164
8.4.5	Polyacrylamide gel electrophoresis (SDS-PAGE)	164
8.5	Protein expression and purification of rhTDO	165
8.6	UV-visible spectroscopy	166
8.7	Determination of heme absorption coefficients	167
8.8	Ligand-bound derivative spectra	167
8.9	Ligand binding equilibria	168
8.10	Xanthine/xanthine oxidase method for determination of Fe <sup>III</sup> /Fe <sup>II</sup> reduction potential	169
8.11	Steady-state kinetics	169
8.12	Transient-state kinetics	170
8.12.1	Kinetics of binding of L-Trp, cyanide and O <sub>2</sub> to rhIDO and its variants	170
8.12.2	Detection of intermediate species during reaction of reduced enzyme with L-Trp and O <sub>2</sub>	171
8.12.3	Preparation of O <sub>2</sub> -saturated solutions	173
8.13	Liquid Chromatography Mass Spectrometry	173
8.13.1	Reaction of rhIDO, rhTDO and its variants with 1-Me-Trp	173
8.13.2	Reaction of rhIDO and rhTDO with H <sub>2</sub> O <sub>2</sub> and L-Trp	174
8.14	EPR and ENDOR spectroscopy	174

8.15	Crystal screens	175
8.16	References	179
	<b>Appendix A</b>	<b>xv</b>
	<b>Appendix B</b>	<b>xvii</b>
	<b>Appendix C</b>	<b>xxi</b>
	<b>Appendix D</b>	<b>xxiv</b>
	<b>Appendix E</b>	<b>xxvi</b>
	<b>Publications</b>	<b>xxxiii</b>

# Abbreviations

Amino Acids are abbreviated according to the three-letter codes recommended by the I.U.P.A.C Joint Commission on Biochemical Nomenclature (1985).

## Enzymes

hIDO	human indoleamine 2,3-dioxygenase
rhIDO	recombinant human indoleamine 2,3-dioxygenase
SIDO	<i>Shewanella oneidensis</i> indoleamine 2,3-dioxygenase
hTDO	human tryptophan 2,3-dioxygenase
rhTDO	recombinant human tryptophan 2,3-dioxygenase
XcTDO	<i>Xanthomonas campestris</i> tryptophan 2,3-dioxygenase
Mb	myoglobin
Hb	hemoglobin
DNase	deoxyribonuclease
HRP	horseradish peroxidase

## Amino acids

Ala	A	alanine
Asn	N	asparagine
Asp	D	aspartic acid
Arg	R	arginine
Cys	C	cysteine
Glu	E	glutamic acid
Gln	Q	glutamine
Gly	G	glycine
His	H	histidine
Met	M	methionine
Pro	P	proline
Ser	S	serine
Thr	T	threonine

Tyr	Y	tyrosine
Lys	K	lysine
Leu	L	leucine
Ile	I	isoleucine
Phe	F	phenylalanine
Trp	W	tryptophan
Val	V	valine

## Chemicals

Amp	ampicillin
CHES	2-(cyclohexylamino)ethanesulfonic acid
DTT	dithiothreitol
dNTPs	deoxynucleotide triphosphates
EDTA	ethylenediaminetetraacetic acid
IPTG	isopropyl- $\beta$ -D-thiogalactopyranoside
Kan	kanamycin
NTA	nitrilotriacetic acid
PMSF	phenylmethylsulfonyl fluoride
SDS	sodium dodecyl sulphate
Tris	trizma base (tri[hydroxymethyl]aminomethane)
L-Trp	L-tryptophan
1-Me-Trp	1-methyl-tryptophan

## Techniques

ENDOR	electron nuclear double resonance
EPR	electron paramagnetic resonance
ESI-MS	electrospray ionisation mass spectrometry
FPLC	fast protein liquid chromatography
HPLC	high performance liquid chromatography

LC-MS	liquid chromatography mass spectrometry
MCD	magnetic circular dichroism
NMR	nuclear magnetic resonance
PAGE	polyacrylamide gel electrophoresis
PCR	polymerase chain reaction
$R_z$	Reinheitzahl
UV	ultra violet

## Units/Symbols

A	Absorption
$\epsilon$	absorption coefficient
Å	Ångström ( $1 \text{ Å} = 10^{-10} \text{ m}$ )
c	concentration
°C	degrees Celsius
g	grams
kb	kilobases
kDa	kilo Daltons
l	litres
mV	milliVolts
min	minutes
M	molar
OD	optical density
rpm	revolutions per minute
s	seconds
v/v	volume to volume
$\lambda$	wavelength
w/v	weight per volume

## Miscellaneous

cDNA	complementary deoxyribonucleic acid
CT	charge transfer
DNA	deoxyribonucleic acid
<i>E. coli</i>	<i>Escherichia coli</i>
FAD	flavin adenine dinucleotide
IFN- $\gamma$	interferon gamma
I. U. P. A.C.	International Union of Pure and Applied Chemistry
MDL	Molecular Dimensions Ltd.
NAD	nicotine adenine dinucleotide
PNACL	Protein and Nucleic Acid Chemistry Laboratory
PDB	Protein Data Bank

# **Chapter 1**

---

## **Introduction**

## 1.1 Chemical properties of dioxygen

All living organisms need oxygen for respiration. Green plants produce oxygen by photosynthesis in sunlight and many biochemical molecules include oxygen atoms *e.g.* carbohydrates, proteins and nucleic acids. These oxygen insertion reactions involve the incorporation of one or both of the oxygen atoms of dioxygen into organic substrates and often involve the cleavage of the oxygen-oxygen bond and are energetically very favourable, *i.e.* exothermic. Despite this strong thermodynamic driving force, the chemical reactivity of dioxygen with organic molecules at ambient temperatures is intrinsically low. If this were not the case, dioxygen would spontaneously oxidise organic compounds and would be harmful rather than useful for living things.

This low reactivity is due to the ground state of molecular oxygen. It is a triplet, diradical in the ground state with two unpaired electrons residing in antibonding  $\pi^*$  orbitals, Figure 1.1. The molecular orbital energy level configuration of triplet dioxygen is  $(1s\sigma)^2 (1s\sigma^*)^2 (2s\sigma)^2 (2s\sigma^*)^2 (2p\sigma)^2 (2p\pi)^4 (2p\pi x^*)^1 (2p\pi y^*)^1$ .

Although dioxygen has a triplet ground state, essentially all stable organic compounds are singlets; *i.e.*, all of their electrons are paired. Direct reactions between the triplet and the singlet molecules to yield a singlet product are spin-forbidden because the chemical combination reaction rates are faster than spin inversion rates. Such reactions can proceed via the spin-allowed, but high energy formation of an unstable triplet intermediate, followed by a slow spin inversion to form a singlet product. In contrast to the inherent difficulty of triplet dioxygen reacting with singlet organic molecules, it will react readily with organic radicals ( $R^\bullet$ ), *i.e.* doublets (Equation [1.1]).



Another way to overcome the high kinetic barrier inherent to the reactions of triplet  $O_2$  is to utilise a transition metal ion such as iron or copper as the cofactor in enzymes that carry out biological oxidations. Transition metals in the appropriate oxidation states are able to react directly with triplet  $O_2$  to form dioxygen adducts that can participate in reaction pathways leading either to the incorporation of

oxygen atoms into organic substrates or to the oxidation of the organic substrates (1).

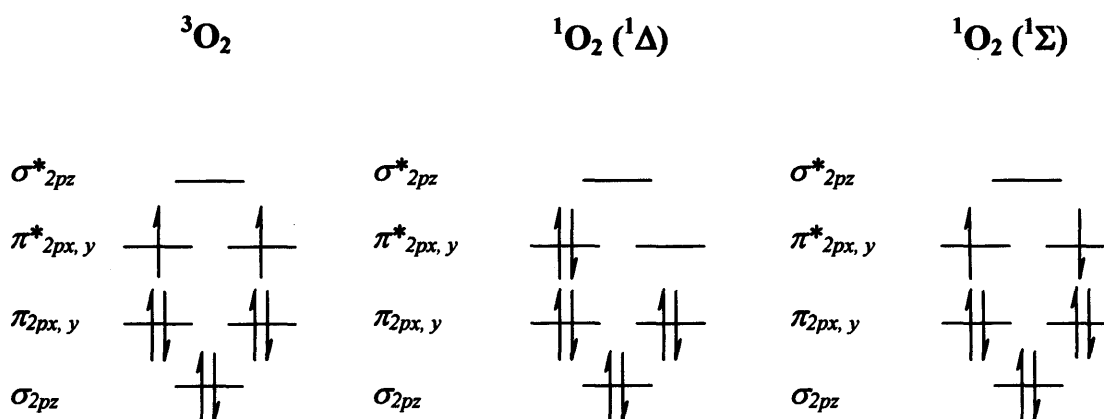


Figure 1.1: Molecular orbital diagrams for  $^3O_2$ ,  $^1O_2 (^1\Delta)$  and  $^1O_2 (^1\Sigma)$ .

## 1.2 Oxygen activation by metal ions

Nature has devised a large number of redox active groups, utilising transition metal ions, heme and organic cofactors to mediate dioxygen activation. Transition metal ions, containing  $3d$  unpaired electrons, can use three strategies to activate dioxygen (2).

- *Orbital overlap with a metal ion.* When dioxygen forms a bond with a transition metal ion containing unpaired  $3d$  electrons, the unpaired electrons in the dioxygen  $\pi^*$  orbitals are able to overlap with those on the metal ion (3). The reaction of such a transition metal-dioxygen with a singlet organic reagent is then allowed, provided that the overall number of unpaired electrons in the complex remains constant.
- *Single electron transfer.* Dioxygen activation by metallo-enzymes that contain transition metals often have two consecutive oxidation states (e.g.  $Fe^{II}/Fe^{III}$ ,  $Cu^I/Cu^{II}$ ); the metal centre is able to carry out single electron transfer to bound dioxygen. The  $^3O_2$  oxygen ground state can accept a single electron to form superoxide, which is an allowed reaction, and is one possible route for oxygen

activation. Superoxide can then participate in a variety of 1- or 2-electron chemical reactions (4).

A criticism of this route is that it is apparently energetically unfavourable; the reduction potential for the  $O_2/O_2^{\bullet-}$  couple is -0.16 V in water at pH 7.0 and the reduction potential for the  $Fe^{II}/Fe^{III}$  couple is +0.77 V. Therefore, the redox potential for the activation of dioxygen to superoxide by  $Fe^{II}$  is -0.93 V. However, the redox potentials for the  $Fe^{II}/Fe^{III}$  and dioxygen/superoxide couples in the metallo-enzyme would be dependent upon the particular microenvironment of the active site. It is also known that redox enzymes can strongly influence the redox potential of cofactors bound to their active sites, by selective stabilisation of the oxidised or the reduced form (5). The conversion of dioxygen to superoxide has been observed in hemoglobin (6), and in EDTA- $Fe^{III}$  complexes (7). Therefore, it is feasible that this route can be used by metallo-enzymes.

- *Reaction with a substrate radical.* Since the reaction of dioxygen via radical mechanisms is a spin-allowed process, reaction with a substrate radical is an alternative possible mechanism. It has been proposed that a substrate activation mechanism of this kind occurs in the intradiol catechol dioxygenases, in which case a bound catechol semiquinone intermediate attacks dioxygen to form a hydroperoxide radical (2, 8).

### 1.3 Oxygen activation by heme

Iron protoporphyrin IX, also known as heme, is an iron-containing macrocycle that is an integral component of many proteins in bacteria, plants and animals. Heme consists of a protoporphyrin ring and a central iron (Fe) atom. A protoporphyrin ring is made up of four pyrrole rings linked by methene bridges. Four methyl, two vinyl, and two propionate side chains are attached (Figure 1.2(A)). The iron atom binds to the four pyrrole nitrogens in the centre of the protoporphyrin ring, giving rise to a square planar structure; the net charge on the heme with four-coordinate iron (III) is +1 (9). The iron can form two additional bonds, one on either side of the heme plane and are termed as fifth (or proximal) and sixth (or distal) coordination sites (Figure 1.2(B)). The nature of the two axial ligands varies between heme proteins, although in many cases the proximal ligand is a histidine. The iron can either be in the ferrous

(Fe<sup>II</sup>) or the ferric (Fe<sup>III</sup>) oxidation state. However, in heme proteins such as the peroxidases and cytochrome P450s, the iron is known to be able to access ferryl (Fe<sup>IV</sup>) oxidation states (10, 11).

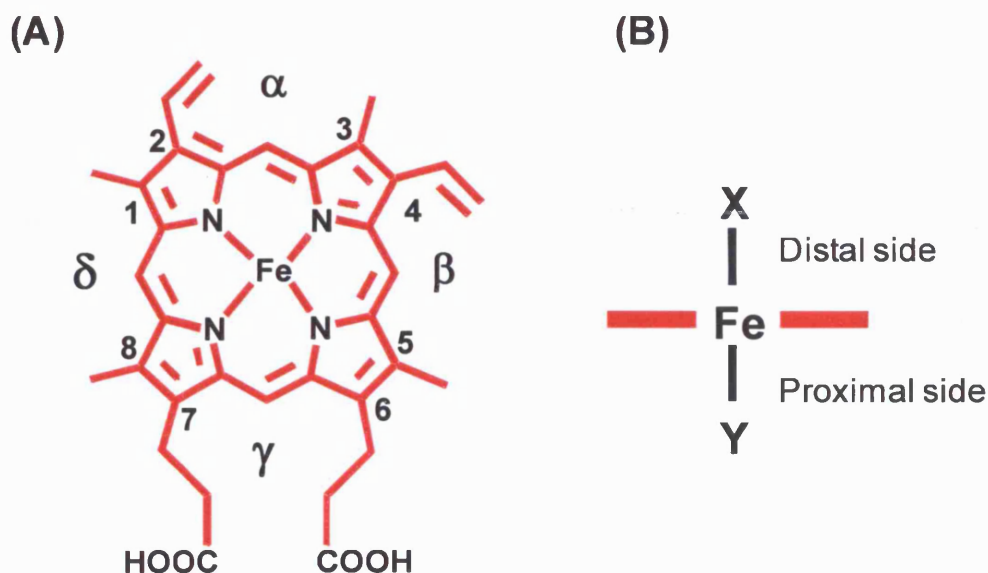


**Figure 1.2:** (A) The structure of heme. The methene bridges are designated  $\alpha$ ,  $\beta$ ,  $\gamma$  and  $\delta$ . (B) A representation of heme. The red lines represent the heme plane and Y and X represent the 5<sup>th</sup> and 6<sup>th</sup> ligand, respectively.

The dioxygen activation mechanism by heme enzymes involves complex formation between the 6<sup>th</sup> coordination site on the ferrous high-spin ( $d^6$ ,  $S = 2$ ) heme iron and triplet dioxygen. This yields a low-spin complex that is generally described as either Fe<sup>II</sup>-O<sub>2</sub> or Fe<sup>III</sup>-O<sub>2</sub><sup>-</sup> or a resonance hybrid of these two forms because the actual electronic structure may involve partial electron transfer between iron and bound dioxygen. An unpaired electron on the superoxide resides in its antibonding  $\sigma$  orbital ( $\sigma O_2^*$ ), while a second unpaired electron resides in a nonbonding iron orbital ( $d_{xy}$ ). In the ferrous dioxygen or ferric superoxide configuration, the complex is *diamagnetic*.

## 1.4 Oxygenases

In 1955, Mason (12) and Hayashi (13) demonstrated by  $^{18}\text{O}_2$  labelling that one or both oxygen atoms of dioxygen can be directly incorporated into organic molecules such as 3,4-dimethyl phenol and catechol.

Prior to that date, it was thought that the sole role of dioxygen in biological systems was as an electron acceptor in dioxygen-utilising oxidase or dehydrogenase reactions. Hayashi then designated enzymes that incorporate oxygen atoms from dioxygen as oxygenases. It is now known that oxygenases are extensively distributed in nature and throughout the plant, animal, and microorganism kingdoms. Oxygenases can be further classified into two categories (14), monooxygenases and dioxygenases, depending on whether one or both the oxygen atoms from dioxygen are incorporated into the substrate (Equation [1.2] and [1.3], respectively).

### ***Monooxygenases:***



### ***Dioxygenases:***



## 1.5 Monooxygenases

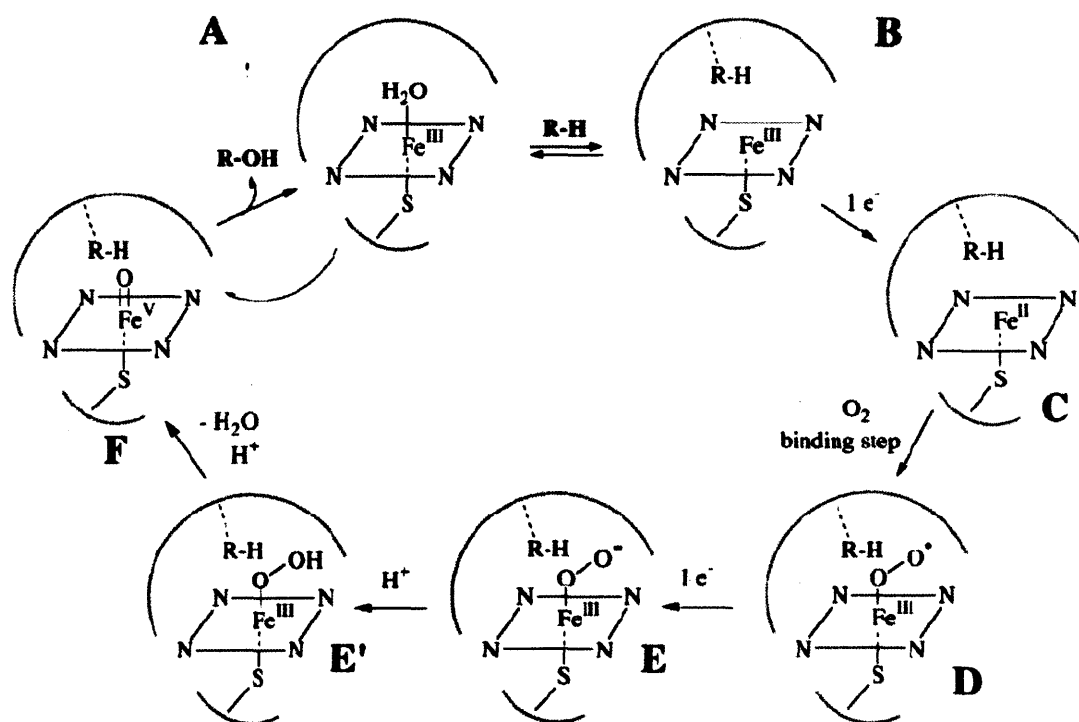
Monooxygenases require two electrons to reduce the second oxygen atom of dioxygen to water (Equation [1.2]). The two electrons can come from a reducing agent or from the substrate itself. The flavooxygenases were the first family of monooxygenases to be studied in detail by Sutton *et al.*, which require reduced flavin (FAD or FMN) for activity (5). Lactate monooxygenase, which catalyses the oxidative decarboxylation of lactate to acetate, was found in extracts of *Mycobacterium phlei* and both Sutton and Hayashi established the incorporation of  $^{18}\text{O}$  from  $^{18}\text{O}_2$  (15). There are many examples in the literature of non-heme iron monooxygenases, some of which include tryptophan hydroxylase which catalyses the hydroxylation of L-tryptophan to 5-hydroxy-tryptophan (16) and methane monooxygenase (17, 18) which is found in methanotropic bacteria. Methanotropic

bacteria respire on methane and catalyse the oxidation of methane to methanol, in the first step of the conversion of methane to carbon dioxide. There are many different forms of methane monooxygenase, including both membrane bound and soluble forms, and these are thought to contain copper and iron centres, although this remains a widely debated issue.

### ***1.5.1 Cytochrome P450s***

Heme-containing monooxygenases include secondary amine monooxygenase (14), heme oxygenase (18) and the cytochrome P450s (14). The most studied and famous monooxygenases are the family of cytochrome P450 enzymes for their ability to catalyse the oxidation of a huge variety of organic compounds. The cytochrome P450s are heme-containing enzymes which bind carbon monoxide to form a characteristic absorption band at 450 nm. The unusual spectral properties were first attributed in 1965 by Mason *et al.* to the coordination of a sulfhydryl sulfur atom to the fifth ligation site of the heme iron (19). The cytochrome P450s have been found in virtually every mammalian tissue and organ as well as in plants, bacteria, yeast and insects.

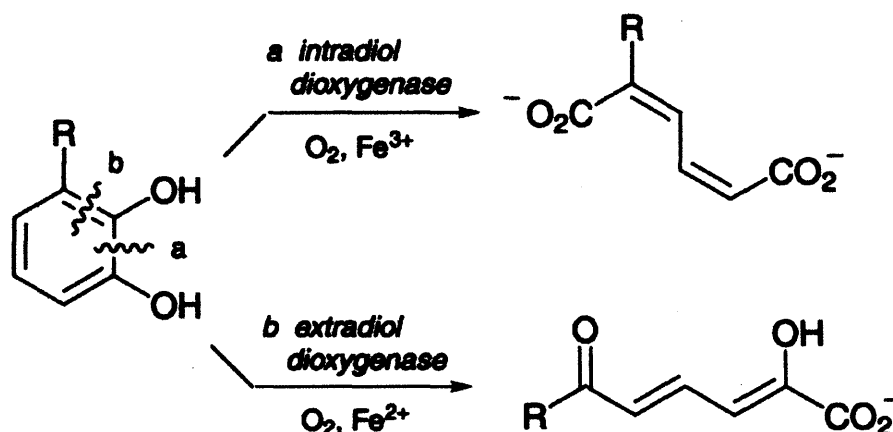
A common catalytic cycle of the cytochrome P450s was proposed in 1968 (20) and still provides the core description of the role of the iron, protein and dioxygen in catalysis and now is accepted in an updated form (Scheme 1.1). The resting form of the enzyme is six-coordinate low-spin with water as the distal ligand (A). Upon addition of substrate, a five-coordinate high-spin ferric heme is generated, which has a vacant coordination site that will be available for dioxygen binding (B). In most cases, the substrate bound complex has a more positive reduction potential and is therefore easier to reduce to the ferrous state. After reduction of the substrate-bound ferric enzyme by a redox partner (C), dioxygen binds to the ferrous enzyme to form the ferrous-oxy complex or the ferric-superoxide complex (D). Addition of the second electron is proposed to yield a ferric-peroxide adduct (E) which can be protonated to give a hydroperoxide complex (E'). A second protonation of the same oxygen atom leads to hetrolytic O-O bond cleavage releasing water and generates a Compound I intermediate (F) and oxygenated substrate.



**Scheme 1.1:** The proposed catalytic cycle of cytochrome P450. This scheme is reproduced from reference (21).

## 1.6 Dioxygenases

The family of catechol dioxygenases, which include intradiol dioxygenases and extradiol dioxygenases, are non-heme iron-dependant dioxygenases and were first discovered by Hayaishi in the 1950s (22) (Scheme 1.2). The catechol dioxygenases catalyse the oxidative cleavage of catechol which is a key step in the bacterial degradation of aromatic compounds in the environment. The intradiol dioxygenases require ferric iron for activity and the iron centre is ligated by two tyrosine residues and a histidine residue; in contrast the extradiol dioxygenases require ferrous iron for activity and the iron centre is ligated to two histidine residues and a glutamate residue (2). It has been proposed that substrate coordinates to the metal first concurrently displacing two solvent molecules from the metal centre followed by coordination of dioxygen to the iron centre in a site adjacent to the substrate. It is thought that both reactions undergo catalysis via Criegee rearrangement (23).

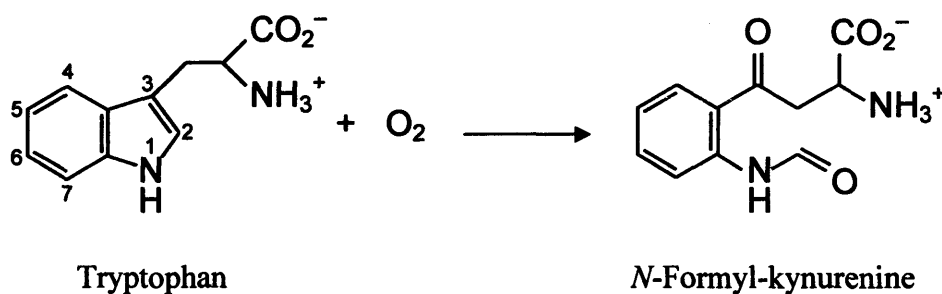


**Scheme 1.2:** Reactions catalysed by intradiol and extradiol dioxygenases.

Further examples of non-heme dioxygenases include quercetin dioxygenase which is the only known copper-dependant dioxygenase (24, 25), cysteine dioxygenase which metabolises cysteine into cysteinesulfonic acid in mammals (26) and acetylacetone dioxygenase (2, 27).

### 1.6.1 Indoleamine 2,3-dioxygenase and tryptophan 2,3-dioxygenase

Heme-containing dioxygenases include indoleamine 2,3-dioxygenase (IDO) and tryptophan 2,3-dioxygenase (TDO), both of which catalyse the oxidative cleavage of the C<sup>2</sup>-C<sup>3</sup> double bond of tryptophan to produce *N*-formyl-kynurenine (Scheme 1.3). To date, these are the only two heme-containing dioxygenases have been identified. Both IDO and TDO are currently of great scientific interest due to their roles in many diverse physiological and immunological diseases. Investigation of the structure-function relationships and the catalytic mechanism employed by IDO and TDO would greatly aid understanding of these important enzymes.



**Scheme 1.3:** Reaction catalysed by IDO and TDO.

### 1.7 Discovery of IDO and TDO

The L-kynurenine pathway, which, ultimately, leads to the formation of NAD is the major catabolic route of L-tryptophan in mammals (Figure 1.3). The initial rate-limiting step in this pathway is the oxidative cleavage of L-tryptophan to *N*-formyl-kynurenine and, as mentioned earlier, is catalysed by IDO and TDO.

Kynurenine, which is the major intermediate of this pathway, was isolated by Kotake in 1937 (28) and in that same year an enzyme was isolated that catalysed the conversion of tryptophan to formylkynurenine, and called it tryptophan pyrrolase (29). This enzyme was later renamed tryptophan 2,3-dioxygenase (TDO). In mammals, this enzyme is found only in the liver and is induced by administration of tryptophan. It has been recognised for some time that elevated levels of various tryptophan metabolites can be found in the urine of patients suffering from a variety of diseases, such as rheumatoid arthritis, tuberculosis, leukaemia, Hodgkins disease, bladder cancer, and prostate disorders. However, TDO concentrations are not elevated in the liver in these patients. These findings suggested that TDO may not be the only enzyme initiating the catabolism of tryptophan (30). In 1937, Kotake and Ito (28) found that rabbits fed with D-tryptophan excreted D-kynurenine in the urine (in 1980, hepatic tryptophan 2,3-dioxygenase in certain species of animals was found to cleave the pyrrole ring of the D-isomer (31)). In 1950 Knox and Mehler (32) demonstrated that the primary product was formylkynurenine and that a second enzyme, “formamidase”, hydrolysed the formyl group of formylkynurenine to yield kynurenine and formic acid. Later, Tanaka and Knox (33) presented evidence that tryptophan pyrrolase is a hemoprotein containing protoporphyrin IX as its prosthetic

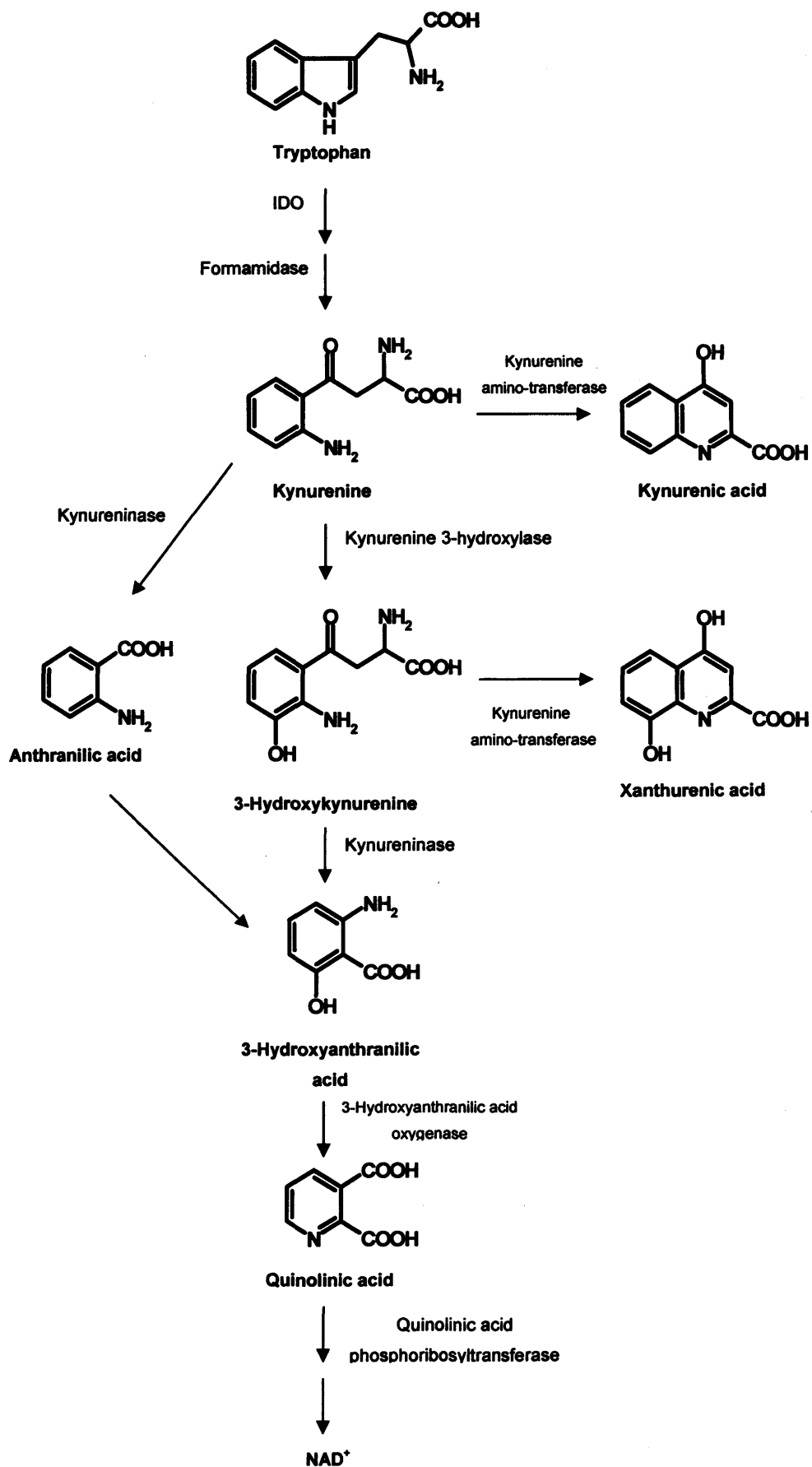


**Figure 1.3:** The kynurenine pathway of tryptophan degradation in mammalian cells.

group. In 1975, Hirata was able to demonstrate with the use of a heavy oxygen isotope ( $^{18}\text{O}_2$ ) that molecular oxygen was directly incorporated into formylkynurenine (34).

In 1963, Hayaishi and colleagues isolated a second enzyme that catalysed the conversion of tryptophan to kynurenine and in 1967 the same workers reported the discovery of an enzyme capable of oxidizing D-tryptophan to *N*-formyl-D-kynurenine in a homogenate of rabbit small intestine (35, 36). Unlike TDO, this enzyme is not found predominantly in the liver, but is distributed ubiquitously in non-hepatic organs of mammals, with the lung and placenta having the highest activities (36, 37). It has a wider spectrum of substrates than TDO and can utilise many indoleamine derivatives including L- and D-tryptophan, tryptamine, 5-hydroxytryptophan, and serotonin and is therefore called indoleamine 2,3-dioxygenase (IDO).

## 1.8 Occurrence

As mentioned earlier, IDO is found in many eukaryotes where it is expressed ubiquitously throughout the body, except in the liver. IDO expression is induced by several complex immunological signals including interferon- $\gamma$  and inflammatory cytokines (38). Mammalian IDO is monomeric and contains ~400 amino acids, displaying high sequence identity between eukaryotic species, at ~61% for human and mouse IDO (39, 40).

TDO is found in both eukaryotes and prokaryotes and its expression in mammals is normally restricted to the liver. However, TDO expression has been discovered in the brain and on the skins (41) of some species and TDO production has been reported to be induced by tryptophan, tyrosine, histidine, glucocorticoids and kynurenine (42). TDO is a homotetrameric enzyme and eukaryotic TDOs contain ~400 amino acids whilst prokaryotic TDOs contain ~300 amino acids (43, 44). Sequence identities between prokaryotic and eukaryotic TDOs are around 20-40% (44) and ~16% between human IDO and human TDO. The amino acid sequence alignment of human IDO, human TDO, *Xanthomonas campestris* TDO (*XcTDO*) and *Shewenella oneidensis* IDO (*SIDO*) is presented in Figure 1.4.

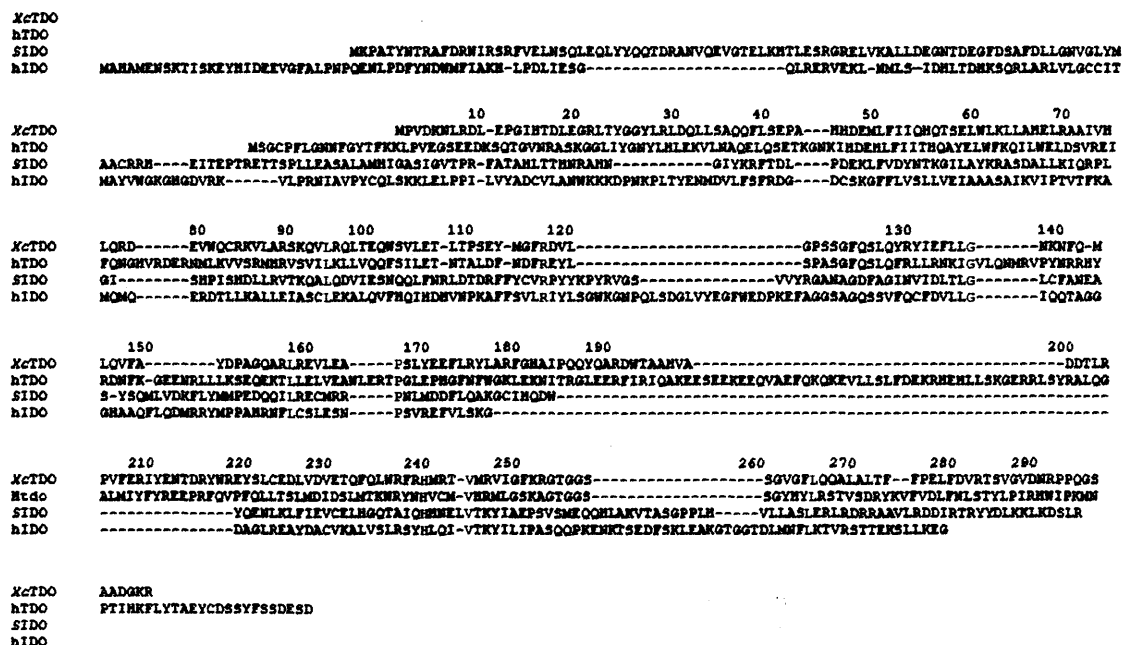


Figure 1.4: An amino acid sequence alignment of *XcTDO*, human TDO, *SIDO* and human IDO. Conserved residues are highlighted in red.

## 1.9 The effect of IDO and TDO in biological systems

### 1.9.1 *The kynurenine pathway*

The kynurenine pathway processes over 90% of L-tryptophan (L-Trp) utilised by humans and ultimately leads to the formation of NADH, an essential redox cofactor (Figure 1.3). Tryptophan degradation leads to the formation of dangerous metabolites, which display neuroactive and neurotoxic properties and one such example is quinolinic acid. High levels of quinolinic acid in cerebrospinal fluid may be involved in various neurological disorders, including cerebral malaria, multiple sclerosis, AIDS related dementia, and neural death when injected into the brain (45-47). Kynurenine pathway metabolites have also been implicated in cataract formation (48). The kynurenine pathway metabolites 3-hydroxyanthranilic acid and 3-hydroxykynurenine are UV filters found in the lens of the eye which protect the retina from UV light. These filters are synthesised from tryptophan in the lens, and with increasing age, less turnover of metabolites occur. 3-Hydroxyanthranilic acid and 3-hydroxykynurenine accumulate in the lens and “kynurenination” occurs, causing the lens to turn opaque (49). In addition, some kynurenine pathway metabolites are immunomodulatory and, consequently, can contribute to immunosuppressive pathways and suppress proliferation (or even cause apoptosis) of T-cells (50). However, the mechanisms of action of such metabolites are currently unknown.

### 1.9.2 *The physiological role of IDO*

In contrast to the relatively simple tryptophan metabolising role of hepatic TDO, which initiates the kynurenine pathway leading to the formation of NADH, several possible physiological roles have been suggested for IDO. Most significantly, it is associated with the antiviral and antiproliferative activities of interferon- $\gamma$  (IFN- $\gamma$ ) (Figure 1.5). IFN- $\gamma$  is a cytokine produced by activated T lymphocytes and natural killer cells, plays a vital role in host-cell defense against a variety of nonviral microbial pathogens, regulates immune responses, and inhibits cell growth (51). IFN- $\gamma$  induces the synthesis of a number of gene products in cells. Several of the induced gene products have been implicated in the IFN- $\gamma$ -mediated resistance to microbial infection (*Chlamydia psittaci*, *Taxoplasma gondii*) (52, 53). This includes

the production of nitric oxide synthase, activation of macrophages, and starvation of tryptophan due to induction of IDO enzyme, which catalyses the first step in tryptophan degradation. Although IFN- $\gamma$  is the most potent inducer of IDO activity, other cytokines probably act, either directly or in combination with IFN- $\gamma$ , to promote enzyme expression, *e.g.* interferon- $\alpha$ , interleukin-1 $\alpha$  and tumor necrosis factor- $\alpha$ .

It has also been discovered that IDO is involved in the proliferation of numerous cancers in the human body (54). IDO expression allows tumours to induce tolerance from the host's immune system by interacting with T-cells and depleting L-Trp levels. This is crucial for tumour progression, and certain cancers can be highlighted due to their IDO expression. Consequently, IDO has emerged as an attractive drug target in cancer treatments (55, 56).

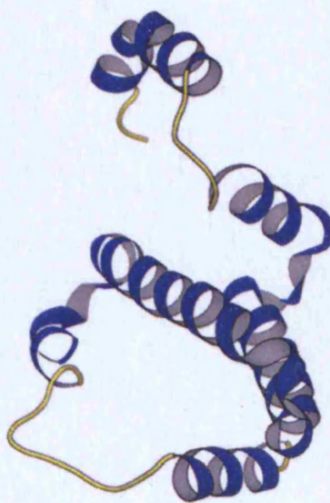


**Figure 1.5:** X-ray structure of IFN- $\gamma$  (monomer) (PDB 1HIG).

### 1.10 Bacterial expression of IDO and TDO enzymes

IDO has been purified from rabbit intestine by a combination of streptomycin treatment, ammonium sulfate fractionation and affinity chromatography, to apparent homogeneity as judged by polyacrylamide gel electrophoresis and analytical centrifugation. All studies on IDO were carried on rabbit IDO until Maeda *et al.*

developed an expression system for human IDO, where the protein was expressed in *E. coli* as a glutathione *S*-transferase (GST) fusion protein (57). However, the enzyme activity of the GST fusion protein (57) was only 20% of that of the native enzyme (58), suggesting that the addition of the GST tag significantly modified the structure of IDO. Taking into account these problems, Littlejohn *et al.* developed an efficient *E. coli* expression and purification system of hexahistidyl tagged recombinant human IDO (59). The hexahistidyl tag is an ideal short tag to overcome problems associated with GST fusion proteins (60, 61). Since then modifications have been made to the expression system of recombinant human IDO (rhIDO) to improve the yield of purified enzyme (62, 63).

TDO has been purified from rat liver and from bacteria by combination of methods similar to those mentioned above for rabbit IDO (streptomycin treatment, ammonium sulfate fractionation and affinity chromatography) (33, 64, 65). TDO isolated from rat liver and bacteria can be expressed and purified; as a result, the biochemical and biophysical properties of rat and bacterial TDO have been investigated for several decades. In contrast, a truncated form of recombinant human TDO (rhTDO) was only isolated in 2007 (66) and, more importantly, a few months later expression and purification of full length recombinant human TDO was reported (67). Consequently, there is very little mechanistic and structural information in the literature regarding human TDO.

### 1.11 The catalytic cycle of IDO and TDO

The commonly proposed catalytic cycle of IDO and TDO is schematically illustrated in Figure 1.6. Under physiological steady-state conditions, the majority of the enzyme is likely to be in the active, ferrous form. However, *in vitro* catalysis starts from the inactive ferric form; as a result electron transfer mediators are employed in this reaction (58). Interestingly, a recent study by Maghzal *et al.* suggested that cytochrome *b*<sub>5</sub>, an electron transfer protein, is most likely to donate an electron to ferric IDO *in vivo* (68). In this study they ruled out activation of ferric IDO by superoxide which was the favoured method of activation at the time proposed by Taniguchi (69). It is unknown whether cytochrome *b*<sub>5</sub> also reduces TDO, but a similar mechanism would appear likely.

After reduction of ferric IDO, ferrous IDO binds to tryptophan and  $O_2$ , although the exact order of sequence is not yet known, to form the ternary complex [IDO<sup>II</sup>-Trp- $O_2$ ]. Once the ternary complex is formed, it decomposes to yield the ferrous enzyme and product. For TDO, the lower reaction sequence in Figure 1.6 is the principal catalytic cycle, since ferrous TDO does not readily bind  $O_2$  in the absence of L-Trp (65).

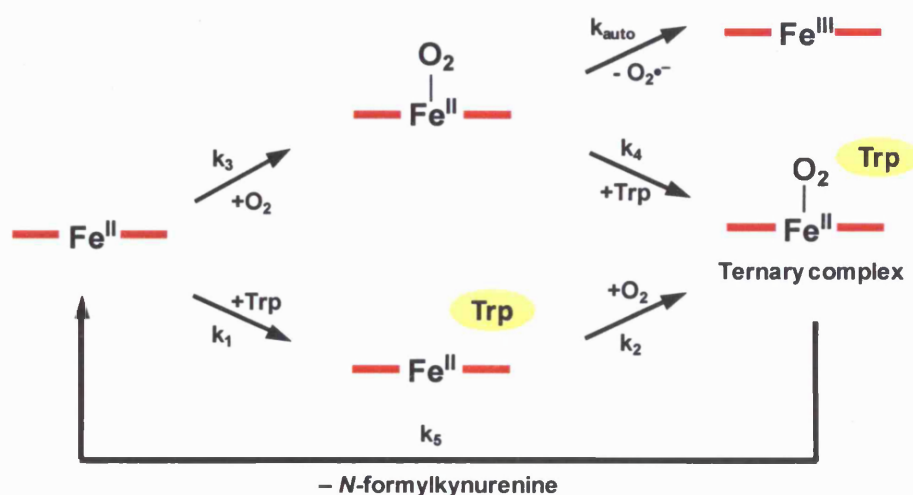


**Figure 1.6:** Proposed catalytic reaction cycles for IDO and TDO. The porphyrin macrocycle is abbreviated as a red line and the possible reaction intermediates are shown.

## 1.12 Crystallographic studies

### 1.12.1 The X-ray crystal structure of rhIDO

The X-ray crystal structure of ferric rhIDO was solved in 2006 by Sugimoto *et al.* (70) in complex with 4-phenylimidazole (PIM), a known inhibitor and heme ligand to IDO (71), and with cyanide (CN) bound. Interestingly, the enzyme was crystallized as a dimer (Figure 1.7), with a disulfide bridge formed between Cys308 residues from each monomer. The distance between the two monomers appears to be quite large ( $\sim 13$  Å), but a great number of water molecules form a hydrogen bond network between the two monomers. To date, there is no evidence in the literature of

IDO being a functional dimer, and it is known that dimerisation is a common crystallization artifact.

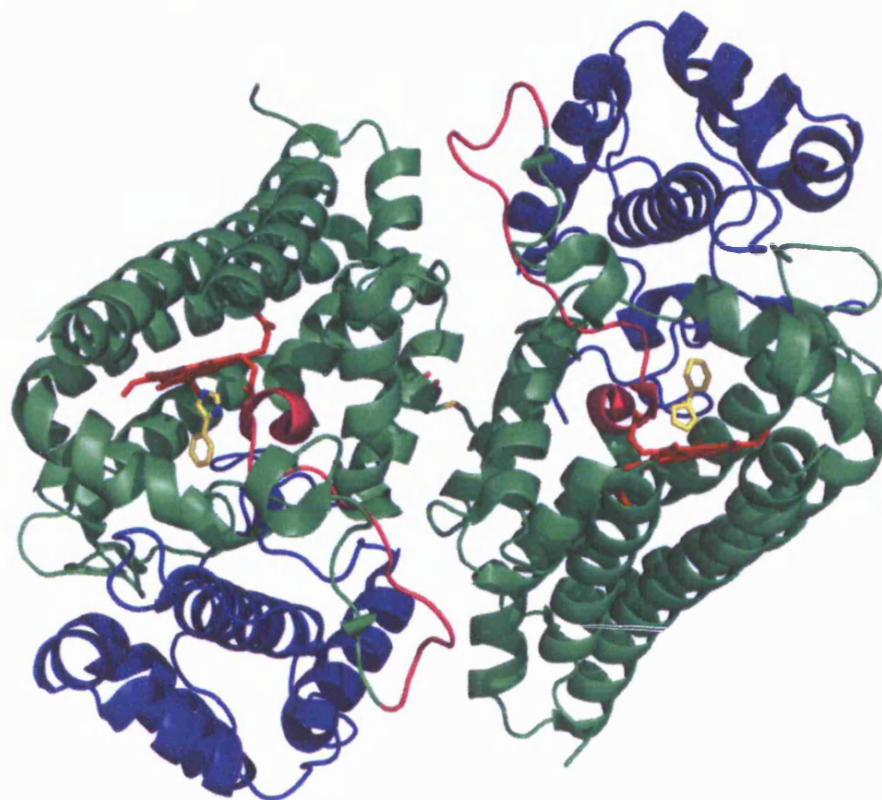


**Figure 1.7:** Crystal structure of rhIDO, showing the dimeric structure. The heme centres are shown in a red stick model. The disulfide bridge between the two Cys308 residues is shown in the centre.

The overall monomeric structure reveals the presence of a large (green) domain and small (blue) domain (Figure 1.8). While the smaller domain contains nine  $\alpha$ -helices and two  $\beta$ -sheets, the larger one is composed is an all  $\alpha$ -helical domain and is comprised of 15  $\alpha$ -helices and contains the catalytic pocket. Four long helices (G, I, Q and S) in the large domain run parallel to the heme plane. Helix Q provides an endogenous ligand (His346) for the heme iron at the fifth coordination position (proximal side). The heme binding pocket is created mainly by these four helices. The two domains are linked by a long loop, comprising of residues 250-267 which lies above the distal face of the heme, providing part of the binding cavity.

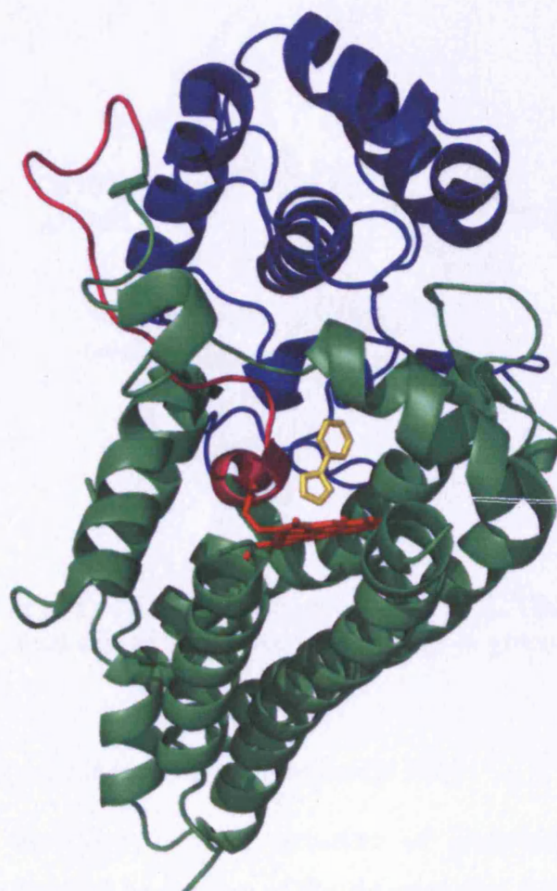


**Figure 1.8:** Ribbon representation of the overall structure of rhIDO in complex with 4-phenylimidazole (PIM) complex. The small and large domains are represented by blue and green ribbons, respectively. The long loop connecting the two domains is coloured magenta. The heme (red) and the inhibitor PIM (yellow) are shown in a ball-and-stick model.

The crystal structure of rhIDO also revealed a large abundance of hydrophobic residues around the heme centre (Phe163, Phe226, Phe227) (Figure 1.9), indicating a hydrophobic pathway for the entrance of the substrate. In the PIM-bound form, Phe163 is thought to interact with the phenyl group of PIM through  $\pi$ - $\pi$  stacking. Ser167, which is located 3.7 Å above the 3-methyl group of the heme, is one of the closest residues to the iron.

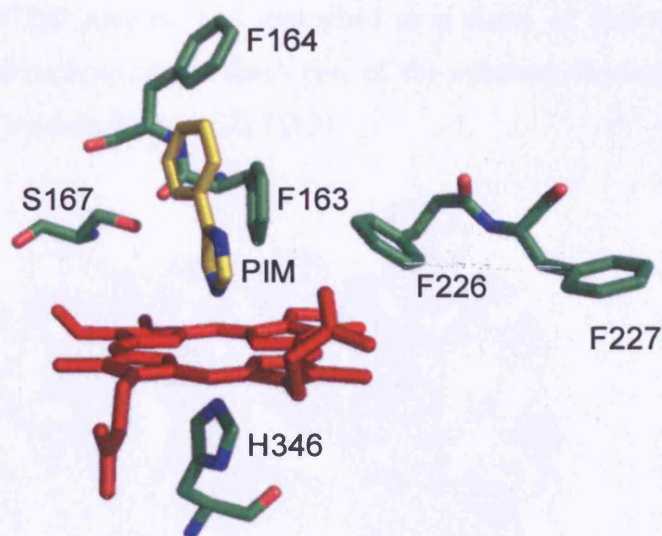


**Figure 1.9:** Active site of rhIDO in complex with PIM. The heme is shown in red, PIM in yellow and the rest of the active site residues in green.

### 1.12.2 The X-ray crystal structures of bacterial TDO

More recently, the X-ray crystal structure of *Ralstonia metallidurans* TDO (*RmTDO*), in the inactive ferric form of the enzyme, was solved by Zhang *et al* (44). Subsequently, the crystal X-ray crystal structure of *XcTDO* was solved by Forouhar *et al.* and it was obtained in the active ferrous form of the enzyme in complex with L-Trp (72), although crystal structures of *XcTDO* were also obtained in the absence of L-Trp. The crystal structures of *RmTDO* and *XcTDO* show that the enzymes are essentially identical (47% sequence identity), with the regions of the highest sequence similarity located near to the active site. Since the structure of *XcTDO* was obtained in the active ferrous form with substrate bound (L- or 6-fluoro-Trp) and is at a higher resolution, it will, therefore, provide the best ‘snapshot’ of the substrate-protein interactions present within the active site. For this reason, the crystal structure of *XcTDO* will be discussed in more detail than that of *RmTDO*.

*XcTDO* is an intimately associated tetramer and  $\sim 4500 \text{ \AA}^2$  of the surface area of each monomer is buried in the tetramer (Figure 1.10(A)). The structure of the *XcTDO* monomer contains 12  $\alpha$ -helices and no  $\beta$ -strands (Figure 1.10(B)).

The tetramer of *Xc*TDO may be best described as a dimer of dimers as the N-terminal residues of each monomer form part of the substrate-binding site in the adjacent monomer (residues 21-40 of *Xc*TDO).

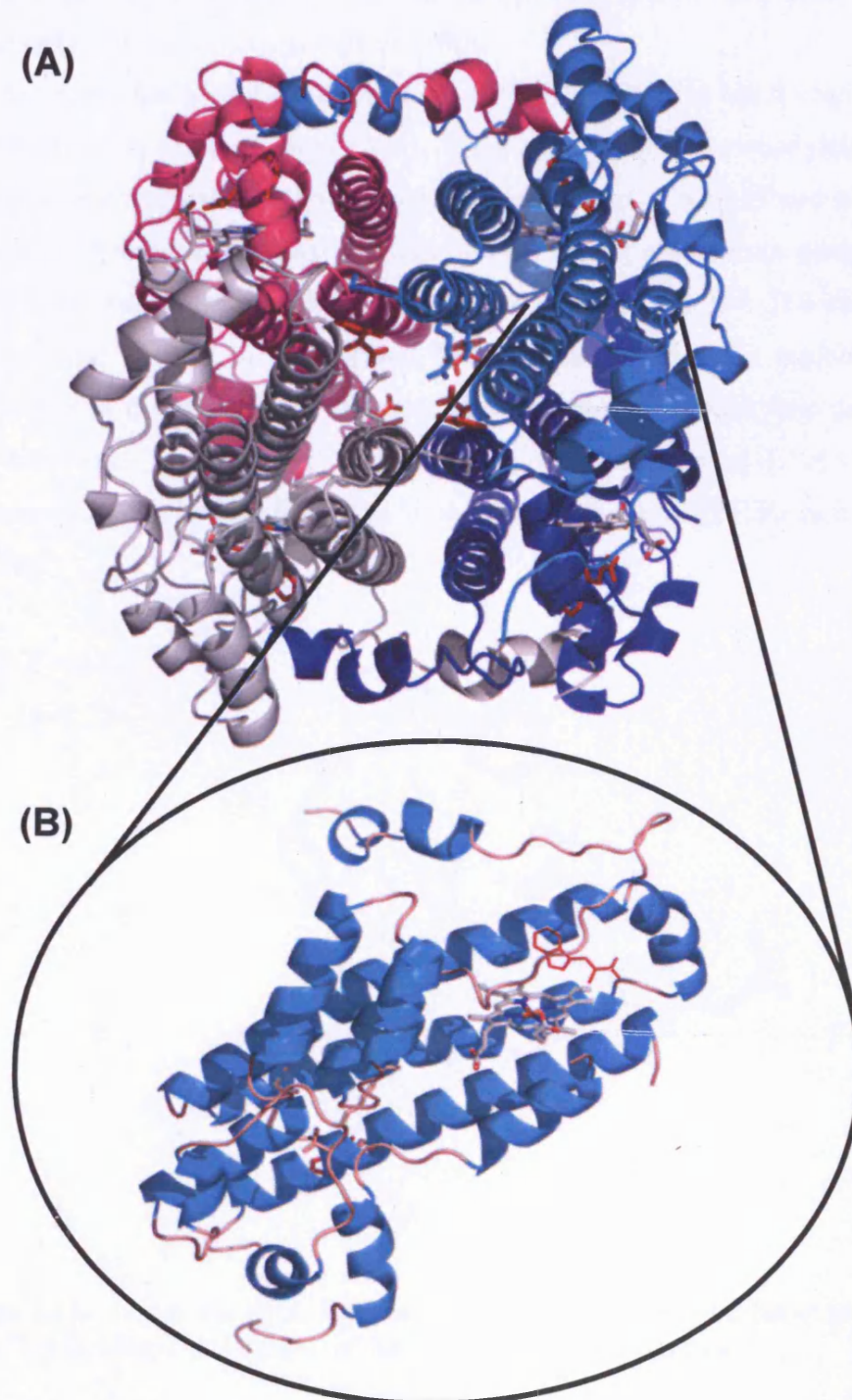


**Figure 1.10:** Crystal structure of *Xc*TDO showing the (A) tetrameric structure and (B) monomeric structure (in complex with L-Trp) where the helices are displayed in cyan and loop and joints in pink.

The active site of ferrous *Xc*TDO in complex with L-Trp is presented in Figure 1.11, and shows that the proximal site of the heme porphyrin is occupied by a histidine residue (His240). Interactions between L-Trp and the active site residues can be split into two groups: interactions with the indole ring system and those with the carboxylate and ammonium groups of L-Trp.

Like the active site of rhIDO, the distal cavity of *Xc*TDO also has a preponderance of hydrophobic residues, such as Phe51, Tyr24 and Tyr27. The carboxylate group of L-Trp has an electrostatic interaction with the side chain of Arg117 and is hydrogen bonded to the side chain hydroxyl group of Tyr113. The ammonium group of L-Trp is hydrogen bonded to the side chain hydroxyl group of Thr254. The carboxylate-binding motif appears to be essential for substrate binding; the arginine residue reorientates in the presence of substrate, coordinating the carboxylate group of L-Trp, with “open” and “closed” conformations observed (Figures 1.12(A) and (B), respectively); the open conformation is observed with ferric *Xc*TDO in the absence of L-Trp.

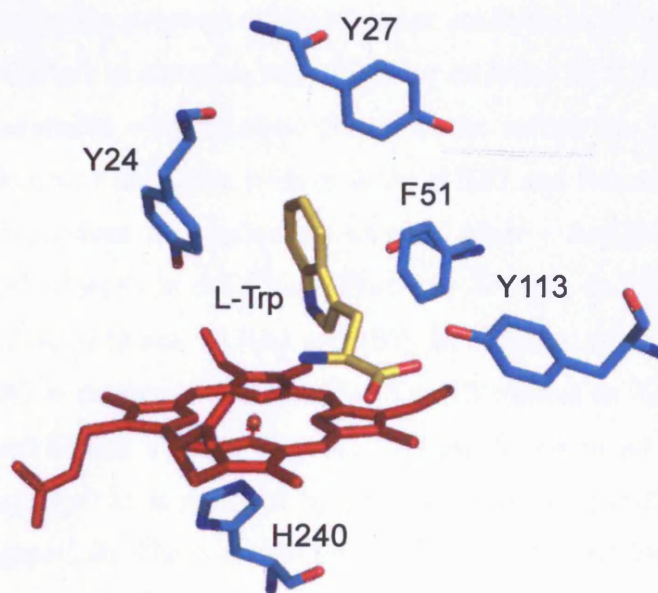


**Figure 1.11:** Active site of *Xc*TDO in complex with L-Trp. The heme is shown in red, L-Trp in yellow and the rest of the active site residues in cyan.

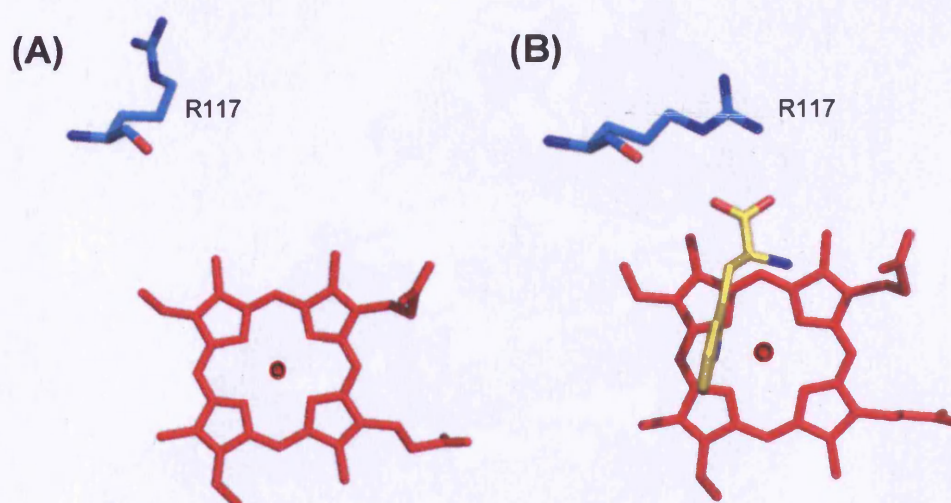


**Figure 1.12:** The crystal structures of (A) ferric *XcTDO* and (B) ferrous *XcTDO* in complex with L-Trp showing the active site residue R117 in different conformations.

### 1.12.3 Comparison of IDO and TDO crystal structures

As mentioned earlier, the structure of rhIDO is not available in complex with L-Trp, but instead was solved in complex with PIM, an inhibitor to IDO. Currently, the only structures available with substrate-bound at the active site are for *XcTDO*. Structural alignments of the active sites of ferric rhIDO and ferrous *XcTDO* reveal many active site residues are equivalent to each other - Arg231 in rhIDO and Arg117 in *XcTDO*, Phe163 in rhIDO and Phe51 in *XcTDO*, and Tyr126 in rhIDO and Tyr24 in *XcTDO* (Figures 1.13(A) and (B)). In addition, the position occupied by Phe226 in IDO is replaced with a similar Tyr113 residue in *XcTDO*. Residues equivalent to Arg117 and Tyr113 from *XcTDO* are found in all TDO and IDO enzymes, although Tyr113 is replaced by phenylalanine in approximately 50% of IDO species (Figure 1.4). The most striking difference between the active sites of the two dioxygenase enzymes is the presence of His55 in *XcTDO* and in rhIDO the equivalent residue is Ser167. In *XcTDO*, the histidine side chain is hydrogen bonded with the indole nitrogen atom of L-Trp and it has been proposed that His55 could play a role in the reaction mechanism; the role of Ser167 in rhIDO is less clear in the absence of a substrate-bound crystal structure.

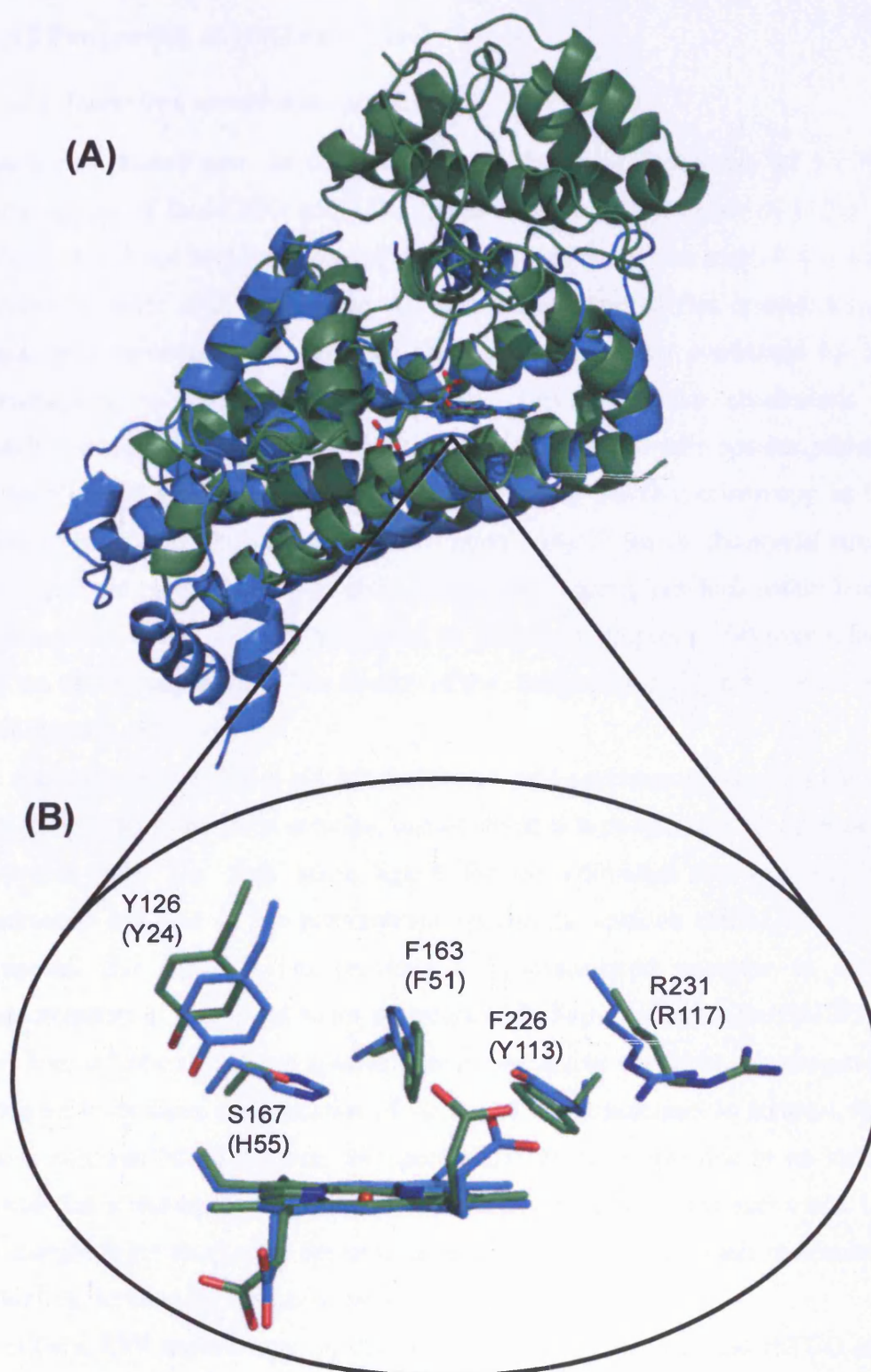


**Figure 1.13:** (A) Structural overlay between the rhIDO-PIM complex (green) and the *Xc*TDO-Trp complex (cyan). The heme centres are shown in a stick model. (B) Overlay of the active sites of the two dioxygenases with the residues for rhIDO (green) indicated and those for *Xc*TDO (cyan) in parentheses.

## 1.13 Properties of IDO and TDO

### 1.13.1 Heme iron coordination structures

Numerous studies have been carried out to determine the nature of the distal environment of ferric IDO and TDO in the absence and presence of L-Trp. UV-visible, MCD and EPR spectroscopy at pH 6.0 revealed the presence of two distinct species in ferric IDO: a high-spin and a low-spin heme species in approximately equal population (63, 73, 74). The high-spin species was confirmed by MCD spectroscopy as arising from histidine/water ligation. Similar conclusions were reached using resonance Raman spectroscopy (74). The low-spin species, which has been observed previously (73, 74), was assigned by MCD spectroscopy as being consistent with bis-nitrogenous ligation (Figure 1.14). However, the crystal structure of rhIDO did not reveal any potential nitrogenous ligating residues within bonding distance of the iron. Hydroxide-ligation, as previously proposed (74), was ruled out by the MCD analyses (63). The identity of the nitrogenous 6<sup>th</sup> ligand in ferric rhIDO still remains unknown.

In the presence of L-Trp at pH 8.0, MCD and EPR spectroscopy confirm that there are three distinct species in solution, one of which is high-spin and the other two are low-spin (63). The sixth heme ligand for the additional low-spin species is hydroxide and this is the predominant species in solution (60%). It was also proposed that bound L-Trp provides a hydrogen-bond acceptor to stabilise deprotonation of the bound water molecule (63). Ferric substrate-free rhIDO does not form a hydroxide-bound species because the active site lacks a hydrogen-bond acceptor to facilitate deprotonation of the bound water molecule. In contrast, for the ferric substrate-bound enzyme, the spectra are pH dependent due to an ionisable interaction affecting the formation of the hydroxide species in the active site. L-Trp is thought to act as a proton acceptor, deprotonating the bound water molecule and, therefore, forming the hydroxide bound species (Figure 1.14).

Similarly, EPR experiments on *Pseudomonas* TDOs, rat liver and rhTDO in the ferric state have shown the presence of two distinct species in solution, a high-spin form and a low-spin form (67, 75). The high-spin species is postulated to be a water molecule whilst that of the low-spin species is postulated to be hydroxide. This is possible for substrate-free TDO since a histidine residue is present in the active site to deprotonate the heme-bound water molecule in *Xc*TDO (72). EPR data show that

addition of L-Trp to the ferric enzyme causes an increase in the low-spin component with a decrease in the high-spin component (75). This indicates that L-Trp binding to the ferric protein causes increased deprotonation of the heme-bound water and could be caused by L-Trp deprotonating the bound water molecule, rather than the active site histidine.

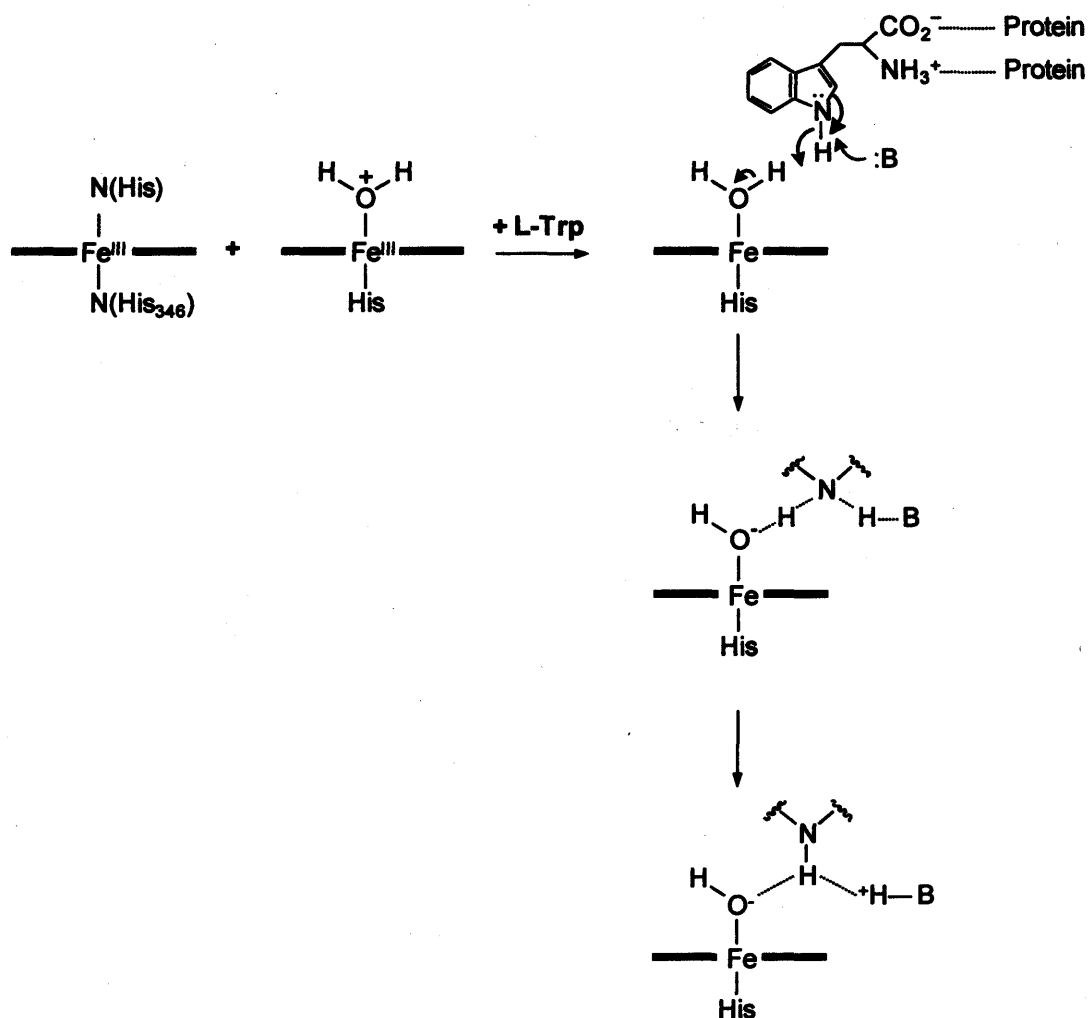


**Figure 1.14:** Proposed mechanism for substrate binding and hydrogen-bond formation in ferric IDO. This figure is reproduced from reference (63).

### 1.13.2 O<sub>2</sub> and CO binding

The oxygenated form of rabbit IDO was detected by Taniguchi *et al.* (76) and this intermediate was reported to have similar spectral characteristics to other O<sub>2</sub> utilising heme proteins such as myoglobin and hemoglobin (77). In contrast, upon reaction of *Pseudomonas fluorescens* TDO with O<sub>2</sub>, a species was detected that resembled the ferric form *Pseudomonas fluorescens* TDO and it was proposed that the enzyme was oxidised by O<sub>2</sub> (65). But when the same reaction was carried out in the presence of L-Trp an 'oxygenated species' was detected which had spectral features that resembled other well-characterised oxygenated heme proteins. To date, no such studies have been carried out on the human heme dioxygenases.

In 1980, Sono determined that rabbit IDO could also bind CO and that upon addition of L-Trp small spectral changes (blue shifts) were observed of the Soret band (78). In addition, equilibrium studies of L-Trp binding to the CO-bound enzyme [IDO<sup>II</sup>-CO]<sup>a</sup> suggested that the binding of L-Trp to the ferrous enzyme ( $K_D = 13 \mu\text{M}$ ), rather than that of L-Trp to the CO-bound enzyme ( $K_D = 350 \mu\text{M}$ ), is the order of binding adopted in the catalytic reaction cycle (78, 79). However, the reverse binding order has not been excluded. More recently, resonance Raman spectroscopy of CO and NO binding to ferrous TDO and IDO suggests that in TDO the C<sup>2</sup>-C<sup>3</sup> double bond of the indole ring (from L-Trp) faces the distal heme bound ligand (66). Whereas in IDO, the indole nitrogen appears to hydrogen bond with the heme-bound ligand (74). These differences between TDO and IDO suggest that the two dioxygenases may carry out the oxidative cleavage of L-Trp via different mechanisms

There are numerous reports in the literature that H<sub>2</sub>O<sub>2</sub> can activate oxidised TDO (46, 80-82); however, the reaction of oxidized TDO with H<sub>2</sub>O<sub>2</sub> has not been extensively studied.

### 1.13.3 Catalytic activity

Numerous studies with rabbit and human IDO have shown that both enzymes can catalyse the dioxygenation of L- and D-Trp, 5-hydroxy-D- and L-Trp, and tryptamine (Figure 1.15) (36, 58, 83). The above results indicate that human IDO is essentially

---

<sup>a</sup> Assuming that the CO-bound enzyme (Fe<sup>II</sup>-CO) has a tryptophan-binding property similar to that of the oxygenated enzyme (Fe<sup>II</sup>-O<sub>2</sub>).

identical to the rabbit enzyme in terms of molecular and catalytic properties. In addition to this, rabbit IDO has also been shown to utilise 4-, 5- and 6-fluoro-Trp (14). TDO, on the other hand, can only utilise L-Trp, 5-fluoro-Trp and 6-fluoro-Trp (Figure 1.15). D-Trp is a competitive inhibitor of TDO at high concentrations (14).

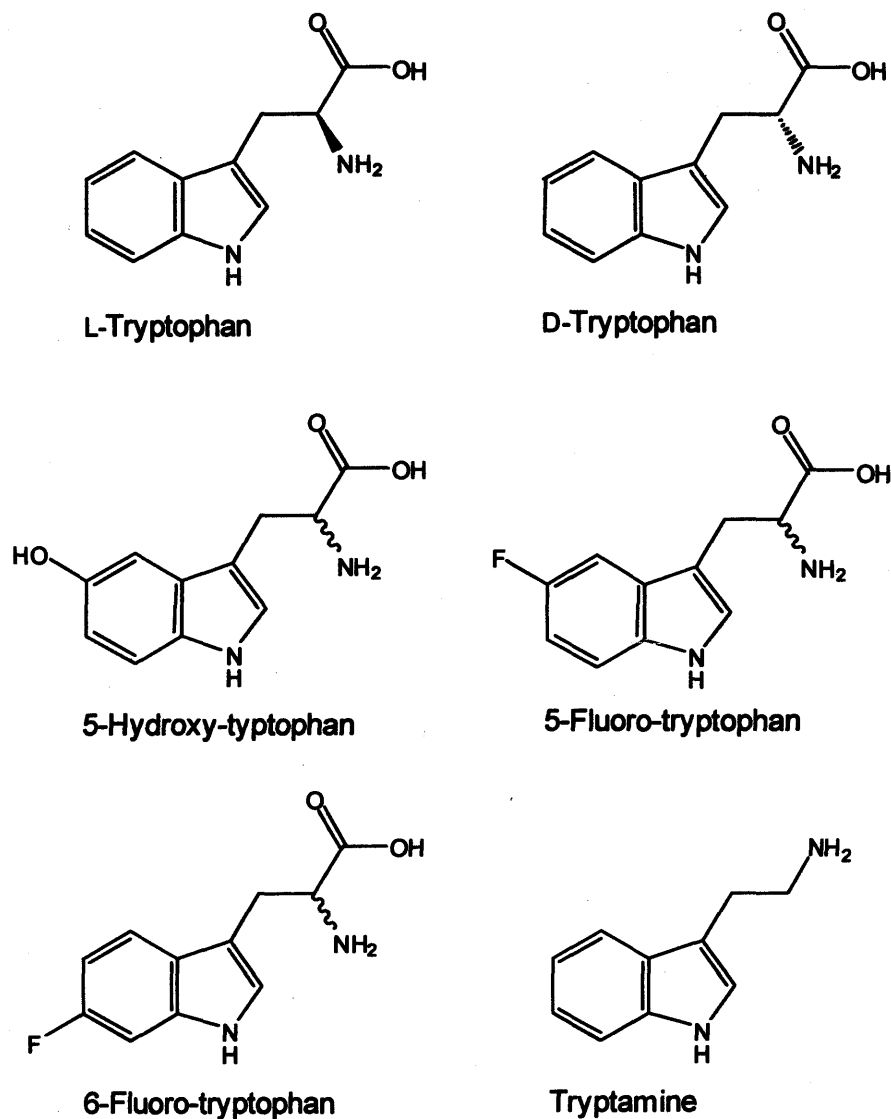


**Figure 1.15:** Structures of tryptophan analogues.

As mentioned earlier, the active form of IDO and TDO is the ferrous form of the enzyme and therefore *in vitro*, reducing agents are employed in the reaction. However, there are several reports in the literature that ferric TDO and IDO can dioxygenate L-Trp and D-Trp, respectively, and the reactions were monitored by

formation of *N*-formyl-kynurenine, in the absence of any reducing agents. The mechanism of this unusual and atypical activity still remains to be revealed.

#### 1.13.4 IDO and TDO inhibition

IDO is a therapeutic target for the development of new anticancer drugs and because of this great importance has been given to the design of new, highly selective and potent inhibitors of its action (84-88).  $\beta$ -Carboline derivatives were the first inhibitors of IDO and TDO to be identified in the literature by Eguchi *et al* (89). More specifically, they found that  $\beta$ -carboline derivatives inhibited both IDO (22-96% inhibition) and TDO (9-75% inhibition) activities from various sources. Among them, norharman (Figure 1.16(A)) was most potent for both enzymes from mammalian sources. Norharman, a relatively large ligand, does not readily form complexes with myoglobin or horseradish peroxidase (HRP), but can bind to IDO and TDO (90). Norharman binds directly to the heme iron of the enzyme as a nitrogen donor ligand. Thus, it competes with O<sub>2</sub> for the heme iron ferrous enzyme, resulting in inhibition (71).

A few years later, Cady *et al.* reported L-Trp analogues that were competitive inhibitors of rabbit IDO (91). These inhibitors are 1-methyl-DL-tryptophan (Figure 1.16(B)),  $\beta$ -[3-benzo(b)thienyl]-DL-alanine (the sulfur analogue of Trp, Figure 1.16(C)) and  $\beta$ -(3-benzofuranyl)-DL-alanine (the oxygen analogue of Trp, (Figure 1.16(D)). All three analogues showed competitive inhibition kinetics indicating that the analogues are binding to the same site in the enzyme as the substrate, L-Trp. However, the most potent inhibitor was found to be 1-methyl-DL-tryptophan, with a  $K_i$  of 6.6  $\mu$ M. These results suggested that the free form of the indole NH is important for binding and that its replacement with more electron-inductive atoms such as sulfur and oxygen removes the ability of L-Trp to act as a substrate.

Most of the known IDO inhibitors are tryptophan analogues, which are active only at concentrations of  $>6 \mu$ M, making them marginal drug candidates. This prompted several groups to find inhibitors from alternative sources. In 2006, annulin C and exigamine A (Figures 1.17(A) and (B)), which are both natural products, were extracted from the marine orange hydroid *Garveia annulata* and from the marine sponge *Neopetrosia exigua*, respectively. They were both found to be potent

inhibitors of IDO with  $K_i$  values of 140 nM for annulin C and 210 nM for exiguamine A (92, 93). The potency of the natural product inhibitors should make them useful tools to investigate the mechanism of action of IDO *in vitro*, but further studies on human cells will be required to determine if they have potential as drug leads or cell biology tools.

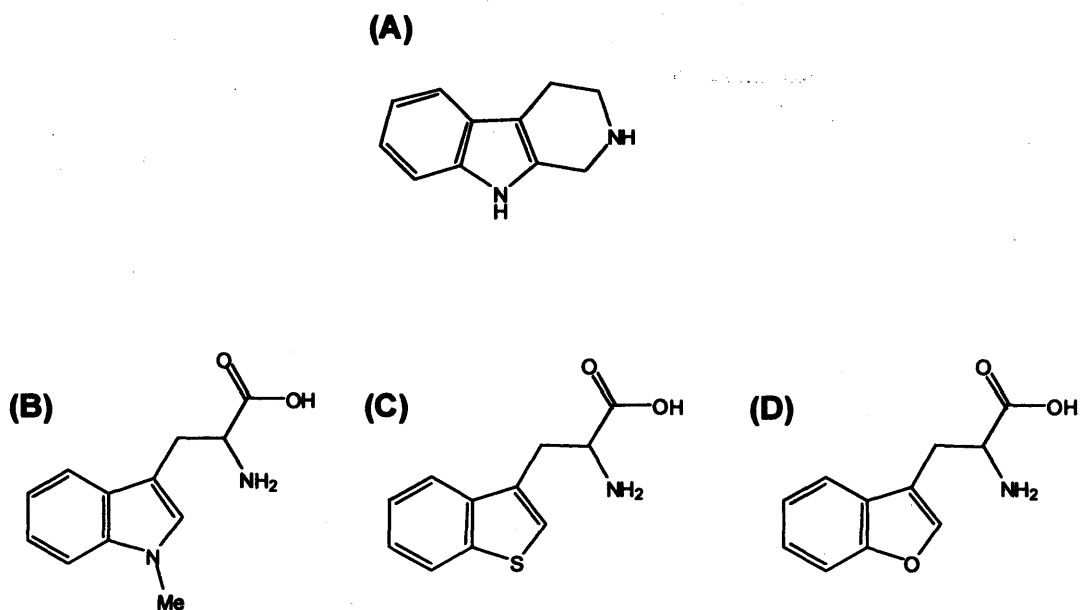


**Figure 1.16:** Structures of (A) norharman ( $\beta$ -carboline), (B) 1-methyl-DL-tryptophan, (C)  $\beta$ -[3-benzo(b)thienyl]-DL-alanine and (D)  $\beta$ -(3-benzofuranyl)-DL-alanine.

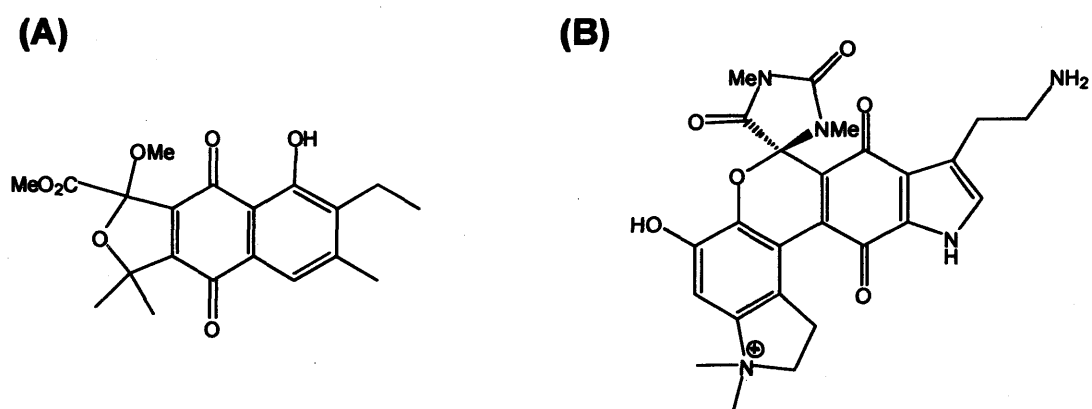


**Figure 1.17:** Structures of (A) annulin C and (B) exiguamine A, both of which are natural products and potent inhibitors of IDO.

### 1.13.5 Redox properties of IDO and TDO

There is very little information in the literature regarding the reduction potentials of the heme dioxygenases, but those values that have been reported are presented in Table 1.1. Upon substrate binding, there is an increase in reduction potential for both IDO and TDO, reflecting additional stabilisation of the ferrous derivative. The increase is larger for TDO proteins (except for rhTDO), compared to IDO proteins. The large positive change in the reduction potential for both enzymes suggests that there is a significant stabilisation of the ferrous form when substrate is bound. This stabilisation could also play a physiological role in keeping the proteins reduced, and therefore active, when L-Trp is present.

**Table 1.1:** Reduction Potentials for the Fe<sup>III</sup>/Fe<sup>II</sup> couple in the absence and presence of L-Trp.

Enzyme	<i>E</i> <sup>o</sup> /mV			Ref
	Substrate-free	Substrate-bound	Δ	
rhIDO	-30	-16	+46	(63)
rhTDO	-92	-76	+16	(67)
XcTDO	+8	+144	+136	(72)
Rat liver TDO	+100	+160	+60	(94)

### 1.14 Proposed reaction mechanisms

In contrast to the heme monooxygenases (cytochrome P450 and heme oxygenase) and non-heme dioxygenases (catechol dioxygenase and naphthalene dioxygenase) (14, 95-99), the reaction mechanism of IDO and TDO are still poorly understood, this is mainly because:

- of a lack of structural information in the literature for the heme dioxygenases (crystal structures of rhIDO, *Xc*TDO and *Rm*TDO were solved in 2006 and onwards),
- the reactive catalytic intermediates have not been identified and characterised,
- no similar reaction is observed in other heme enzymes.

As mentioned earlier, once the IDO and TDO enzymes have been reduced to the active ferrous form, they then bind L-Trp and O<sub>2</sub> to form the ternary complex [Fe<sup>II</sup>-Trp-O<sub>2</sub>]. Various mechanisms have been proposed for oxygen activation following the formation of the ternary complex in IDO and TDO. Sono *et al.* proposed that catalysis can proceed either *via* an ionic or a radical mechanism (14). Leeds was the first to propose a radical mechanism for rat liver TDO in 1993 (Figure 1.18) (100). The proposed radical mechanism involved base-catalysed deprotonation of the N<sup>1</sup> hydrogen to generate the L-Trp anion, followed by addition of oxygen to the C<sup>3</sup> position of the indole ring. Subsequent cyclization of oxygen to the C<sup>2</sup> position results in formation of a dioxetane intermediate.

However, formation of such a tryptophan radical has been reported to be thermodynamically unfavourable and as a result this radical mechanism was discounted as a valid route for product formation (14).

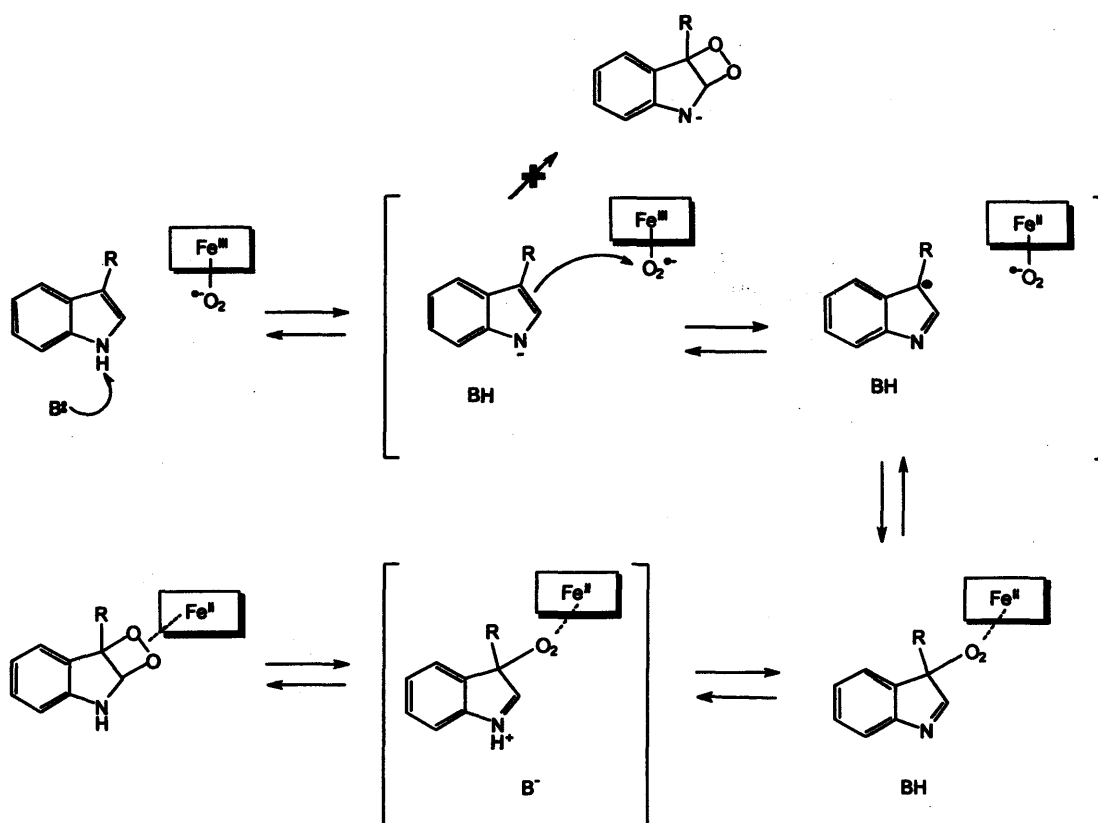


**Figure 1.18:** Reaction mechanism for TDO dioxygenation proposed by Leeds *et al* (100). This mechanism is reproduced from reference (100).

A few years later Sono *et al.* proposed an ionic mechanism (Figure 1.19) (14, 101) which was thought to proceed via deprotonation of the N<sup>1</sup> hydrogen by an active site base, which then stimulates nucleophilic attack by the electron-rich indole carbon (third position) on the distal oxygen atom. This results in a 3-indolenylperoxy-Fe<sup>II</sup> intermediate being formed (X), which can then be converted to *N*-formyl-kynurenine in one of two ways. The intermediate could undergo (a) Criegee rearrangement (102) producing another intermediate, which would then undergo further rearrangement to yield the product; or, the pathway may also proceed via (b) a dioxetane intermediate, which would then rearrange to form *N*-formyl-kynurenine.

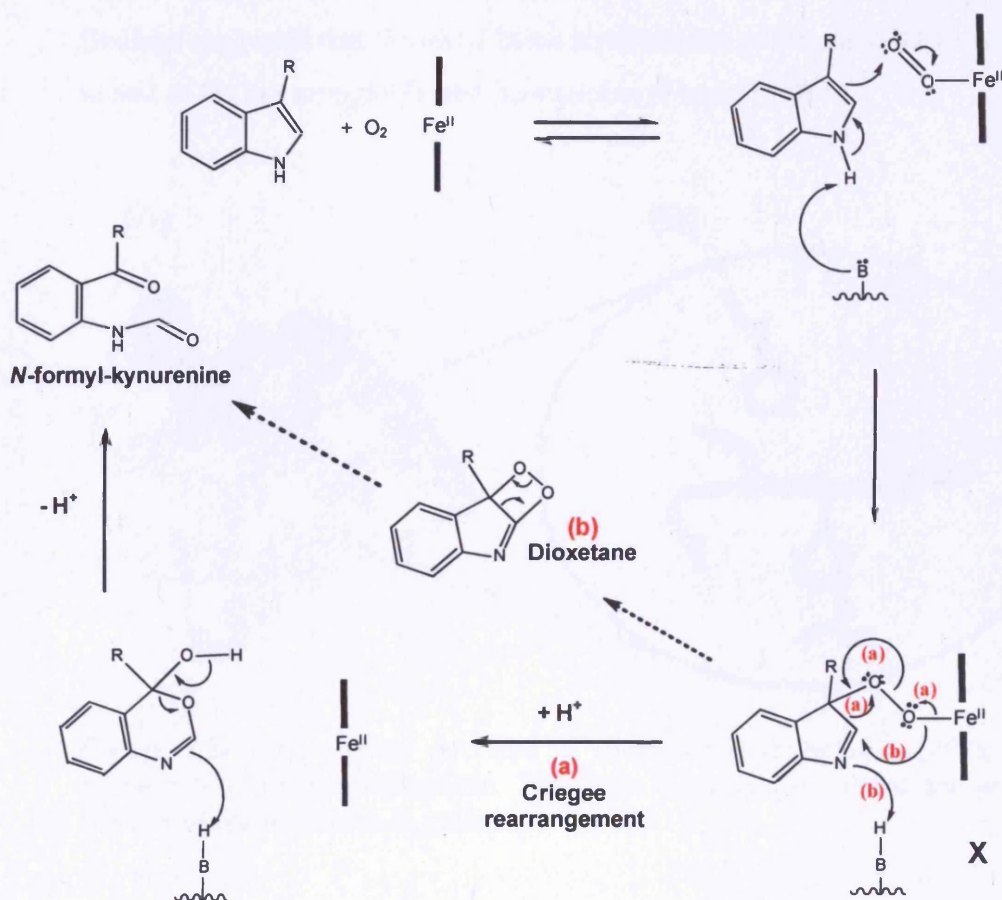


**Figure 1.19:** Possible reaction mechanisms for IDO and TDO as proposed by Sono *et al* (14). This mechanism is reproduced from reference (14).

For several years, it was assumed that the reaction mechanism of IDO and TDO was initiated by deprotonation of the N<sup>1</sup> hydrogen from L-Trp by an active site base. Several reports in the literature led to the proposal of this mechanism.

- EPR spectroscopy of IDO (36), suggested that the fifth (proximal) ligand of the heme was nitrogenous, probably from a histidine imidazole ring. The sixth (distal) ligand in substrate-free IDO was proposed to be from a histidine imidazole nitrogen (73, 103) based on MCD spectroscopy. Uchida *et al.* (103) suggested that, in substrate-bound ferric IDO, the sixth ligand was also a histidine. In addition, MCD spectroscopy of ferrous IDO confirmed the presence of five-coordinate high-spin heme; there was no evidence for low-spin heme, which suggests that any internal (nitrogenous)

ligands that were present in the ferric form are no longer coordinated. The findings suggested that the distal heme environment of ferrous IDO is similar to that of ferrous myoglobin and hemoglobin (Figure 1.20).

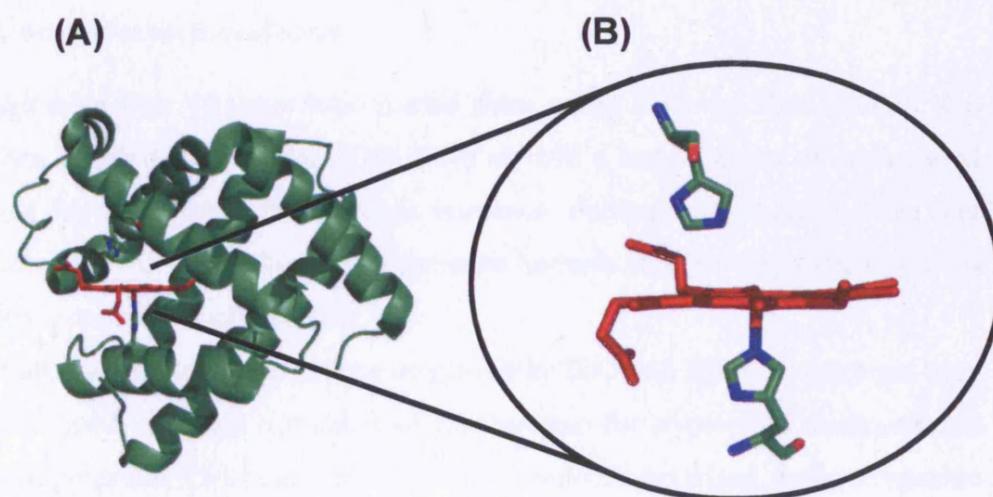


**Figure 1.20:** (A) Crystal structure of horse heart myoglobin (104), (B) Active site of ferrous myoglobin. The heme is shown in red and the active site histidines are shown in green.

- Sequence alignment studies by Suzuki *et al.* (105) between mollusc IDO-like myoglobins, human IDO, mouse IDO and a homologue in yeast revealed a 37% sequence identity. From these studies, it was revealed that there are two histidine residues, at position 335 and 380, that are conserved in all the sequences, one of which is most likely to correspond to the heme binding proximal histidine. If His380 is assigned to the heme binding proximal histidine, then His335 may be assigned to the distal histidine by analogy with usual myoglobins and hemoglobins. The amino acid sequence for rhIDO identified the two residues as His346 (proximal) and His303 (distal).
- As mentioned earlier, Cady and Sono demonstrated that methylation of the indole nitrogen (1-methyl-tryptophan) converts the substrate into a competitive inhibitor of IDO (91). This led to the proposal that deprotonation of the N<sup>1</sup> hydrogen was essential for catalysis, and since it was already believed that a histidine residue, an ideal active site base, was present in the distal cavity of IDO (from EPR studies and sequence alignments with

mollusc IDO-like myoglobins), deprotonation of the N<sup>1</sup> hydrogen was proposed to occur by the active site histidine.

### 1.15 Unanswered questions

Although more than 40 years have passed since rabbit IDO was first isolated, and more than 70 years for rat liver TDO, there are still a large number of unanswered questions for these heme dioxygenase enzymes. Furthermore, there is even less information for the human heme dioxygenases because efficient expression systems have been established only recently.

First of all, the catalytic mechanisms employed by IDO and TDO have not yet been fully elucidated, although a number of mechanisms for tryptophan dioxygenation have been proposed. This is in contrast to other, well-characterised, heme oxygenase enzymes such as the cytochrome P450 enzymes. Catalytic intermediates utilised by the cytochrome P450s have been characterised using crystallographic analysis and by using specialised techniques such as EPR and <sup>1</sup>H ENDOR spectroscopy, which allows identification of reactive intermediates at cryogenic temperatures.

Second, there is no crystal structure for rhIDO in the presence of substrate; therefore, the nature of the substrate binding and Fe-oxygen interactions, the role of individual residues in catalytic activity and substrate binding are all unknown. The role of individual active site residues can also be probed using site-directed mutagenesis; however, only a preliminary analysis of rhIDO has been reported in the literature.

Structural alignments of the active sites of ferric rhIDO and ferrous *Xc*TDO reveal that His55 from *Xc*TDO, which is proposed to play an important role in the catalytic mechanism, is replaced by Ser167 in rhIDO. The role of this residue in rhIDO still remains unclear.

## **1.16 Thesis aims**

In the context of the above discussion, the objectives of this thesis were:

- To investigate the role of Ser167 in rhIDO
- To elucidate the precise catalytic mechanism of rhIDO and rhTDO.
- To identify and characterise reaction intermediates of rhIDO and compare them with other members of the heme oxygenase family.
- To investigate the roles of individual active site residues of rhIDO on dioxygen and substrate binding and in catalysis.
- To gain structural information.

The results of the above studies can be used to build a more detailed picture of the possible mechanism of the rhIDO and rhTDO enzymes, and the collective implications of these results can be used to inform our current understanding of the mechanism of heme dioxygenase catalysis.

## 1.17 References

1. Valentine, J. S., Foote, C.S., Greenberg, A., and Liebman, J.F. (1995) *Active Oxygen in Biochemistry*, Chapter 1.
2. Bugg, T. D. H. (2003) Dioxygenase enzymes: catalytic mechanisms and chemical models, *Tetrahedron* 59, 7075-7101.
3. Jones, R. D., Summerville, D. A., and Basolo, F. (1979) Synthetic oxygen carriers related to biological systems, *Chem. Rev.* 79, 139-179.
4. Lee-Ruff, E. (1977) The organic chemistry of superoxide, *Chem. Soc. Rev.* 6, 195-214.
5. Sutton, W. B. (1954) Isolation and properties of a lactic oxidative decarboxylase from *Mycobacterium phlei*, *J. Biol. Chem.* 210, 309-320.
6. Winterhalter, K. H. (1976) *Chimia* 30, 9.
7. Brigelius, R., Spottl, R., Bors, W., Lengfelder, E., Saran, M., Weser, U. (1974) Superoxide dismutase activity of low molecular weight  $\text{Cu}^{2+}$ -chelates studied by pulse radiolysis, *FEBS Lett.* 47, 72-75.
8. Que, L., Jr., and Ho, R. Y. (1996) Dioxygen Activation by Enzymes with Mononuclear Non-Heme Iron Active Sites, *Chem. Rev.* 96, 2607-2624.
9. Dunford, H. B. (1999) *Heme peroxidases*, John Wiley & Sons, New York.
10. English, A. M., and Tsaprailis, G. (1995) Catalytic structure-function relationships in heme peroxidases, *Adv. Inorg. Chem* 43, 79-125.
11. Wong, L. L. (1998) Cytochrome P450 monooxygenases, *Curr. Opin. Chem. Biol.* 2, 263-268.
12. Mason, H. S., Fowlks, W. L., Peterson, E. (1955) Oxygen transfer and electron transport by the phenolase complex, *J. Am. Chem. Soc.* 77, 2914-2915.
13. Hayaishi, O., Katagiri, M., Rothberg, S. (1955) Mechanism of the pyrocatechase reaction, *J. Am. Chem. Soc.* 77, 5450-5451.
14. Sono, M., Roach, M. P., Coulter, E. D., and Dawson, J. H. (1996) Heme-Containing Oxygenases, *Chem. Rev.* 96, 2841-2888.
15. Hayaishi, O., Sutton, W. B. (1957) Enzymatic oxygen fixation into acetate concomitant with the enzymatic decarboxylation of L-Lactate, *J. Am. Chem. Soc.* 79, 4809.

16. Foster, T. L., Caradonna, J. P. (2004) Non-heme mono-iron enzymes, *Comp. Coord. Chem. II* 8, 343-368.
17. Liu, J., Wu, X., Li, F., Su, Z., and Zhang, Y. (2006) Recent progress in oxygenase-catalyzed biotransformations, *Huagong Shengchan Yu Jishu* 13, 36-39.
18. Bollinger, J. M., and Krebs, C. (2006) Stalking intermediates in oxygen activation by iron enzymes: Motivation and method, *J. Inorg. Biochem.* 100, 586-605.
19. Mason, H. S., North, J. C., and Vanneste, M. (1965) Microsomal mixed-function oxidations: the metabolism of xenobiotics, *Fed. Proc. Fed. Am. Soc. Exp. Biol.* 24, 1172-1180.
20. Gunsalus, I. C., Pederson, T. C., and Sligar, S. G. (1975) Oxygenase-catalyzed biological hydroxylations, *Annu. Rev. Biochem.* 44, 377-407.
21. Meunier, B., de Visser, S. P., and Shaik, S. (2004) Mechanism of oxidation reactions catalyzed by cytochrome P450 enzymes, *Chem. Rev.* 104, 3947-3980.
22. Hayaishi, O., Hashimoto, K. (1950) Pyrocatecase a new enzyme catalyzing oxidative breakdown of pyrocatechin, *J. Biochem.* 37, 371-374.
23. Bugg, T. D. (2001) The development of mechanistic enzymology in the 20<sup>th</sup> century, *Nat. Prod. Rep.* 18, 465-493.
24. Oka, T., and Simpson, F. J. (1971) Quercetinase, a dioxygenase containing copper, *Biochem. Biophys. Res. Commun.* 43, 1-5.
25. Hund, H. K., Breuer, J., Lingens, F., Huttermann, J., Kappl, R., and Fetzner, S. (1999) Flavonol 2,4-dioxygenase from *Aspergillus niger* DSM 821, a type 2 Cu<sup>II</sup>-containing glycoprotein, *Eur. J. Biochem.* 263, 871-878.
26. Lombardini, J. B., Singer, T. P., and Boyer, P. D. (1969) Cystein oxygenase. II. Studies on the mechanism of the reaction with <sup>18</sup>oxygen, *J. Biol. Chem.* 244, 1172-1175.
27. Straganz, G., Brecker, L., Weber, H. J., Steiner, W., and Ribbons, D. W. (2002) A novel beta-diketone-cleaving enzyme from *Acinetobacter johnsonii*: acetylacetone 2,3-oxygenase, *Biochem. Biophys. Res. Commun.* 297, 232-236.

28. Kotake, Y., Ito, N. (1937) Studien uber den intermediaren stoff-wechsel des tryptophans: XXV. Isolierung des d-kynurenins, *Biochem. J.* 25, 71-77.
29. Kotake, Y., Masayama, T. (1937) *Hoppe-Seyler's J. Phys. Chem.* 243, 237-238.
30. Hayaishi, O., Takikawa, O., Yoshida, R., Yasui, H. (1984) Indoleamine-dioxygenase - A possible biological function, *Progress in Tryptophan and Serotonin Research*, 33-42.
31. Watanabe, Y., Fujiwara, M., Yoshida, R., and Hayaishi, O. (1980) Stereospecificity of hepatic L-tryptophan 2,3-dioxygenase, *Biochem. J.* 189, 393-405.
32. Knox, W. E., and Mehler, A. H. (1951) The adaptive increase of the tryptophan peroxidase-oxidase system of liver, *Science* 113, 237-238.
33. Tanaka, T., and Knox, W. E. (1959) The nature and mechanism of the tryptophan pyrrolase (peroxidase-oxidase) reaction of *Pseudomonas* and of rat liver, *J. Biol. Chem.* 234, 1162-1170.
34. Hirata, F., and Hayaishi, O. (1975) Studies on indoleamine 2,3-dioxygenase. I. Superoxide anion as substrate, *J. Biol. Chem.* 250, 5960-5966.
35. Higuchi, K., Hayaishi, O. (1967) Enzymic formation of D-kynurenine from D-tryptophan, *Arch. Biochem. Biophys.*, 120, 397-403.
36. Shimizu, T., Nomiyama, S., Hirata, F., and Hayaishi, O. (1978) Indoleamine 2,3-dioxygenase. Purification and some properties, *J. Biol. Chem.* 253, 4700-4706.
37. Yamazaki, F., Kuroiwa, T., Takikawa, O., and Kido, R. (1985) Human indolylamine 2,3-dioxygenase. Its tissue distribution, and characterization of the placental enzyme, *Biochem. J.* 230, 635-638.
38. Mellor, A. L., and Munn, D. H. (2004) IDO expression by dendritic cells: tolerance and tryptophan catabolism, *Nat. Rev. Immunol.* 4, 762-774.
39. Habara-Ohkubo, A., Takikawa, O., and Yoshida, R. (1991) Cloning and expression of a cDNA encoding mouse indoleamine 2,3-dioxygenase, *Gene* 105, 221-227.
40. Tone, S., Takikawa, O., Habara-Ohkubo, A., Kadoya, A., Yoshida, R., and Kido, R. (1990) Primary structure of human indoleamine 2,3-dioxygenase

- deduced from the nucleotide sequence of its cDNA, *Nucleic Acids Res.* 18, 367.
41. Ishiguro, I., Naito, J., Saito, K., and Nagamura, Y. (1993) Skin L-tryptophan-2,3-dioxygenase and rat hair growth, *FEBS Lett.* 329, 178-182.
  42. Taylor, M. W., and Feng, G. S. (1991) Relationship between interferon-gamma, indoleamine 2,3-dioxygenase, and tryptophan catabolism, *FASEB J.* 5, 2516-2522.
  43. Ren, S., Liu, H., Licad, E., and Correia, M. A. (1996) Expression of rat liver tryptophan 2,3-dioxygenase in *Escherichia coli*: structural and functional characterization of the purified enzyme, *Arch. Biochem. Biophys.* 333, 96-102.
  44. Zhang, Y., Kang, S. A., Mukherjee, T., Bale, S., Crane, B. R., Begley, T. P., and Ealick, S. E. (2007) Crystal structure and mechanism of tryptophan 2,3-dioxygenase, a heme enzyme involved in tryptophan catabolism and in quinolinate biosynthesis, *Biochemistry* 46, 145-155.
  45. Sanni, L. A., Thomas, S. R., Tattam, B. N., Moore, D. E., Chaudhri, G., Stocker, R., and Hunt, N. H. (1998) Dramatic changes in oxidative tryptophan metabolism along the kynurenine pathway in experimental cerebral and noncerebral malaria, *Am. J. Pathol.* 152, 611-619.
  46. Takikawa, O. (2005) Biochemical and medical aspects of the indoleamine 2,3-dioxygenase-initiated L-tryptophan metabolism, *Biochem. Biophys. Res. Commun.* 338, 12-19.
  47. Saito, K., Fujigaki, S., Heyes, M. P., Shibata, K., Takemura, M., Fujii, H., Wada, H., Noma, A., and Seishima, M. (2000) Mechanism of increases in L-kynurenine and quinolinic acid in renal insufficiency, *Am. J. Physiol. Renal. Physiol.* 279, F565-572.
  48. Takikawa, O., Truscott, R. J., Fukao, M., and Miwa, S. (2003) Age-related nuclear cataract and indoleamine 2,3-dioxygenase-initiated tryptophan metabolism in the human lens, *Adv. Exp. Med. Biol.* 527, 277-285.
  49. Takikawa, O., Littlejohn, T. K., and Truscott, R. J. (2001) Indoleamine 2,3-dioxygenase in the human lens, the first enzyme in the synthesis of UV filters, *Exp. Eye Res.* 72, 271-277.

50. Mellor, A. (2005) Indoleamine 2,3 dioxygenase and regulation of T cell immunity, *Biochem. Biophys. Res. Commun.* 338, 20-24.
51. Gupta, S. L., Carlin, J. M., Pyati, P., Dai, W., Pfefferkorn, E. R., and Murphy, M. J., Jr. (1994) Antiparasitic and antiproliferative effects of indoleamine 2,3-dioxygenase enzyme expression in human fibroblasts, *Infect. Immun.* 62, 2277-2284.
52. Byrne, G. I., Lehmann, L. K., and Landry, G. J. (1986) Induction of tryptophan catabolism is the mechanism for gamma-interferon-mediated inhibition of intracellular *Chlamydia psittaci* replication in T24 cells, *Infect. Immun.* 53, 347-351.
53. Pfefferkorn, E. R. (1984) Interferon gamma blocks the growth of *Toxoplasma gondii* in human fibroblasts by inducing the host cells to degrade tryptophan, *Proc. Natl. Acad. Sci. USA* 81, 908-912.
54. Munn, D. H., and Mellor, A. L. (2007) Indoleamine 2,3-dioxygenase and tumor-induced tolerance, *J. Clin. Invest.* 117, 1147-1154.
55. Muller, A. J., and Scherle, P. A. (2006) Targeting the mechanisms of tumoral immune tolerance with small-molecule inhibitors, *Nat. Rev. Cancer* 6, 613-625.
56. Hou, D. Y., Muller, A. J., Sharma, M. D., DuHadaway, J., Banerjee, T., Johnson, M., Mellor, A. L., Prendergast, G. C., and Munn, D. H. (2007) Inhibition of indoleamine 2,3-dioxygenase in dendritic cells by stereoisomers of 1-methyl-tryptophan correlates with antitumor responses, *Cancer Res.* 67, 792-801.
57. Maeda, H., Tone, S., Kadoya, A. Iwamamoto, Y., Minatogawa, Y., Kido, R. (1992) Expression of human indoleamine 2,3-dioxygenase in *E. coli*, *Advances Trypt. Res.*, 417-420.
58. Takikawa, O., Kuroiwa, T., Yamazaki, F., and Kido, R. (1988) Mechanism of interferon-gamma action. Characterization of indoleamine 2,3-dioxygenase in cultured human cells induced by interferon-gamma and evaluation of the enzyme-mediated tryptophan degradation in its anticellular activity, *J. Biol. Chem.* 263, 2041-2048.

59. Littlejohn, T. K., Takikawa, O., Skylas, D., Jamie, J. F., Walker, M. J., and Truscott, R. J. (2000) Expression and purification of recombinant human indoleamine 2,3-dioxygenase, *Protein Expr. Purif.* 19, 22-29.
60. Holzinger, A., Phillips, K. S., and Weaver, T. E. (1996) Single-step purification/solubilization of recombinant proteins: application to surfactant protein B, *Biotechniques* 20, 804-806, 808.
61. Janknecht, R., de Martynoff, G., Lou, J., Hipkind, R. A., Nordheim, A., and Stunnenberg, H. G. (1991) Rapid and efficient purification of native histidine-tagged protein expressed by recombinant vaccinia virus, *Proc. Natl. Acad. Sci. USA* 88, 8972-8976.
62. Austin, C. J., Mizdrak, J., Matin, A., Sirijovski, N., Kosim-Satyaputra, P., Willows, R. D., Roberts, T. H., Truscott, R. J., Polekhina, G., Parker, M. W., and Jamie, J. F. (2004) Optimised expression and purification of recombinant human indoleamine 2,3-dioxygenase, *Protein Expr. Purif.* 37, 392-398.
63. Papadopoulou, N. D., Mewies, M., McLean, K. J., Seward, H. E., Svistunenko, D. A., Munro, A. W., and Raven, E. L. (2005) Redox and spectroscopic properties of human indoleamine 2,3-dioxygenase and a His303Ala variant: implications for catalysis, *Biochemistry* 44, 14318-14328.
64. Poillon, W. N., Maeno, H., Koike, K., and Feigelson, P. (1969) Tryptophan oxygenase of *Pseudomonas acidovorans*. Purification, composition, and subunit structure, *J. Biol. Chem.* 244, 3447-3456.
65. Ishimura, Y., Nozaki, M., and Hayaishi, O. (1970) The oxygenated form of L-tryptophan 2,3-dioxygenase as reaction intermediate, *J. Biol. Chem.* 245, 3593-3602.
66. Batabyal, D., and Yeh, S. R. (2007) Human tryptophan dioxygenase: a comparison to indoleamine 2,3-dioxygenase, *J. Am. Chem. Soc.* 129, 15690-15701.
67. Basran, J., Rafice, S. A., Chauhan, N., Efimov, I., Cheesman, M. R., Ghamsari, L., and Raven, E. L. (2008) A kinetic, spectroscopic, and redox study of human tryptophan 2,3-dioxygenase, *Biochemistry* 47, 4752-4760.

68. Maghzal, G. J., Thomas, S. R., Hunt, N. H., and Stocker, R. (2008) Cytochrome b5, not superoxide anion radical, is a major reductant of indoleamine 2,3-dioxygenase in human cells, *J. Biol. Chem.* 283, 12014-12025.
69. Taniguchi, T., Hirata, F., and Hayaishi, O. (1977) Intracellular utilization of superoxide anion by indoleamine 2,3-dioxygenase of rabbit enterocytes, *J. Biol. Chem.* 252, 2774-2776.
70. Sugimoto, H., Oda, S., Otsuki, T., Hino, T., Yoshida, T., and Shiro, Y. (2006) Crystal structure of human indoleamine 2,3-dioxygenase: catalytic mechanism of O<sub>2</sub> incorporation by a heme-containing dioxygenase, *Proc. Natl. Acad. Sci. USA* 103, 2611-2616.
71. Sono, M., and Cady, S. G. (1989) Enzyme kinetic and spectroscopic studies of inhibitor and effector interactions with indoleamine 2,3-dioxygenase. 1. Norharman and 4-phenylimidazole binding to the enzyme as inhibitors and heme ligands, *Biochemistry* 28, 5392-5399.
72. Forouhar, F., Anderson, J. L., Mowat, C. G., Vorobiev, S. M., Hussain, A., Abashidze, M., Bruckmann, C., Thackray, S. J., Seetharaman, J., Tucker, T., Xiao, R., Ma, L. C., Zhao, L., Acton, T. B., Montelione, G. T., Chapman, S. K., and Tong, L. (2007) Molecular insights into substrate recognition and catalysis by tryptophan 2,3-dioxygenase, *Proc. Natl. Acad. Sci. USA* 104, 473-478.
73. Sono, M., and Dawson, J. H. (1984) Extensive studies of the heme coordination structure of indoleamine 2,3-dioxygenase and of tryptophan binding with magnetic and natural circular dichroism and electron paramagnetic resonance spectroscopy, *Biochim. Biophys. Acta* 789, 170-187.
74. Terentis, A. C., Thomas, S. R., Takikawa, O., Littlejohn, T. K., Truscott, R. J., Armstrong, R. S., Yeh, S. R., and Stocker, R. (2002) The heme environment of recombinant human indoleamine 2,3-dioxygenase. Structural properties and substrate-ligand interactions, *J. Biol. Chem.* 277, 15788-15794.
75. Makino, R., Sakaguchi, K., Iizuka, T., and Ishimura, Y. (1980) Acid-alkaline transition and thermal spin equilibrium of the heme in ferric L-tryptophan 2,3-dioxygenases, *J. Biol. Chem.* 255, 11883-11891.

76. Taniguchi, T., Sono, M., Hirata, F., Hayaishi, O., Tamura, M., Hayashi, K., Iizuka, T., and Ishimura, Y. (1979) Indoleamine 2,3-dioxygenase. Kinetic studies on the binding of superoxide anion and molecular oxygen to enzyme, *J. Biol. Chem.* 254, 3288-3294.
77. Antonini, M., and Brunori E. (1971) *Hemoglobin and Myoglobin and their reactions with ligands*, North Holland Publishers, Amsterdam.
78. Sono, M., Taniguchi, T., Watanabe, Y., and Hayaishi, O. (1980) Indoleamine 2,3-dioxygenase. Equilibrium studies of the tryptophan binding to the ferric, ferrous, and CO-bound enzymes, *J. Biol. Chem.* 255, 1339-1345.
79. Ishimura, Y., Makino, R., Ueno, R., Sakaguchi, K., Brady, F. O., Feigelson, P., Aisen, P., and Hayaishi, O. (1980) Copper is not essential for the catalytic activity of L-tryptophan 2,3-dioxygenase, *J. Biol. Chem.* 255, 3835-3837.
80. Brady, F. O., Forman, H. J., and Feigelson, P. (1971) The role of superoxide and hydroperoxide in the reductive activation of tryptophan-2,3-dioxygenase, *J. Biol. Chem.* 246, 7119-7124.
81. Li, J. S., Han, Q., Fang, J., Rizzi, M., James, A. A., and Li, J. (2007) Biochemical mechanisms leading to tryptophan 2,3-dioxygenase activation, *Arch. Insect Biochem. Physiol.* 64, 74-87.
82. Hirata, F., and Hayaishi, O. (1971) Possible participation of superoxide anion in the intestinal tryptophan 2,3-dioxygenase reaction, *J. Biol. Chem.* 246, 7825-7826.
83. Hirata, F., and Hayaishi, O. (1972) New degradative routes of 5-hydroxytryptophan and serotonin by intestinal tryptophan 2,3-dioxygenase, *Biochem. Biophys. Res. Commun.* 47, 1112-1119.
84. Carr, G., Chung, M. K., Mauk, A. G., and Andersen, R. J. (2008) Synthesis of indoleamine 2,3-dioxygenase inhibitory analogues of the sponge alkaloid exiguamine A, *J. Med. Chem.* 51, 2634-2637.
85. Macchiarulo, A., Camaioni, E., Nuti, R., and Pellicciari, R. (2008) Highlights at the gate of tryptophan catabolism: a review on the mechanisms of activation and regulation of indoleamine 2,3-dioxygenase (IDO), a novel target in cancer disease, *Amino Acids*.
86. Malachowski, W. P., Metz, R., Prendergast, G.C., Muller, A.J. (2005) A new cancer immunosuppression target: indoleamine 2,3-dioxygenase (IDO). A

- review of the IDO mechanism, inhibition and therapeutic applications, *Drugs Future* 30, 897-909.
87. Volgraf, M., Lumb, J. P., Brastianos, H. C., Carr, G., Chung, M. K., Munzel, M., Mauk, A. G., Andersen, R. J., and Trauner, D. (2008) Biomimetic synthesis of the IDO inhibitors exiguamine A and B, *Nat. Chem. Biol.* 4, 535-537.
  88. Muller, A. J., DuHadaway, J. B., Donover, P. S., Sutanto-Ward, E., and Prendergast, G. C. (2005) Inhibition of indoleamine 2,3-dioxygenase, an immunoregulatory target of the cancer suppression gene Bin1, potentiates cancer chemotherapy, *Nat. Med.* 11, 312-319.
  89. Eguchi, N., Watanabe, Y., Kawanishi, K., Hashimoto, Y., and Hayaishi, O. (1984) Inhibition of indoleamine 2,3-dioxygenase and tryptophan 2,3-dioxygenase by beta-carboline and indole derivatives, *Arch. Biochem. Biophys.* 232, 602-609.
  90. Sono, M. (1990) Spectroscopic and equilibrium studies of ligand and organic substrate binding to indoleamine 2,3-dioxygenase, *Biochemistry* 29, 1451-1460.
  91. Cady, S. G., and Sono, M. (1991) 1-Methyl-DL-tryptophan, beta-(3-benzofuranyl)-DL-alanine (the oxygen analog of tryptophan), and beta-[3-benzo(b)thienyl]-DL-alanine (the sulfur analog of tryptophan) are competitive inhibitors for indoleamine 2,3-dioxygenase, *Arch. Biochem. Biophys.* 291, 326-333.
  92. Pereira, A., Vottero, E., Roberge, M., Mauk, A. G., and Andersen, R. J. (2006) Indoleamine 2,3-dioxygenase inhibitors from the Northeastern Pacific Marine Hydroid *Garveia annulata*, *J. Nat. Prod.* 69, 1496-1499.
  93. Brastianos, H. C., Vottero, E., Patrick, B. O., Van Soest, R., Matainaho, T., Mauk, A. G., and Andersen, R. J. (2006) Exiguamine A, an indoleamine-2,3-dioxygenase (IDO) inhibitor isolated from the marine sponge *Neopetrosia exigua*, *J. Am. Chem. Soc.* 128, 16046-16047.
  94. Makino, R., Sakaguchi, K., Iizuka, T., and Ishimura, Y. (1980) *Dev. Biochem.* 16, 179-187.

95. Costas, M., Mehn, M. P., Jensen, M. P., and Que, L., Jr. (2004) Dioxygen activation at mononuclear nonheme iron active sites: enzymes, models, and intermediates, *Chem. Rev.* *104*, 939-986.
96. Abu-Omar, M. M., Loaiza, A., and Hontzeas, N. (2005) Reaction mechanisms of mononuclear non-heme iron oxygenases, *Chem. Rev.* *105*, 2227-2252.
97. Denisov, I. G., Makris, T. M., Sligar, S. G., and Schlichting, I. (2005) Structure and chemistry of cytochrome P450, *Chem. Rev.* *105*, 2253-2277.
98. Poulos, T. L. (2005) Structural biology of heme monooxygenases, *Biochem. Biophys. Res. Commun.* *338*, 337-345.
99. Shaik, S., Kumar, D., de Visser, S. P., Altun, A., and Thiel, W. (2005) Theoretical perspective on the structure and mechanism of cytochrome P450 enzymes, *Chem. Rev.* *105*, 2279-2328.
100. Leeds, J. M., Brown, P. J., McGeehan, G. M., Brown, F. K., and Wiseman, J. S. (1993) Isotope effects and alternative substrate reactivities for tryptophan 2,3-dioxygenase, *J. Biol. Chem.* *268*, 17781-17786.
101. Hamilton, G. A. (1969) Mechanisms of two- and four-electron oxidations catalyzed by some metalloenzymes, *Adv. Enzymol. Relat. Areas Mol. Biol.* *32*, 55-96.
102. Muto, S. (1980) Differentiation between Criegee rearrangement and dioxatane rearrangement mechanisms for the decomposition of  $\alpha,\beta$ -unsaturated hydroperoxides., *J. Am. Chem. Soc.* *102*, 7379-7381.
103. Uchida, K., Shimizu, T., Makino, R., Sakaguchi, K., Iizuka, T., Ishimura, Y., Nozawa, T., and Hatano, M. (1983) Magnetic and natural circular dichroism of L-tryptophan 2,3-dioxygenases and indoleamine 2,3-dioxygenase. II. Spectra of their ferric cyanide and ferrous carbon monoxide complexes and an oxygenated form, *J. Biol. Chem.* *258*, 2526-2533.
104. Hersleth, H. P., Uchida, T., Rohr, A. K., Teschner, T., Schunemann, V., Kitagawa, T., Trautwein, A. X., Gorbitz, C. H., and Andersson, K. K. (2007) Crystallographic and spectroscopic studies of peroxide-derived myoglobin compound II and occurrence of protonated  $\text{Fe}^{\text{IV}}=\text{O}$ , *J. Biol. Chem.* *282*, 23372-23386.

105. Suzuki, T., Kawamichi, H., and Imai, K. (1998) A myoglobin evolved from indoleamine 2,3-dioxygenase, a tryptophan-degrading enzyme, *Comp. Biochem. Physiol. B. Biochem. Mol. Biol.* 121, 117-128.

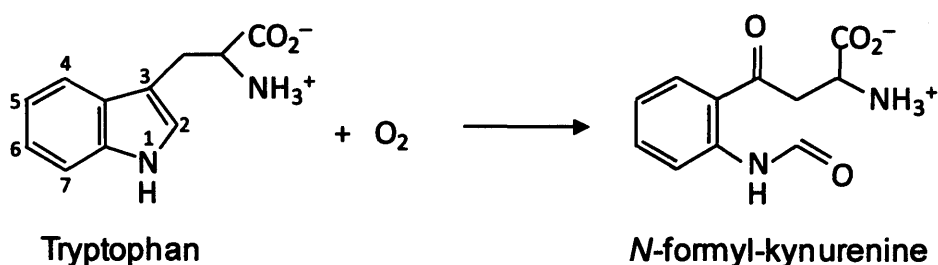
## Chapter 2

---

### The role of serine 167 in rhIDO: a comparison with TDO

## 2.1 Introduction

The initial, rate-limiting step in the L-kynurenine pathway is the oxidative cleavage of L-tryptophan (L-Trp) to *N*-formyl-kynurenine (Scheme 2.1) and is catalysed by one of two heme dioxygenase enzymes, indoleamine 2,3-dioxygenase (IDO) or tryptophan 2,3-dioxygenase (TDO). Although they catalyse the same reaction, IDO and TDO are otherwise distinct and little is known about their structure and mechanism.



**Scheme 2.1:** Reaction catalysed by IDO and TDO.

As reviewed in Chapter 1, the first detailed structural and functional information that appeared was for recombinant human IDO (rhIDO). A recent crystal structure for ferric rhIDO (1) reveals an active site that is much more hydrophobic than for other, well-characterised O<sub>2</sub>-dependent heme enzymes, Figure 2.1(A), and which is presumably configured to encourage binding of the hydrophobic substrate. Subsequently, a structure for the bacterial *X. campestris* TDO (*Xc*TDO) in complex with L-Trp (2) was published (Figure 2.1(B), (C)) and indicated that an active site histidine, His55, hydrogen bonds to the indole nitrogen of the substrate in the substrate-bound complex (Figure 2.1(C)). Although these structures have provided critical insight into the molecular details of the active site architecture and the substrate binding interactions, they also raise a number of important questions for which there are currently no satisfactory answers. To begin with, the most striking feature of the rhIDO active site is that, with the notable exception of Ser167, it is almost devoid of polar residues (Figure 2.1(A)). This marks rhIDO as distinct from some other heme proteins (*e.g.* the globins and peroxidases), which often have an

active site histidine residue in the distal pocket that provides hydrogen bonding stabilisation to ligands bound at the heme iron.

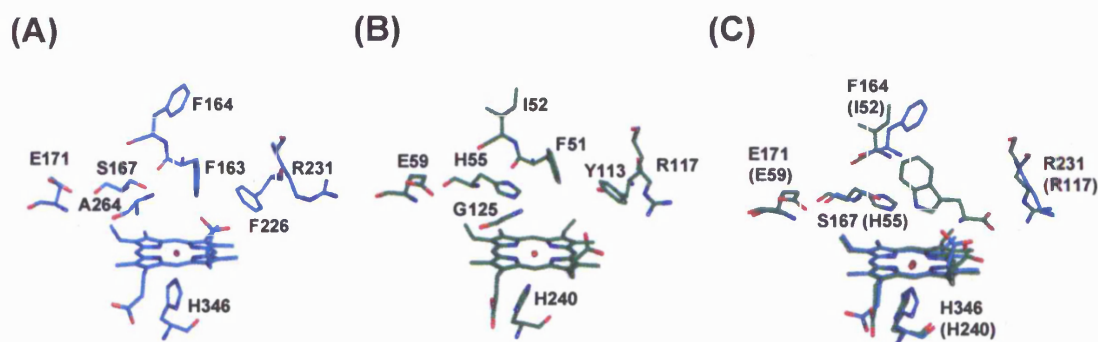


**Figure 2.1:** A comparison of the active sites of rhIDO and *XcTDO*. (A) The active site of rhIDO (in cyan (1)). (B) The active site of *XcTDO* (in green (2)) in the same orientation as that shown for rhIDO. Active site residues for rhIDO are H346, R231, F226, F163, S167, A264, F164, E171 which correspond to H240, R117, Y113, F51, H55, G125, I52 and E59 in *XcTDO*. (C) An overlay of rhIDO (cyan) and the *XcTDO*-Trp (green) complex, with the residues for rhIDO indicated and those for *XcTDO* in parentheses.

The first questions that arise, therefore, are whether similar hydrogen bonding stabilisation of the ferrous-oxy species is required during rhIDO catalysis, how is this provided, and whether this applies universally across the heme dioxygenase family. A second notable difference between *XcTDO* and rhIDO is that the critical His55 residue is missing in rhIDO, replaced by a serine residue at position 167 that is conserved across all IDOs (Figure 2.1) (3). Sequence alignments indicate that this active site histidine is similarly conserved amongst all TDOs isolated to date (4) (including recombinant human TDO (rhTDO)), raising the question as to its specific role in the reaction mechanism.

In this Chapter, the role of the conserved active site Ser167 residue in rhIDO (S167A and S167H variants), which is replaced with a histidine in other mammalian and bacterial TDO enzymes, is addressed. Kinetic and spectroscopic data reveal significant differences between the rhIDO and TDO enzymes, and the implications of these results are discussed in terms of our current understanding of IDO and TDO catalysis.

## 2.2 Results

### 2.2.1 Expression and purification

#### 2.2.1.1 Expression system

Samples of rhIDO were prepared from *E. coli* SG1300 cells incorporating a pQE30-derived expression vector and purified as described in Chapter 8, using the incorporated His-tag (six histidine residues on the N-terminal end of the protein).

For active site variants S167A and S167H, site-directed mutagenesis was performed according to the Quickchange<sup>TM</sup> protocol as described in Chapter 8. Both S167 variants were expressed and purified using the same procedures as for rhIDO.

All protein samples were purified by means of affinity chromatography, using a Ni<sup>2+</sup>-nitrilotriacetic acid (NTA) agarose column (Qiagen). The protein was then further purified by Fast Protein Liquid Chromatography, FPLC (Chapter 8).

#### 2.2.1.2 SDS-PAGE analysis

Protein purity was monitored using SDS-PAGE gel electrophoresis. The SDS-PAGE gel showed only one band after the purification procedure was carried out. A typical SDS-PAGE gel for rhIDO and S167 variants is shown in Figure 2.2 and was characteristic for all batches of protein expressed.

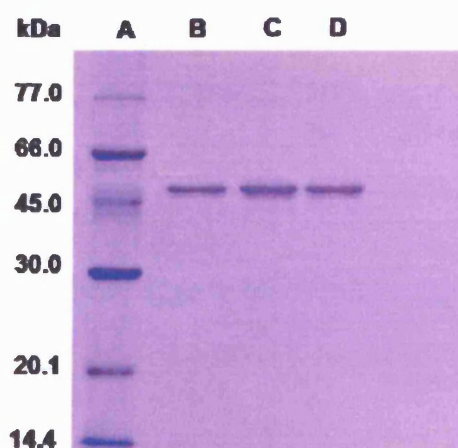


**Figure 2.2:** A 15% SDS-PAGE gel of rhIDO and S167 variants. From the left: marker standards (lane A), rhIDO (lane B), S167A (lane C) and S167H (lane D).

### 2.2.2 Electronic absorption spectra

Analysis of the electronic spectrum of ferric S167A reveals that the wavelength maxima ( $\lambda_{\text{max}} = 404, 500, 537, 575$  and  $628$  nm, Figure 2.3(B)) are very similar to those for rhIDO ( $404, 500, 533$  and  $635$  nm, Figure 2.3(A)); rhIDO is known to exist as a mixed population of high-spin, water bound heme and low-spin bis-histidine ligated heme (5). For S167H (Figure 2.3(C)), the Soret band is red-shifted to  $408$  nm ( $\lambda_{\text{max}} = 408, 499, 536, 570$  and  $628$  nm), which is indicative of an increased proportion of low-spin heme, possibly as a result of coordination of His167 to the heme iron.

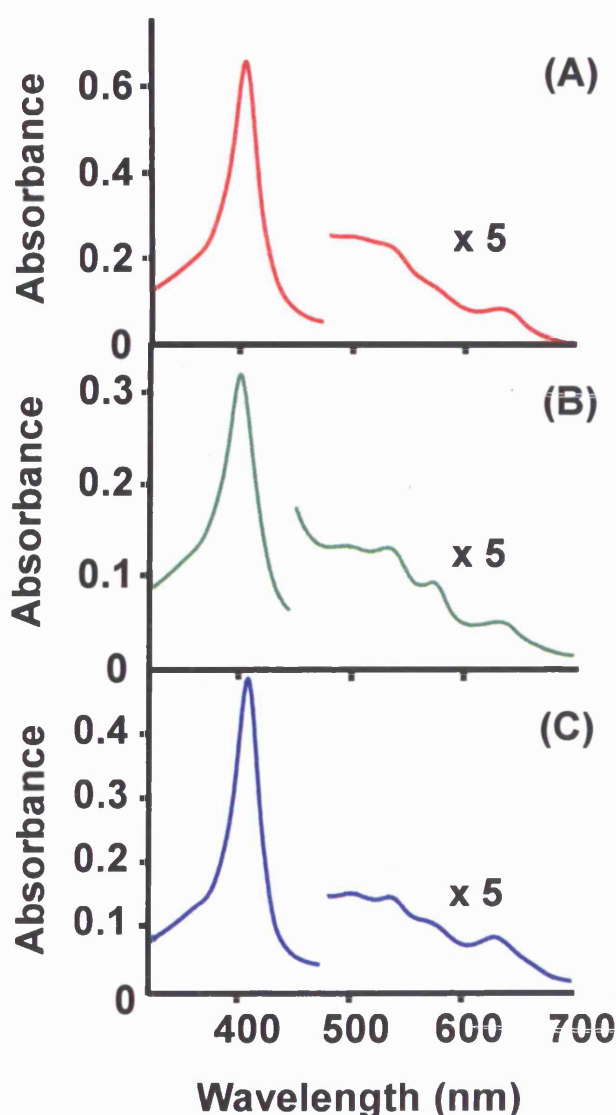


**Figure 2.3:** UV-visible spectra of ferric (A) rhIDO, (B) S167A and (C) S167H. Absorbance values in the visible region have been multiplied by a factor of 5. Conditions: 50 mM Tris/HCl buffer, pH 8.0, 25.0 °C.

The electronic spectra of the ferrous derivatives of S167A and S167H are similar to those of rhIDO. This is consistent with the presence of a 5-coordinate heme species in all cases and indicates that the low-spin component in ferric S167H is converted to high-spin, 5-coordinate heme on reduction (Table 2.1).

### 2.2.3 EPR spectroscopy

EPR spectroscopy was carried out by Dr. Dimitri Svistunenko (University of Essex) and was used as a means of providing further information on the heme coordination geometry in S167A and S167H. The EPR spectrum of ferric rhIDO is shown in Figure 2.4(A); axial and rhombic high-spin ( $g = 5.82, 1.99$  and  $6.17, 5.52, 1.99$  respectively) and low-spin ( $g = 2.85, 2.27, 1.62$ ) species have been previously assigned (5). The EPR spectrum of S167A (Figure 2.4(B)), has an increased proportion of high-spin heme compared to rhIDO, which consists mainly of an axial ( $g = 5.85, 1.99$ ) form. In contrast, the spectrum of S167H (Figure 2.4(C)) contains a major low-spin species ( $g = 2.88, 2.28, 1.63$ ) which is likely to arise from bis-histidine axial ligation in which the imidazole planes are aligned approximately parallel to each other (6, 7).

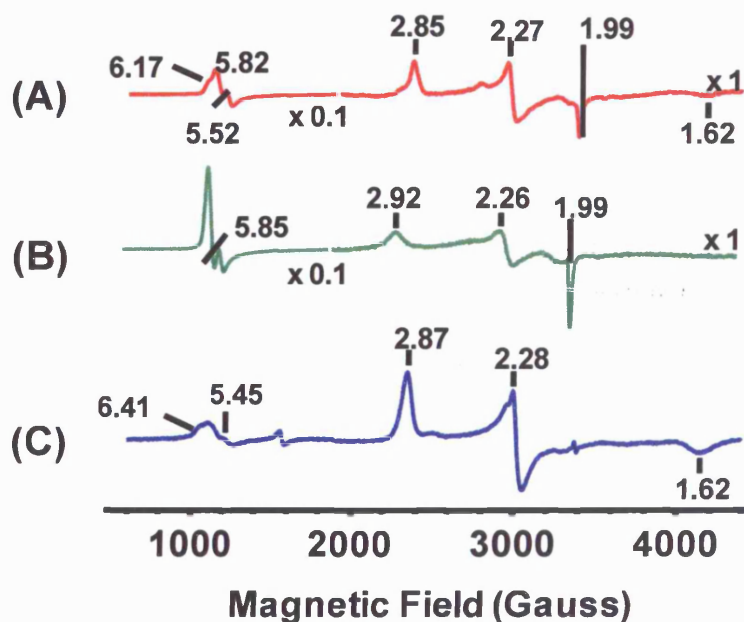


**Figure 2.4:** EPR spectra of (A) ferric rhIDO, (B) ferric S167A and (C) ferric S167H. Conditions:  $T = 10$  K, modulation amplitude 10 G, modulation frequency 100 kHz, microwave frequency 9.67 GHz, microwave power 2 mW.

### 2.2.4 Binding of non-catalytic ligands

The binding of various non-catalytic ligands to ferric enzyme is informative because it provides further information on the different coordination environments of the heme. Absorption maxima for the various ferric and ferrous anionic derivatives of rhIDO, S167A and S167H are presented in Table 2.1. Addition of various exogenous ligands to rhIDO and S167A resulted in spectral changes that are indicative of ligand binding to the sixth coordination site. S167H was unable to bind weak field ligands such as fluoride and azide, as evidenced by lack of spectral change; in contrast, addition of azide and fluoride to rhIDO and S167A resulted in spectral changes that are characteristic of ligand binding to the sixth coordination site (Table 2.1).

**Table 2.1:** Absorption maxima for various ferric and ferrous derivatives of rhIDO, S167A and S167H. Conditions: 50 mM Tris/HCl buffer, pH 8.0, 25.0 °C.

Derivative	$\lambda_{\max}$ (nm)		
	rhIDO	S167A	S167H
Ferric	404, 500, 533, 635	404, 500, 537, 575, 628	408, 500, 536, 570, 628
Ferrous	425, 527 <sup>sh</sup> , 558	426, 529 <sup>sh</sup> , 557	426, 535 <sup>sh</sup> , 558
Ferrous-oxy	416, 539, 576	416, 539, 576	416, 538, 575
Ferric + L-Trp	410, 540, 576	409, 539, 572	409, 539, 573
Ferric-azide	413, 535, 572, 643	410, 540, 576, 627	n.d <sup>a</sup>
Ferric-fluoride	404, 502, 532, 635	405, 500, 537, 575, 628	n.d <sup>a</sup>
Ferric-cyanide	419, 538, 569 <sup>sh</sup>	419, 540, 570 <sup>sh</sup>	418, 540, 568 <sup>sh</sup>

sh = shoulder.

<sup>a</sup>No spectroscopic changes were observed on binding of either azide or fluoride to S167H.

Addition of cyanide (CN) gives changes in the visible region that are indicative of formation of a six coordinate low-spin species for both S167A ( $\lambda_{\max}$  = 419, 540, 570<sup>sh</sup> nm) and S167H ( $\lambda_{\max}$  = 418, 540, 568<sup>sh</sup> nm), Table 2.1. The corresponding binding constants,  $K_D$ , are given in Table 2.2, with spectra shown in Figure 2.5 for

rhIDO. Values of  $K_D$  for rhIDO and S167A are broadly similar, but that for S167H is increased by a factor of  $\approx 170$ , which is in agreement with the spectroscopic data above and consistent with binding of His167 to the iron.

**Table 2.2:** Kinetic<sup>a</sup> and thermodynamic parameters for binding of cyanide to ferric rhIDO, S167A and S167H. Conditions: 50 mM Tris/HCl buffer, pH 8.0, 25.0 °C.

	rhIDO	S167A	S167H
$K_D$ ( $\mu\text{M}$ )	$3.57 \pm 0.37$	$1.92 \pm 0.17$	$594 \pm 30$
$k_{\text{on}}$ ( $\mu\text{M}^{-1} \text{s}^{-1}$ )	$0.0214 \pm 0.0006$	$0.1708 \pm 0.0032$	$0.0004 \pm 1.2 \times 10^{-5}$

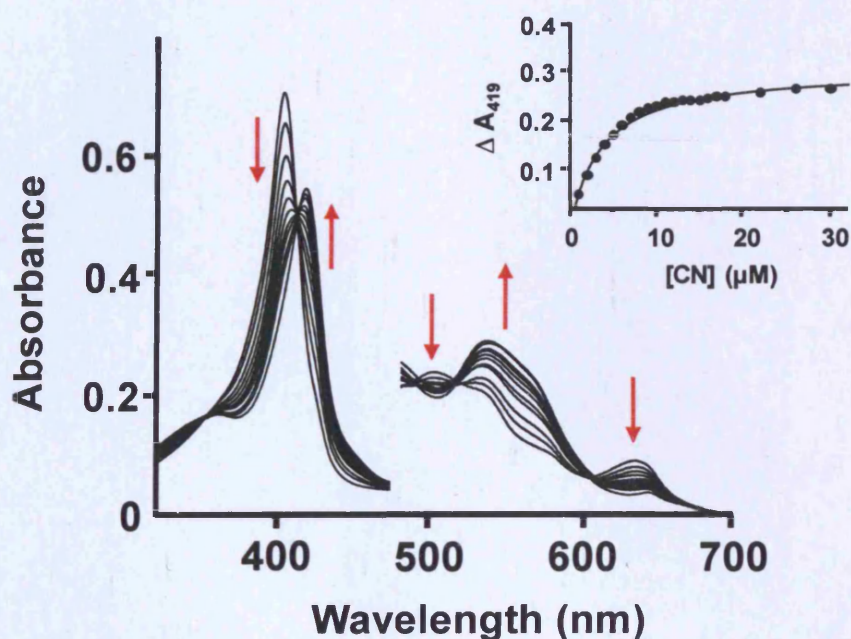


**Figure 2.5:** Representative data set for the determination of  $K_D$  for binding of CN to rhIDO. The arrows indicate the direction of change in absorbance upon successive additions of CN. Absorbance values in the visible region have been multiplied by a factor of 5. (Inset) Fit of data at 419 nm to Equation [8.4], Chapter 8. Conditions: 50 mM Tris/HCl buffer, pH 8.0, 25.0 °C

<sup>a</sup>  $k_{\text{on}}$  values were determined by Dr. Jaswir Basran

Binding of cyanide was also determined kinetically. Second-order rate constants,  $k_{\text{on}}$ , were derived from a plot of  $k_{\text{obs}}$  against [cyanide], Figure 2.6, and values are given in Table 2.2. As for the binding data above, the  $k_{\text{on}}$  value for S167H was  $\sim 50$  times smaller than for rhIDO. This is informative because it tells us that the weaker  $K_{\text{D}}$  for S167H is due to a decreased  $k_{\text{on}}$ , which is consistent with the bis-histidine ligated heme detected by EPR. The  $k_{\text{on}}$  value obtained for S167A is  $\approx 8$ -fold faster than for rhIDO.

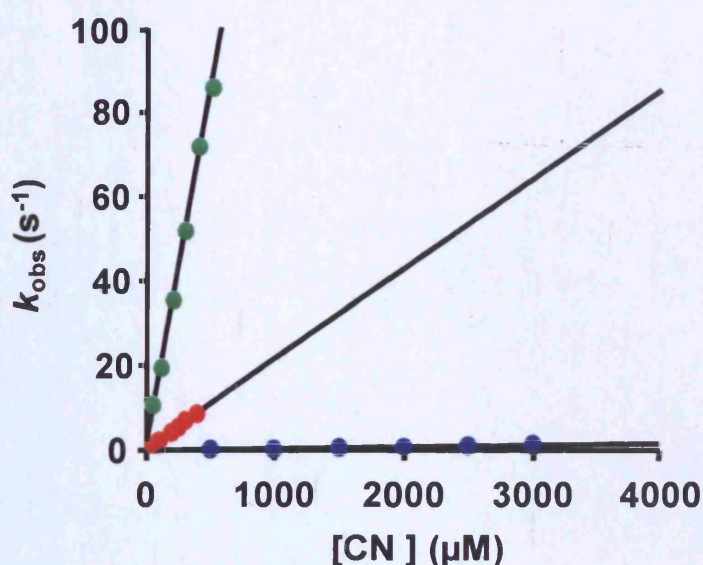


**Figure 2.6:** Concentration-dependence of the apparent binding rates of cyanide to ferric rhIDO ( $\bullet$ ), S167A ( $\circ$ ) and S167H ( $\bullet$ ). Linear regression analysis of the data yielded an apparent association constant ( $k_{\text{on}}$ ) from the slope.

### 2.2.5 Substrate binding

Both S167A and S167H exhibited characteristic spectroscopic changes upon binding of L-Trp at pH 8.0 (Table 2.1): the Soret band shifts to 409 nm in both cases. Similar changes in absorbance are observed for rhIDO and are consistent with the loss of high-spin heme and the formation of a low-spin, hydroxide-bound species on binding of L-Trp, most likely as a consequence of deprotonation of a water molecule in the active site (5). The similarity of the spectroscopic changes for S167A and S167H indicates that binding of substrate occurs in a similar manner and that the

corresponding deprotonation of the distal water molecule to form a hydroxide-bound species occurs by a similar mechanism.

Binding constants,  $K_D$ , for binding of L-Trp to S167A and S167H were determined from the above data as  $7900 \pm 820$  and  $6920 \pm 1100 \mu\text{M}$  (pH 8.0), respectively (Table 2.3). Both of these values are significantly larger than the corresponding value for rhIDO ( $285 \pm 6 \mu\text{M}$ , Figure 2.7), although we note that binding of substrate to the ferrous form of both variants (as evidenced by the  $K_M$  values, *vide infra*) is similar in all three cases. Derived rate constants are given in Table 2.3, and show a marked decrease in  $k_{\text{on}}$  for S167H (Figure 2.8). Values for  $K_D$  ( $= k_{\text{off}}/k_{\text{on}}$ ) derived from these data were within error of those determined under equilibrium conditions. Binding constants for binding of L-Trp to the ferric-cyanide complexes were also determined under equilibrium conditions and derived values of  $16.4 \pm 1.5 \mu\text{M}$  for rhIDO and  $992 \pm 200 \mu\text{M}$  for S167A were obtained (Table 2.3). These values are significantly lower than those for the ferric enzyme alone, Table 2.3, and are indicative of enhanced affinity for L-Trp in the presence of cyanide. The same experiment on the ferric-cyanide complex of S167H gave spectral changes that were much smaller than those for either rhIDO or S167A (both in terms of shift of the Soret band and total change in absorbance). We have interpreted this to mean that binding of L-Trp probably occurs, but the spectroscopic changes were too small to extract a meaningful  $K_D$ .

**Table 2.3:** Kinetic and thermodynamic parameters for binding of L-Trp to ferric rhIDO, S167A and S167H. Conditions: 50 mM Tris/HCl buffer, pH 8.0, 25.0 °C.

Variant	rhIDO	S167A	S167H
$K_D$ ( $\mu\text{M}$ )	$285 \pm 6$	$7900 \pm 820^b$	$6920 \pm 1100^b$
$K_D$ ( $\mu\text{M}$ ) (in the presence of CN)	$16.0 \pm 2^a$	$992 \pm 200^c$	ND
$k_{\text{on}}$ ( $\text{M}^{-1} \text{s}^{-1}$ )	$15500 \pm 350$	$15600 \pm 1670$	$5930 \pm 200$
$k_{\text{off}}$ ( $\text{s}^{-1}$ )	$9.12 \pm 0.6$	$60.3 \pm 3$	$41.6 \pm 4$

<sup>a</sup> rhIDO was fully saturated with cyanide (80  $\mu\text{M}$ ) before addition of L-Trp

<sup>b</sup> Errors on these values are larger because the limited solubility of L-Trp in solution (maximum concentration  $\approx 50$  mM) mean that larger volumes are needed during the titration and corrections for this dilution were necessary.

<sup>c</sup> S167A was fully saturated with cyanide (20  $\mu\text{M}$  cyanide) before addition of L-Trp.

ND,  $K_D$  could not be measured because the spectral changes upon addition of L-Trp were too small to monitor.

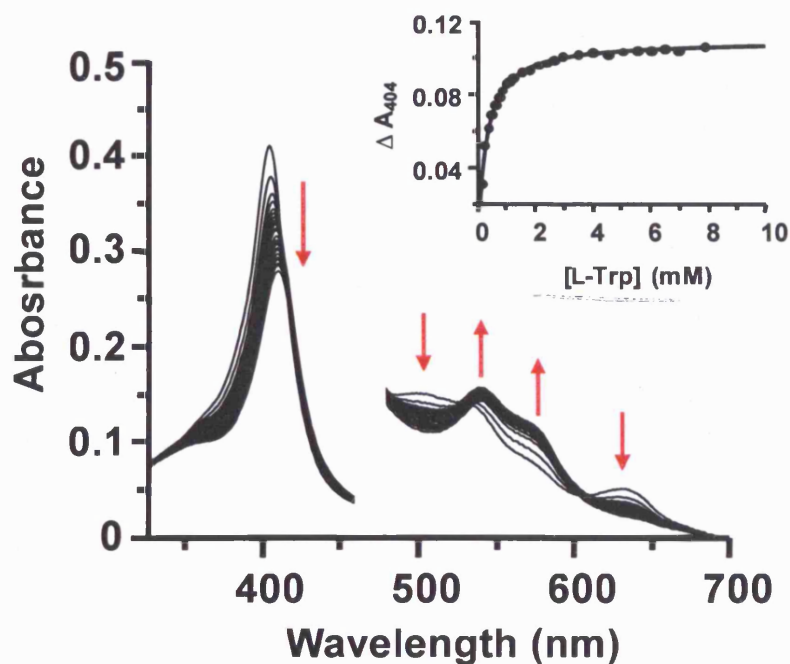


**Figure 2.7:** Representative data set for the determination of  $K_D$  for binding of L-Trp to rhIDO. The arrows indicate the direction of change in absorbance upon successive additions of L-Trp. Absorbance values in the visible region have been multiplied by a factor of 5. (Inset) Fit of data at 404 nm to Equation [8.4], Chapter 8. Conditions: 50 mM Tris/HCl buffer, pH 8.0, 25.0 °C.

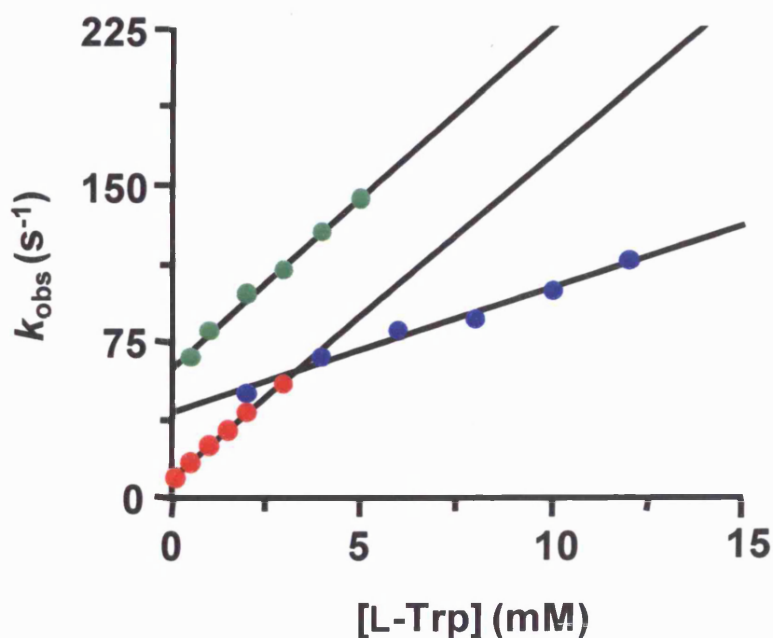


**Figure 2.8:** Concentration-dependence of the apparent binding rates of L-Trp to ferric rhIDO (●), S167A (●) and S167H (●). Linear regression analysis of the data yielded an apparent association constant ( $k_{on}$ ) from the slope, a dissociation rate constant ( $k_{off}$ ) from the ordinate intercept.

### 2.2.6 Crystal screens

The purity of rhIDO samples used in the crystallisation experiments were determined by measuring Reinheitszahl ( $R_Z$ ) values (the ratio of the absorbance of the Soret peak at 404 nm and that of the protein peak at 280 nm) and by polyacrylamide gel electrophoresis (SDS-PAGE). The protein was then further purified by Fast Protein Liquid Chromatography (FPLC). All screens were prepared as described in Chapter 8 (Section 8.15).

Crystallisation screens of ferric rhIDO and S167H based around the conditions used to crystallise rhIDO in complex with 4-phenyl-imidazole (*I*) were unsuccessful. Variation in protein concentration (15-40 mg/ml), pH of CHES buffer (pH 8.5-9.5, increments of 0.5 pH units), concentration of polyethylene glycol (4-26%, increments of 2%) and substitution of the bound complex (4-phenyl-imidazole replaced with either L-trp or 1-Me-Trp) also proved unsuccessful.

Crystallisation screens, based around the conditions used to crystallise rhIDO, were also set up in an anaerobic environment using ferrous rhIDO and were carried out in collaboration with Dr. Chris Mowat (Department of Chemistry, University of Edinburgh); in addition to this, commercial screens were attempted using both ferric and ferrous rhIDO and these screens were set up in aerobic and anaerobic environments, respectively. Unfortunately, all of the crystallisation attempts were unsuccessful.

### 2.2.7 Redox measurements

The  $\text{Fe}^{\text{III/II}}$  reduction potentials for rhIDO, S167A and S167H were determined using the xanthine/xanthine oxidase assay with simultaneous reduction of a dye of known potential. This method has the advantage over potentiometric titrations in that it allows better equilibria to be obtained because electron exchange occurs in the bulk solution; this means that the method is quicker than the potentiometric titration method and does not require the correct choice of mediators. The assay compromises of xanthine, xanthine oxidase, ferric enzyme and a dye of a known potential.

The  $\text{Fe}^{\text{III/II}}$  reduction potential for S167A was found to be  $-12$  mV, this compares to a value of  $-63$  mV for rhIDO (Figure 2.9(A)) which was determined using the same method. The  $\text{Fe}^{\text{III/II}}$  reduction potential for S167H ( $-203$  mV, Figure 2.9(B)) was significantly lower than that for both rhIDO and S167A.

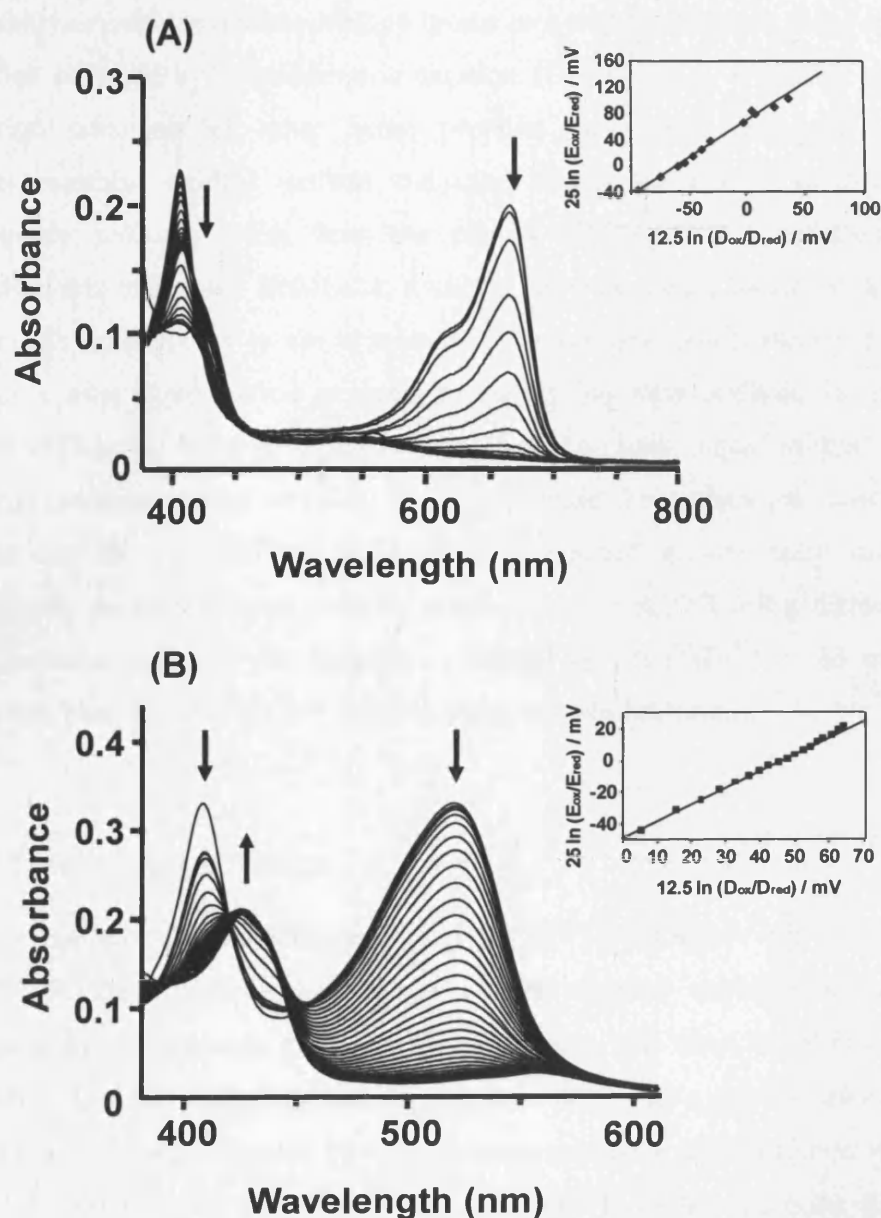


**Figure 2.9:** Family of spectra collected during determination of  $\text{Fe}^{\text{III/II}}$  reduction potential for (A) rhIDO with methylene blue and (B) S167H with phenosafranine. Arrows indicate direction of absorption changes at various parts of the spectrum during the reductive titration. (Inset) The corresponding linear Nernst plot. Conditions: 50 mM potassium phosphate buffer, pH 7.0.

The reduction potential for S167A after addition of 15 mM L-Trp, was found to have increased to +59 mV, this compares with a value of +18 mV for rhIDO. The  $\text{Fe}^{\text{III/II}}$  reduction potential for S167H (-203 mV) was significantly lower than rhIDO and S167A; upon addition of 15 mM L-Trp this value increased to - 83 mV, an increase of 120 mV.

The xanthine/xanthine oxidase method produces a slightly different value for rhIDO than that obtained by potentiometric titration (-30 mV (5)). Different values for reduction potentials of other heme proteins have been determined by the xanthine/xanthine oxidase method and other electrochemical methods (8). The discrepancy probably arises from the use of dithionite as a reductant in the potentiometric technique. Dithionite, a strong reducing agent, transfers all electron equivalents immediately to the protein, with subsequent equilibration assisted by mediators after equilibration at each potential; the next addition of dithionite corresponding to another potential requires a new equilibration. In the xanthine/xanthine oxidase method, xanthine oxidase feeds electrons slowly to the protein and the dye, so that equilibrium is reached at any point during the experiment. As an important control, experiments on rhIDO using different dyes gave the same value for the reduction potential ( $E^{\circ'} (\text{Fe}^{\text{III}}/\text{Fe}^{\text{II}}) = -63 \text{ mV}$  using methylene blue;  $E^{\circ'} (\text{Fe}^{\text{III}}/\text{Fe}^{\text{II}}) = -68 \text{ mV}$  using Nile blue chloride).

### 2.2.8 Steady-state kinetics

A plot of the initial rate of dioxygenase activity ( $V/[E] \text{ s}^{-1}$ ), where  $V$  is the initial rate and  $[E]$  is the enzyme concentration in the reaction mixture) *versus* L-Trp concentration ( $\mu\text{M}$ ) shows a hyperbolic response. The data were fitted to the Michaelis-Menten equation (Chapter 8, Equation [8.5]) and a representative plot for rhIDO is presented in Figure 2.10. Steady-state oxidation of L-Trp gave values for  $k_{\text{cat}} = 1.6 \pm 0.04 \text{ s}^{-1}$  and  $K_{\text{M}} = 21 \pm 1.9 \mu\text{M}$  for S167A, which is similar to that for rhIDO ( $k_{\text{cat}} = 1.4 \pm 0.05 \text{ s}^{-1}$ ,  $K_{\text{M}} = 7 \pm 0.8 \mu\text{M}$ ). The corresponding values for S167H were  $k_{\text{cat}} = 0.006 \pm 2.8 \times 10^{-5} \text{ s}^{-1}$  and  $K_{\text{M}} = 26 \pm 1.3 \mu\text{M}$ , showing that S167H is effectively inactive for oxidation of L-Trp.

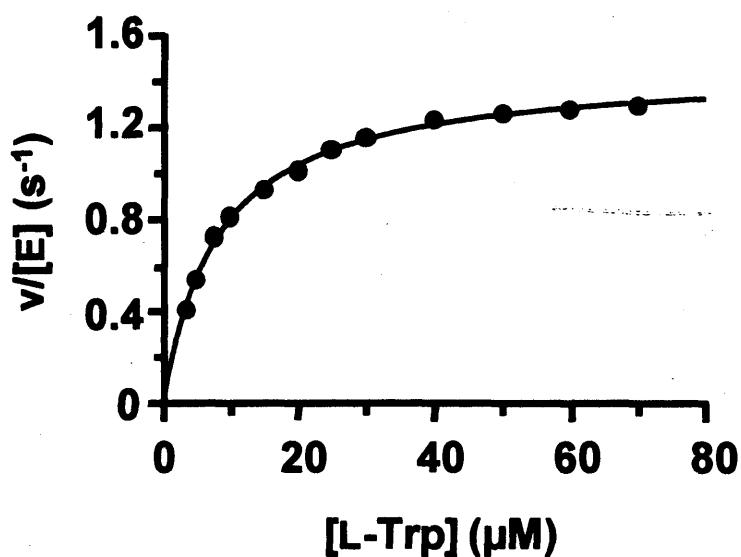


**Figure 2.10:** Steady state oxidation of L-Trp by rhIDO. Solid line shows a fit of the data to the Michaelis-Menten equation (Equation [8.5]). Conditions: 50 mM Tris/HCl buffer, pH 8.0, 25.0 °C.

## 2.2.9 The catalytic ferrous-oxy complex

### 2.2.9.1 rhIDO and its variants

Spectroscopic changes observed on reaction of rhIDO, S167A and S167H with O<sub>2</sub> were monitored using stopped-flow photodiode array spectroscopy. For rhIDO, the data were collected over a period of 1 s from the mixing event and were best fitted to a one-step model (A → B, Figures 2.11(A) and (B)) in which species A (red solid line) clearly represents the ferrous form of rhIDO ( $\lambda_{\max} = 425, 527^{\text{sh}}, 558$  nm) and species B (black dashed line) has spectral properties characteristic of the ferrous-oxy complex ( $\lambda_{\max} = 416, 539, 576$  nm).

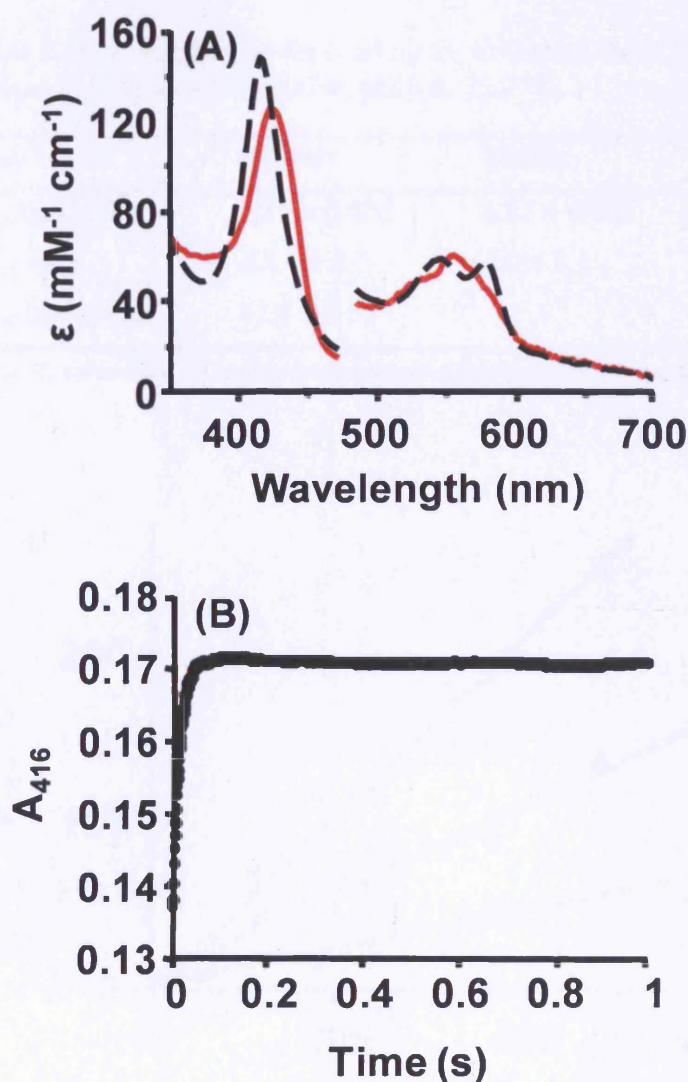


**Figure 2.11:** Reaction of rhIDO with  $\text{O}_2$  monitored by stopped-flow spectroscopy. (A) Deconvoluted spectra for the time-dependent spectral changes on mixing  $1 \mu\text{M}$  ferrous rhIDO with  $130 \mu\text{M}$   $\text{O}_2$  (time base of 1 s). The data were fitted to a single-step model  $\text{A} \rightarrow \text{B}$  (obtained from global fitting). (B) Absorption transient at 416 nm observed upon mixing of  $1 \mu\text{M}$  ferrous rhIDO with  $130 \mu\text{M}$   $\text{O}_2$ .

The ferrous-oxy complex was also observed for S167A and S167H and both variants exhibited similar wavelength maxima to that seen for rhIDO, Table 2.1.

The concentration dependence of the rate constant ( $k_{\text{obs}}$ ) for ferrous-oxy complex formation in rhIDO and the Ser167 mutants was monitored at 416 nm using the single-wavelength mode of the stopped-flow apparatus. The corresponding rate constants for  $\text{O}_2$  binding ( $k_{\text{on}}$ ,  $k_{\text{off}}$ , Equation [8.6]) to rhIDO, S167A and S167H are given in Table 2.4 and data are shown in Figure 2.12.

**Table 2.4:** Kinetic parameters for binding O<sub>2</sub> to ferrous rhIDO, S167A and S167H. Conditions: 50 mM Tris/HCl buffer, pH 8.0, 25.0 °C.

Variant	rhIDO	S167A	S167H
$k_{\text{on}}$ ( $\mu\text{M}^{-1} \text{s}^{-1}$ )	$0.53 \pm 0.006$	$0.25 \pm 0.002$	$0.11 \pm 0.02$
$k_{\text{off}}$ ( $\text{s}^{-1}$ )	$6.8 \pm 1.8$	$6.9 \pm 8.2$	$3.0 \pm 3.7$
$k_{\text{off}}/k_{\text{on}}$ ( $= K_{\text{D}}$ )	$12.8 \pm 3.53$	- <sup>a</sup>	- <sup>a</sup>

<sup>a</sup> An accurate  $K_{\text{D}}$  value could not be determined because of the large error value associated with  $k_{\text{off}}$ .

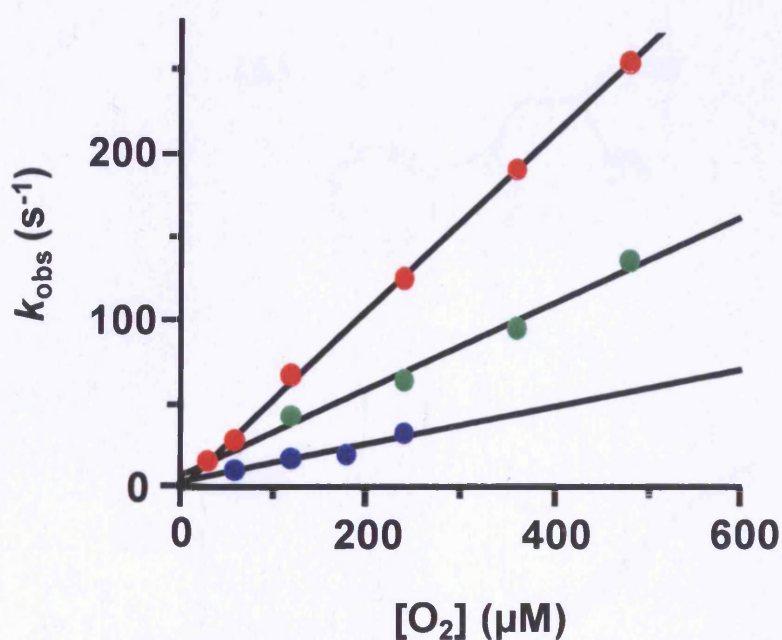


**Figure 2.12:** Concentration dependence of the observed rate constant ( $k_{\text{obs}}$ ) of O<sub>2</sub> binding to ferrous rhIDO (●), S167A (●) and S167H (●).

These ferrous-oxy complexes spontaneously decompose to ferric enzyme, for all three proteins under anaerobic conditions (monitored at 576 nm). For S167H, the ferrous-oxy complex was particularly unstable, as evidenced by the half life for this variant ( $t_{1/2} = 0.7$  s), which is much faster than the corresponding half lives of both rhIDO and S167A ( $t_{1/2} = 36$  s and 47 s, respectively).

### 2.2.9.2 Reaction of O<sub>2</sub> with rhIDO in the presence of 1-methyl-tryptophan

It is difficult to determine a rate constant for reaction of O<sub>2</sub> with rhIDO in the presence of L-Trp under pre-steady-state conditions, because turnover occurs during the experiment. Instead, the rate constant was determined in the presence of excess 1-methyl-tryptophan (1-Me-Trp) (as a substrate analogue, Figure 2.13(A)), which has been reported to be a potent inhibitor of IDO (9, 10). The data are shown in Figure 2.13(B), which yields values for  $k_{\text{on}}$  and  $k_{\text{off}}$  of  $0.52 \pm 0.03 \mu\text{M}^{-1}\text{s}^{-1}$  and  $6 \pm 9 \text{s}^{-1}$ , respectively, and were very similar to the values calculated for O<sub>2</sub> binding to the ferrous enzyme alone, Table 2.4.

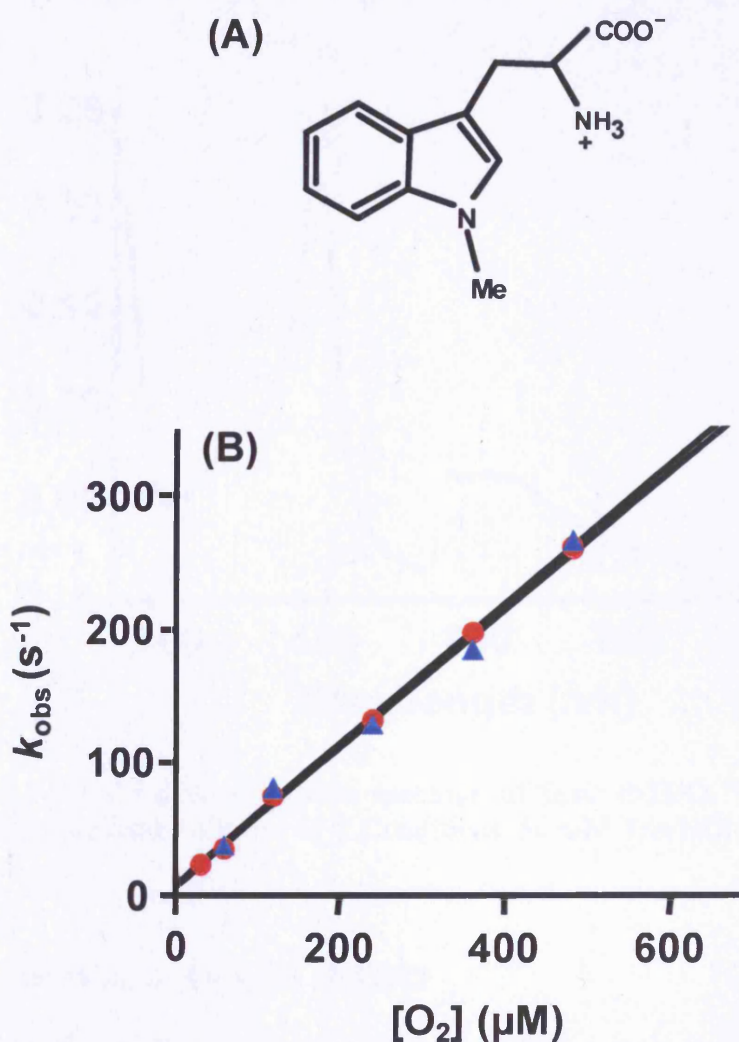


**Figure 2.13:** (A) The chemical structure of 1-Me-Trp. (B) Concentration dependence of the observed rate constant ( $k_{\text{obs}}$ ) of O<sub>2</sub> binding ferrous rhIDO in the absence (●) and presence of 300 μM 1-Me-Trp (▲).

### 2.2.10 Expression, purification and spectroscopic characterisation of rhTDO

Samples of rhTDO were prepared from *E. coli* BL21 (DE3) pLysS cells (harboring the pETHtDO8 expression plasmid) and purified as described in Chapter 8. All rhTDO protein samples used for this work were prepared by Dr. Jaswir Basran.

Purified rhTDO exists as a mixture of apo- and holo-enzyme forms. For this reason rhTDO was reconstituted with hemin prior to use in biochemical studies. Analysis of the UV-visible spectrum for ferric rhTDO reveals wavelength maxima at 408, 499, 530, 568<sup>sh</sup> and 632 nm (Figure 2.14) (11). Enzyme concentrations for rhTDO were determined using an absorption coefficient of  $\epsilon_{408} = 196 \text{ mM}^{-1}\text{cm}^{-1}$ .

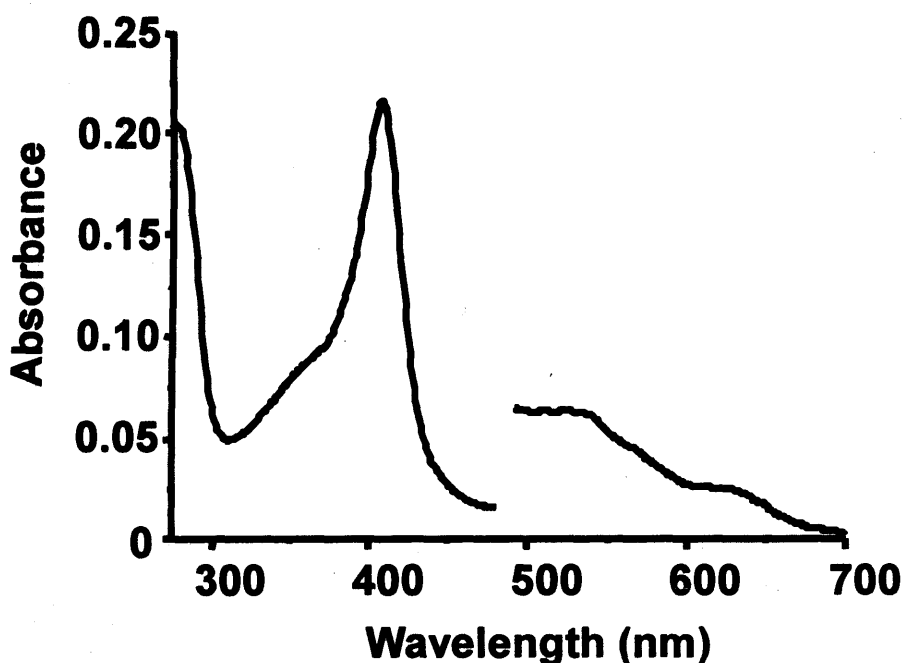


**Figure 2.14:** UV-visible absorption spectrum of ferric rhTDO. The visible region has been multiplied by a factor of 5. Conditions: 50 mM Tris/HCl buffer, pH 8.0, 25 °C.

### 2.2.11 Reaction of O<sub>2</sub> with rhTDO

Parallel kinetic studies were carried out with rhTDO and O<sub>2</sub> by Dr. Jaswir Basran. Spectroscopic changes observed on reaction of rhTDO with O<sub>2</sub> were monitored using stopped-flow photodiode array spectroscopy. In this experiment, data were collected over a period of 10 s from the mixing event. When mixed with O<sub>2</sub>, ferrous

rhTDO shows an overall decrease in absorbance in the visible region and the Soret band decreases in intensity and is blue-shifted (to 417 nm). There is no evidence for formation of the characteristic ferrous-oxy peaks (expected at  $\approx 540$  and  $\approx 580$  nm) even if the reaction is observed over an extended period (*e.g.* 200 s) (Figure 2.15). By means of comparison, absorption transients for the reaction of rhTDO and S167H with  $O_2$ , monitored over the same time-scale, are presented in Figure 2.16.

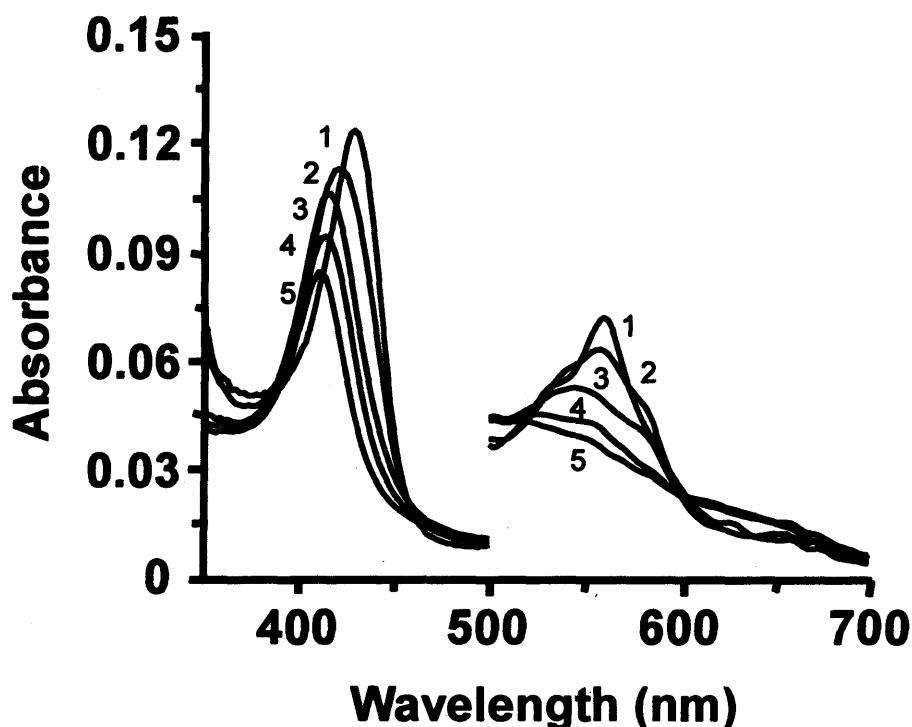


**Figure 2.15:** Reaction of rhTDO with  $O_2$  monitored by stopped-flow photodiode array spectroscopy. Time-dependent spectral changes on mixing rhTDO with  $O_2$  (time base of 10 s). For clarity, only selected spectra are shown at (1) 1.28 ms, (2) 100 ms, (3) 1 s, and (4) 10 s after mixing. The spectrum collected 200 s after mixing (5) is also shown. The visible region has been multiplied by a factor of 5. Conditions: 50 mM Tris/HCl, pH 8.0, 25.0 °C.

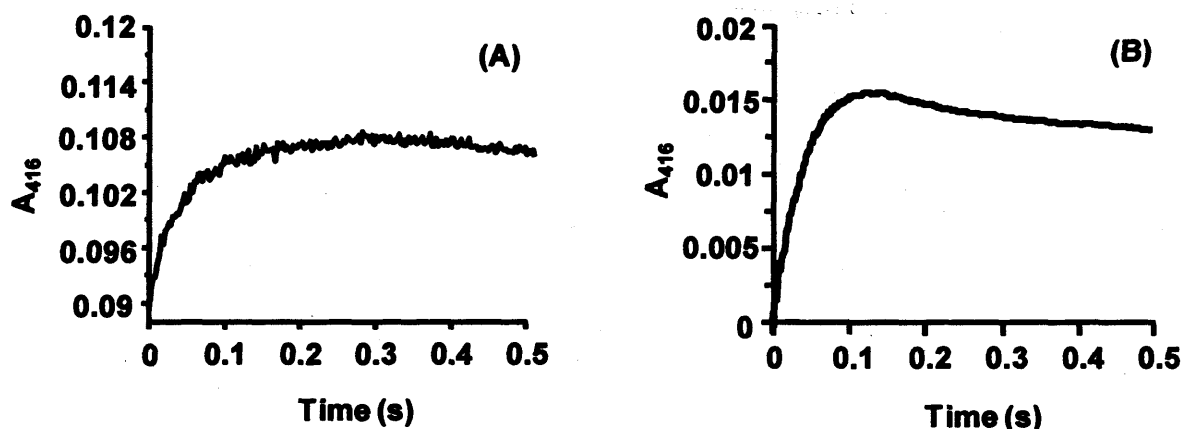


**Figure 2.16:** Typical transient traces for the reaction of (A) rhTDO and (B) S167H with 130  $\mu\text{M}$   $\text{O}_2$  followed as an increase in absorbance at 416 nm by stopped-flow spectroscopy.

### 2.2.12 Detection of intermediate species during reaction of reduced enzyme with L-Trp and $\text{O}_2$

The above data clearly show that the S167H variant is unable to form a ferrous-oxy complex that is as stable as that observed for both rhIDO and S167A. We therefore sought to establish whether this instability was the source of the poor catalytic activity of S167H in the steady-state. This was achieved by monitoring spectroscopic changes (by stopped-flow) during the course of the catalytic reaction of S167H and comparing them to those observed for rhIDO.

rhIDO was incubated with  $\text{O}_2$  for a period of 1 s (to allow for formation of the ferrous-oxy complex) and then mixed with excess L-Trp and the spectral changes monitored for 50 s. The first spectrum (collected at 1.28 ms after mixing of L-Trp) clearly represents the enzyme in the ferrous-oxy form (Figure 2.17(A) (black line),  $\lambda_{\text{max}} = 416, 539, 576$  nm). For the next 0.75 s no major spectral change was observed (apart from a small (2 nm) shift in the Soret peak from 416 nm to 414 nm) and no *N*-formyl-kynurenine was detected as evidenced by a lack of absorbance change at 321 nm (Figure 2.17(A), (inset)). We therefore propose that this species represents the ternary complex  $[\text{rhIDO}^{\text{II}}\text{-Trp-O}_2]$  (Figure 2.17(A) (red line),  $\lambda_{\text{max}} = 414$  nm, 544,

576 nm). A ternary complex with similar characteristics ( $\lambda_{\text{max}} = 413, 541, 576 \text{ nm}$ ) has been observed previously (12). During the steady-state phase, formation of *N*-formyl-kynurenine is apparent as there is a linear increase in absorbance at 321 nm over 5 s (Figure 2.17(A), (inset)). The spectrum of the species present during the steady-state phase is similar to that of the proposed ternary complex (Figure 2.17 (green line),  $\lambda_{\text{max}} = 413, 543, 576 \text{ nm}$ ).

When the experiment was repeated but ferrous rhIDO was incubated with L-Trp first and then mixed with O<sub>2</sub>, the first spectrum after final mixing was in this case identified as a ferrous-Trp complex (Figure 2.17(B), (black line)  $\lambda_{\text{max}} = 413, 551, 575^{\text{sh}} \text{ nm}$ ). After 0.75 s, the next species identified (Figure 2.17(B), (red line)) had a spectral form identical to that seen above and we therefore assign it as arising from the ternary complex [rhIDO<sup>II</sup>-Trp-O<sub>2</sub>]. The steady-state intermediate (Figure 2.17(B), (green line)) that was detected was also identical to that observed in the experiment above. These two experiments indicate that, regardless of the order of mixing, a species is identified in rhIDO that closely resembles a ferrous oxy intermediate and that we assign as the catalytic ternary complex [rhIDO<sup>II</sup>-Trp-O<sub>2</sub>].

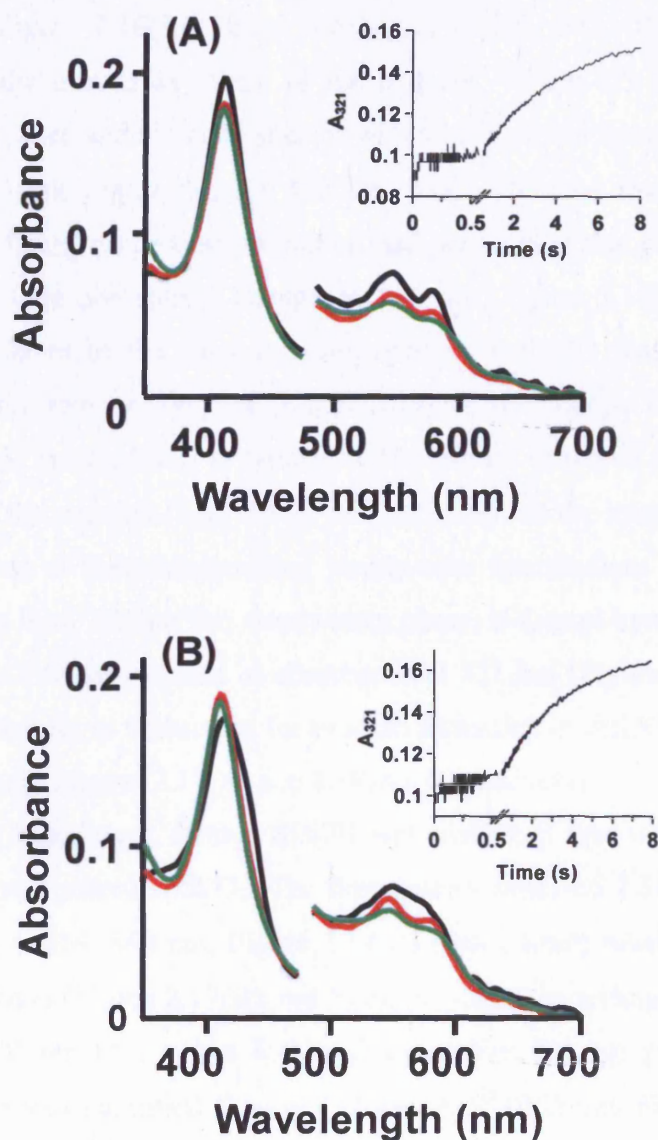


**Figure 2.17:** Detection of steady-state intermediates. (A) rhIDO pre-mixed with  $O_2$  followed by mixing with L-Trp. (B) rhIDO pre-mixed with L-Trp followed by mixing with  $O_2$ . (Inset) Time-dependence of absorbance changes at 321 nm, which report on *N*-formyl-kynurenine formation. Absorbance values in the visible region have been multiplied by a factor of 3. Black line shows the spectrum at 1.28 ms, red line at 0.75 s and green line at 5 s.

Parallel experiments with S167H were also carried out. In the first experiment, ferrous S167H was mixed first with  $O_2$  and after a pre-determined period of time (typically 0.8 s) the solution was mixed with excess L-Trp and the spectral changes

monitored over a period of 500 s. The first species observed, 2.56 ms after mixing with L-Trp (Figure 2.18(A), (black line)  $\lambda_{\max} = 416, 543, 581$  nm), is clearly identified as the ferrous-oxy form of the enzyme. Within 0.5 s, this ferrous-oxy species has decayed and a second species with a blue-shifted Soret band and a broad band in the visible region ( $\lambda_{\max} = 412$  nm,  $433^{\text{sh}}, 553$  nm) was detected (Figure 2.18(A), (red line)); no product formation had occurred at this point (as shown by the absence of an absorbance change at 321 nm, Figure 2.18(A), (inset)). This species is different to the corresponding species in rhIDO that was assigned as arising from the ternary complex (Figure 2.17(A), (red line)). The final spectrum (Figure 2.18(A) (green line)) is typical of the species observed during the steady-state phase of the reaction ( $\lambda_{\max} = 412, 543, 577$  nm) but the intensities are reduced when compared to the corresponding steady-state intermediate in rhIDO (Figure 2.17(A), green line). During this steady-state phase, *N*-formyl-kynurenine formation is observed as a linear increase in absorbance at 321 nm (Figure 2.18(A), (inset)). Note the differences in timescales for product formation in rhIDO (5 s) and S167H (200 s) (insets) to Figures 2.17(A) and 2.18(A), respectively).

In the second experiment, ferrous S167H was incubated first with L-Trp and then this complex was mixed with O<sub>2</sub>. The first species observed 2.56 ms after mixing with O<sub>2</sub> ( $\lambda_{\max} = 414, 549$  nm, Figure 2.18(B) (black line)) which, by comparison with rhIDO above (Figure 2.17(B), red line), we assign as arising from the ferrous-Trp complex. After 0.5 s (when *N*-formyl-kynurenine has not yet been formed) a second species was identified ( $\lambda_{\max} = 412$  nm,  $425^{\text{sh}}, 553$  nm, Figure 2.18(B) (red line)) which is similar to that observed at the same time point in Figure 2.18(A). During the steady-state phase, *N*-formyl-kynurenine formation is observed as a linear increase in absorbance at 321 nm (Figure 2.18(B), (inset)) and the intermediate that is detected at this point (Figure 2.18(B), (green line)) is identical to that in (Figure 2.18(A) (green line)). At no stage, is clear formation of a ferrous-oxy species observed.

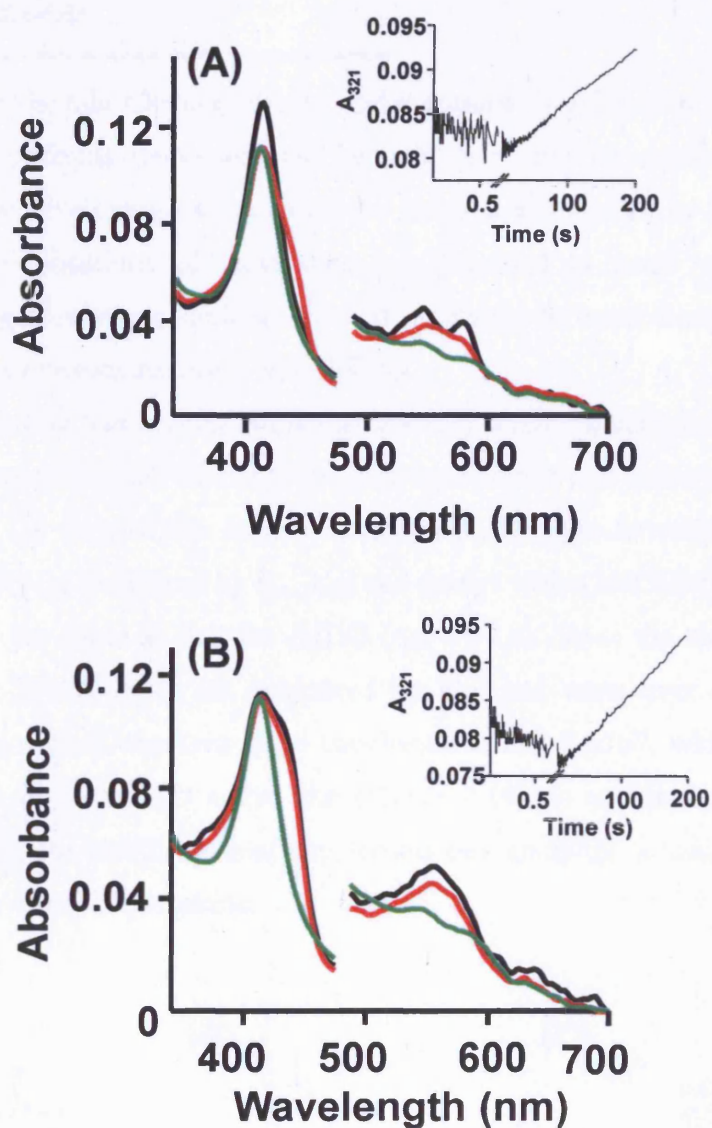


**Figure 2.18:** Detection of steady-state intermediates. (A) S167H pre-mixed with  $O_2$  followed by mixing with L-Trp. (B) S167H pre-mixed with L-Trp followed by mixing with  $O_2$ . (Inset) Time-dependence of absorbance changes at 321 nm, which report on *N*-formyl-kynurenine formation. Absorbance values in the visible region have been multiplied by a factor of 3. Black line shows the spectrum at 2.56 ms; red line at 0.5 s and green line at 100 s.

These experiments for S167H indicate (i) that the proposed ternary complex identified for rhIDO above is not observed in S167H and (ii) that the species present in the steady-state for S167H is not the same as that for rhIDO nor does it resemble a ferrous-oxy species (as for rhIDO), regardless of the order of mixing.

## 2.3 Discussion

The intention in this Chapter was to make comparisons between the active site structures of different mammalian and bacterial heme dioxygenases and to use this as a basis for developing our ideas on the reaction mechanism in these enzymes. Below, the implications of these data are discussed in terms of our broader understanding of substrate binding and catalysis across the heme dioxygenase family and direct comparisons are made with rhTDO.

*Hydrogen bonding interactions in the active site of rhIDO.* Electronic spectra for the ferrous form of S167A are similar to the wild type protein and indicate this variant is 5-coordinate (as for rhIDO). In accordance with this, the ferrous-oxy derivative forms normally (as evidenced by  $k_{\text{on}}$ ,  $k_{\text{off}}$ ) and decays with a half life ( $t_{1/2} = 47$  s) that is essentially the same as that for rhIDO ( $t_{1/2} = 37$  s). Since the steady-state data indicate that S167A binds (as evidenced by  $K_M$ ) and turns over ( $k_{\text{cat}}$ ) substrate essentially as normal, the immediate conclusion is that Ser167, which is the only polar residue in the rhIDO active site (Figure 2.19), is not important either for binding of  $O_2$ , for stabilisation of the ferrous-oxy complex or conversion of the substrate to *N*-formyl-kynurenine.

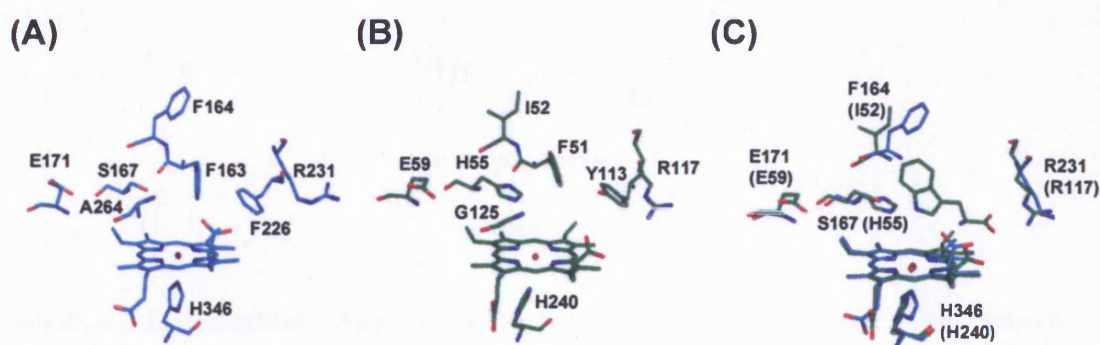
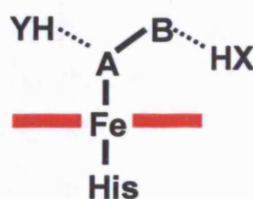


**Figure 2.19:** A comparison of the active sites of rhIDO and *XcTDO*. (A) The active site of rhIDO (in cyan (1)). (B) The active site of *XcTDO* (in green (2)) in the same orientation as that shown for rhIDO. Active site residues for rhIDO are H346, R231, F226, F163, S167, A264, F164, E171 which correspond to H240, R117, Y113, F51, H55, G125, I52 and E59 in *XcTDO*. (C) An overlay of rhIDO (cyan) and the *XcTDO*-Trp (green) complex, with the residues for rhIDO indicated and those for *XcTDO* in parentheses.

There are no other potential hydrogen bonding residues in the active site of rhIDO (Figure 2.19). This is in contrast to the globins, in which a distal histidine residue is located directly above the iron and is poised to hydrogen bond to the bound  $O_2$  (13, 14). We therefore interpret these data to mean that any hydrogen bonding stabilisation of the bound  $O_2$  ligand in rhIDO is most likely to be through an active site water molecule(s), as occurs in some other catalytic  $O_2$  binding proteins (*e.g.* heme oxygenase and cytochrome P450) (15-17). Although water molecules are not present in the crystal structure of rhIDO (1), the actual hydration structure is likely to be different since the crystal structure contained two CHES molecules and the inhibitor 4-phenyl-imidazole in the active site, neither of which would be present physiologically. The presence of water molecules in the active site of rhIDO is further examined in Chapter 4.

The precise mode of substrate binding in rhIDO is not yet known, but we envisage that in the presence of L-Trp these hydrogen bonding interactions to  $O_2$  are replaced with hydrogen bonds to the substrate, Scheme 2.2. This would also account for the fact that the affinity of L-Trp for both ferric rhIDO and ferric S167A is considerably enhanced in the presence of cyanide, Table 2.3, where these hydrogen bonding interactions to the substrate are also presumably possible (Scheme 2.2).



**Scheme 2.2:** Schematic diagram of the possible hydrogen bonding interactions (dashed lines) to a bound diatomic ligand (either  $O_2$  or CN, represented by AB) in rhIDO (2). Hydrogen bond donors are indicated as XH and YH and are envisaged as being provided by either active site water molecules or substrate.

*Comparisons with bacterial and human TDOs: S167H variant.* In XcTDO, Ser167 is replaced with a histidine residue (His55, Figure 2.19(C)). Sequence alignments with human TDO indicate that it also has a His at this position (His76). In the following

sections, we compare the properties of the S167H variant with these other two dioxygenases.

The spectroscopic and ligand binding data indicate that the ferric derivative of the S167H variant most likely has His167 bound to the iron, but that this is displaceable on binding of other strong ligands (*e.g.* cyanide) or on reduction. Hence, although the new ligand is not located directly 'above' the heme (as in other bis-histidine ligated heme proteins such as cytochrome *b<sub>5</sub>* and neuroglobin (18, 19)), it appears that His167 is within bonding distance of the heme. This is in contrast to the presumed coordination geometry in rhTDO, which contains a histidine (His76) at the position equivalent to Ser167, for which spectroscopic data indicate mainly a high-spin, water-bound heme species in the ferric form (11). We conclude that there are differences in the precise orientation of the histidine residue between the two enzymes, such that coordination to the heme occurs in one case but not the other.

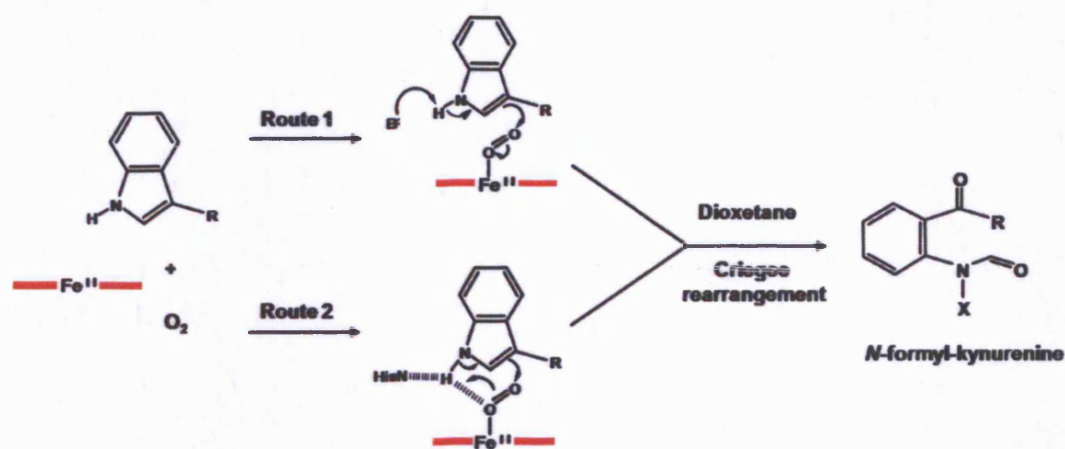
*Comparisons with bacterial and human TDOs: stability of the ferrous-oxy complex.*

The ferrous-oxy complex of S167H is very greatly destabilised compared to rhIDO. This behaviour for S167H replicates that in *Pseudomonas* TDO (20) and in rhTDO, where the ferrous-oxy complex is similarly unstable. The very low reduction potential for S167H (-203 mV) is certainly likely to be influential in destabilising the ferrous-oxy complex, but does not provide a complete explanation because the reduction potential of rhTDO (-92 mV) (11) is higher and in this enzyme the ferrous-oxy species is not detected at all. By way of comparison, reduction potentials for myoglobin – in which the ferrous-oxy complex is much more stable – are typically in the range  $\approx +50$  mV (21). The absence of potential hydrogen bonding residues within the active site of rhIDO and the presumed failure of rhIDO to duplicate the stabilising hydrogen bonding interactions observed in the globins (*vide supra*) might also be influential however.

The poor stability of the ferrous-oxy complex in S167H is reflected in the fact that the enzyme has lost >99% of its activity (as evidenced by  $k_{cat}$ ), although we note that it binds L-Trp normally (as evidenced by  $K_M$ ). The formation of the ferrous-oxy complex is an important junction in the overall dioxygenase mechanism: this intermediate needs to be stable enough to interact with the substrate so that effective conversion to product can occur. Our stopped-flow kinetic data for rhIDO in the steady-state indicate that significant amounts of the ferrous-oxy complex are present

under turnover conditions. For S167H this is not the case, however: this presumably reflects the rapid and unproductive decay of the ferrous-oxy species, which then competes with the slower (productive) conversion of substrate to product.

*Mechanistic implications.* Our kinetic data for rhIDO reveal that the enzyme shows no substantial preference for binding of O<sub>2</sub> over L-Trp because the steady-state  $K_M$  for L-Trp is in a similar range to the  $K_D$  for O<sub>2</sub> binding. Also, the kinetic data with 1-Me-Trp show no enhancement of affinity for O<sub>2</sub> in the presence of this substrate analogue. By implication we conclude that substrate binding does not preferentially favour O<sub>2</sub> binding in rhIDO. This is consistent with our pre-steady-state data in which we observe a catalytic intermediate, proposed as the ternary complex [rhIDO<sup>II</sup>-Trp-O<sub>2</sub>], at the same point in the reaction mechanism regardless of whether O<sub>2</sub> or L-Trp is mixed with the enzyme first. In contrast, previous studies with bacterial TDO have shown that ferrous TDO does not readily bind O<sub>2</sub> in the absence of L-Trp and addition of O<sub>2</sub> leads directly to the oxidised enzyme (20). This led to the assumption that binding of L-Trp and O<sub>2</sub> to form the ternary complex [TDO<sup>II</sup>-Trp-O<sub>2</sub>] was an ordered process with L-Trp binding first followed by O<sub>2</sub> (2, 20). It now appears that this ordered binding process could exist universally across all bacterial and human TDO enzymes since the ferrous-oxy complex of rhTDO could not be detected even on the stopped-flow time-scale.



**Scheme 2.3:** Possible reaction mechanisms for the conversion of L-Trp to *N*-formyl-kynurenine catalysed by IDO and TDO.

There are two possible mechanisms for initial reaction of the ferrous-oxy complex with bound substrate (Scheme 2.3). One mechanism involves base-catalysed abstraction of the indole NH (route 1), the other does not (route 2). Early suggestions (10) favoured the base-catalysed mechanism. However, there is no evidence from our data that the only polar residue present in the active site of rhIDO, Ser167, plays any role in controlling the reaction mechanism. The alternative route (route 2), does not involve base-catalysed proton abstraction (22). However, in XcTDO the N<sup>ε</sup> of His55 is hydrogen bonded to the indole nitrogen of the bound substrate, Scheme 2.3, and although removal of this residue (H55A) lowers activity ( $k_{\text{cat(H55A)}} = 0.1 \times k_{\text{cat(wild type)}}$  (2)) some activity remains indicating that catalysis still occurs even in the absence of His55. This would be consistent with the fact that His55 is not needed in rhIDO, and is replaced with Ser167. This would mean that the most likely role for His55 is not in base-catalysed abstraction but in orienting the indole hydrogen, through hydrogen bonding, in a suitable position for catalysis. Presumably, the same interaction exists in rhTDO (through His76).

## 2.4 References

---

1. Sugimoto, H., Oda, S., Otsuki, T., Hino, T., Yoshida, T., and Shiro, Y. (2006) Crystal structure of human indoleamine 2,3-dioxygenase: catalytic mechanism of O<sub>2</sub> incorporation by a heme-containing dioxygenase, *Proc. Natl. Acad. Sci. USA* 103, 2611-2616.
2. Forouhar, F., Anderson, J. L., Mowat, C. G., Vorobiev, S. M., Hussain, A., Abashidze, M., Bruckmann, C., Thackray, S. J., Seetharaman, J., Tucker, T., Xiao, R., Ma, L. C., Zhao, L., Acton, T. B., Montelione, G. T., Chapman, S. K., and Tong, L. (2007) Molecular insights into substrate recognition and catalysis by tryptophan 2,3-dioxygenase, *Proc. Natl. Acad. Sci. USA* 104, 473-478.
3. Littlejohn, T. K., Takikawa, O., Truscott, R. J., and Walker, M. J. (2003) Asp274 and his346 are essential for heme binding and catalytic function of human indoleamine 2,3-dioxygenase, *J. Biol. Chem.* 278, 29525-29531.
4. Dick, R., Murray, B. P., Reid, M. J., and Correia, M. A. (2001) Structure--function relationships of rat hepatic tryptophan 2,3-dioxygenase: identification of the putative heme-ligating histidine residues, *Arch. Biochem. Biophys.* 392, 71-78.
5. Papadopoulou, N. D., Mewies, M., McLean, K. J., Seward, H. E., Svistunenko, D. A., Munro, A. W., and Raven, E. L. (2005) Redox and spectroscopic properties of human indoleamine 2,3-dioxygenase and a His303Ala variant: implications for catalysis, *Biochemistry* 44, 14318-14328.
6. Gadsby, P. M., and Thomson, A. J. (1990) Assignment of the axial ligands of ferric ion in low-spin hemoproteins by near-infrared magnetic circular dichroism and electron paramagnetic resonance spectroscopy, *J. Am. Chem. Soc.* 112, 5003-5011.
7. More, C., Belle, V., Asso, M., Fournel, A., Roger, G., Guigliarelli, B., and Bertrand, P. (1999) Biospectroscopy, *S5*, S3-S18.
8. Efimov, I., Papadopoulou, N. D., McLean, K. J., Badyal, S. K., Macdonald, I. K., Munro, A. W., Moody, P. C., and Raven, E. L. (2007) The Redox Properties of Ascorbate Peroxidase, *Biochemistry* 46, 8017-8023.

9. Cady, S. G., and Sono, M. (1991) 1-Methyl-DL-tryptophan, beta-(3-benzofuranyl)-DL-alanine (the oxygen analog of tryptophan), and beta-[3-benzo(b)thienyl]-DL-alanine (the sulfur analog of tryptophan) are competitive inhibitors for indoleamine 2,3-dioxygenase, *Arch. Biochem. Biophys.* 291, 326-333.
10. Sono, M., Roach, M. P., Coulter, E. D., and Dawson, J. H. (1996) Heme-Containing Oxygenases, *Chem. Rev.* 96, 2841-2888.
11. Basran, J., Rafice, S. A., Chauhan, N., Efimov, I., Cheesman, M. R., Ghamsari, L., and Raven, E. L. (2008) A kinetic, spectroscopic, and redox study of human tryptophan 2,3-dioxygenase, *Biochemistry* 47, 4752-4760.
12. Sono, M. (1986) Spectroscopic and equilibrium properties of the indoleamine 2,3-dioxygenase-tryptophan-O<sub>2</sub> ternary complex and of analogous enzyme derivatives. Tryptophan binding to ferrous enzyme adducts with dioxygen, nitric oxide, and carbon monoxide, *Biochemistry* 25, 6089-6097.
13. Springer, B. A., Sligar, S. G., Olson, J. S., and Philips, G. N. (1994) Mechanisms of Ligand Recognition in Myoglobin, *Chem. Rev.* 94, 699-714.
14. Antonini, M., and Brunori E. (1971) *Hemoglobin and Myoglobin and their reactions with ligands*, North Holland Publishers, Amsterdam.
15. Davydov, R., Chemerisov, S., Werst, D. E., Rajh, T., Matsui, T., Ikeda-Saito, M., and Hoffman, B. M. (2004) Proton transfer at helium temperatures during dioxygen activation by heme monooxygenases, *J. Am. Chem. Soc.* 126, 15960-15961.
16. Davydov, R., Perera, R., Jin, S., Yang, T. C., Bryson, T. A., Sono, M., Dawson, J. H., and Hoffman, B. M. (2005) Substrate modulation of the properties and reactivity of the oxy-ferrous and hydroperoxo-ferric intermediates of cytochrome P450cam as shown by cryoreduction-EPR/ENDOR spectroscopy, *J. Am. Chem. Soc.* 127, 1403-1413.
17. Davydov, R., Matsui, T., Fujii, H., Ikeda-Saito, M., and Hoffman, B. M. (2003) Kinetic isotope effects on the rate-limiting step of heme oxygenase catalysis indicate concerted proton transfer/heme hydroxylation, *J. Am. Chem. Soc.* 125, 16208-16209.

18. Cowley, A. B., Altuve, A., Kuchment, O., Terzyan, S., Zhang, X., Rivera, M., and Benson, D. R. (2002) Toward engineering the stability and heme-binding properties of microsomal cytochromes *b5* into rat outer mitochondrial membrane cytochrome *b5*: examining the influence of residues 25 and 71, *Biochemistry* 41, 11566-11581.
19. Dewilde, S., Kiger, L., Burmester, T., Hankeln, T., Baudin-Creuzat, V., Aerts, T., Marden, M. C., Caubergs, R., and Moens, L. (2001) Biochemical characterization and ligand binding properties of neuroglobin, a novel member of the globin family, *J. Biol. Chem.* 276, 38949-38955.
20. Ishimura, Y., Nozaki, M., and Hayaishi, O. (1970) The oxygenated form of L-tryptophan 2,3-dioxygenase as reaction intermediate, *J. Biol. Chem.* 245, 3593-3602.
21. Raven, E. L., and Mauk, A. G. (2001) Chemical reactivity of the active site of myoglobin, *Adv. Inorg. Chem.* 51, 1-49.
22. Terentis, A. C., Thomas, S. R., Takikawa, O., Littlejohn, T. K., Truscott, R. J., Armstrong, R. S., Yeh, S. R., and Stocker, R. (2002) The heme environment of recombinant human indoleamine 2,3-dioxygenase. Structural properties and substrate-ligand interactions, *J. Biol. Chem.* 277, 15788-15794.

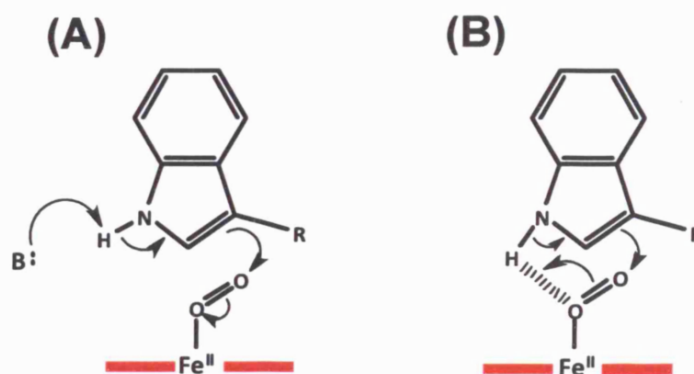
# **Chapter 3**

---

## **Reassessment of the reaction mechanism in heme dioxygenases**

### 3.1 Introduction

The detailed catalytic mechanism of indoleamine 2,3-dioxygenase (IDO) and tryptophan 2,3-dioxygenase (TDO) has been a matter of ongoing investigation. As reviewed in Chapter 1, early studies suggested that base-catalysed deprotonation of the indole NH group (Scheme 3.1(A)) was the most likely initiation step. This suggestion was based partly on the observation that 1-methyl-tryptophan (1-Me-Trp (Figure 3.1(B)) is an inhibitor of dioxygenase activity (1), and seemed plausible since base-catalysed abstraction is not possible with the methylated compound. However, there are problems with this mechanism. To begin with, it is inconsistent with the chemistry of indoles (2), which typically react by electrophilic addition across the C<sup>3</sup> position and subsequent formation of a cation at N<sup>1</sup>. The pK<sub>a</sub> of the indole nitrogen (≈17 (3)) is also outside of the expected biological range. In addition, the crystal structure of recombinant human IDO (rhIDO) (4) reveals that there is no active-site base close enough for proton abstraction at N<sup>1</sup>. The only polar active site residue is Ser167, but evidence was presented in Chapter 2 to demonstrate that this residue is not essential for activity (5). Although *X. campestris* TDO (XcTDO) does contain an active site histidine (His55, equivalent to Ser167 in rhIDO) (6) which hydrogen bonds to the indole N<sup>1</sup>, substitution of His55 does not eliminate activity (6, 7). Together, this led to the hypothesis that the bound dioxygen itself might act as the active-site base (Scheme 3.1(B)) (4, 6), with no involvement from active site residues.



**Scheme 3.1:** Possible mechanisms for oxidation of L-Trp. (A) Abstraction of the indole proton by an active site base. (B) Abstraction of the indole proton by the heme-bound dioxygen.

Interestingly, sequence alignments (6) with *Xc*TDO and recombinant human TDO (rhTDO) indicate that rhTDO also contains a histidine (His76) in the same position as His55 (*Xc*TDO).

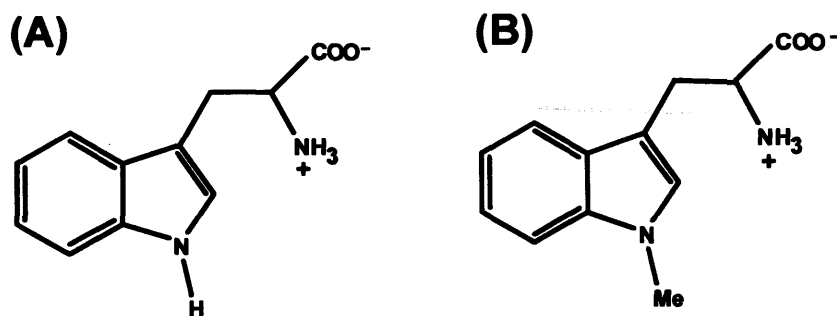


**Figure 3.1:** The chemical structures of tryptophan (A) and 1-methyl-tryptophan (B).

In this Chapter, the activity of 1-Me-Trp with rhIDO, rhTDO and site-directed variants focused on the Ser167/His76 location were examined. In addition, the activity of 1-Me-Trp with *Xc*TDO and its H55S variant are also discussed in some detail. We find, in contrast to previous studies (1), that 1-Me-Trp is a substrate and these observations are inconsistent with previously published mechanisms for substrate oxidation by the heme dioxygenase family (rhIDO, rhTDO and *Xc*TDO). In this work, an alternative reaction mechanism, based on the known chemistry of indoles, is presented.

## 3.2 Results

### 3.2.1 Purification of 1-Methyl-Tryptophan

Commercially available 1-Me-L-Trp (95% purity) was purified by HPLC to remove any contaminating species (5%) which could act as a substrate. The HPLC trace before purification of 1-Me-Trp (Figure 3.2(A)) showed that several contaminants were present in the sample (the largest contaminating species is labelled with \* and co-elutes at 6 min). After elution of 1-Me-Trp at ~10 min (Figure 3.2(A)), the sample was subjected to further HPLC analysis (Figure 3.2(B)) which revealed the presence of one peak corresponding to 1-Me-Trp<sup>a</sup>. The <sup>1</sup>H NMR spectrum of purified 1-Me-Trp also confirmed the removal of any contaminating species (Figure 3.3).

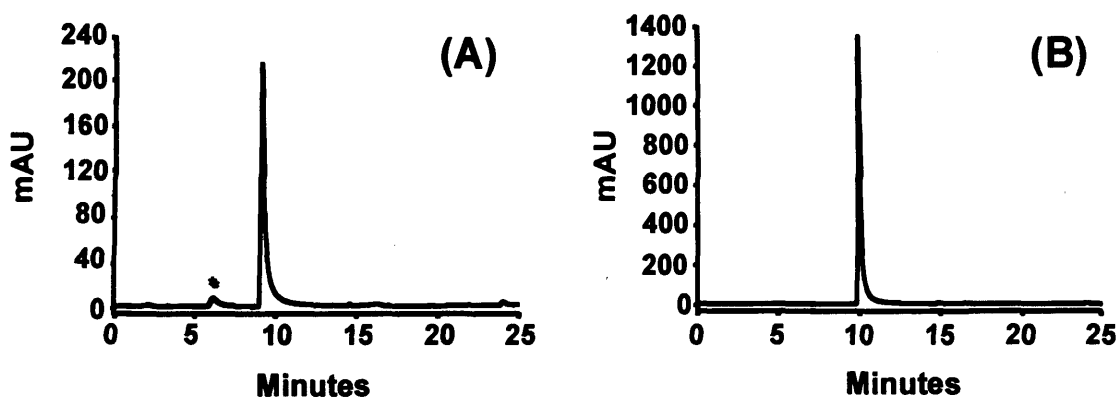


**Figure 3.2:** Chromatogram of commercially available 1-Me-Trp (A) before and (B) after purification by HPLC. Conditions:  $\lambda$  - 280 nm; RP C18, 250 x 4.6 mm; H<sub>2</sub>O:MeCN, 90:10 v/v; 1 ml/min.

<sup>a</sup> HPLC purification of 1-Me-Trp was kindly carried out by Mr Michael Lee (Department of Chemistry, University of Leicester).

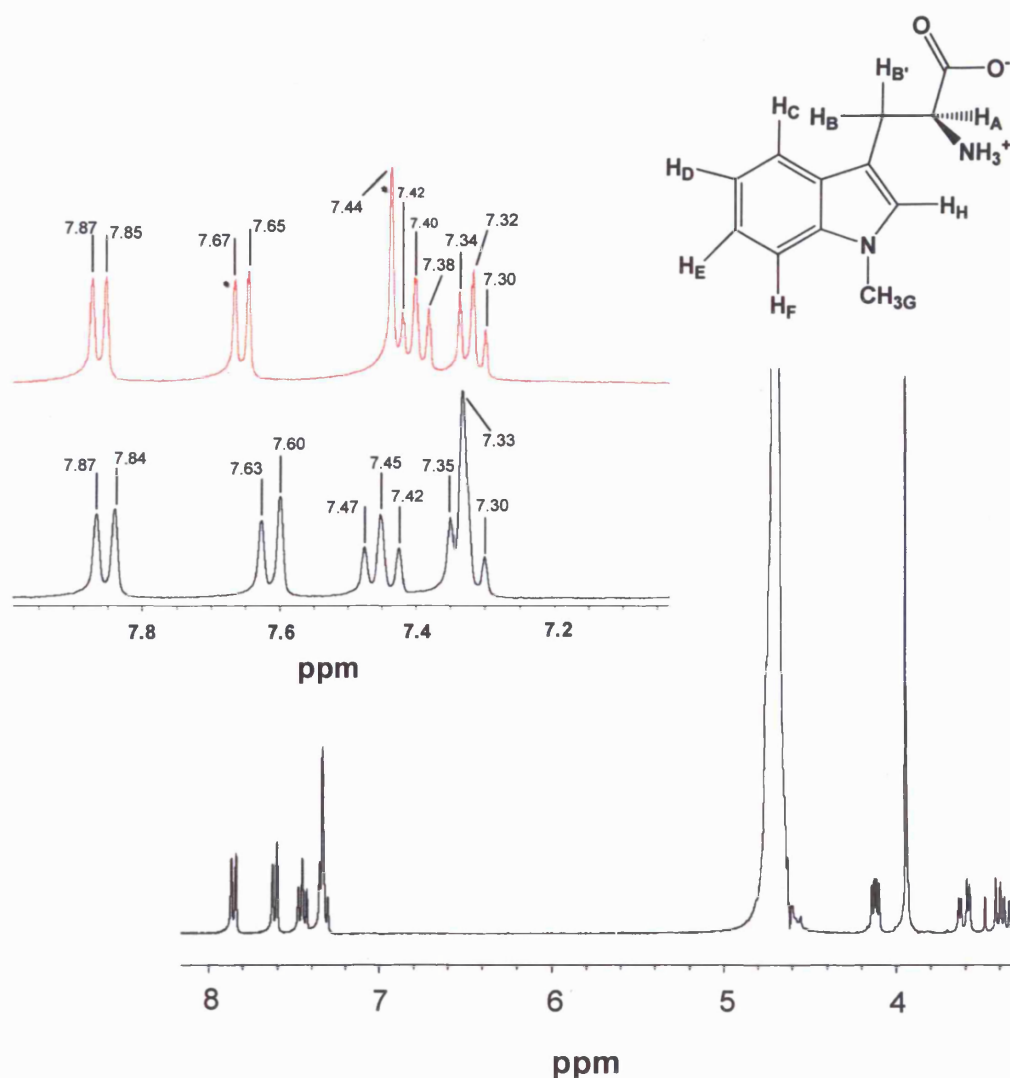


**Figure 3.3:** NMR spectrum of purified 1-Me-Trp from Figure 3.2(B).  $^1\text{H}$  NMR (300 MHz,  $\text{D}_2\text{O}/\text{CD}_3\text{CN}$ )  $\delta$  3.33-3.65 (m, 2H,  $\text{H}_\text{B} + \text{H}_{\text{B}'}$ ), 3.93 (s, 3H,  $\text{H}_\text{G}$ ), 4.12 (dd, 1H,  $J = 8.2$  Hz, 4.7 Hz,  $\text{H}_\text{A}$ ), 7.33 (s + t, 2H,  $J = 7.5$  Hz,  $\text{H}_\text{H} + \text{H}_{\text{D/E}}$ ), 7.45 (t, 1H,  $J = 7.5$  Hz,  $\text{H}_{\text{D/E}}$ ), 7.61 (d, 1H,  $J = 8.5$  Hz,  $\text{H}_{\text{C/F}}$ ), 7.85 (d, 1H,  $J = 8.1$  Hz,  $\text{H}_{\text{C/F}}$ ). Inset:  $^1\text{H}$  NMR spectra of commercially available L-Trp (red) and purified 1-Me-Trp (black) expanded between the 7-8 ppm region. \* indicates the peaks that have shifted significantly in respect to the spectrum of 1-Me-L-Trp and therefore confirms the removal of L-Trp from purified 1-Me-Trp. Conditions: Bruker DPX300; basic frequency,  $^1\text{H} = 300.03$  MHz; spectral width 16 ppm.

### 3.2.2 Expression, purification and spectroscopic characterisation of rhIDO and S167A

All rhIDO and S167A protein samples were prepared, purified and spectroscopically characterised as described in Chapter 2 (5).

### 3.2.3 Identification of reaction products catalysed by rhIDO and S167A

#### 3.2.3.1 UV-visible spectroscopy

To determine if rhIDO could utilise 1-Me-Trp as a substrate, identification of the methylated product was essential. This was carried out using steady-state analysis, which would allow accumulation of *N*-formyl-methylkynurenine. UV-visible spectroscopy was used to monitor absorbance changes upon the addition of 1-Me-Trp and L-Trp with rhIDO. Increases in absorbance at 321 nm were observed upon reaction of rhIDO with 1-Me-Trp, indicating formation of *N*-formyl-methylkynurenine (Figure 3.4, red line). The reaction with 1-Me-Trp was repeated in the absence of enzyme (Figure 3.4, yellow line) and no absorbance change at 321 nm was observed, confirming that product formation is from enzymatic oxidation. Formation of *N*-formyl-kynurenine, from L-Trp, was confirmed by the presence of an absorption band at the same wavelength (Figure 3.4, green line).

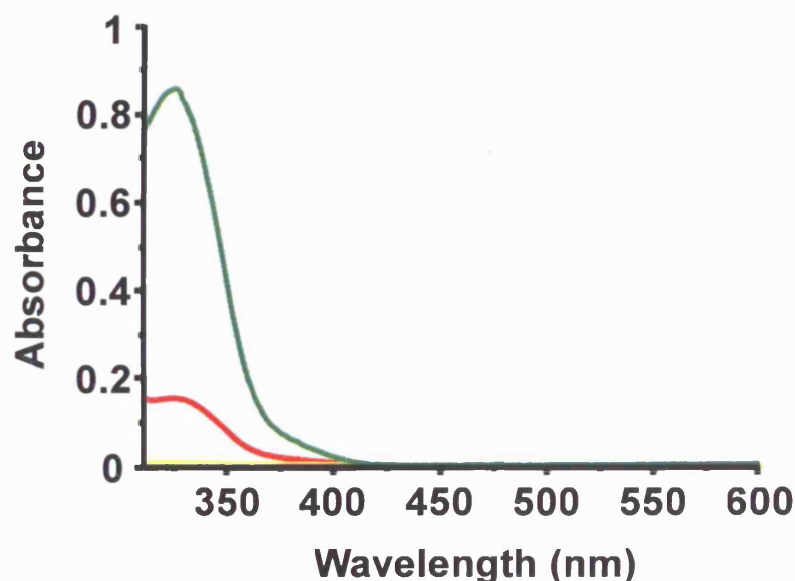


**Figure 3.4:** UV-visible spectrum of *N*-formyl-kynurenine (green line) and *N*-formyl-methylkynurenine (red line) showing absorption bands at 321 nm. Spectra were obtained *after* isolation of the compounds from steady-state assays with rhIDO. Parallel experiments carried out with 1-Me-Trp in the absence of enzyme show no product formation at 321 nm (yellow line).

### 3.2.3.2 LC-MS analysis

LC-MS analysis using selected ion monitoring (Figure 3.5) was then carried out to confirm the identity of the product formed upon reaction of rhIDO with 1-Me-Trp (Figure 3.4 red line). First, a control reaction was carried out with rhIDO upon reaction with L-Trp, where an ion with  $m/z = 237$  was detected (Figure 3.5(A)) which corresponds to the mass of *N*-formyl-kynurenine ( $m/z = 236$ ). For the reaction with 1-Me-Trp, an equivalent ion was detected with  $m/z = 251$  (Figure 3.5(B)) as expected for *N*-formyl-methylkynurenine ( $m/z = 250$ ).

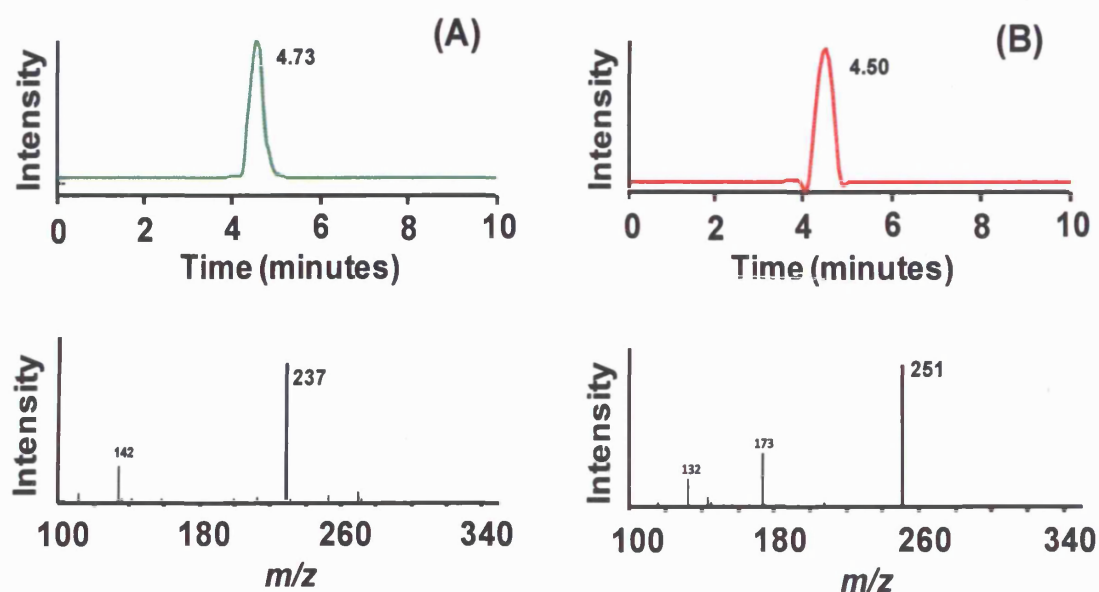


**Figure 3.5:** LC-MS analysis of products obtained on reaction of rhIDO with L-Trp (Panel A) and 1-Me-Trp (Panel B). Panel A: (top) elution profile for selected ion chromatogram with  $m/z$  of 237 and (bottom) the corresponding positive ESI mass spectrum for the product eluted at 4.73. Panel B: (top) elution profile for selected ion chromatogram with  $m/z$  of 251 and (bottom) the corresponding positive ESI mass spectrum for the product eluted at 4.50.

LC-MS analysis was repeated with S167A upon reaction with either L-Trp or 1-Me-Trp (Appendix A, Figure 1) and confirmed the presence of ions with  $m/z$  corresponding to *N*-formyl-kynurenine ( $m/z = 237$ ) and *N*-formyl-methylkynurenine ( $m/z = 251$ ), respectively. This clearly indicates that both rhIDO and S167A are able to utilise 1-Me-Trp as a substrate.

### 3.2.4 Expression, purification and spectroscopic characterisation of rhTDO

All rhTDO protein samples were prepared, purified and spectroscopically characterised as described in Chapter 2.

### 3.2.5 LC-MS analysis of the reaction products catalysed by rhTDO

LC-MS analysis was carried out upon reaction of rhTDO with L-Trp and 1-Me-Trp. For the reaction with L-Trp, an ion with  $m/z = 237$  (Figure 3.7) was detected which corresponds to the mass of *N*-formyl-kynurenine ( $m/z = 236$ ). However, for the reaction with 1-Me-Trp, no ions were eluted that corresponded to a  $m/z$  of 251. The reaction of rhTDO with 1-Me-Trp was also monitored by UV-visible spectroscopy where no increase in absorbance was observed at 321 nm (unlike rhIDO, Figure 3.4, red line), thus confirming that rhTDO cannot utilise 1-Me-Trp as a substrate.

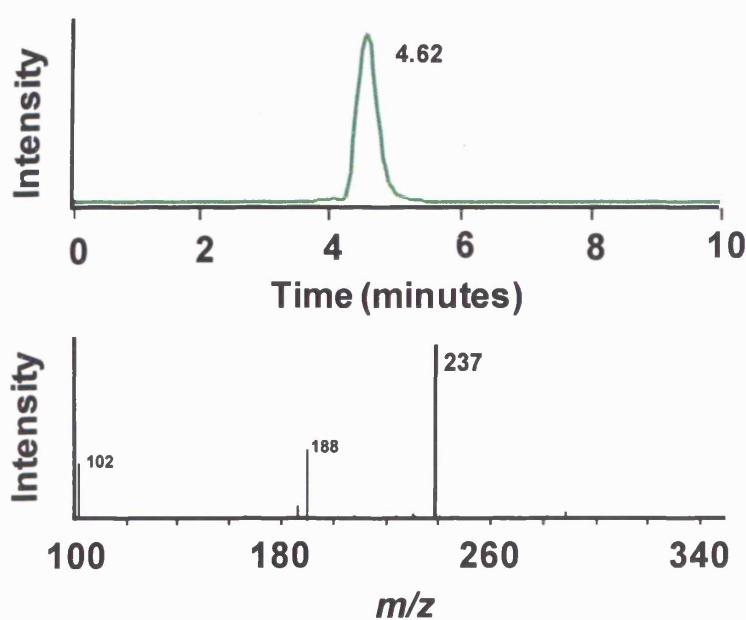


**Figure 3.7:** LC-MS analysis of a product obtained on reaction of rhTDO with L-Trp. Elution profile (top) for selected ion chromatogram with  $m/z$  of 237 and (bottom) the corresponding positive ESI mass spectrum for the product eluted at 4.62 minutes.

### 3.2.6 Expression, purification and spectroscopic characterisation of H76S variant

Site-directed mutagenesis was performed, according to the Quickchange<sup>TM</sup> protocol, as described in Chapter 8. The H76S variant (of rhTDO) was expressed and purified as described in Chapter 8.

The purity of freshly isolated H76S variant was checked using SDS-PAGE analysis, and the preparations were judged to be homogeneous by the observation of a single band on a Coomassie Blue-stained reducing SDS-PAGE gel. All H76S protein samples used for this work were kindly prepared and provided by Miss Sara Rafice. Analysis of the UV-visible spectrum for ferric H76S reveals wavelength maxima at 407, 499, 535, 568<sup>sh</sup> and ~628 nm (Figure 3.8). Enzyme concentrations for H76S were determined using an absorption coefficient of  $\epsilon_{407} = 105 \text{ mM}^{-1}\text{cm}^{-1}$ .

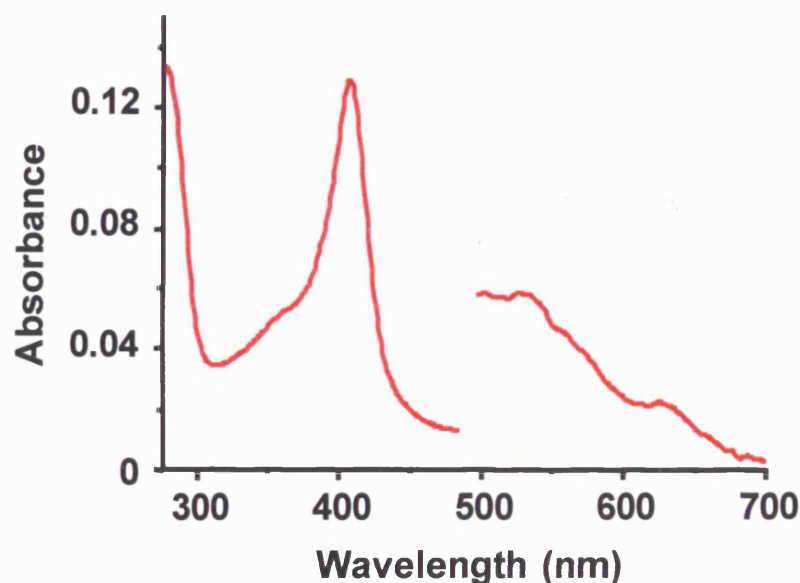


**Figure 3.8:** UV-visible absorption spectrum of ferric H76S. The visible region has been multiplied by a factor of 5. Conditions: 50 mM Tris/HCl buffer, pH 8.0, 25 °C.

### 3.2.7 LC-MS analysis of the reaction products catalysed by H76S

LC-MS analysis using was then carried out for the reaction of H76S with L-Trp and 1-Me-Trp. For the reaction with L-Trp, an ion with  $m/z = 237$  (Figure 3.9(A)) was detected which corresponds to the mass of *N*-formyl-kynurenine ( $m/z = 236$ ); for the

reaction with 1-Me-Trp, an equivalent ion was detected with  $m/z = 251$  (Figure 3.9(B)) as expected for *N*-formyl-methylkynurenine ( $m/z = 250$ )<sup>b</sup>.

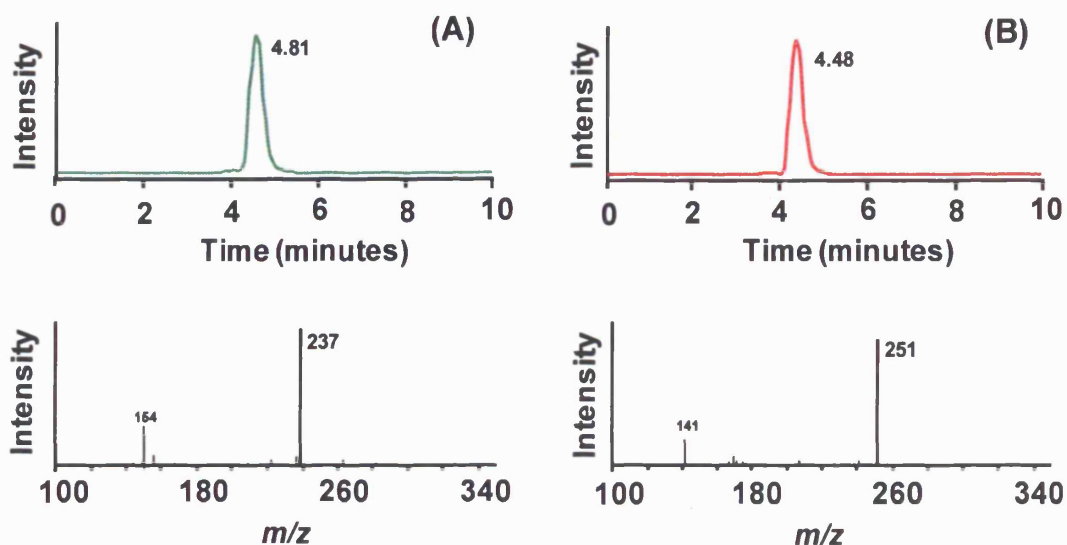


**Figure 3.9:** LC-MS analysis of products obtained on reaction of H76S with L-Trp (Panel A) and 1-Me-Trp (Panel B). Panel A: (top) elution profile for selected ion chromatogram with  $m/z$  of 237 and (bottom) the corresponding positive ESI mass spectrum for the product eluted at 4.81. Panel B: (top) elution profile for selected ion chromatogram with  $m/z$  of 251 and (bottom) the corresponding positive ESI mass spectrum for the product eluted at 4.48.

### 3.2.8 Steady-state kinetics

Steady-state kinetic parameters for the oxidation of 1-Me-Trp were also determined. Clear increases in absorbance, corresponding to product formation, are observed for rhIDO (Figure 3.10), as well as for the S167A variant of rhIDO and the H76S variant of rhTDO (Table 3.1).

<sup>b</sup> Parallel LC-MS analysis were carried out on *Xc*TDO and H55S (variant of *Xc*TDO) by Dr Sarah Thackray (University of Edinburgh). For the reaction of *Xc*TDO with 1-Me-trp, no ions with  $m/z$  were detected that correspond to a mass of *N*-formyl-methylkynurenine; however, an ion with  $m/z$  of 251 corresponding to *N*-formyl-methylkynurenine was detected upon reaction of H55S and 1-Me-Trp.

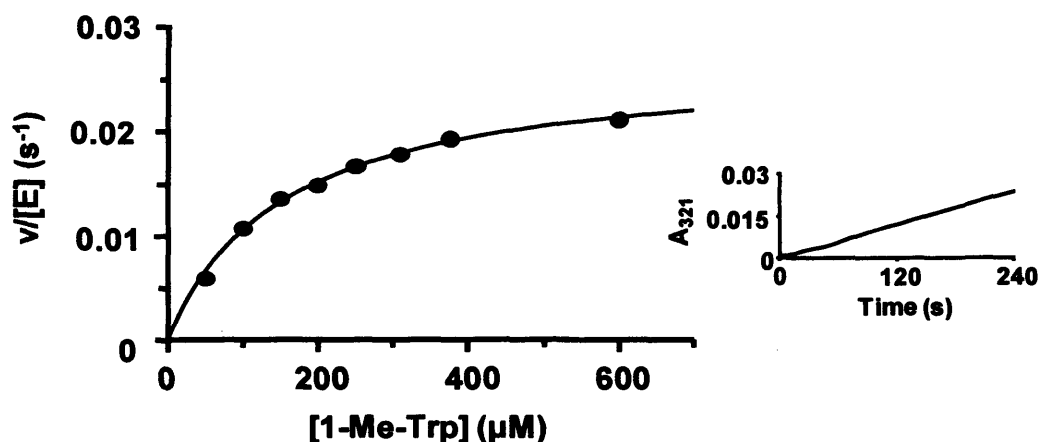


**Figure 3.10:** Steady state oxidation of 1-Me-Trp by rhIDO. Solid line shows a fit of the data to the Michaelis-Menten equation. Inset: Time-dependence of absorbance changes at 321 nm, which report on *N*-formyl-methylkynurenine formation.

**Table 3.1:** Steady-state parameters for the oxidation of 1-Me-Trp and L-Trp by rhIDO, rhTDO, *Xc*TDO<sup>c</sup> and variants.

	1-Me-Trp		L-Trp		
	Variant	$k_{\text{cat}}$ ( $\text{s}^{-1}$ )	$K_M$ ( $\mu\text{M}$ )	$k_{\text{cat}}$ ( $\text{s}^{-1}$ )	$K_M$ ( $\mu\text{M}$ )
<b>rhIDO</b>	wild type	$0.027 \pm 0.001$	$150 \pm 11$	$1.4 \pm 0.05$	$7 \pm 0.8$
	S167A	$0.032 \pm 0.002$	$31 \pm 5.0$	$1.6 \pm 0.04$	$21 \pm 1.9$
<b>rhTDO</b>	wild type	No activity	-	$1.4 \pm 0.02$	$222 \pm 15$
	H76S	$0.023 \pm 0.001$	$2300 \pm 230$	Not determined	-
<b><i>Xc</i>TDO</b>	wild type	No activity	-	$19.5 \pm 1.2$	$114 \pm 1$
	H55S	$0.052 \pm 0.009$	$70 \pm 11$	$2.6 \pm 0.01$	$197 \pm 2$

<sup>c</sup> All steady-state kinetic data for *Xc*TDO and H55S were determined by Dr Sarah Thackray and are included in this Chapter for comparison only.

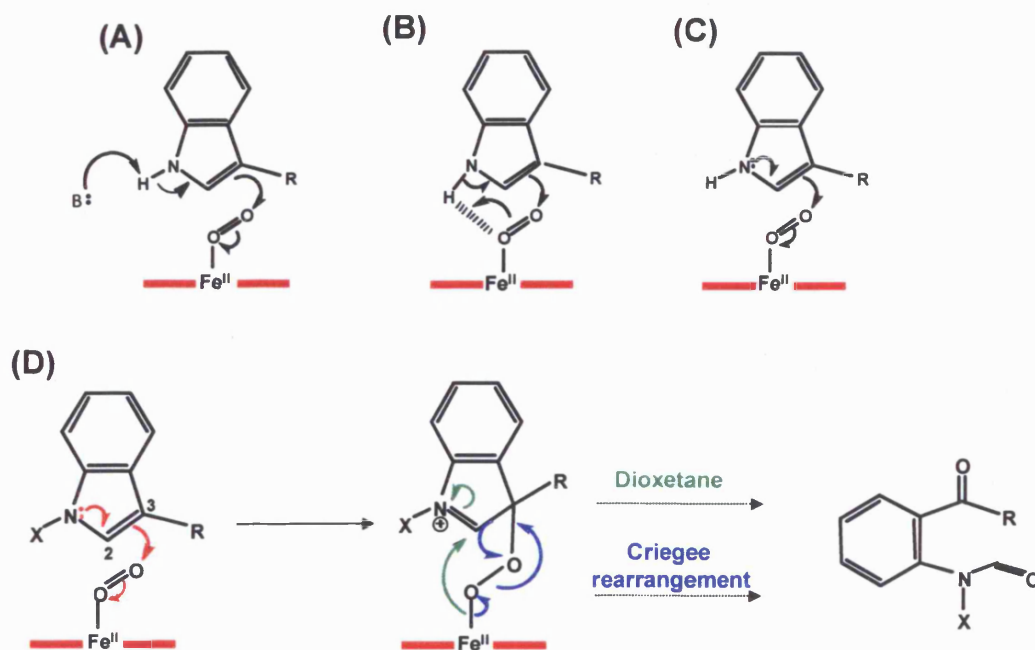
### 3.3 Discussion

---

As mentioned earlier, the detailed catalytic mechanism of IDO and TDO is still a matter of ongoing investigation. Originally, proposed (8, 9) mechanisms for tryptophan oxidation suggested removal of  $H^1$  as the first step, as base-catalysed abstraction of the indole nitrogen (Scheme 3.2(A)), but when it became clear that a suitable active site base was not present in rhIDO (although it is in XcTDO (His55)) an alternative mechanism for loss of the indole NH was put forward (Scheme 3.2(B)) (4).

The data presented in this Chapter rule out both mechanisms on the grounds that reaction of 1-Me-Trp would not be possible through this route because deprotonation is not possible in this case. In fact, the chemistry of indoles is very well documented (2) and does not occur by loss of the indole proton. Instead, when an indole reacts with an electrophile ( $O_2$  in this case) the lone pair on  $N^1$  initiates the process (Scheme 3.2(C)) and the electrophile becomes attached preferentially at the 3-position (Scheme 3.2(D)). Attack at the  $C^3$  position generates a positive charge on  $C^2$ , as shown in Scheme 3.2(D), which is resonance stabilized by the lone pair on  $N^1$ . Attack at the  $C^2$  position, as proposed recently (10), is less favourable and not observed in indole chemistry because this generates a positive charge on  $C^3$ , which is less well stabilized (through the benzene ring) (2).

We propose direct electrophilic addition as a more likely mechanism for tryptophan oxidation in the heme dioxygenases because this mechanism would allow both L-Trp and 1-Me-Trp to react, Scheme 3.2(D), with the role of the iron merely as a donor of the required oxygen molecule. It would be consistent with the absence of an active site base in certain cases (*e.g.* rhIDO) and, more importantly, would avoid needing to implicate loss of a proton on  $N^1$  with  $pK_a$  which is well out of range (Figure 3.11) (3). Interestingly, a recent density functional theory (DFT) study (10) found that direct electrophilic addition has a lower activation energy than a base-catalysed deprotonation mechanism. The latter proved to be energetically unfavourable by these theoretical calculations because the indole NH group needs to adopt a bent orientation in order to have any interaction with the heme-bound dioxygen and, consequently, a large amount of steric strain would be placed on the NH bond. These DFT studies are consistent with our experimental observations.



**Scheme 3.2:** Possible mechanisms for oxidation of L-Trp. (A) Abstraction of the indole proton by an active site base. (B) Abstraction of the indole proton by the heme-bound dioxygen. (C) Direct electrophilic addition. (D) A revised mechanism for product formation in heme dioxygenases, where X=H or Me. The conversion to product is proposed to occur either by a Criegee or a dioxetane mechanism (8, 9, 11).

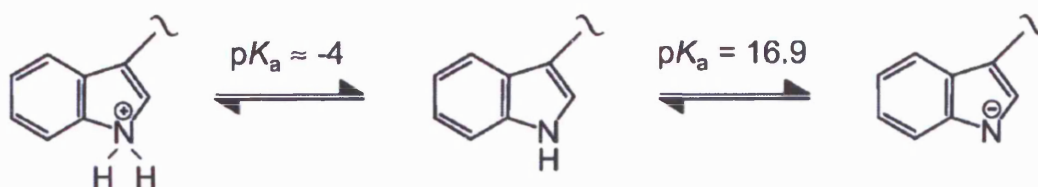


**Figure 3.11:** pH-dependant properties of tryptophan. Deprotonation of the indole nitrogen atom occurs at a  $pK_a$  of 16.9 (3).

No activity was detected for rhTDO and XcTDO with 1-Me-Trp in either steady-state or LC-MS analyses. The crystal structure of XcTDO in complex with L-Trp (6) reveals a hydrogen bond (2.6 Å) between the indole NH of L-Trp and His55 (Figure 3.12(A)). This introduces a potential steric clash with the methyl group of 1-Me-Trp. Indeed, a model of 1-Me-Trp binding to XcTDO (Figure 3.12(B)) shows a non-bonding distance of ~1.5 Å between the N<sup>ε</sup> of His55 and the carbon atom of the

methyl group on 1-Me-Trp. We propose that binding of 1-Me-Trp to *Xc*TDO, in comparison to L-Trp, is very low as a consequence. As mentioned earlier, sequence alignments (6) indicate that rhTDO also contains a histidine (His76) in the same position, so that the same steric restrictions would apply and would explain the observed lack of activity. Substitution of this histidine in rhTDO (H76S) or *Xc*TDO (H55S) would allow accommodation of the additional methyl group hence accounting for the activity in these cases, Table 3.1. This hypothesis is supported by fact that rhIDO (no His present) and its S167A variant are both active towards 1-Me-Trp; S167A has a higher binding affinity for 1-Me-Trp than rhIDO, as evidenced by  $K_M$ , Table 3.1.

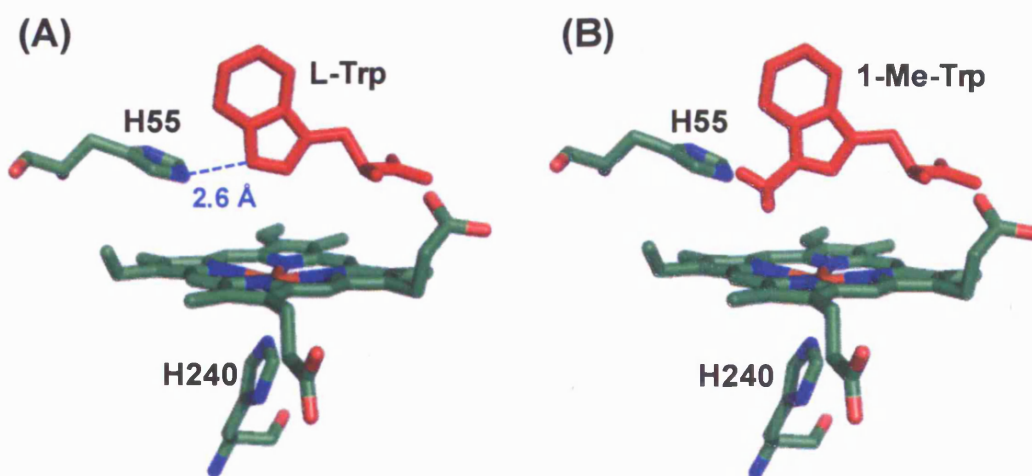


**Figure 3.12:** (A) Crystal structure of *Xc*TDO in complex with (A) L-Trp (6); (B) A model of 1-Me-Trp binding to *Xc*TDO generated by overlay of 1-Me-Trp on the L-Trp coordinates in (A).

In conclusion, we show that 1-Me-Trp is a substrate for rhIDO and variants of rhTDO and *Xc*TDO in which the active site histidine has been replaced. This shows that deprotonation of the indole  $N^1$  is not required for catalysis. We propose that direct electrophilic addition to dioxygen, facilitated by the lone pair on the indole  $N^1$ , occurs instead.

### 3.4 References

---

1. Cady, S. G., and Sono, M. (1991) 1-Methyl-DL-tryptophan, beta-(3-benzofuranyl)-DL-alanine (the oxygen analog of tryptophan), and beta-[3-benzo(b)thienyl]-DL-alanine (the sulfur analog of tryptophan) are competitive inhibitors for indoleamine 2,3-dioxygenase, *Arch. Biochem. Biophys.* 291, 326-333.
2. Joule, J. A., and Mills, K. (2000) *Heterocyclic Chemistry Fourth Edition*, Blackwell, Oxford, 319-371.
3. Yagil, G. (1967) The proton dissociation constant of pyrrole, indole and related compounds, *Tetrahedron* 23, 2855-2861.
4. Sugimoto, H., Oda, S., Otsuki, T., Hino, T., Yoshida, T., and Shiro, Y. (2006) Crystal structure of human indoleamine 2,3-dioxygenase: catalytic mechanism of O<sub>2</sub> incorporation by a heme-containing dioxygenase, *Proc. Natl. Acad. Sci. USA* 103, 2611-2616.
5. Chauhan, N., Basran, J., Efimov, I., Svistunenko, D. A., Seward, H. E., Moody, P. C., and Raven, E. L. (2008) The role of serine 167 in human indoleamine 2,3-dioxygenase: a comparison with tryptophan 2,3-dioxygenase, *Biochemistry* 47, 4761-4769.
6. Forouhar, F., Anderson, J. L., Mowat, C. G., Vorobiev, S. M., Hussain, A., Abashidze, M., Bruckmann, C., Thackray, S. J., Seetharaman, J., Tucker, T., Xiao, R., Ma, L. C., Zhao, L., Acton, T. B., Montelione, G. T., Chapman, S. K., and Tong, L. (2007) Molecular insights into substrate recognition and catalysis by tryptophan 2,3-dioxygenase, *Proc. Natl. Acad. Sci. USA* 104, 473-478.
7. Thackray, S. J., Bruckmann, C., Anderson, J. L., Campbell, L. P., Xiao, R., Zhao, L., Mowat, C. G., Forouhar, F., Tong, L., and Chapman, S. K. (2008) Histidine 55 of Tryptophan 2,3-Dioxygenase Is Not an Active Site Base but Regulates Catalysis by Controlling Substrate Binding, *Biochemistry* 47, 10677-10684.
8. Leeds, J. M., Brown, P. J., McGeehan, G. M., Brown, F. K., and Wiseman, J. S. (1993) Isotope effects and alternative substrate reactivities for tryptophan 2,3-dioxygenase, *J. Biol. Chem.* 268, 17781-17786.

9. Sono, M., Roach, M. P., Coulter, E. D., and Dawson, J. H. (1996) Heme-Containing Oxygenases, *Chem. Rev.* **96**, 2841-2888.
10. Chung, L. W., Li, X., Sugimoto, H., Shiro, Y., and Morokuma, K. (2008) Density Functional Theory Study on a Missing Piece in Understanding of Heme Chemistry: The Reaction Mechanism for Indoleamine 2,3-Dioxygenase and Tryptophan 2,3-Dioxygenase, *J. Am. Chem. Soc.*, 12299-12309.
11. Hamilton, G. A. (1969) Mechanisms of two- and four-electron oxidations catalyzed by some metalloenzymes, *Adv. Enzymol. Relat. Areas Mol. Biol.* **32**, 55-96.

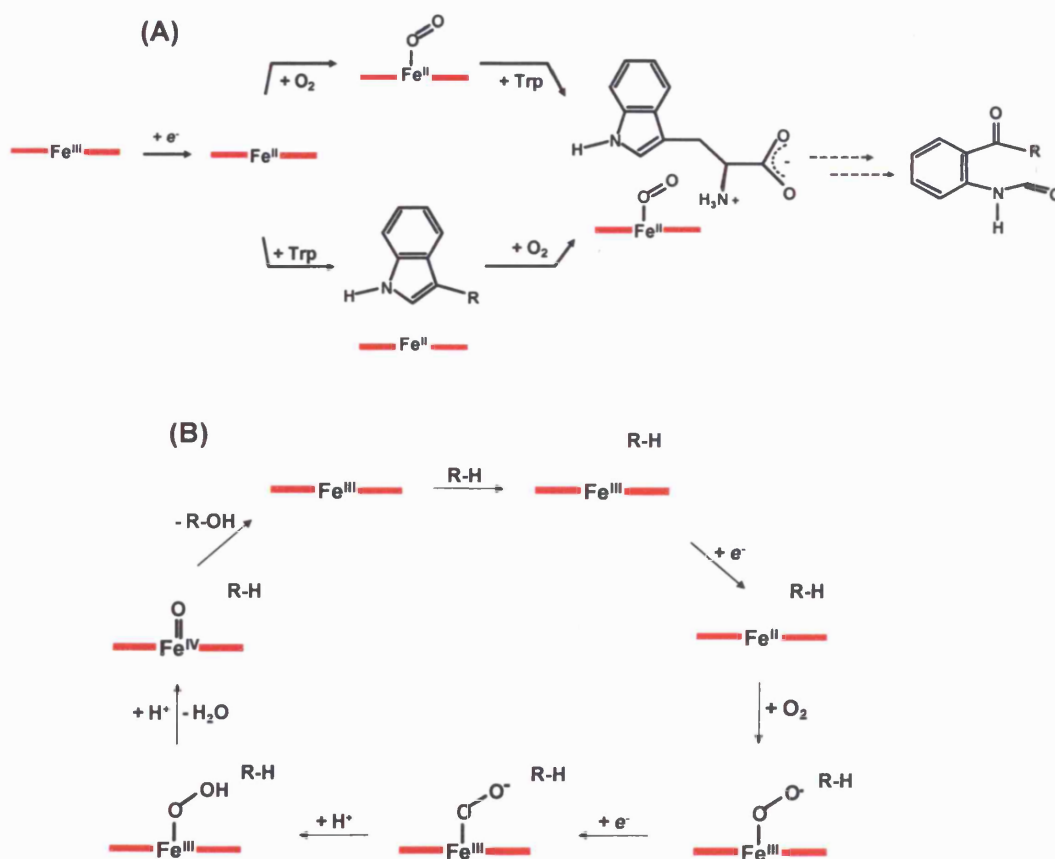
## **Chapter 4**

---

### **Analysis of the heme centre in the ferrous-oxy and ternary complexes of rhIDO as probed by EPR and ENDOR spectroscopy**

## 4.1 Introduction

As discussed in Chapter 1, the mechanism of tryptophan oxidation involves binding of  $O_2$  and L-Trp to ferrous heme to form the ternary  $[rhIDO^{II}\text{-Trp-O}_2]$  complex, followed by formation of *N*-formyl-kynurenine (Scheme 4.1(A)). This process requires only one-electron reduction of the ferric heme iron (to ferrous iron) and the presence of substrate, and therefore differs from other catalytic heme enzymes (*e.g.* P450s, peroxidases) in which two-electron reduction of the heme occurs prior to cleavage of the O-O bond and formation of high-valent iron intermediates (Scheme 4.1(B)). Therefore, for the heme dioxygenases there is no formal change in oxidation state of the metal during catalysis, so that the role of the iron appears to be as a suitable binding location for oxygen.



**Scheme 4.1:** Proposed catalytic reaction cycle for (A) IDO and (B) cytochrome P450.

In early work, spectroscopic data (1, 2) had implicated the presence of an active site histidine in the heme dioxygenases. This was based largely on the idea that stabilisation of the bound oxygen by hydrogen bonding might be necessary, and participation of an active site histidine, as observed in the globins and the peroxidases, might be involved. In addition, base-catalysed abstraction of the indole NH group (3, 4) by an active site histidine had been proposed as the most likely mechanistic pathway. However, when the crystal structure of rhIDO (5) was solved it revealed a hydrophobic active site that contained no active site histidine, Figure 4.1(A). In contrast, the crystal structure of *X. campestris* TDO (*Xc*TDO (6)) (Figure 4.1(B)) reveals an active site histidine that hydrogen bonds to the bound substrate, but it is not known whether this residue affects the formation or otherwise of the ferrous-oxy complex.

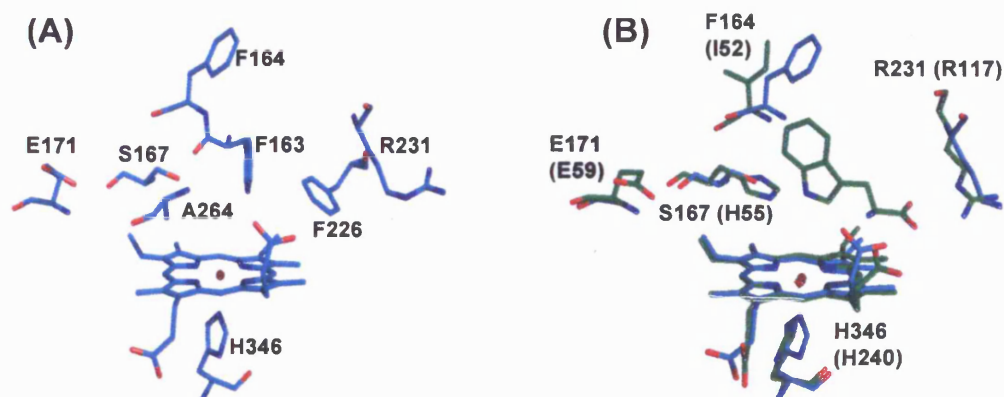


**Figure 4.1:** (A) The active site of rhIDO (in cyan, (5)). (B) An overlay of rhIDO (cyan) and the *Xc*TDO-Trp (green) complex (6), with the residues for rhIDO indicated and those for *Xc*TDO in parentheses.

Although these structural data have been most helpful, there are a number of open questions in relation to the formation and stability of the catalytically competent ferrous-oxy complex and the ternary [rhIDO<sup>II</sup>-Trp-O<sub>2</sub>] complex. In particular, we do not know how or whether hydrogen bonding stabilisation of these catalytic intermediates is important, and how this is achieved. In Chapter 2, evidence was presented to demonstrate that S167, the only polar residue in the active site, was not involved in hydrogen bonding to the heme-bound dioxygen; by implication we proposed that this interaction came from a water molecule. However, no direct

evidence has been obtained to confirm this. Information of this kind is difficult to access, in part due to the transient nature of the intermediates and in part because the spectroscopic changes in the visible region are small (7).

It has been shown previously that EPR and  $^1\text{H}$  ENDOR spectroscopy of cryoreduced ferrous-oxy heme proteins provide valuable structural information on the oxy precursors (8-14). In this approach, EPR silent ferrous-oxy samples are reduced at 77 K by radiolytically generated thermolized electrons; the cryoreduced species trapped at 77 K are sensitive EPR and  $^1\text{H}$  ENDOR probes because they retain the conformations of the precursors. The structure of the primary cryoreduced species trapped at 77 K depends essentially on the presence of a proton donor, usually a water molecule that is incorporated in a hydrogen bonding network to the heme-bound dioxygen. In the absence of a water molecule, the cryoreduced species trapped at 77 K has been shown to be a peroxy ferric ( $\text{Fe}^{\text{III}}$ ) intermediate (10, 13). In this species, the basic peroxy ferric species ( $\text{Fe}^{\text{III}}-\text{O}_2^{2-}$ ) joins with a proton to form a hydroperoxy ferric intermediate ( $\text{Fe}^{\text{III}}-\text{OOH}^{\cdot}$ ), as a rule, at temperatures above 170 K. At these temperatures, a proton can migrate to the peroxy ligand from a proton donor situated beyond the distal cavity. In cases where a water molecule is involved in hydrogen bonding to the heme-bound dioxygen, protonation of the peroxy ligand occurs, as a rule, at temperatures below 77 K. As a result of this, a hydroperoxy ferric intermediate ( $\text{Fe}^{\text{III}}-\text{OOH}^{\cdot}$ ) is trapped at 77 K (8, 10, 11).

In this Chapter<sup>a</sup>, we have applied these techniques to ask questions about the ferrous-oxy and ternary complexes (L-Trp and 1-Me-Trp) of rhIDO. The results reveal important information on the surrounding environment of the heme-bound dioxygen and the interactions present in the ternary complex. The mechanistic implications of such interactions are also discussed in this work.

---

<sup>a</sup> The work presented in this Chapter was carried out in collaboration with Dr. Roman Davydov (Department of Chemistry, Northwestern University).

## 4.2 Results

---

### 4.2.1 Ferrous rhIDO

It has been shown previously that irradiation of ferrous ( $\text{Fe}^{\text{II}}$ ) heme proteins at 77 K generates one-electron reduced ( $\text{Fe}^{\text{I}}$ ) and oxidized ( $\text{Fe}^{\text{III}}$ ) species trapped in conformations of the original ferrous precursor (14) and are sensitive probes for the EPR silent ferrous states.

The EPR spectrum of cryoreduced ferrous rhIDO (Figure 4.2) reveals an axial EPR signal with  $g$ -values ( $g_{\perp} = 2.22$ ,  $g_{\parallel} = 1.94$ ) that are characteristic of a 5-coordinate  $\text{Fe}^{\text{I}}$  species with the unpaired electron residing on the  $d_{z^2}$  orbital. The  $g_{\parallel}$  feature in the spectrum discloses a well resolved superhyperfine structure from the proximal histidine (His) nitrogen.

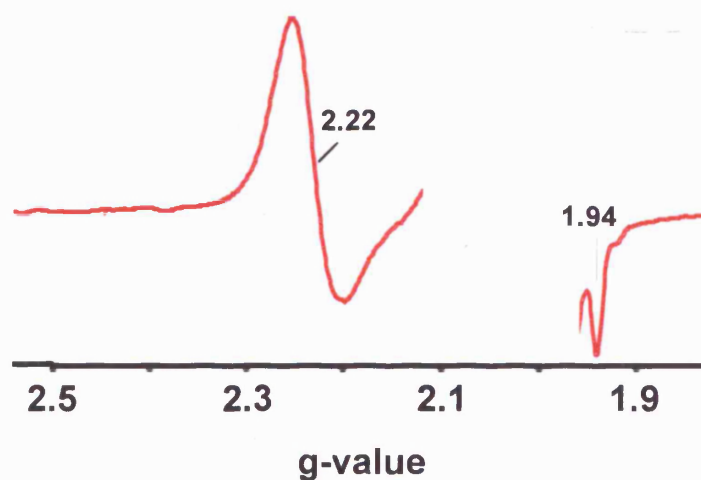


**Figure 4.2:** Q-band EPR spectrum of cryoreduced rhIDO. Conditions:  $T = 2$  K, modulation amplitude 2 G, microwave frequency 34.95 GHz.

The EPR spectrum of cryoxidized ferrous rhIDO (Figure 4.3, red line) reveals a slightly rhombic EPR signal with  $g$ -values ( $g = 5.96, 5.59$ ) that differ from those that have been observed in the resting ferric state (Figure 4.3, green line). The distinctions in the shapes of the compared signals are explained by the fact that the 5-coordinate ferric state is trapped during cryooxidation of 5-coordinate ferrous rhIDO whilst in ferric rhIDO the 6<sup>th</sup> position is occupied by water (15, 16).

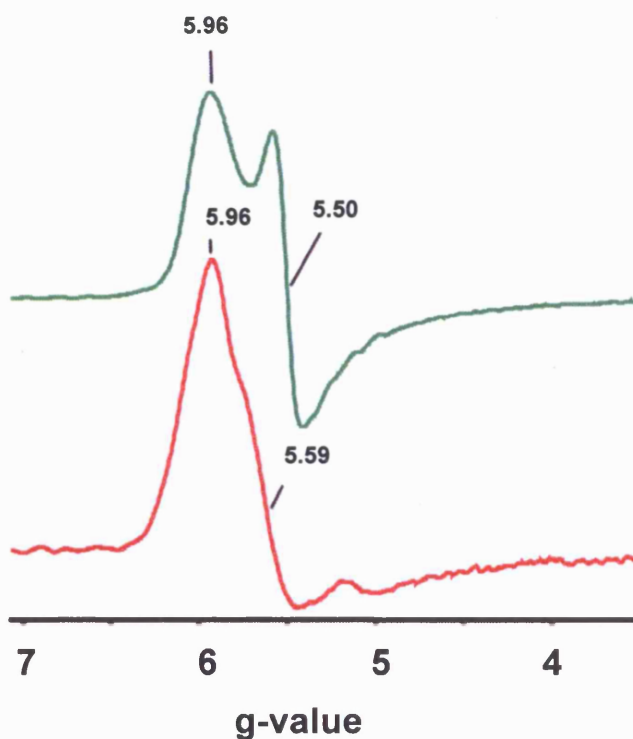


**Figure 4.3:** Q-band EPR spectra of cryooxidized ferrous rhIDO (red line) and ferric rhIDO (green line). Conditions:  $T = 2$  K, modulation amplitude 2 G, microwave frequency 34.95 GHz.

#### 4.2.2 Ferrous-oxy rhIDO

The EPR spectrum of radiolytically reduced ferrous-oxy rhIDO at 77 K (Figure 4.4) reveals several rhombic signals with different  $g$ -tensors. In this spectrum there are two dominating signals,  $g = 2.32, 2.17, 1.95$  (signal A) and  $g = 2.35, 2.26, 1.92$  (signal B), which are both typical of hydroperoxy ferric heme intermediates (11). Two additional signals, with significantly smaller intensities, were also resolved with  $g$ -tensor components,  $g = 2.22, 2.12$  (signal C) and  $g = 2.20, 2.10$  (signal D), corresponding to peroxy ferric heme intermediates (13). During annealing within temperatures of 116–145 K, species C and D are converted into species A and B. Further stepwise annealing, between temperatures of 145–190 K, results in the conversion of species A into species B. Overall, these observations suggest that in major conformational sub-states A and B, cryoreduction of the ferrous-oxy heme is accompanied by protonation at 77 K but this is not the case for minor conformers C and D.

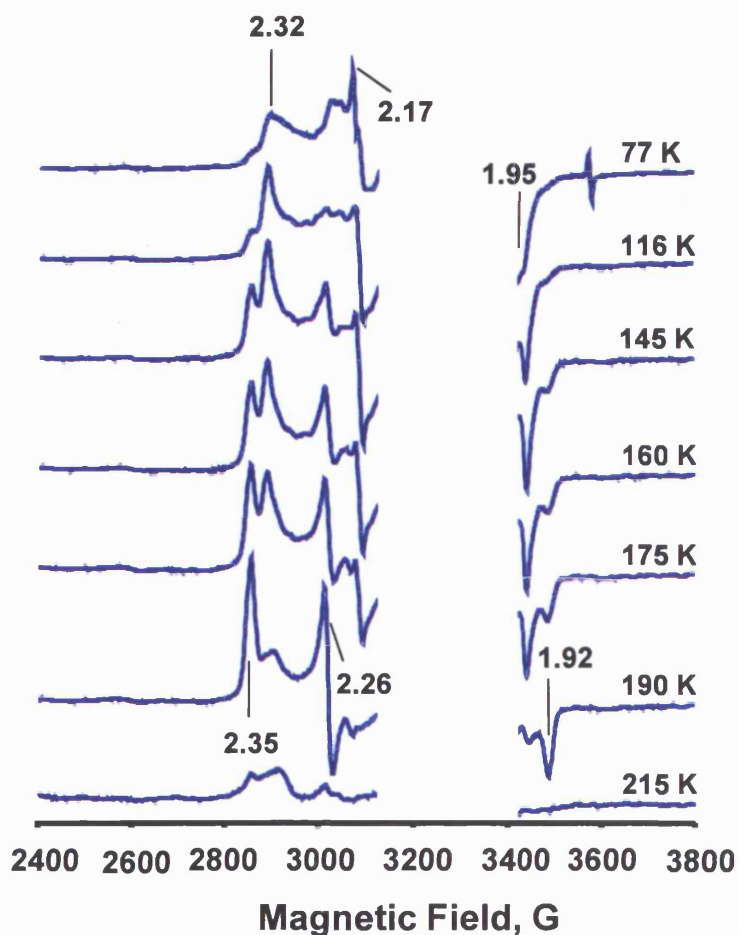


**Figure 4.4:** X-band EPR spectra of cryoreduced ferrous-oxy rhIDO annealed at indicated temperatures. Conditions:  $T = 25$  K, modulation amplitude 5 G, microwave frequency 9.36 GHz.

$^1\text{H}$  ENDOR spectroscopy was carried out to confirm that the peroxy ligands in cryogenerated species A and B were, indeed, protonated. The representative  $^1\text{H}$  ENDOR spectra (Figure 4.5) for cryoreduced ferrous-oxy rhIDO annealed at 145 K (dominant species A) and at 190 K (dominant species B) reveal  $A_{\text{max}}$  of 12 MHz and 10 MHz, respectively, which are characteristic of protonation of the peroxy ligand (10, 17).

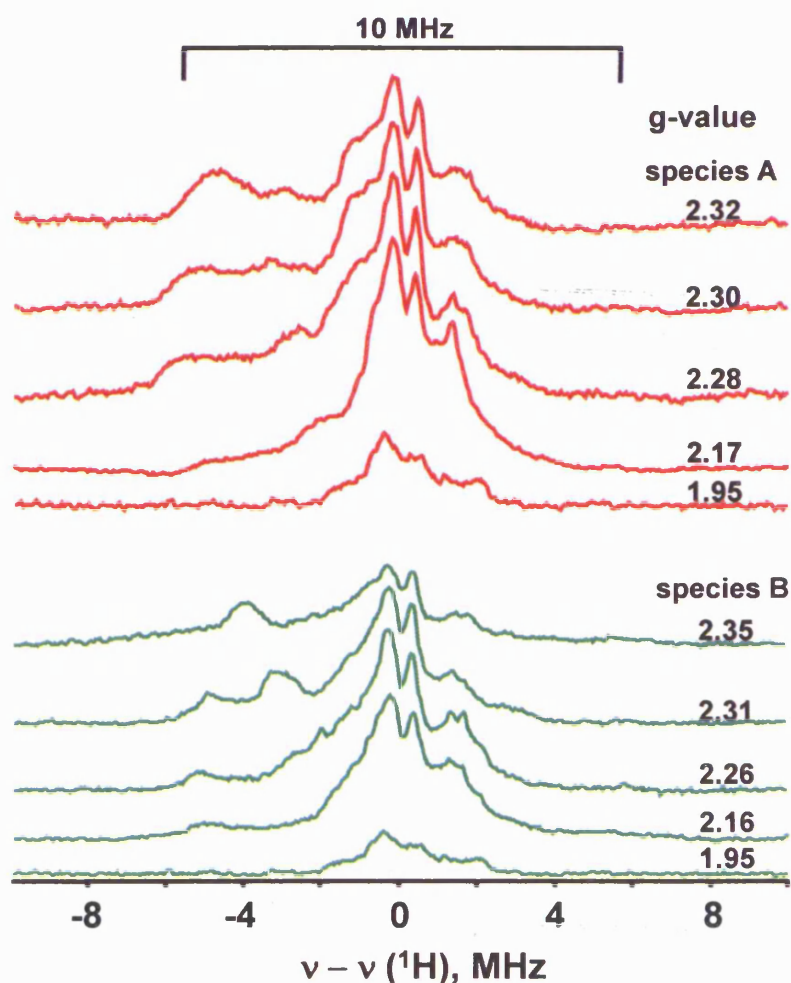


**Figure 4.5:**  $^1\text{H}$  ENDOR spectra of cryogenerated ferrous-oxy rhIDO. Conditions:  $T = 2\text{ K}$ , modulation amplitude 2 G, microwave frequency 34.95 GHz, RF power 5 W, RF sweep rate, 0.5 MHz/s, 20 scans.

### 4.2.3 Ferrous-NO and ferrous-Trp-NO

EPR spectroscopy was carried out on the ferrous-NO (which was used as a mimic for the catalytically active ferrous-oxy complex) and ferrous-NO-Trp complexes of rhIDO to examine the effect of L-Trp on the ferrous-NO complex.

The ferrous-NO complex displayed a rhombic EPR spectrum (Figure 4.6, green line) with  $g$ -values of 2.07, 2.00 and 1.97. A well resolved superhyperfine pattern, centered at  $g_z = 2.00$  composed of nine regularly spaced lines can be grouped as a triplet (coupling  $\sim 17\text{ G}$ ) of triplets (coupling 6.5 G), which are characteristic of 6-coordinate ferrous heme with His346 and NO as the 5<sup>th</sup> and 6<sup>th</sup> ligands, respectively.

The addition of L-Trp results in decreasing rhombicity of the EPR signal ( $g = 2.04, 2.01, 1.97$  (Figure 4.6, red line)) and the disappearance of the superhyperfine structure with coupling 6.5 G from the proximal nitrogen. The presented data thus indicate that binding L-Trp induces cleavage of the  $\text{Fe}^{\text{II}}$ -His bond which results in 5-coordinate NO bound heme.

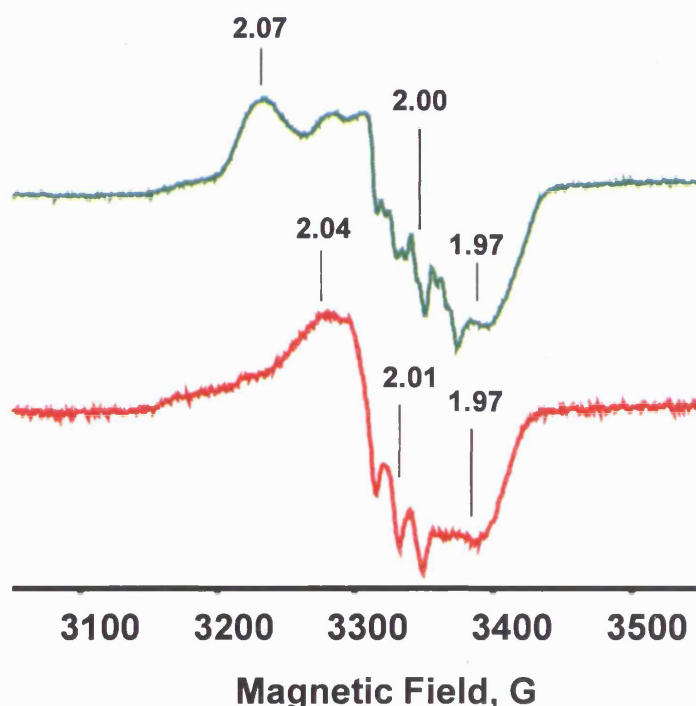


**Figure 4.6:** X-band EPR spectra of the ferrous-NO (green line) and ferrous-NO-Trp (red line) complexes. Conditions:  $T = 30 \text{ K}$ , modulation amplitude 2 G, microwave frequency 9.37 GHz.

#### 4.2.4 Ternary complex - $[\text{rhIDO}^{\text{II}}\text{-Trp-O}_2]$

The ternary  $[\text{rhIDO}^{\text{II}}\text{-Trp-O}_2]$  complex is far less stable than the ferrous-oxy complex even at temperatures of  $-40 \text{ }^\circ\text{C}$  (7). This makes sample preparation of the ternary complex, even at  $-40 \text{ }^\circ\text{C}$ , extremely difficult without introducing any contamination of ferric heme to the EPR sample. As a result, prepared samples contained  $\sim 15\text{-}20 \%$  of ferric contaminating species. The EPR spectrum of the cryoreduced ternary  $[\text{rhIDO}^{\text{II}}\text{-Trp-O}_2]$  complex at 77 K (Figure 4.7) reveal one signal with  $g$ -tensor components ( $g = 2.26, 2.17, 1.94$ ) that are characteristic of a peroxy ferric heme intermediate (9).

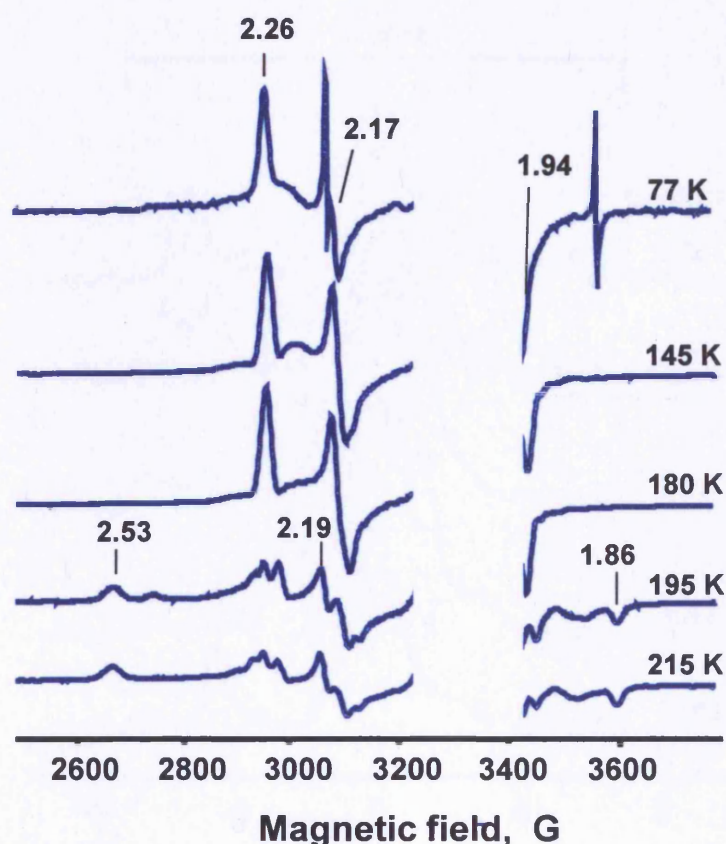


**Figure 4.7:** X-band EPR spectra of the cryoreduced ternary [rhIDO<sup>II</sup>-Trp-O<sub>2</sub>] complex annealed at indicated temperatures. Conditions: T = 25 K, modulation amplitude 5 G, microwave frequency 9.36 GHz.

<sup>1</sup>H ENDOR spectra of the ternary [rhIDO<sup>II</sup>-Trp-O<sub>2</sub>] complex (Figure 4.8) display exchangeable proton signals with  $A_{\max} = 15$  MHz which is commonly observed for peroxy ferric heme intermediates. Unlike cryoreduced ferrous-oxy rhIDO, this species remains unchanged upon annealing at 180 K and begins to decay only at T > 190 K. In this complex, it is likely that bound L-Trp protects the interaction of the ferrous-oxy heme with the proton donor (likely H<sub>2</sub>O). As a result, protonation of the basic peroxy ligand occurs with a noticeable rate at T > 190 K, as it takes place in the oxy-globins (13, 18). This suggests that the proton donor (most likely H<sub>2</sub>O) is situated beyond the distal cavity. On the other hand, a strongly coupled <sup>1</sup>H ENDOR signal with  $A_{\max}$  of ~15 MHz indicates that there is a hydrogen bonding donor within hydrogen bonding distance to the heme-bound dioxygen. One likely candidate for this hydrogen bond donor is the indole NH group.

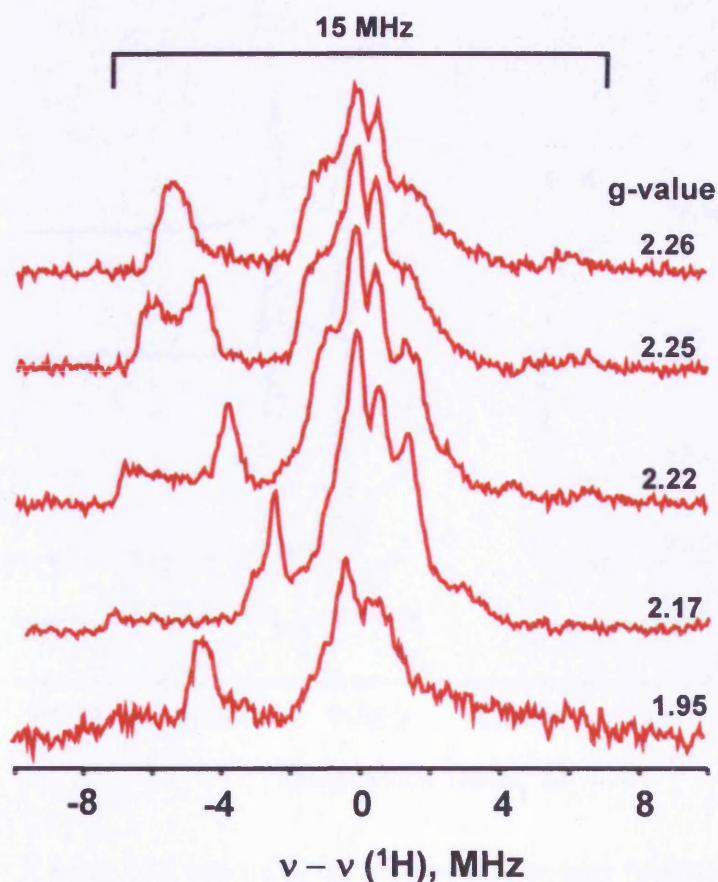


**Figure 4.8:**  $^1\text{H}$  ENDOR spectra of the cryoreduced ternary  $[\text{rhIDO}^{\text{II}}\text{-Trp-O}_2]$  complex. Conditions:  $T = 2\text{ K}$ , modulation amplitude 2 G, microwave frequency 34.95 GHz, RF power 5 W, RF sweep rate 0.5 MHz/s, 20 scans.

#### 4.2.5 Ternary complex - $[\text{rhIDO}^{\text{II}}\text{-methylTrp-O}_2]$

To confirm the presence of a hydrogen bonding interaction between the indole NH group and the heme-bound dioxygen, analogous studies were carried out with 1-Me-Trp. The EPR spectra of the cryoreduced ternary  $[\text{rhIDO}^{\text{II}}\text{-methylTrp-O}_2]$  complex (Figure 4.9) reveal g-tensor components ( $g = 2.27, 2.17, 1.94$ ) that are very similar, if not identical, to those for found in the irradiated L-Trp complex, Figure 4.7.

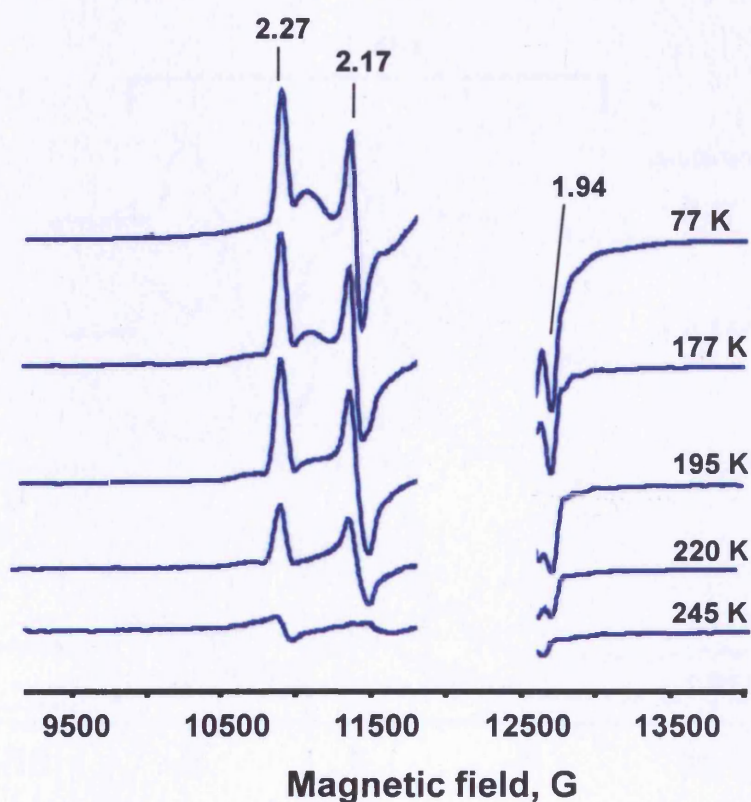


**Figure 4.9:** X-band EPR spectra of the cryoreduced ternary [rhIDO<sup>II</sup>-methylTrp-O<sub>2</sub>] complex annealed at indicated temperatures. Conditions: T = 25 K, modulation amplitude 5 G, microwave frequency 9.36 GHz.

<sup>1</sup>H ENDOR spectra of the ternary [rhIDO<sup>II</sup>-methylTrp-O<sub>2</sub>] complex (Figure 4.10) display a pattern for the cryotrapped peroxy intermediate that is very similar to that found in the ternary [rhIDO<sup>II</sup>-Trp-O<sub>2</sub>] complex (Figure 4.8).

This suggests that the strongly coupled <sup>1</sup>H ENDOR signal that was observed in the latter is not due to hydrogen bonding interactions between the heme-bound dioxygen and the indole NH group.

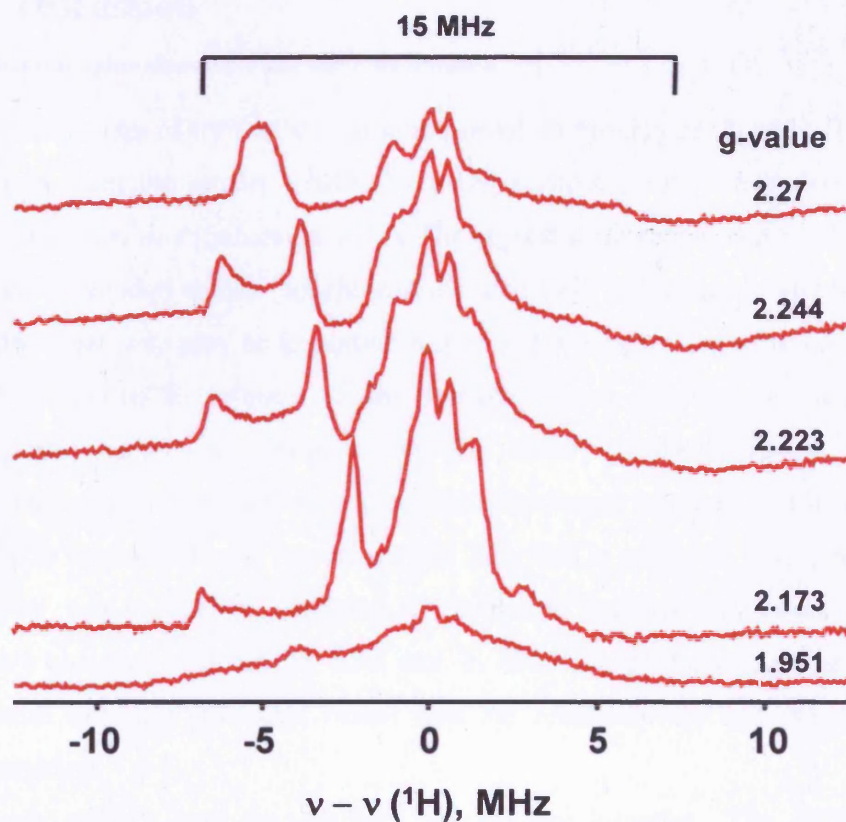


**Figure 4.10:** <sup>1</sup>H ENDOR spectra of the cryoreduced ternary [rhIDO<sup>II</sup>-methylTrp-O<sub>2</sub>] complex. Conditions: T = 2 K, modulation amplitude 2 G, microwave frequency 34.95 GHz, RF power 5 W, RF sweep rate 0.5 MHz/s, 20 scans.

### 4.3 Discussion

---

The mechanism of tryptophan oxidation involves binding of O<sub>2</sub> and L-Trp to ferrous heme to form the ternary [rhIDO<sup>II</sup>-Trp-O<sub>2</sub>] complex, followed by formation of *N*-formyl-kynurenine (Scheme 4.1(A)). The crystal structures of rhIDO (5) and rhTDO (6) have provided critical insight into the active site architectures and have revealed residues that may play an important role in L-Trp binding but there are a number of open questions in relation to the formation and stability of the catalytically competent ferrous-oxy complex and the ternary [rhIDO<sup>II</sup>-Trp-O<sub>2</sub>] complex. In particular, we do not know how or whether hydrogen bonding stabilisation of these catalytic intermediates is important, and how this is achieved. The intention in this Chapter was to analyse catalytic intermediates such as the ferrous-oxy and the ternary complex of rhIDO by EPR and <sup>1</sup>H ENDOR spectroscopy. The implications of these data are discussed below and the results reveal important mechanistic information.

*Ferrous rhIDO and the catalytic ferrous-oxy complex.* The EPR spectra of cryoreduced and cryoxidised ferrous rhIDO both indicate that the heme iron is 5-coordinate (Scheme 4.2) (14); these data are consistent with solution studies and MCD spectroscopy (15) which show clean formation of 5-coordinate heme iron upon reduction.

EPR and <sup>1</sup>H ENDOR spectroscopy of cryoreduced ferrous-oxy rhIDO revealed the presence of hydroperoxy ferric intermediates, which suggests that a proton donor (presumably H<sub>2</sub>O) is located within hydrogen bonding distance to the heme-bound dioxygen. This has also been observed with the heme monooxygenases (8, 10, 11); the role, however, of the proton donor in the monooxygenases is to allow formation of the catalytically competent oxo-ferryl intermediate which occurs by donating two protons consecutively to the ferric peroxide intermediate, followed by heterolytic O-O bond cleavage and the release of water (Scheme 4.1(B)). This reaction mechanism is not feasible with the heme dioxygenases because both oxygen atoms are inserted into the substrate and as a result heterolytic cleavage of the O-O is not needed. An alternative role of the proton donor could be to provide hydrogen bonding stabilisation to the heme-bound dioxygen, as in the globins (Scheme 4.2). In Chapter 2, kinetic studies were carried out and revealed that the ferrous-oxy complex of

rhIDO was relatively stable (19); in contrast, the ferrous-oxy complex of rhTDO was not detected under the same conditions (19, 20). This suggests that the proton donor detected in ferrous-oxy rhIDO could be absent from the active site of rhTDO, therefore, resulting in an unstable ferrous-oxy complex for rhTDO.

The spectroscopic data also revealed the presence of several conformational sub-states in ferrous-oxy rhIDO, all of which have different distal surroundings. In conformers A and B there is a proton donor that forms a hydrogen bond with the bound dioxygen; in minor conformers C and D, the proton donor does not hydrogen bond with dioxygen. One possible explanation for this could be that the proton donor adopts a different orientation in conformers C and D, this will increase the distance between the proton and the bound dioxygen. The distal cavity of rhIDO has been reported to be able to accommodate large organic substrates (21), which would enable the proton donor to deviate from the usual binding site.

Analogous studies were carried out with ferrous rhIDO and NO (dioxygen analogue) to observe the effect of L-Trp on the ferrous-NO complex. EPR spectroscopy of the ferrous-NO and the ferrous-NO-Trp complex revealed spectra that are characteristic of 6-coordinate and 5-coordinate ferrous heme, respectively. Previous resonance Raman spectroscopic studies have shown that the addition of NO to ferrous rhIDO caused cleavage to the Fe-His bond, which resulted in the formation of a 5-coordinate NO heme-bound species (22). However, binding of L-Trp was found to stabilise the 6-coordinate ferrous-NO complex. The data presented in this Chapter contradict the data of analogous resonance Raman spectroscopic studies reported. The discrepancy could be due to different experimental conditions, such as pH or concentration of the protein sample (higher protein concentration may cause protein aggregation).

*Hydrogen-bonding interactions within the ternary complex.* Cryoreduction of the ternary [rhIDO<sup>II</sup>-Trp-O<sub>2</sub>] complex leads to the formation of peroxy ferric heme which indicates that upon addition of L-Trp the proton donor is ejected from the active site. Interestingly, the <sup>1</sup>H ENDOR spectrum reveals the presence of a hydrogen bond interaction to the heme-bound dioxygen from an unknown hydrogen donor. Previous studies on the model [rhIDO<sup>II</sup>-Trp-CO] complex using resonance Raman spectroscopy suggested that a hydrogen-bond interaction was present between the NH group and the heme bound CO (16). However, LC-MS analyses

and kinetic studies with 1-Me-Trp (Chapter 3) have shown that this analogue is, in fact, a substrate and as a result we proposed a direct electrophilic addition mechanism for the heme dioxygenases (23). Since EPR and  $^1\text{H}$  ENDOR spectroscopy directly report on the nature of the hydrogen bond to the heme-bound dioxygen, this proposal was tested further by using 1-Me-Trp as a substitute for L-Trp in the ternary complex. The  $^1\text{H}$  ENDOR spectrum of the ternary  $[\text{rhIDO}^{\text{II}}\text{-methylTrp-O}_2]$  complex revealed that the hydrogen bond donor is still present in this complex. This eliminates the possibility of the NH group acting as the hydrogen bond donor. It is unlikely that this donor comes from a nearby active site residue because the active site is devoid of polar residues with the exception of S167. However, evidence was presented in Chapter 2 to demonstrate that this residue does not affect the oxygen binding process, and by implication we assume is not involved in hydrogen bond stabilisation to dioxygen (19). Structural data for *Xc*TDO have been used to create a model for the ternary complex (Figure 4.11) (6), which suggests a hydrogen bond interaction between the ammonium group of the substrate to the distal oxygen atom. The hydrogen bond donor is present in both  $[\text{rhIDO}^{\text{II}}\text{-Trp-O}_2]$  and  $[\text{rhIDO}^{\text{II}}\text{-methylTrp-O}_2]$  complexes and is likely to come from the ammonium group (Scheme 4.2).

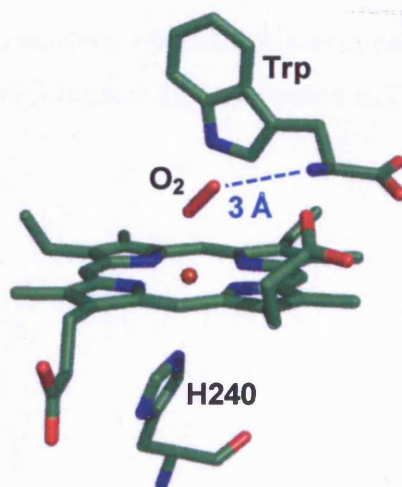
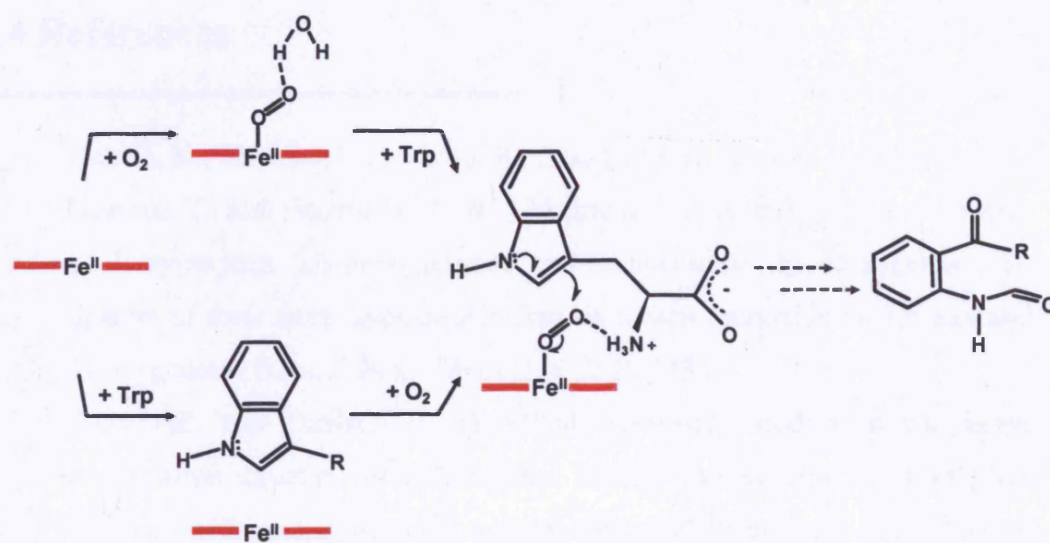


**Figure 4.11:** Model of the ternary  $[\text{XcTDO}^{\text{II}}\text{-Trp-O}_2]$  complex (6). Produced with Molscript and rendered with Raster3D.



**Scheme 4.2:** Proposed hydrogen bonding structures in the ferrous-oxy complex and ternary complex of rhIDO.

*Mechanistic implications.* Our spectroscopic data show there is no hydrogen bond interaction between the indole NH group and the heme-bound dioxygen. If proton abstraction of the NH group by the distal oxygen was the initiation step in the reaction mechanism, a hydrogen bond between these two groups would be essential. By implication, we rule out this mechanism and the spectroscopic data in this Chapter are therefore consistent with direct electrophilic addition of the pyrrole double bond to dioxygen (Scheme 4.2), as proposed in Chapter 3.

## 4.4 References

---

1. Uchida, K., Shimizu, T., Makino, R., Sakaguchi, K., Iizuka, T., Ishimura, Y., Nozawa, T., and Hatano, M. (1983) Magnetic and natural circular dichroism of L-tryptophan 2,3-dioxygenases and indoleamine 2,3-dioxygenase. II. Spectra of their ferric cyanide and ferrous carbon monoxide complexes and an oxygenated form, *J. Biol. Chem.* 258, 2526-2533.
2. Sono, M., and Dawson, J. H. (1984) Extensive studies of the heme coordination structure of indoleamine 2,3-dioxygenase and of tryptophan binding with magnetic and natural circular dichroism and electron paramagnetic resonance spectroscopy, *Biochim. Biophys. Acta* 789, 170-187.
3. Hamilton, G. A. (1969) Mechanisms of two- and four-electron oxidations catalyzed by some metalloenzymes, *Adv. Enzymol. Relat. Areas Mol. Biol.* 32, 55-96.
4. Sono, M., Roach, M. P., Coulter, E. D., and Dawson, J. H. (1996) Heme-Containing Oxygenases, *Chem. Rev.* 96, 2841-2888.
5. Sugimoto, H., Oda, S., Otsuki, T., Hino, T., Yoshida, T., and Shiro, Y. (2006) Crystal structure of human indoleamine 2,3-dioxygenase: catalytic mechanism of O<sub>2</sub> incorporation by a heme-containing dioxygenase, *Proc. Natl. Acad. Sci. USA* 103, 2611-2616.
6. Forouhar, F., Anderson, J. L., Mowat, C. G., Vorobiev, S. M., Hussain, A., Abashidze, M., Bruckmann, C., Thackray, S. J., Seetharaman, J., Tucker, T., Xiao, R., Ma, L. C., Zhao, L., Acton, T. B., Montelione, G. T., Chapman, S. K., and Tong, L. (2007) Molecular insights into substrate recognition and catalysis by tryptophan 2,3-dioxygenase, *Proc. Natl. Acad. Sci. USA* 104, 473-478.
7. Sono, M. (1986) Spectroscopic and equilibrium properties of the indoleamine 2,3-dioxygenase-tryptophan-O<sub>2</sub> ternary complex and of analogous enzyme derivatives. Tryptophan binding to ferrous enzyme adducts with dioxygen, nitric oxide, and carbon monoxide, *Biochemistry* 25, 6089-6097.
8. Davydov, R., Makris, T. M., Kofman, V., Werst, D. E., Sligar, S. G., and Hoffman, B. M. (2001) Hydroxylation of camphor by reduced oxy-

- cytochrome P450cam: mechanistic implications of EPR and ENDOR studies of catalytic intermediates in native and mutant enzymes, *J. Am. Chem. Soc.* *123*, 1403-1415.
9. Davydov, R., Satterlee, J. D., Fujii, H., Sauer-Masarwa, A., Busch, D. H., and Hoffman, B. M. (2003) A superoxo-ferrous state in a reduced oxy-ferrous hemoprotein and model compounds, *J. Am. Chem. Soc.* *125*, 16340-16346.
  10. Davydov, R., Chemerisov, S., Werst, D. E., Rajh, T., Matsui, T., Ikeda-Saito, M., and Hoffman, B. M. (2004) Proton transfer at helium temperatures during dioxygen activation by heme monooxygenases, *J. Am. Chem. Soc.* *126*, 15960-15961.
  11. Davydov, R., Perera, R., Jin, S., Yang, T. C., Bryson, T. A., Sono, M., Dawson, J. H., and Hoffman, B. M. (2005) Substrate modulation of the properties and reactivity of the oxy-ferrous and hydroperoxo-ferric intermediates of cytochrome P450cam as shown by cryoreduction-EPR/ENDOR spectroscopy, *J. Am. Chem. Soc.* *127*, 1403-1413.
  12. Davydov, R., Matsui, T., Fujii, H., Ikeda-Saito, M., and Hoffman, B. M. (2003) Kinetic isotope effects on the rate-limiting step of heme oxygenase catalysis indicate concerted proton transfer/heme hydroxylation, *J. Am. Chem. Soc.* *125*, 16208-16209.
  13. Davydov, R., Kofman, V., Nocek, J. M., Noble, R. W., Hui, H., and Hoffman, B. M. (2004) Conformational substates of the oxyheme centers in alpha and beta subunits of hemoglobin as disclosed by EPR and ENDOR studies of cryoreduced protein, *Biochemistry* *43*, 6330-6338.
  14. Davydov, R., and Hoffman, B. M. (2008) EPR and ENDOR studies of Fe(II) hemoproteins reduced and oxidized at 77 K, *J. Biol. Inorg. Chem.* *13*, 357-369.
  15. Papadopoulou, N. D., Mewies, M., McLean, K. J., Seward, H. E., Svistunenko, D. A., Munro, A. W., and Raven, E. L. (2005) Redox and spectroscopic properties of human indoleamine 2,3-dioxygenase and a His303Ala variant: implications for catalysis, *Biochemistry* *44*, 14318-14328.

16. Terentis, A. C., Thomas, S. R., Takikawa, O., Littlejohn, T. K., Truscott, R. J., Armstrong, R. S., Yeh, S. R., and Stocker, R. (2002) The heme environment of recombinant human indoleamine 2,3-dioxygenase. Structural properties and substrate-ligand interactions, *J. Biol. Chem.* 277, 15788-15794.
17. Davydov, R., Osborne, R. L., Kim, S. H., Dawson, J. H., and Hoffman, B. M. (2008) EPR and ENDOR studies of cryoreduced compounds II of peroxidases and myoglobin. Proton-coupled electron transfer and protonation status of ferryl hemes, *Biochemistry* 47, 5147-5155.
18. Garcia-Serres, R., Davydov, R. M., Matsui, T., Ikeda-Saito, M., Hoffman, B. M., and Huynh, B. H. (2007) Distinct reaction pathways followed upon reduction of oxy-heme oxygenase and oxy-myoglobin as characterized by Mossbauer spectroscopy, *J. Am. Chem. Soc.* 129, 1402-1412.
19. Chauhan, N., Basran, J., Efimov, I., Svistunenko, D. A., Seward, H. E., Moody, P. C., and Raven, E. L. (2008) The role of serine 167 in human indoleamine 2,3-dioxygenase: a comparison with tryptophan 2,3-dioxygenase, *Biochemistry* 47, 4761-4769.
20. Basran, J., Rafice, S. A., Chauhan, N., Efimov, I., Cheesman, M. R., Ghamsari, L., and Raven, E. L. (2008) A kinetic, spectroscopic, and redox study of human tryptophan 2,3-dioxygenase, *Biochemistry* 47, 4752-4760.
21. Sono, M., and Cady, S. G. (1989) Enzyme kinetic and spectroscopic studies of inhibitor and effector interactions with indoleamine 2,3-dioxygenase. 1. Norharman and 4-phenylimidazole binding to the enzyme as inhibitors and heme ligands, *Biochemistry* 28, 5392-5399.
22. Samelson-Jones, B. J., and Yeh, S. R. (2006) Interactions between nitric oxide and indoleamine 2,3-dioxygenase, *Biochemistry* 45, 8527-8538.
23. Chauhan, N., Thackray, S. J., Rafice, S. A., Eaton, G., Lee, M., Efimov, I., Basran, J., Jenkins, P. R., Mowat, C. G., Chapman, S. K., and Raven, E. L. (2009) Reassessment of the Reaction Mechanism for the Heme Dioxygenases, *J. Am. Chem. Soc.* *In press*.

# **Chapter 5**

---

## **Mutagenesis of active site residues in rhIDO**

## 5.1 Introduction

Before the crystal structure of rhIDO was solved in 2006, several attempts were made to identify the fifth and sixth ligands of the heme iron and to identify the residues involved in heme and substrate binding in rhIDO (1-4). These attempts were based largely on sequence alignments between IDO-like myoglobins and rhIDO which share 37% sequence homology and led to the proposal that several residues (H16, V109, H303, H346, K352) may play an important role in rhIDO (1). Site-directed mutagenesis of these residues led to the proposal that H346 is the proximal heme ligand in IDO; this was later confirmed by the release of the crystal structure. The crystal structure of rhIDO also revealed a large abundance of hydrophobic residues around the heme centre (F163, F164, F226, F227) (Figure 5.1(A)), indicating a hydrophobic pathway for the entrance of the substrate. Similarly, the distal cavity of *Xc*TDO also has a preponderance of hydrophobic residues, such as F51, Y24, Y27 and Y113 (Figure 5.1(B)).

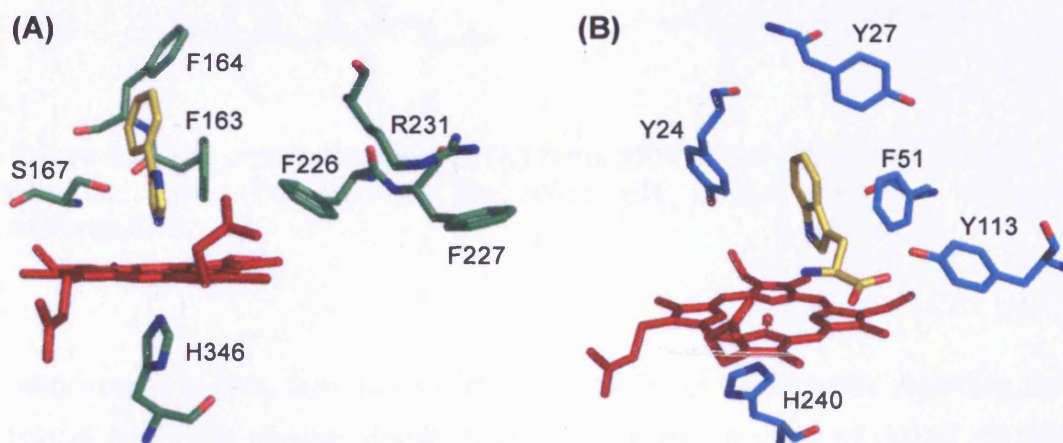


**Figure 5.1:** Active site of (A) rhIDO in complex with 4-phenyl-imidazole and (B) *Xc*TDO in complex with L-Trp.

As discussed in Chapter 1, the crystal structure of rhIDO was obtained in the inactive, ferric form in complex with 4-phenyl-imidazole, a known inhibitor and heme ligand to the enzyme; in contrast, the crystal structure of *Xc*TDO was solved in the active, ferrous form, in complex with L-Trp. This is useful because it allows

us to see the putative interactions present between protein amino acids and L-Trp, which is something the crystal structure of rhIDO cannot tell us. One useful example of this is the carboxylate group of L-Trp which has an electrostatic interaction with the side chain of R117 in *Xc*TDO (equivalent to R231 in rhIDO). Crystallographic data (obtained in the absence and presence of substrate) clearly show that this residue repositions itself in the presence of L-Trp and coordinates to the carboxylate group of L-Trp, with “open” and “closed” conformations (Figures 5.2(A) and (B), respectively). A similar arrangement is also possible in rhIDO.

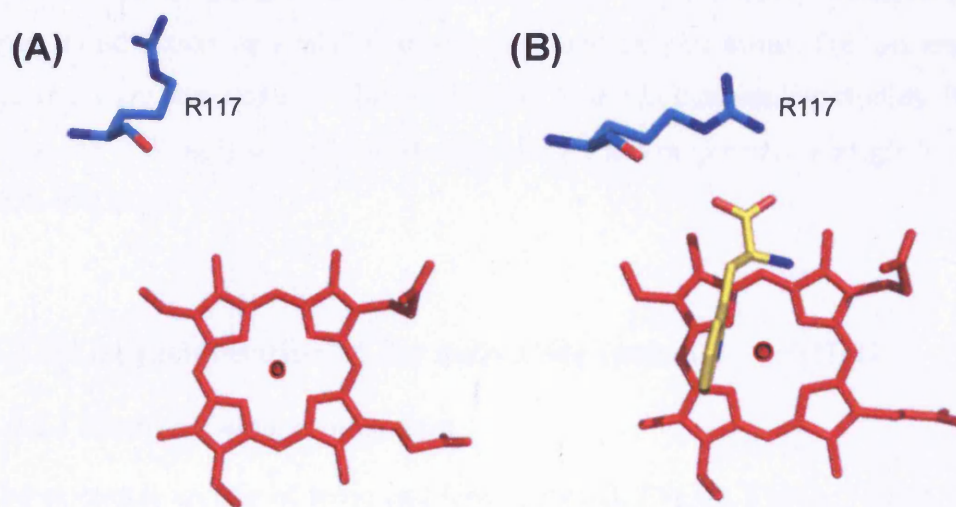


**Figure 5.2:** The crystal structures of (A) ferric *Xc*TDO and (B) ferrous *Xc*TDO in complex with L-Trp showing the active site residue R117 in different conformations.

Surprisingly, to date, there is very little information in the literature regarding the role of active site residues despite having the crystal structure of rhIDO. In this Chapter, we undertook site-directed mutagenesis of several active site residues (F163, F164, F226, F227 and R231) with the aim of identifying those that are involved in dioxygen and substrate binding, and in catalysis. Spectroscopic, kinetic and ligand binding analyses have been undertaken and we assess the effect of the mutations on the properties of the proteins.

## 5.2 Results

---

### 5.2.1 Mutagenesis, expression, isolation and purification

Preparation of the F163A, F164A<sup>a</sup>, F226A, F226Y, F227A and R231K<sup>a</sup> variants of rhIDO using site-directed mutagenesis was conducted according to the Quickchange™ protocol (Stratagene), using the rhIDO encoded gene and the relevant mutagenic oligonucleotides, respectively (see Appendix C, Table II). Sequence of the whole rhIDO gene confirmed the desired mutation. All variants were expressed, isolated and purified according to published procedures (5) and were found to exist as a mixture of apo- and holo-enzyme forms. For this reason all variants were reconstituted with hemin prior to use in biochemical studies. Purified proteins (~1.5 mg/l) were obtained with  $R_z > 1.0$  and migrated as a single band on a SDS-PAGE gel.

### 5.2.2 Characterisation of the active site variants of rhIDO

#### 5.2.2.1 Electronic absorption spectra

The electronic spectra of ferric and ferrous rhIDO, F163A, F164A, F226A, F226Y and F227A are presented in Figure 5.3. Analysis of the electronic spectra of the five ferric rhIDO variants reveal wavelength maxima (Table 5.1) that are very similar to those for rhIDO; for rhIDO, the high- and low-spin species were assigned as arising from a six-coordinate, water-bound heme derivative, and from coordination of a distal histidine residue (the identity of this residue is still unknown) to the heme, respectively (6).

The electronic spectra of the ferrous derivatives of F163A, F164A, F226A, F226Y and F227A are essentially identical to that of rhIDO (Figure 5.3(A) (red line), Table 5.1). Ferrous rhIDO has previously been assigned as containing five-coordinate high-spin heme (6, 7); therefore, a similar coordination geometry can be assumed to exist in the ferrous derivatives of the variants.

---

<sup>a</sup> F164A and R231K variants were kindly provided by Dr. Jaswir Basran.

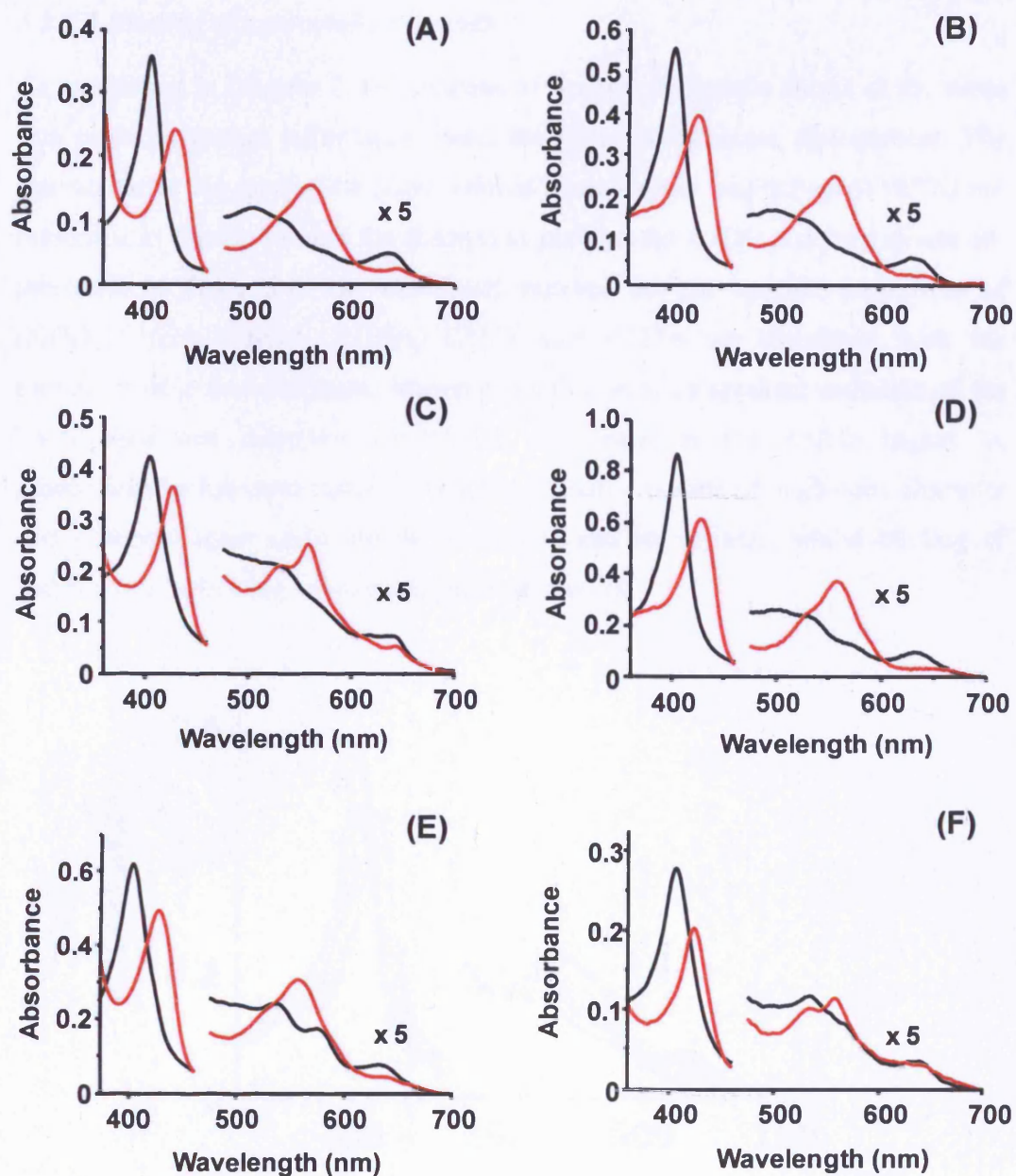


**Figure 5.3:** UV-visible spectra showing the ferric (black line) and ferrous species (red line) of (A) rhIDO, (B) F163A, (C) F164A, (D) F226A, (E) F226Y and (F) F227A. Absorbance values in the visible region have been multiplied by a factor of 5. Conditions: 50 mM Tris/HCl buffer, pH 8.0, 25.0 °C.

### 5.2.2.2 Binding of non-catalytic ligands

As mentioned in Chapter 2, the analysis of exogenous ligands bound at the heme iron provides further information about the distal coordination environment. The representative spectra for the ferric anionic ligand-bound derivatives of rhIDO are presented in Figure 5.4 and the absorption maxima for rhIDO and its variants are presented in Table 5.1. The absorption maxima for the cyanide derivatives of rhIDO, F163A, F164A, F226A, F226Y and F227A are consistent with the formation of a six-coordinate, low-spin species with an apparent red-shift of the Soret band and disappearance of the CT<sub>1</sub> band in the visible region. A predominantly low-spin species containing small amounts of high-spin character was observed upon azide binding to rhIDO and its variants, whilst binding of fluoride results in a high-spin six-coordinate species.

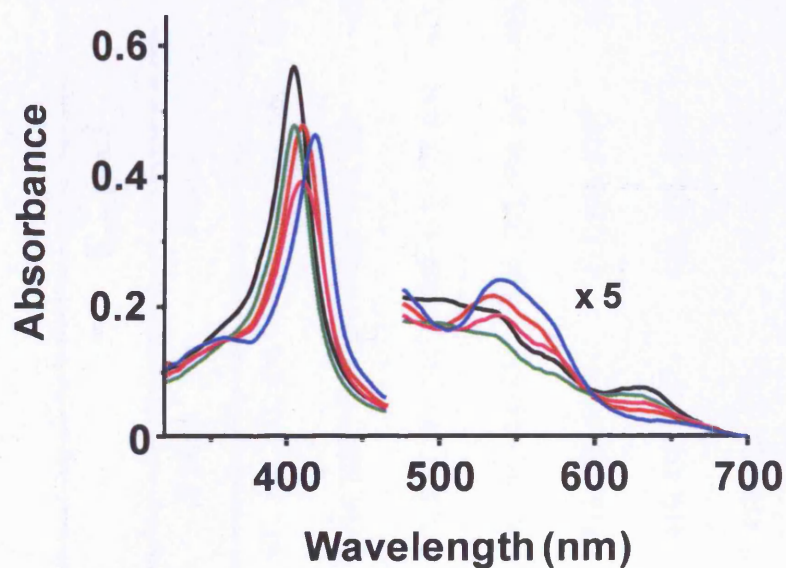


**Figure 5.4:** Absorption spectra of ferric anionic ligand-bound derivatives of rhIDO: ferric (black), ferric + L-Trp (red), ferric-cyanide (blue), ferric-azide (pink) and ferric-fluoride (green). Absorbance values in the visible region have been multiplied by a factor of 5. Conditions: 50 mM Tris/HCl buffer, pH 8.0, 25.0 °C.

**Table 5.1:** Wavelength maxima for the ferric and ferrous derivatives of rhIDO, F163A, F164A, F226A, F226Y and F227A. Conditions: 50 mM Tris/HCl buffer, pH 8.0, 25.0 °C.

Derivative	$\lambda_{\max}$ (nm)					
	rhIDO	F163A	F164A	F226A	F226Y	F227A
<b>Ferric</b>	404, 500, 533, 635	404, 501, 533, 634	404, 500, 531, 640	404, 500, 533, 635	404, 500, 535, 574, 638	404, 501, 533, 636
<b>Ferrous</b>	425, 527 <sup>sh</sup> , 558	426, 524 <sup>sh</sup> , 558	425, 531, 560	426, 524 <sup>sh</sup> , 558	425, 527 <sup>sh</sup> , 558	425, 531 <sup>sh</sup> , 561
<b>Ferric-azide</b>	413, 535, 572, 643	413, 501, 534, 640	409, 535, 573, 640	413, 536, 573, 643	413, 540, 574, 634	412, 539, 571, 638
<b>Ferric-fluoride</b>	404, 502, 532, 635	404, 501, 534, 634	404, 501, 534, 640	404, 501, 534, 635	404, 501, 538, 576	404, 502, 533, 634
<b>Ferric-cyanide</b>	419, 538, 569 <sup>sh</sup>	418, 539, 569 <sup>sh</sup>	419, 538, 570 <sup>sh</sup>	418, 537, 571 <sup>sh</sup>	419, 538, 569 <sup>sh</sup>	418, 538, 569 <sup>sh</sup>
<b>Ferric-L-Trp</b>	410, 540, 576 <sup>sh</sup>	410, 439, 575 <sup>sh</sup>	408, 535, 570 <sup>sh</sup>	410, 541, 576 <sup>sh</sup>	411, 540, 570 <sup>sh</sup>	411, 538, 576 <sup>sh</sup>
<b>Ferrous-oxy</b>	416, 539, 576	416, 538, 576	416, 539, 576	414, 535, 575	414, 535, 574	416, 539, 576

sh = shoulder.

## 5.2.3 Equilibrium binding experiments

### 5.2.3.1 Cyanide binding

The effect of the mutations at F163, F164, F226 and F227 on the ability of the enzyme to bind exogenous ligands was determined by equilibrium binding measurements (Table 5.2). Figure 5.5 shows a representative family of spectra collected during the titration of F163A with cyanide, the other variants showed similar absorption changes during the cyanide titrations. All variants were found to bind cyanide with a similar affinity to rhIDO (Table 5.2). This, along with the ligand binding information presented in the previous section, indicates that no internal ligands are ligated to the sixth coordination site; this is important because coordination of an internal ligand to the iron centre has been observed previously upon mutation of an active site residue (8). Therefore, the coordination environments in F163A, F164A, F226A, F226Y and F227A are likely to be similar to rhIDO.

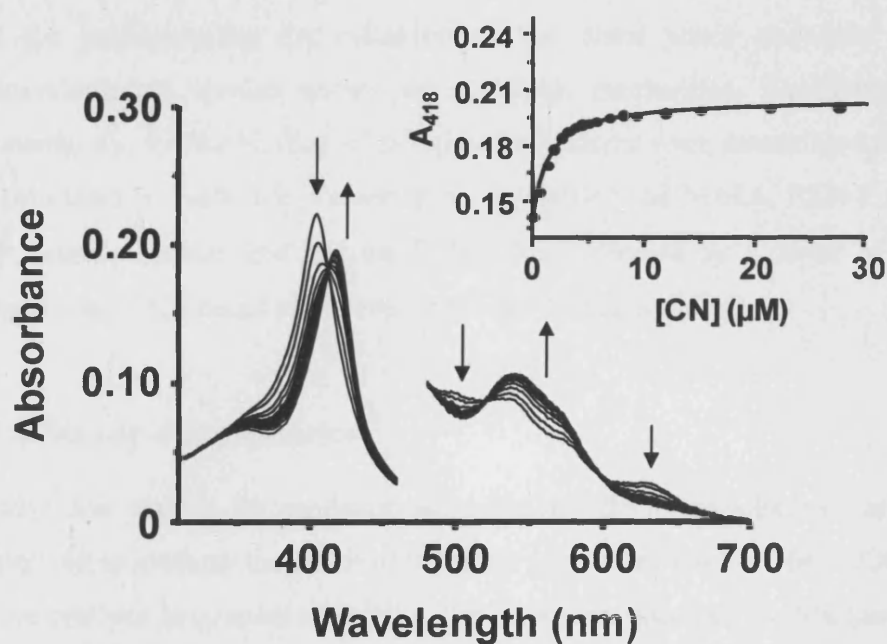


**Figure 5.5:** Representative data set for the determination of  $K_D$  for binding of CN to F163A. The arrows indicate the direction of change in absorbance upon successive additions of CN. Absorbance values in the visible region have been multiplied by a factor of 5. (Inset) Fit of data at 418 nm to Equation [8.4], Chapter 8. Conditions: 50 mM Tris/HCl buffer, pH 8.0, 25.0 °C.

**Table 5.2:** Thermodynamic parameters for the binding of cyanide and L-Trp to ferric rhIDO, F163A, F164A, F226A, F226Y and F227A. Conditions: 50 mM Tris/HCl buffer, pH 8.0, 25.0 °C.

	rhIDO	F163A	F164A	F226A	F226Y	F227A
<b>Cyanide</b>						
$K_D$ ( $\mu\text{M}$ )	$3.57 \pm 0.37$	$1.21 \pm 0.16$	$2.40 \pm 0.43$	$1.45 \pm 0.14$	$2.50 \pm 0.26$	$1.95 \pm 0.24$
<b>L-Trp</b>						
$K_D$ ( $\mu\text{M}$ )	$285 \pm 6$	$450 \pm 30$	$1410 \pm 260$	$2150 \pm 320$	$540 \pm 47$	$635 \pm 20$

### 5.2.3.2 L-Trp binding

As mentioned in Chapter 2, binding of L-Trp to ferric rhIDO leads to the formation of a low-spin hydroxide bound heme (Table 5.1) ( $\lambda_{\text{max}} = 410, 540, 576^{\text{th}}$ ). The similarity of the spectroscopic changes for F163A, F164A, F226A, F226Y and F227A (Table 5.1) indicates that binding of substrate occurs in a similar manner and that the corresponding deprotonation of the distal water molecule to form a hydroxide-bound species occurs by a similar mechanism. Equilibrium binding constants,  $K_D$ , for the binding of L-Trp to the variants were determined and the data are presented in Table 5.2. Values of  $K_D$  for rhIDO and F163A, F226Y and F227A were broadly similar, but that for F226A has increased by a factor of  $\approx 8$ , which suggests that F226 could play a role in L-Trp binding in rhIDO.

### 5.2.4 Steady-state kinetics

Steady-state studies for oxidation of L-Trp by the phenylalanine variants were carried out to evaluate the effect of mutation at residues F163, F164, F226 and F227 on the catalytic properties of rhIDO. The data were fitted to the Michaelis-Menten equation (Chapter 8, Equation [8.5]) and a representative data set for F163A is presented in Figure 5.6. Steady-state parameters,  $k_{\text{cat}}$ ,  $K_M$  and the arithmetically calculated selectivity coefficient ( $k_{\text{cat}}/K_M$ ) are reported in Table 5.3. F163A catalysed the oxidation of L-Trp at a significantly slower rate in comparison to rhIDO ( $\approx 46$  times slower), although the  $K_M$  is not greatly affected. Turnover rates for F164A, F227A and F226A were in a similar range to rhIDO; however the  $K_M$  for F226A

increased by a factor of  $\approx 130$ . This is consistent with the binding constants obtained for ferric F226A with L-Trp and suggests that F226 plays an important role in substrate recognition. In contrast, the rate of oxidation of L-Trp by F226Y is faster than that observed for rhIDO.

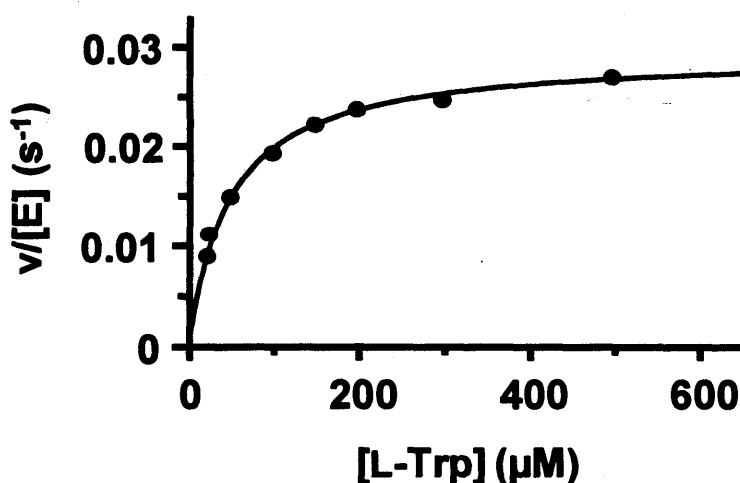


**Figure 5.6:** Steady-state oxidation of L-Trp by F163A. Solid line shows a fit of the data to the Michaelis-Menten Equation (Chapter 8, Section 8.11).

**Table 5.3:** Steady state kinetic data for L-Trp oxidation by rhIDO and a number of active site variants. All data were fitted using the Michaelis-Menten equation (Chapter 8, Equation [8.5]). Each value is an average of at least three independent measurements.

	$k_{cat}$ (s <sup>-1</sup> )	$K_M$ (μM)	$k_{cat}/K_M$ (μM <sup>-1</sup> s <sup>-1</sup> )	Reported $k_{cat}$ (s <sup>-1</sup> ) (9)
rhIDO	1.4 ± 0.05	7.0 ± 0.80	0.20	2.1 ± 0.20
F163A	0.030 ± 0.001	47 ± 5.1	0.000063	2.5 ± 0.15
F164A <sup>b</sup>	0.74 ± 0.01	210 ± 11	0.0035	-
F226A	0.39 ± 0.009	940 ± 69	0.00041	0.022 ± 0.0050
F226Y	6.0 ± 0.15	25 ± 1.7	0.23	-
F227A	0.43 ± 0.0042	9.0 ± 0.4	0.040	0.020 ± 0.0083

<sup>b</sup> Steady-state data for F164A was determined by Dr. Jaswir Basran

Sugimoto *et al.* have reported  $k_{\text{cat}}$  values for F163A, F226A and F227A; however, they differ greatly to the values obtained in this study (Table 5.3). For this reason, all steady-state kinetic parameters were measured using the relevant mutant enzyme which had been isolated from three different batches, and at least three independent steady-state measurements were carried out on each batch of mutant enzyme. The discrepancy in  $k_{\text{cat}}$  values could be due to the different experimental techniques used to measure the oxidation of L-Trp. The steady-state assays used to obtain kinetic parameters throughout this thesis employs ascorbate, catalase and methylene blue; ascorbate and methylene blue are reducing agents, but also react with dioxygen to form superoxide and peroxide by-products, which can bleach the heme and destroy catalytic activity; catalase is present to remove any superoxide or peroxide in solution and therefore allows efficient turnover of substrate. Reaction velocity is calculated by directly monitoring the increase in absorbance of *N*-formyl-kynurenine at 321 nm. This method has been used by numerous research groups for both IDO and TDO enzymes from a variety of sources (6, 10-15). The measurement of rhIDO activity adopted by Sugimoto relies on quantifying the amount of kynurenine, which is a product of hydrolysis from *N*-formyl-kynurenine, produced in the assay media through an indirect means. More specifically, it relies on the formation of a product from the reaction of kynurenine with *p*-dimethylaminobenzaldehyde, and is monitored at  $\lambda_{\text{max}} = 480$  nm.

### 5.2.5 Kinetics of O<sub>2</sub> binding

Spectroscopic changes observed on reaction of F163A, F164A, F226A, F226Y and F227A with O<sub>2</sub> were monitored using stopped-flow photodiode array spectroscopy. The data were collected over a period of 1 s from the mixing event and were best fitted to a one-step model ( $A \rightarrow B$ , a representative data set is shown in Figure 5.7(A)) in which species A (black line) represents the ferrous form of F226A ( $\lambda_{\text{max}} = 426, 524^{\text{sh}}, 558$  nm) and species B (red line) has spectral properties characteristic of the ferrous-oxy complex ( $\lambda_{\text{max}} = 416, 538, 576$  nm). The ferrous-oxy complex was also observed for all other variants and exhibited similar wavelength maxima to that seen for rhIDO, Table 5.1. The concentration dependence of the rate constant ( $k_{\text{obs}}$ ) for ferrous-oxy complex formation in all variants of rhIDO was monitored at 416

nm using the single-wavelength mode of the stopped-flow apparatus. The corresponding rate constants for O<sub>2</sub> binding ( $k_{\text{on}}$ ,  $k_{\text{off}}$ , Equation [8.6]) to all five active site variants are given in Table 5.4 and a representative data set for F226A is shown in Figure 5.7(B).

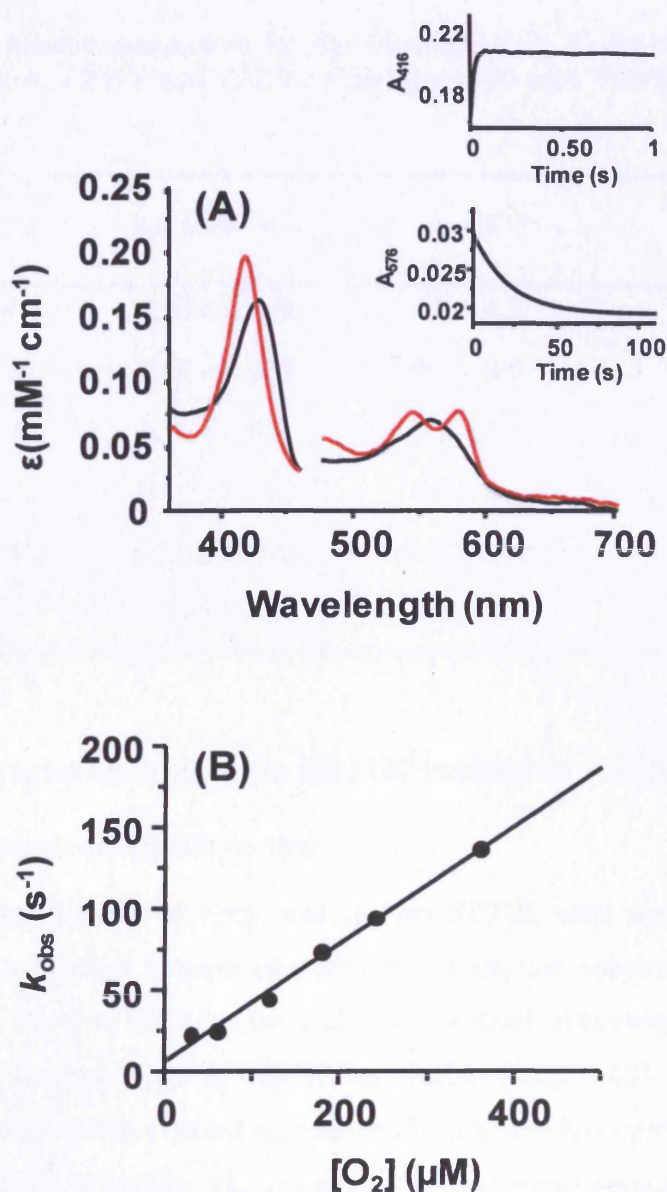


**Figure 5.7:** Reaction of F226A with O<sub>2</sub> monitored by stopped-flow spectroscopy. (A) Deconvoluted spectra for the time-dependent spectral changes on mixing 1 μM ferrous F226A with 130 μM O<sub>2</sub> (time base of 1 s). The data were fitted to a single-step model A → B (obtained from global fitting). (Insets) Absorption transients at (Top) 416 nm and (Bottom) 576 nm observed upon mixing of 1 μM ferrous F226A with 130 μM O<sub>2</sub>. (B) Concentration dependence of the observed rate constant ( $k_{\text{obs}}$ ) of O<sub>2</sub> binding to ferrous F226A.

The ferrous-oxy complexes spontaneously decompose to ferric enzyme for all mutant proteins under anaerobic conditions (monitored at 576 nm); the stability of the ferrous-oxy complexes for all variant enzymes were found to be comparable with that of rhIDO (Table 5.4).

**Table 5.4:** Kinetic parameters for the binding of O<sub>2</sub> to ferrous rhIDO, F163A, F164A, F226A, F226Y and F227A. Conditions: 50 mM Tris/HCl buffer, pH 8.0, 25.0 °C.

	$k_{\text{on}}$ ( $\mu\text{M}^{-1} \text{s}^{-1}$ )	$k_{\text{off}}$ ( $\text{s}^{-1}$ )	$t_{1/2}$ (s)
<b>rhIDO</b>	0.53 ± 0.006	6.8 ± 1.8	36
<b>F163A</b>	0.60 ± 0.035	9.1 ± 8.0	33
<b>F164A</b>	0.21 ± 0.012	3.1 ± 3.4	37
<b>F226A</b>	0.35 ± 0.013	6.5 ± 4.1	16
<b>F226Y</b>	0.18 ± 0.0034	1.8 ± 0.77	15
<b>F227A</b>	0.45 ± 0.065	2.7 ± 14	45

## 5.2.6 Characterisation of the R231K variant of rhIDO

### 5.2.6.1 Electronic absorption spectra

The absorption spectra of ferric and ferrous R231K were recorded (Figure 5.8) following purification. Comparison with the absorption spectrum of ferric rhIDO reveals that the two proteins have almost identical spectroscopic features. The spectrum of the ferric form of R231K has maxima ( $\lambda_{\text{max}} = 404, 501, 533, 630 \text{ nm}$ ) that are consistent with a mixed population of high- and low-spin heme species. The ferrous spectrum of R231K ( $\lambda_{\text{max}} = 425, 526^{\text{sh}}, 559 \text{ nm}$ ) revealed the presence of predominantly five-coordinate heme similar to that observed for rhIDO.

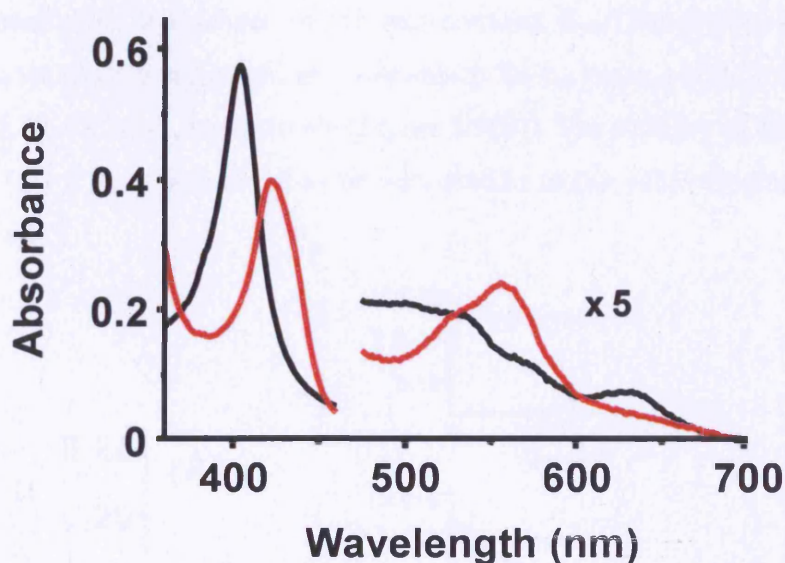


**Figure 5.8:** UV-visible spectra showing the ferric (black line) and ferrous (red line) species of R231K.

#### 5.2.6.2 Equilibrium binding experiments

Absorption maxima for the ferric-cyanide derivative of R231K ( $\lambda_{\max} = 419, 538, 569^{\text{sh}}$  nm) are similar to those for rhIDO (Table 5.1). The equilibrium binding constant,  $K_D$ , for binding of cyanide to ferric enzyme was measured; a value of  $2.3 \pm 0.41 \mu\text{M}$  was determined, which is of a similar magnitude to that of rhIDO.

On binding of L-Trp at pH 8.0, the Soret band shifts to a value ( $\lambda_{\max} = 411$  nm) that is characteristic of low-spin heme formation and is similar to that observed for rhIDO. The equilibrium binding constant for binding of L-Trp to ferric IDO was determined to be  $6700 \pm 900 \mu\text{M}$ .

#### 5.2.6.3 Kinetics of $\text{O}_2$ binding

Spectroscopic changes observed on reaction of R231K with  $\text{O}_2$  were monitored using stopped-flow photodiode array spectroscopy where the data were collected over a period of 1 s from the mixing event and were best fitted to a one-step model ( $A \rightarrow B$ , Figure 5.9(A)). Ferrous (Figure 5.9(A), black line,  $\lambda_{\max} = 426, 526^{\text{sh}}, 558$  nm) and ferrous-oxy R231K (Figure 5.9(A), red line,  $\lambda_{\max} = 416, 538, 576$  nm) were found to have spectroscopic characteristic very similar to that of rhIDO.

The concentration dependence of the rate constant ( $k_{\text{obs}}$ ) for ferrous-oxy complex formation was monitored at 416 nm with values for  $k_{\text{on}}$  and  $k_{\text{off}}$  of  $0.32 \pm 0.0044 \mu\text{M}^{-1} \text{s}^{-1}$  and  $3.80 \pm 1.20 \text{s}^{-1}$ , respectively (Figure 5.9(B)). The stability of the ferrous-oxy complex ( $t_{1/2} = 31 \text{s}$ ) was found to be very similar to the value obtained for rhIDO ( $t_{1/2} = 36 \text{s}$ ).

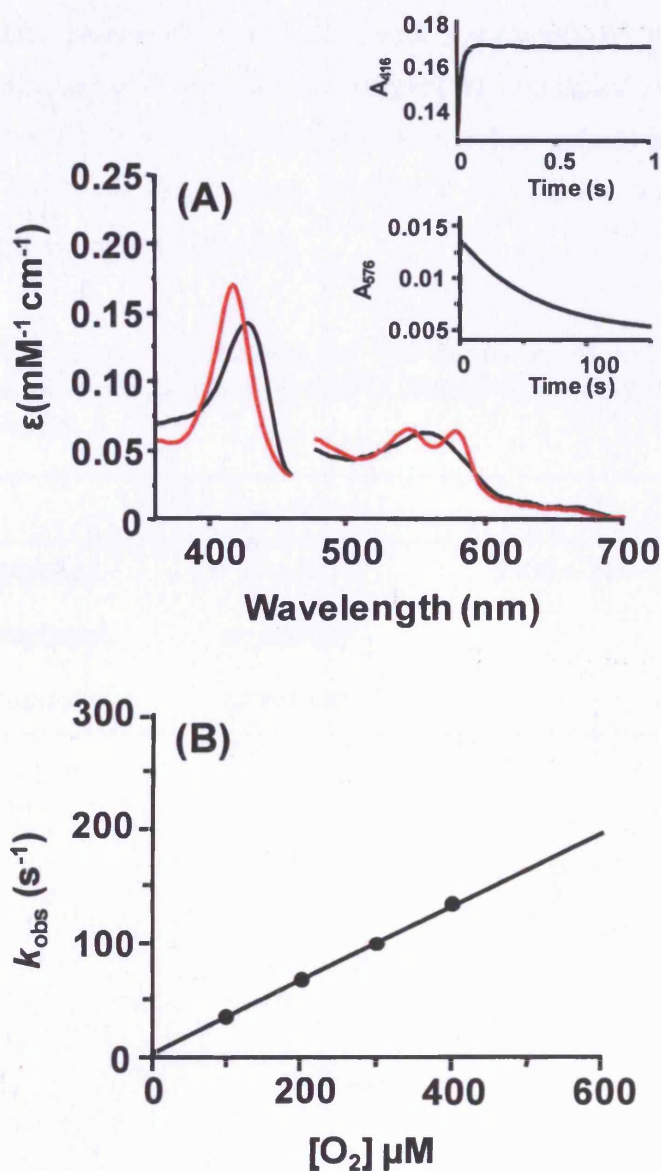


**Figure 5.9:** Reaction of R231K with  $\text{O}_2$  monitored by stopped-flow spectroscopy. (A) Deconvoluted spectra for the time-dependent spectral changes on mixing  $1 \mu\text{M}$  ferrous R231K with  $130 \mu\text{M}$   $\text{O}_2$  (time base of 1 s). The data were fitted to a single-step model  $\text{A} \rightarrow \text{B}$  (obtained from global fitting). (Insets) Absorption transients at (Top) 416 nm and (Bottom) 576 nm observed upon mixing of  $1 \mu\text{M}$  ferrous R231K with  $130 \mu\text{M}$   $\text{O}_2$ . (B) Concentration dependence of the observed rate constant ( $k_{\text{obs}}$ ) of  $\text{O}_2$  binding to ferrous R231K.

#### 5.2.6.4 Steady-state kinetics

The R231K variant was observed to be capable of steady-state oxidation of L-Trp at pH 8.0 under conditions identical to those used for rhIDO, with a turnover rate  $\approx 5$  fold slower than rhIDO (Table 5.5); however removal of R231 has a major impact on L-Trp binding ( $\approx 500$  fold), as evidenced by  $K_M$ .

Steady-state parameters for rhIDO with L-tryptophanol and tryptamine (Figure 5.10), which are both tryptophan analogues with modified carboxylate groups, were determined to show that substrate (carboxylate group)-protein interactions are present within the distal cavity of rhIDO. No activity was detected with either tryptophan analogue (Table 5.5).

**Table 5.5:** Kinetic parameters for the oxidation of L-Trp by R231K, and L-tryptophanol and tryptamine by rhIDO. Steady-state assays were carried out by Dr. Jaswir Basran.

	$k_{cat}$ ( $s^{-1}$ )	$K_M$ ( $\mu M$ )	$k_{cat}/K_M$ ( $\mu M^{-1} s^{-1}$ )
L-tryptophan	$0.31 \pm 0.013$	$3300 \pm 360$	0.000094
L-tryptophanol	no activity	-	-
tryptamine	no activity	-	-

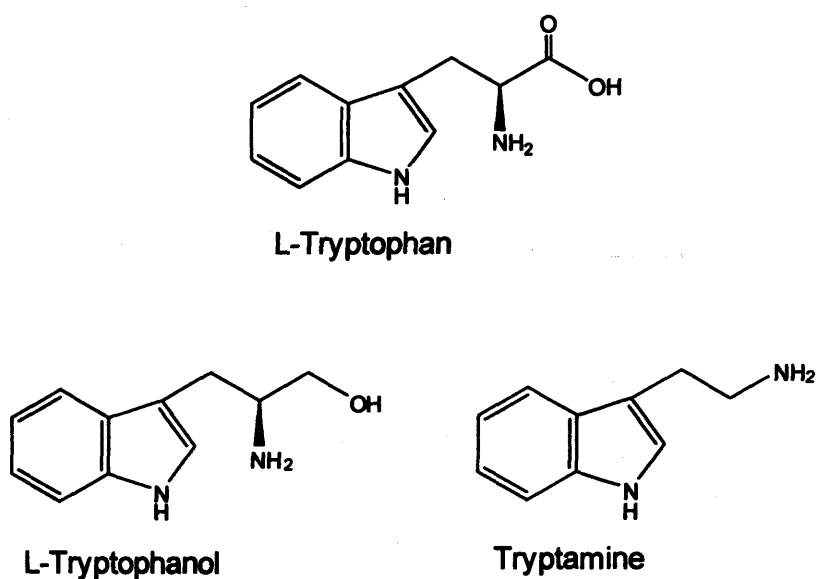


**Figure 5.10:** Structures of tryptophan analogues.

### 5.3 Discussion

---

As mentioned earlier, there is very little information in the literature regarding the role of active site residues despite having the crystal structure of rhIDO. For this reason, site-directed mutagenesis was carried out on a number of active site residues. The F163A variant was prepared because it is the closest aromatic residue to L-Trp (from a structural alignment between rhIDO and substrate-bound XcTDO) and also to the heme iron. The UV-visible spectrum of F163A has characteristics very similar to rhIDO and the variant was also able to bind a number of exogenous ligands including O<sub>2</sub>, as normal. Steady-state analysis of F163A show that this variant has lost a large proportion of its activity, but the  $K_M$  is of the same magnitude of that found for rhIDO with L-Trp. In contrast, Sugimoto *et al.* found that the F163A variant could turnover L-Trp at a faster rate than rhIDO (9); however, different experimental techniques were employed to measure catalytic activity and this is the most likely cause of this discrepancy. Collectively, this information suggests that F163 is important for orientating L-Trp in the correct position for catalysis; this seems plausible since the removal of F163 will create a vacant pocket which would allow substrate to deviate from its usual binding site (Figure 5.11(A)). The F226A variant was found to catalyse the oxidative cleavage of L-Trp with a  $k_{cat}$  comparable to rhIDO but the  $K_M$  for L-Trp was very high. This suggests that the role of F226 is to provide  $\pi$ - $\pi$  stacking interactions with the benzene ring of L-Trp and is likely to contribute to the overall hydrophobicity of the L-Trp binding pocket (Figure 5.11(A)). In addition, spectroscopic studies on the formation and decomposition of the ferrous-oxy derivatives of all variants have shown no distinct differences with rhIDO, indicating that they are not involved in ligand stabilisation in rhIDO.

As discussed earlier, the crystal structure of XcTDO revealed the presence of R117 (equivalent to R231 in rhIDO) in two different conformations: an open conformation in the ferric, substrate-free structure and a closed conformation in the ferrous, substrate-bound structure (Figures 5.2(A) and (B), respectively). Because the crystal structure of rhIDO was solved in ferric form in the presence of 4-phenyl-imidazole, it is not clear whether a similar rearrangement of R231 is possible in rhIDO. Interestingly, Sugimoto *et al.* found that the catalytic activity of R231A was significantly reduced (but no corresponding  $K_M$  was reported) (9); at this time, the

structure of *Xc*TDO was not solved and the possibility of this residue adopting different conformations in the absence and presence of substrate was unknown. Sugimoto therefore ambiguously proposed that R231 is involved in substrate recognition by hydrophobic interactions. Replacement of R231 with K231 did not have a huge impact on catalytic activity with L-Trp ( $\approx 5$  fold) but had a large effect on substrate binding (as evidenced by a  $K_M$  value  $\approx 500$  fold larger than rhIDO with L-Trp) and suggests that the bidentate ion pair interaction is, indeed, essential between the carboxylate group of L-Trp and R231 in rhIDO (Figure 5.11(B)). This is consistent with the fact that two substrate analogues (L-tryptophanol and tryptamine) with modified carboxylate groups no longer effectively served as substrates to rhIDO. This arginine residue is conserved in *Xc*TDO, rhIDO, rhTDO, *SIDO* (Figure 5.11(C)) and is likely to play the same role in this family of heme dioxygenase enzymes.

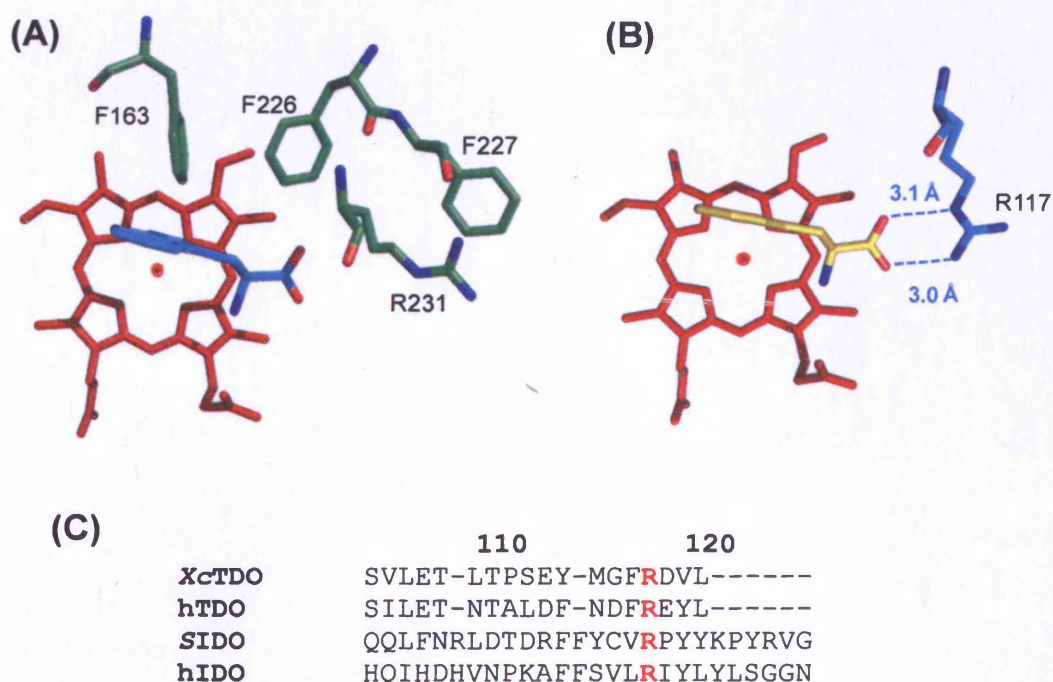


**Figure 5.11:** (A) Active site of rhIDO showing residues F163, F226, F227 and R231; L-Trp (from the *Xc*TDO crystal structure) has been modelled into the active site. (B) The crystal structure of ferrous *Xc*TDO in complex with L-Trp showing the active site residue R117 in a "closed" conformation. (C) An amino acid sequence alignment of *Xc*TDO, human TDO, *SIDO* and human IDO showing the conserved arginine residues in red.

Sugimoto also proposed that the side chain of F227 interacts with the guanidium group of R231 by cation- $\pi$  interactions, and suggested that F227 indirectly contributed to substrate recognition by stabilising the conformation of R231 (Figure 5.11(A)). The fact that F227A is catalytically competent for L-Trp turnover and binds L-Trp with a similar affinity to rhIDO, suggests that F227 is unlikely to stabilise the conformation of R231; this is consistent with there being no equivalent residue in *XcTDO*.

In summary, the analysis of site-directed variants of rhIDO suggests that not only substrate binding but also proper geometry between the substrate and the heme-bound dioxygen is required for catalysis. The recognition of substrate is likely to involve strict complementarities between L-Trp (the indole ring as well as the carboxylate group) and protein amino acids.

## 5.4 References

---

1. Littlejohn, T. K., Takikawa, O., Truscott, R. J., and Walker, M. J. (2003) Asp274 and His346 are essential for heme binding and catalytic function of human indoleamine 2,3-dioxygenase, *J. Biol. Chem.* 278, 29525-29531.
2. Sono, M., and Dawson, J. H. (1984) Extensive studies of the heme coordination structure of indoleamine 2,3-dioxygenase and of tryptophan binding with magnetic and natural circular dichroism and electron paramagnetic resonance spectroscopy, *Biochim. Biophys. Acta* 789, 170-187.
3. Uchida, K., Shimizu, T., Makino, R., Sakaguchi, K., Iizuka, T., Ishimura, Y., Nozawa, T., and Hatano, M. (1983) Magnetic and natural circular dichroism of L-tryptophan 2,3-dioxygenases and indoleamine 2,3-dioxygenase. I. Spectra of ferric and ferrous high spin forms, *J. Biol. Chem.* 258, 2519-2525.
4. Uchida, K., Shimizu, T., Makino, R., Sakaguchi, K., Iizuka, T., Ishimura, Y., Nozawa, T., and Hatano, M. (1983) Magnetic and natural circular dichroism of L-tryptophan 2,3-dioxygenases and indoleamine 2,3-dioxygenase. II. Spectra of their ferric cyanide and ferrous carbon monoxide complexes and an oxygenated form, *J. Biol. Chem.* 258, 2526-2533.
5. Chauhan, N., Basran, J., Efimov, I., Svistunenko, D. A., Seward, H. E., Moody, P. C., and Raven, E. L. (2008) The role of serine 167 in human indoleamine 2,3-dioxygenase: a comparison with tryptophan 2,3-dioxygenase, *Biochemistry* 47, 4761-4769.
6. Papadopoulou, N. D., Mewies, M., McLean, K. J., Seward, H. E., Svistunenko, D. A., Munro, A. W., and Raven, E. L. (2005) Redox and spectroscopic properties of human indoleamine 2,3-dioxygenase and a His303Ala variant: implications for catalysis, *Biochemistry* 44, 14318-14328.
7. Terentis, A. C., Thomas, S. R., Takikawa, O., Littlejohn, T. K., Truscott, R. J., Armstrong, R. S., Yeh, S. R., and Stocker, R. (2002) The heme environment of recombinant human indoleamine 2,3-dioxygenase. Structural properties and substrate-ligand interactions, *J. Biol. Chem.* 277, 15788-15794.

8. Badyal, S. K., Joyce, M. G., Sharp, K. H., Seward, H. E., Mewies, M., Basran, J., Macdonald, I. K., Moody, P. C., and Raven, E. L. (2006) Conformational mobility in the active site of a heme peroxidase, *J. Biol. Chem.* **281**, 24512-24520.
9. Sugimoto, H., Oda, S., Otsuki, T., Hino, T., Yoshida, T., and Shiro, Y. (2006) Crystal structure of human indoleamine 2,3-dioxygenase: catalytic mechanism of O<sub>2</sub> incorporation by a heme-containing dioxygenase, *Proc. Natl. Acad. Sci. USA* **103**, 2611-2616.
10. Batabyal, D., and Yeh, S. R. (2007) Human tryptophan dioxygenase: a comparison to indoleamine 2,3-dioxygenase, *J. Am. Chem. Soc.* **129**, 15690-15701.
11. Ishimura, Y., Nozaki, M., and Hayaishi, O. (1970) The oxygenated form of L-tryptophan 2,3-dioxygenase as reaction intermediate, *J. Biol. Chem.* **245**, 3593-3602.
12. Shimizu, T., Nomiyama, S., Hirata, F., and Hayaishi, O. (1978) Indoleamine 2,3-dioxygenase. Purification and some properties, *J. Biol. Chem.* **253**, 4700-4706.
13. Sono, M., and Cady, S. G. (1989) Enzyme kinetic and spectroscopic studies of inhibitor and effector interactions with indoleamine 2,3-dioxygenase. 1. Norharman and 4-phenylimidazole binding to the enzyme as inhibitors and heme ligands, *Biochemistry* **28**, 5392-5399.
14. Sono, M., Taniguchi, T., Watanabe, Y., and Hayaishi, O. (1980) Indoleamine 2,3-dioxygenase. Equilibrium studies of the tryptophan binding to the ferric, ferrous, and CO-bound enzymes, *J. Biol. Chem.* **255**, 1339-1345.
15. Zhang, Y., Kang, S. A., Mukherjee, T., Bale, S., Crane, B. R., Begley, T. P., and Ealick, S. E. (2007) Crystal structure and mechanism of tryptophan 2,3-dioxygenase, a heme enzyme involved in tryptophan catabolism and in quinolinate biosynthesis, *Biochemistry* **46**, 145-155.

# Chapter 6

---

## H<sub>2</sub>O<sub>2</sub>-mediated catalysis in the heme dioxygenases

## 6.1 Introduction

---

The heme dioxygenases, both ferrous rhIDO and rhTDO, catalyse the dioxygenation of a number L-Trp analogues (see Chapter 1) using dioxygen as a source of oxygen. However, there have been a number of reports in the literature where ferric TDO was found to catalyse the oxidation of L-Trp, under aerobic conditions and in the absence of any reductant. It was proposed that either trace amounts of superoxide or hydrogen peroxide in solution could activate ferric TDO by reduction in solution (1-6). It is unknown whether the heme dioxygenases can utilise oxygen from an alternative source *e.g.* hydrogen peroxide, and there is no information in the literature to support this.

In this Chapter, preliminary experiments were carried out using ferric enzyme (rhTDO and rhIDO) with H<sub>2</sub>O<sub>2</sub> and L-Trp to determine whether the heme dioxygenases can utilise hydrogen peroxide as an alternative oxygen source to dioxygen. We found that rhTDO and rhIDO are able to use hydrogen peroxide as an alternative substrate and we propose a possible reaction mechanism. The work presented in this Chapter will provide a platform for further investigation of this unusual activity.

## 6.2 Results

### 6.2.1 UV-visible spectroscopy

To determine if rhTDO and rhIDO could utilise H<sub>2</sub>O<sub>2</sub> as a substrate, and more importantly determine if it was the sole oxidant of the dioxygenation reaction, both enzymes were separately incubated with L-Trp and H<sub>2</sub>O<sub>2</sub> in the absence of O<sub>2</sub> and any reducing agents. To ensure this, all buffers and solutions were degassed and extensively purged with nitrogen and the incubation was carried out in an anaerobic environment (glove box).

UV-visible spectroscopy was initially used to monitor absorbance changes upon the addition of H<sub>2</sub>O<sub>2</sub> and L-Trp with ferric enzyme (rhTDO and rhIDO). Increases in absorbance at 321 nm were observed upon reaction of rhTDO with H<sub>2</sub>O<sub>2</sub> and L-Trp, indicating formation of *N*-formyl-kynurenine (Figure 6.1, black line). Significantly smaller absorbance changes were observed when the reaction was carried out with rhIDO (Figure 6.1, red line).

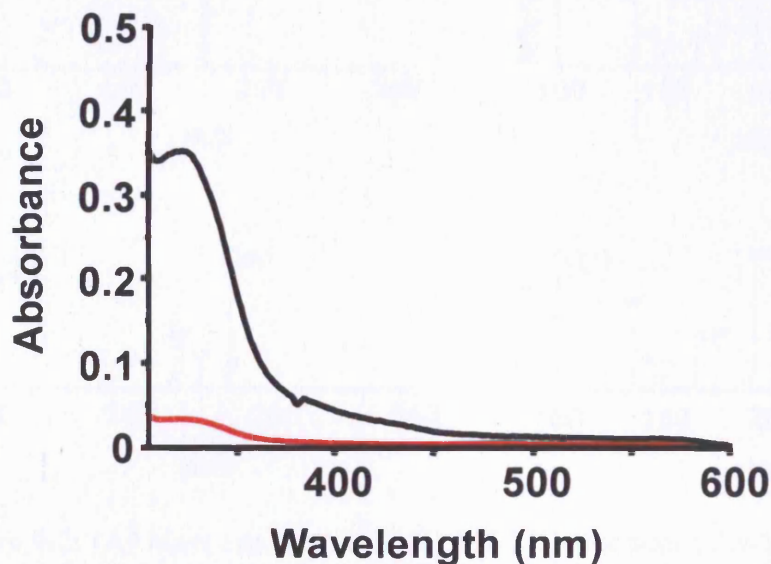


**Figure 6.1:** UV-visible spectrum of *N*-formyl-kynurenine produced upon reaction of H<sub>2</sub>O<sub>2</sub> and L-Trp with rhTDO (black line) and rhIDO (red line) showing absorption bands at 321 nm. Spectra were obtained *after* isolation of the compounds from incubation with rhTDO and rhIDO.

### 6.2.2 LC-MS analysis

LC-MS analysis using selected ion monitoring was carried out to confirm the identity of the product formed upon reaction of rhTDO or rhIDO with H<sub>2</sub>O<sub>2</sub> and L-Trp.

For comparison, the reaction of rhTDO with L-Trp and dioxygen under steady-state conditions gave an ion with  $m/z = 237$  (Figure 6.2(A)) which corresponds to the mass of *N*-formyl-kynurenine (mass = 236) as expected; MS/MS analysis of this ion produced a fragmentation pattern that is consistent with this ion being assigned as *N*-formyl-kynurenine (Figure 6.2(B)). For the reaction of ferric rhTDO with H<sub>2</sub>O<sub>2</sub> and L-Trp, an ion with  $m/z = 237$  (Figure 6.2(C)) was detected which corresponds to the mass of *N*-formyl-kynurenine (mass = 236) and MS/MS analysis of this ion (Figure 6.2(D)) produced a fragmentation pattern similar to that found to Figure 6.2(B) and thus confirms that the product from this reaction is, indeed, *N*-formyl-kynurenine.

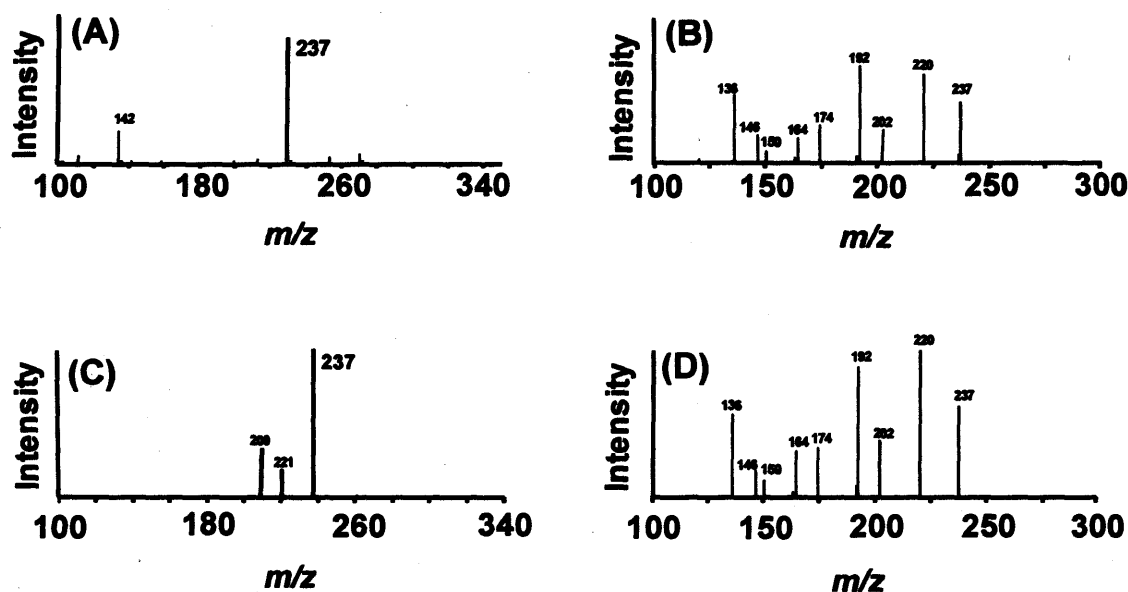


**Figure 6.2:** (A) Mass spectrum and (B) MS/MS spectrum of *N*-formyl-kynurenine produced from a typical reaction of rhTDO with L-Trp under steady-state conditions. (C) Mass spectrum and (D) MS/MS spectrum of *N*-formyl-kynurenine produced upon reaction of rhTDO with H<sub>2</sub>O<sub>2</sub> and L-Trp.

LC-MS analysis was also used to isolate a compound with  $m/z = 221$ ; unfortunately, this compound could not be isolated because it co-eluted with the compound corresponding to *N*-formyl-kynurenine ( $m/z = 237$ ) (Figure 6.3(A)). Therefore, the incubation mixture containing rhTDO, H<sub>2</sub>O<sub>2</sub> and L-Trp was directly subjected to MS/MS analysis and an ion with  $m/z = 221$  (which corresponds to a mass of 220) was detected and is shown in Figure 6.3(B) (*vide infra*).

LC-MS analysis for rhIDO is shown in Figures 6.3(C) and (D) and, like rhTDO, confirmed the presence of an ion with  $m/z$  of 237.

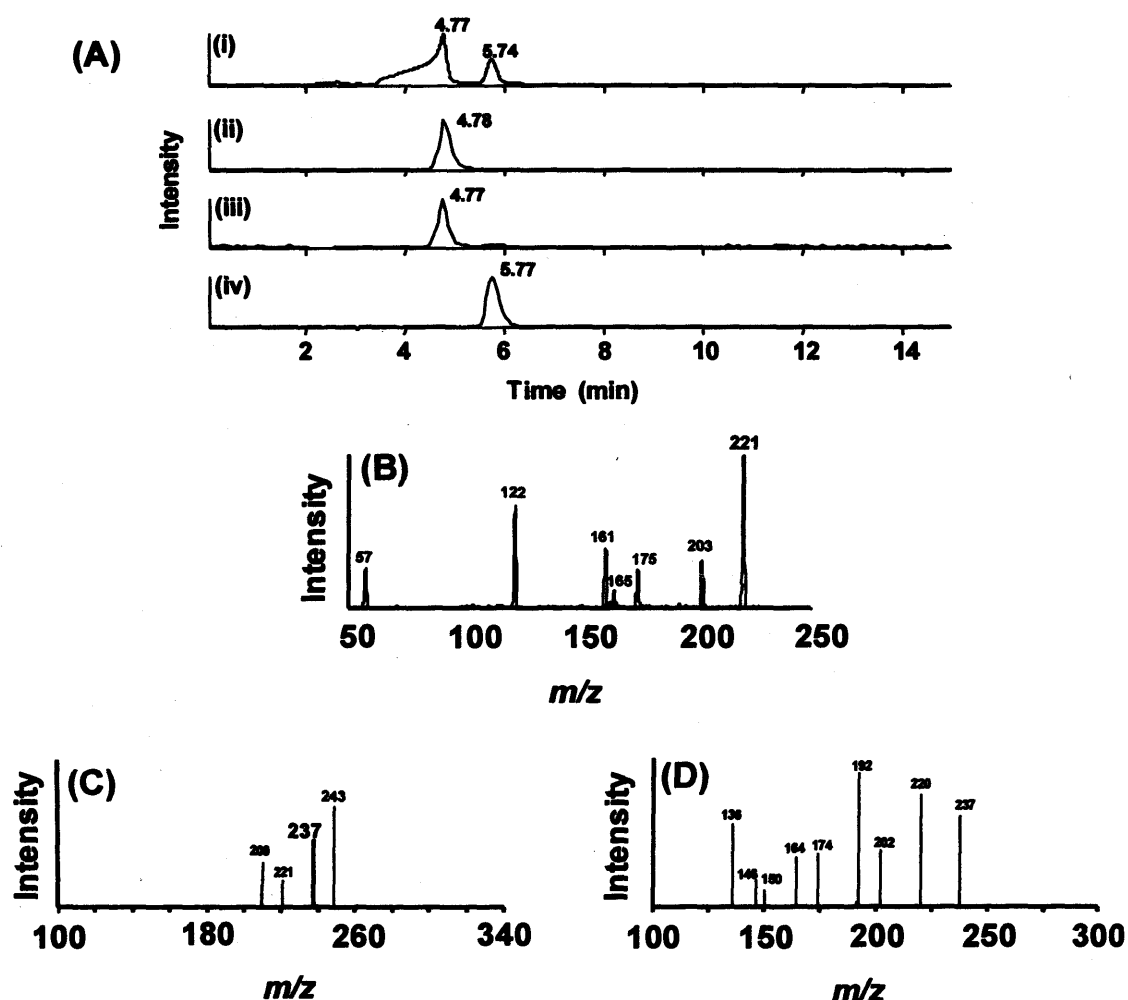


**Figure 6.3:** (A) LC-MS analysis, using selected ion monitoring, of the reaction mixture containing rhTDO, H<sub>2</sub>O<sub>2</sub> and L-Trp. (i) UV trace of the sample monitored at 321 nm. Elution profile for the selected ion chromatogram with  $m/z$  of (ii) 237 (iii) 221 and (iv) 205. (B) MS/MS spectrum of a compound with  $m/z$  of 221. (C) Mass spectrum and (D) MS/MS spectrum of *N*-formyl-kynurenine produced upon reaction of rhIDO with H<sub>2</sub>O<sub>2</sub> and L-Trp.

### 6.2.3 Titration of H<sub>2</sub>O<sub>2</sub> with ferric enzyme and L-Trp

To determine if there was any correlation between the amount of H<sub>2</sub>O<sub>2</sub> consumed and the amount of *N*-formyl-kynurenine produced in this reaction, incremental amounts of H<sub>2</sub>O<sub>2</sub> were added to ferric rhTDO in the presence L-Trp. After a five-step anaerobic addition of a total of 200 μM H<sub>2</sub>O<sub>2</sub>, approximately half the amount of *N*-formyl-kynurenine (monitored at 321 nm) was formed (Figure 6.4(A)).

These results indicate that two molecules of H<sub>2</sub>O<sub>2</sub> are required for the production of one molecule of *N*-formyl-kynurenine under ideal conditions. However, when the same titration was carried out with rhIDO, no correlation was found between the amount of H<sub>2</sub>O<sub>2</sub> consumed and the amount of *N*-formyl-kynurenine produced in the titration (Figure 6.4(B)).

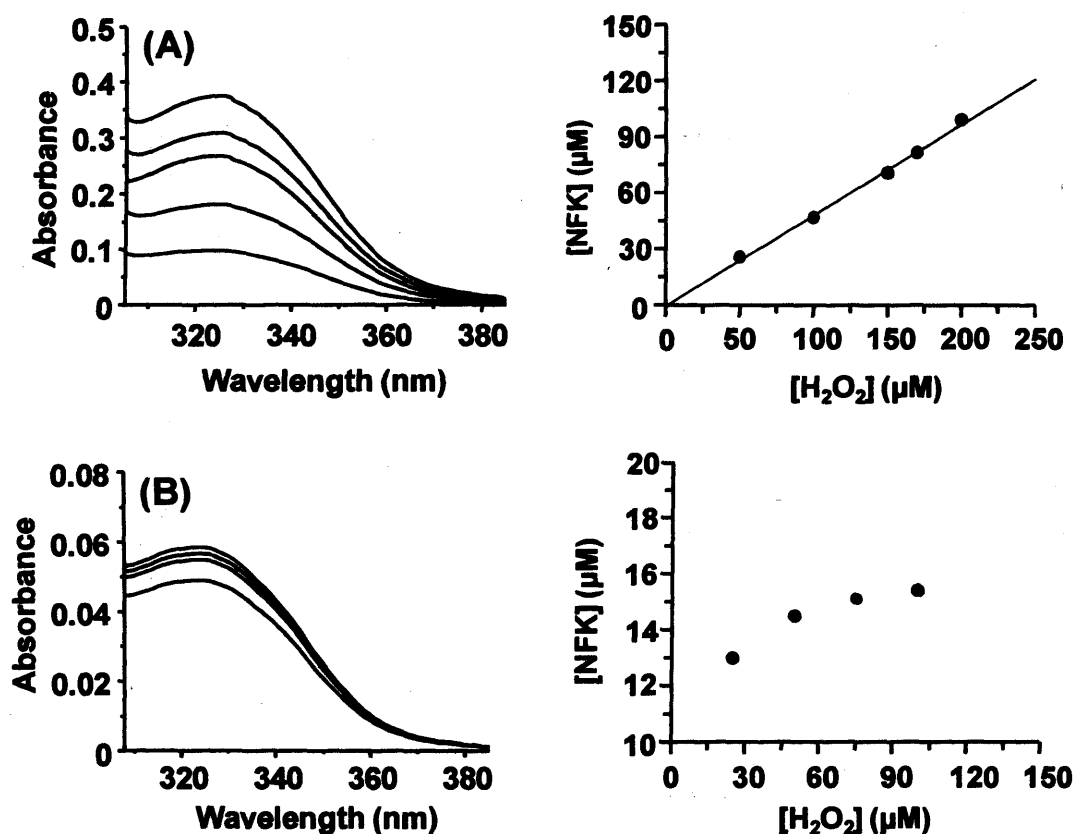


**Figure 6.4:** (Left) UV-visible spectra of *N*-formyl-kynurenine produced upon addition of incremental amounts of H<sub>2</sub>O<sub>2</sub> to (A) ferric rhTDO and (B) ferric rhIDO with L-Trp under anaerobic conditions. (Right) Calculated *N*-formyl-kynurenine (NFK) concentration as a function of the added H<sub>2</sub>O<sub>2</sub> for (A) rhTDO and (B) rhIDO. Conditions: 50 mM Tris/HCl buffer, pH 8.0, 25.0 °C, [enzyme] = 5 μM.

### 6.2.4 Detection of possible intermediate species

Many heme proteins are known to form a Compound I intermediate upon reaction of ferric enzyme with H<sub>2</sub>O<sub>2</sub>; for this reason the reaction of rhTDO and rhIDO with H<sub>2</sub>O<sub>2</sub> was monitored by UV-visible spectroscopy.

The reaction with ferric rhTDO and H<sub>2</sub>O<sub>2</sub> was found to form a species (Figure 6.5(A),  $\lambda_{\text{max}} = 410, 534, 568^{\text{sh}}, 657$ ) that has spectroscopic characteristics that are similar to those seen in the well-characterized Compound I species. As an example, reaction of ascorbate peroxidase with H<sub>2</sub>O<sub>2</sub> gives wavelength maxima at 409, 530, 569<sup>sh</sup>, 655 nm (7); these are characteristic of a ferryl porphyrin  $\pi$ -cation radical species, especially the Soret band which is of lower intensity. Furthermore, the reaction of rhIDO with H<sub>2</sub>O<sub>2</sub> formed a similar intermediate to that found in rhTDO (Figure 6.5(B),  $\lambda_{\text{max}} = 407, 535, 567^{\text{sh}}$ ). Due to time constraints, further progress on the kinetic analysis of rhTDO and rhIDO enzymes with H<sub>2</sub>O<sub>2</sub> proved difficult.

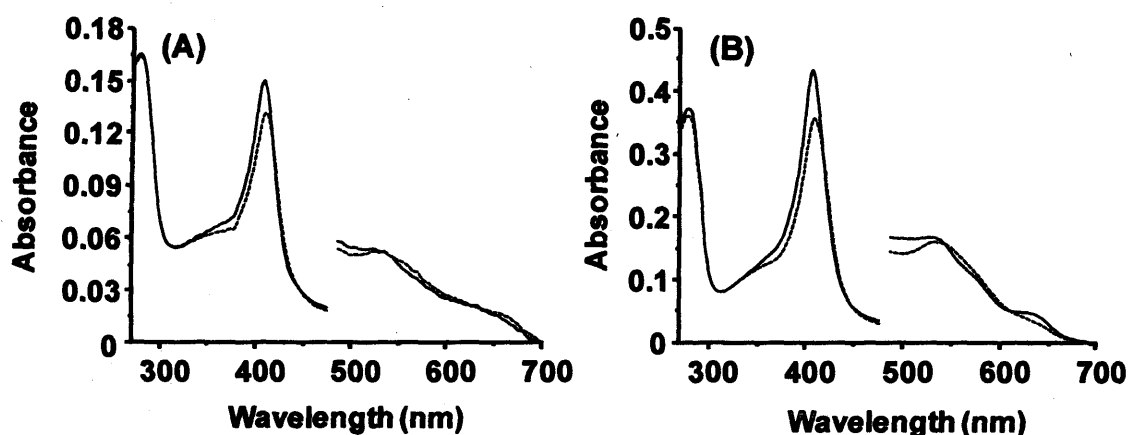
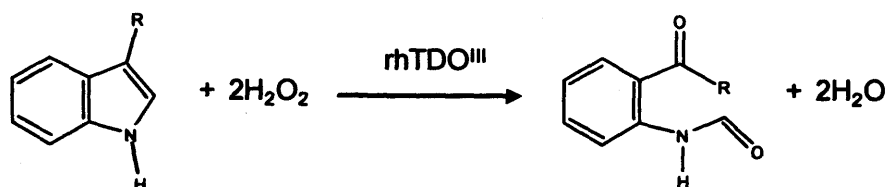


**Figure 6.5:** Absorption spectra of ferric (A) rhTDO and (B) rhIDO prior to the addition of H<sub>2</sub>O<sub>2</sub> (solid line) and ferric (A) rhTDO and (B) rhIDO immediately after reaction with 20 equivalents of H<sub>2</sub>O<sub>2</sub> (dotted line). Absorbance values in the visible region have been multiplied by a factor of 5. Conditions: 50 mM Tris/HCl buffer, pH 8.0, 25.0 °C, [rhTDO] = 0.75  $\mu\text{M}$ , [rhIDO] = 2.5  $\mu\text{M}$ .

### 6.3 Discussion

As mentioned earlier, the ability of hydrogen peroxide to function as an oxygen donor to L-Trp has not previously been established, although ferric rhTDO has been shown to be activated by superoxide and hydrogen peroxide.

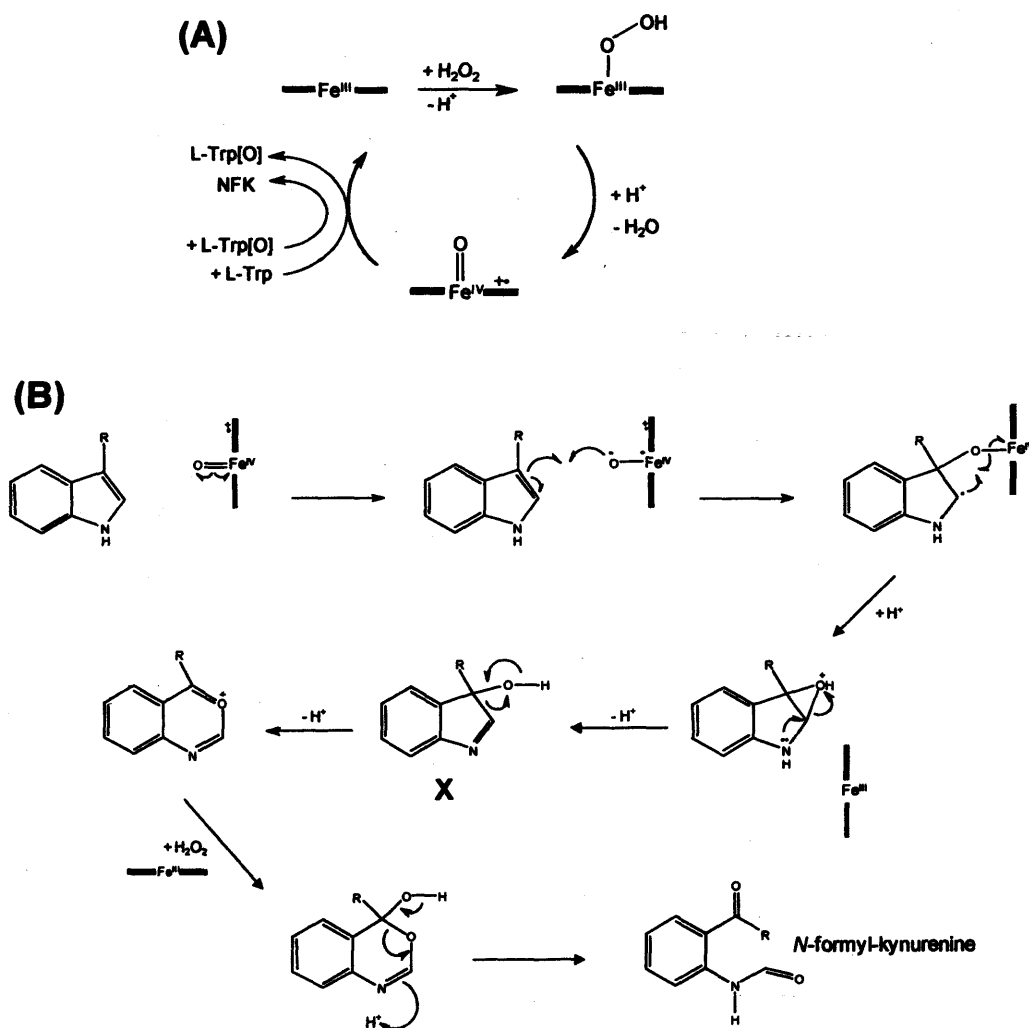
In the H<sub>2</sub>O<sub>2</sub>-driven oxygenation reaction of L-Trp, approximately two equivalents of H<sub>2</sub>O<sub>2</sub> were consumed in the production of one molecule of *N*-formyl-kynurenine in the anaerobic titration experiments. To balance this stoichiometric ratio, two oxygen atoms must have been reduced to water molecules while two are incorporated into *N*-formyl-kynurenine (Scheme 6.1). It is important to note that the coordination geometry of the heme does not allow simultaneous coordination of two molecules of peroxide to the iron; therefore, the dioxygenation product observed from the peroxide experiment with rhTDO must have gone through the sequential addition of two oxygen atoms into L-Trp with retention of monooxygenated L-Trp in the active site during catalysis (Scheme 6.2(A)). This suggests that it would be necessary for the O-O bond (from H<sub>2</sub>O<sub>2</sub>) to be cleaved, and is feasible since this is a well-known step in the catalytic mechanism of the cytochrome P450s which go through a Compound I intermediate following O-O cleavage (8).



**Scheme 6.1:** The chemical reaction catalysed by ferric rhTDO using H<sub>2</sub>O<sub>2</sub> as a substrate.

Interestingly, the same stoichiometric ratio was not used by rhIDO. The reason for this is not clear at this stage, but in 2006 Poljak *et al.* found that low micromolar quantities of H<sub>2</sub>O<sub>2</sub> were sufficient to inactivate rhIDO and it was also discovered that brief exposure to H<sub>2</sub>O<sub>2</sub> resulted in significant structural changes of the enzyme (9); this is consistent with the fact that only small amounts of *N*-formyl-kynurenine were produced upon reaction of ferric rhIDO and H<sub>2</sub>O<sub>2</sub> with L-Trp (compared to the reaction of rhTDO) and at higher concentrations, no significant increase in product was observed (as evidenced by lack of absorbance change at 321 nm, Figure 6.4(B)).

A possible mechanism for formation of *N*-formyl-kynurenine from the reaction of rhTDO with H<sub>2</sub>O<sub>2</sub> and L-Trp is presented in Scheme 6.2(B) and is purely speculative at this stage. In this mechanism the first molecule of peroxide binds to the ferric iron, and generates an enzyme-based intermediate which is presumably the oxyferryl form of rhTDO (Compound I). Following this, the heme-bound oxygen radical attacks the C<sub>3</sub> position of the indole ring resulting in formation of an epoxide ring; subsequent non-enzymatic opening of the epoxide ring yields the hydroxylated product X, and is consistent with the compound detected by MS/MS analysis (with a mass of 220). The indole ring is then expanded by insertion of the oxygen atom. The second molecule of oxygen (from H<sub>2</sub>O<sub>2</sub>) is then inserted into the intermediate and followed by a Criegee-type rearrangement, which further rearranges to form the product *N*-formyl-kynurenine.



**Scheme 6.2:** Possible catalytic cycle (A) and reaction mechanism (B) for formation of *N*-formyl-kynurenine upon reaction of ferric rhTDO with H<sub>2</sub>O<sub>2</sub> and L-Trp.

In summary, the results presented in this Chapter provide the first experimental evidence that ferric rhTDO and rhIDO can catalyse the dioxygenation of L-Trp using H<sub>2</sub>O<sub>2</sub> as an oxygen donor. The activation mechanism by H<sub>2</sub>O<sub>2</sub> is not yet fully understood, it does, however, show that when necessary the heme dioxygenases can use alternative sources of oxygen and, ultimately, can undergo catalysis via a different mechanistic pathway suggesting that they are more flexible than originally thought. Overall, the work presented in this Chapter provides a platform for which further mechanistic studies with H<sub>2</sub>O<sub>2</sub> can be based on.

## 6.4 References

---

1. Brady, F. O., Forman, H. J., and Feigelson, P. (1971) The role of superoxide and hydroperoxide in the reductive activation of tryptophan-2,3-dioxygenase, *J. Biol. Chem.* **246**, 7119-7124.
2. Li, J. S., Han, Q., Fang, J., Rizzi, M., James, A. A., and Li, J. (2007) Biochemical mechanisms leading to tryptophan 2,3-dioxygenase activation, *Arch. Insect. Biochem. Physiol.* **64**, 74-87.
3. Hirata, F., and Hayaishi, O. (1971) Possible participation of superoxide anion in the intestinal tryptophan 2,3-dioxygenase reaction, *J. Biol. Chem.* **246**, 7825-7826.
4. Batabyal, D., and Yeh, S. R. (2007) Human tryptophan dioxygenase: a comparison to indoleamine 2,3-dioxygenase, *J. Am. Chem. Soc.* **129**, 15690-15701.
5. Takikawa, O. (2005) Biochemical and medical aspects of the indoleamine 2,3-dioxygenase-initiated L-tryptophan metabolism, *Biochem. Biophys. Res. Commun.* **338**, 12-19.
6. Basran, J., Rafice, S. A., Chauhan, N., Efimov, I., Cheesman, M. R., Ghamsari, L., and Raven, E. L. (2008) A kinetic, spectroscopic, and redox study of human tryptophan 2,3-dioxygenase, *Biochemistry* **47**, 4752-4760.
7. Badyal, S. K., Joyce, M. G., Sharp, K. H., Seward, H. E., Mewies, M., Basran, J., Macdonald, I. K., Moody, P. C., and Raven, E. L. (2006) Conformational mobility in the active site of a heme peroxidase, *J. Biol. Chem.* **281**, 24512-24520.
8. Meunier, B., de Visser, S. P., and Shaik, S. (2004) Mechanism of oxidation reactions catalyzed by cytochrome P450 enzymes, *Chem. Rev.* **104**, 3947-3980.
9. Poljak, A., Grant, R., Austin, C. J., Jamie, J. F., Willows, R. D., Takikawa, O., Littlejohn, T. K., Truscott, R. J., Walker, M. J., Sachdev, P., and Smythe, G. A. (2006) Inhibition of indoleamine 2,3 dioxygenase activity by H<sub>2</sub>O<sub>2</sub>, *Arch. Biochem. Biophys.* **450**, 9-19.

# **Chapter 7**

---

## **Forward perspectives**

No more than five years ago, very little was known about indoleamine 2,3-dioxygenase and tryptophan 2,3-dioxygenase, both of which come from a small family of heme dioxygenase enzymes. To start with, there was no crystal structure for either human IDO or bacterial TDO, and human TDO had never even been isolated. At this time it was generally assumed that a histidine residue was present in the active site of IDO and this proposed histidine residue was thought to have a dual purpose. First, it was thought to be involved in stabilisation of the heme-bound dioxygen, like the globins, especially since IDO and mollusc IDO-like myoglobins shared 37% sequence identity; second, it was assumed that this histidine residue served an essential role in the reaction mechanism by initiating catalysis by deprotonating the indole NH group. The crystal structures of rhIDO and XcTDO were released in 2006 and 2007, respectively: this was extremely helpful because it provided a 'snapshot' of substrate-protein interactions present within the active sites of these enzymes and, ultimately, meant that scientists no longer had to work 'blind-folded'.

The first thing that was noticed when comparing the active sites of rhIDO and XcTDO was that S167 from rhIDO was replaced with H55 in XcTDO (H76 in rhTDO from sequence alignments): but no histidine was present in the active site of rhIDO. This raised questions about how, and if, the ferrous-oxy complex in rhIDO was stabilised (it had only been detected in rabbit IDO) and about the catalytic mechanism. Our studies with active site variant S167A indicates that this residue is not involved in dioxygen binding or catalysis. We proposed that instead a water molecule is likely to stabilise this catalytic intermediate and this was later confirmed by EPR and <sup>1</sup>H ENDOR spectroscopy. In fact, this has been observed for other catalytic heme proteins such as the cytochrome P450s and the heme oxygenase enzymes.

Unexpectedly, we found that the ferrous-oxy complex of S167H was greatly destabilised compared to rhIDO. This behaviour for S167H replicates that in rhTDO, where the ferrous-oxy complex is similarly unstable (1, 2). To our knowledge, this is the first time it has been shown that introducing a histidine residue which has always been thought to play an essential role in stabilising the heme-bound dioxygen (*e.g.* globins) can, in fact, destabilise the ferrous-oxy complex and suggests that the correct positioning and orientation of this residue in oxygen

transport/storage proteins is essential. Interestingly, previous kinetic studies with bacterial TDO have shown that ferrous TDO does not readily bind O<sub>2</sub> in the absence of L-Trp. This led to the proposal that binding of L-Trp and O<sub>2</sub> to form the ternary complex [TDO<sup>II</sup>-Trp-O<sub>2</sub>] was an ordered process with L-Trp binding first followed by O<sub>2</sub> (3, 4). In contrast, rhIDO is able to bind dioxygen in the absence of L-Trp. The reason why TDO enzymes do not have the ability to bind dioxygen and why IDO enzymes can form relatively stable ferrous-oxy complexes, and the importance of this physiologically, still remains to be revealed.

In Chapter 3 we have shown that, in contrast to previous findings (5), 1-methyl-tryptophan (1-Me-Trp) is a substrate for rhIDO and S167A and variants of rhTDO and XcTDO. However, no activity was observed with wild type rhTDO and XcTDO. This was explained by looking closely at the crystal structure of XcTDO which revealed a hydrogen bond (2.6 Å) between the indole NH group of L-Trp and His55, which would lead us to expect a steric clash between His55 and the methyl group of 1-Me-Trp upon binding. Substitution of histidine in rhTDO (H76S) and XcTDO (H55S) allows accommodation of the additional methyl group in the active site, and 1-Me-Trp turnover to occur. We therefore concluded that abstraction of the indole NH group is not essential for catalysis and we proposed an alternative reaction mechanism, based on the chemistry of indoles, which involves direct electrophilic addition to dioxygen, facilitated by the lone pair on the indole N<sup>1</sup> (6). Additional experiments using EPR and <sup>1</sup>H ENDOR spectroscopy were carried out to obtain direct evidence on the hydrogen bonding interactions within the ternary complexes of [rhIDO<sup>II</sup>-Trp-O<sub>2</sub>] and [rhIDO<sup>II</sup>-methylTrp-O<sub>2</sub>]. If proton abstraction of the NH group by the distal oxygen was the initiation step in the reaction mechanism, a hydrogen bond between the two groups would be essential. We found that a hydrogen bond donor to the heme-bound dioxygen was present in both complexes and the most likely candidate for this would be the ammonium group from bound substrate, and not the indole NH group (as this is absent in the [rhIDO<sup>II</sup>-methylTrp-O<sub>2</sub>] complex); this is consistent with the idea that rhIDO catalysis occurs by direct electrophilic addition. Interestingly, a recent Density Functional Theory (DFT) study also found that direct electrophilic addition had a lower activation energy than the base-catalysed deprotonation mechanism (7). More specifically, Chung *et al* found that the NH bond would have to be significantly bent in order to hydrogen bond to

the heme-bound dioxygen and, therefore, disfavoured this mechanism (deprotonation of the NH group by dioxygen). The one area in which this thesis offers little comment is in the later parts of the mechanism, beyond the ternary complex. The literature provides little guidance either, so that this remains an area yet to be explored in depth. The most up-to-date information was published at the end of last year (7). Here, Chung *et al* used the DFT calculations to elucidate the reaction mechanism *after* addition of the distal oxygen to L-Trp and they suggested that the Criegee-type rearrangement pathway requires a very high barrier from the neutral indole intermediate. Instead, the zwitterionic and diradical products generated from the direct addition pathways were predicted to undergo charge or radical recombination to afford the comparatively stable dioxetane intermediate (Figure 7.1). An alternative to the dioxetane formation pathway was also proposed by DFT calculations: homolytic O-O bond cleavage of the radical intermediate followed by oxo attack and facile C<sup>2</sup>-C<sup>3</sup> bond cleavage could occur (Figure 7.1). In fact, we have shown that, if necessary, ferric rhIDO and rhTDO can dioxygenate L-Trp using an alternative oxygen analogue, hydrogen peroxide, with a 2:1 ratio (for rhTDO) and we proposed that the O-O bond is cleaved prior to formation of Compound I. It is not clear why rhIDO did not follow the same ratio of hydrogen peroxide consumption but it is likely to be due to inactivation of the enzyme by hydrogen peroxide (8). It is unlikely, however, that rhIDO and rhTDO *typically* undergo catalysis using this route because this pathway involves the formation of a highly reactive oxyferryl species which may lead to the formation of undesired products (9), and it also requires a number of intermediate steps in product formation, unlike the efficient dioxetane rearrangement pathway. Also, enzymes that typically go through a Compound I intermediate during catalysis are known to have low reduction potentials to stabilise the high oxidation state of the iron *e.g.* cytochrome P450<sub>cam</sub>  $E^\circ = -300 \text{ mV} - \text{substrate}$ ,  $E^\circ = -170 \text{ mV} + \text{substrate}$  (10). The reduction potential for rhIDO was found to be -63 mV and +18 mV in the absence and presence of L-Trp, respectively, and both values are significantly higher compared to the reduction potential of cytochrome P450; furthermore, it is consistent with the fact that the enzyme accesses ferrous oxidation state during catalysis. Collectively, this pathway appears less convincing as a possible mechanistic route using dioxygen.

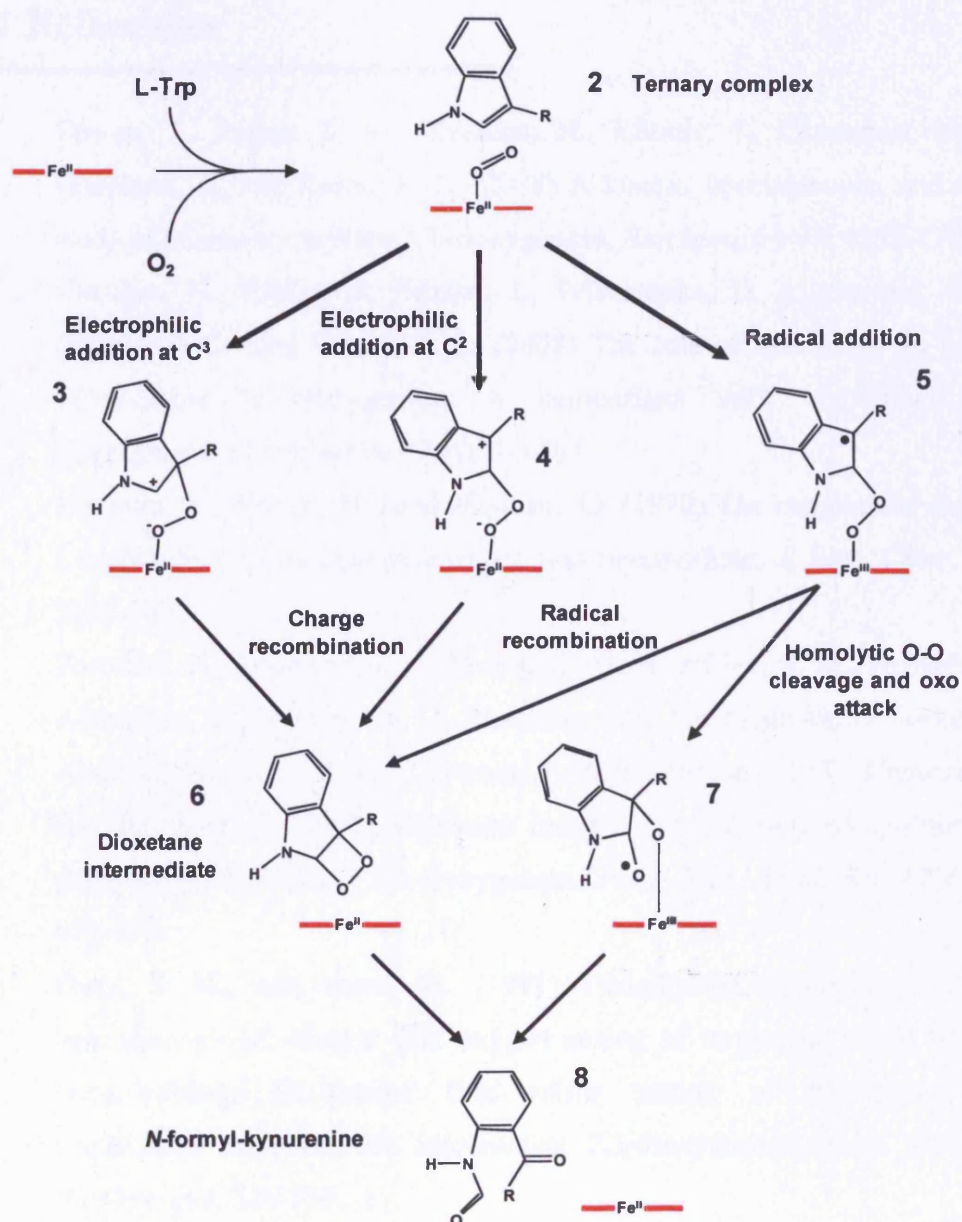


**Figure 7.1:** Reaction mechanism for IDO and TDO dioxygenation proposed by Chung *et al* (7).

Overall, to date no direct experimental evidence has been obtained to confirm any of the mechanistic routes, after initial addition of the distal oxygen to L-Trp *i.e.* dioxetane vs Criegee rearrangement, and further investigations will be necessary before the molecular details that occur further down the mechanism are understood.

## 7.1 References

---

1. Basran, J., Rafice, S. A., Chauhan, N., Efimov, I., Cheesman, M. R., Ghamsari, L., and Raven, E. L. (2008) A kinetic, spectroscopic, and redox study of human tryptophan 2,3-dioxygenase, *Biochemistry* 47, 4752-4760.
2. Chauhan, N., Basran, J., Efimov, I., Svistunenko, D. A., Seward, H. E., Moody, P. C., and Raven, E. L. (2008) The role of serine 167 in human indoleamine 2,3-dioxygenase: a comparison with tryptophan 2,3-dioxygenase, *Biochemistry* 47, 4761-4769.
3. Ishimura, Y., Nozaki, M., and Hayaishi, O. (1970) The oxygenated form of L-tryptophan 2,3-dioxygenase as reaction intermediate, *J. Biol. Chem.* 245, 3593-3602.
4. Forouhar, F., Anderson, J. L., Mowat, C. G., Vorobiev, S. M., Hussain, A., Abashidze, M., Bruckmann, C., Thackray, S. J., Seetharaman, J., Tucker, T., Xiao, R., Ma, L. C., Zhao, L., Acton, T. B., Montelione, G. T., Chapman, S. K., and Tong, L. (2007) Molecular insights into substrate recognition and catalysis by tryptophan 2,3-dioxygenase, *Proc. Natl. Acad. Sci. USA* 104, 473-478.
5. Cady, S. G., and Sono, M. (1991) 1-Methyl-DL-tryptophan, beta-(3-benzofuranyl)-DL-alanine (the oxygen analog of tryptophan), and beta-[3-benzo(b)thienyl]-DL-alanine (the sulfur analog of tryptophan) are competitive inhibitors for indoleamine 2,3-dioxygenase, *Arch. Biochem. Biophys.* 291, 326-333.
6. Chauhan, N., Thackray, S. J., Rafice, S. A., Eaton, G., Lee, M., Efimov, I., Basran, J., Jenkins, P. R., Mowat, C. G., Chapman, S. K., and Raven, E. L. (2009) Reassessment of the Reaction Mechanism for the Heme Dioxygenases, *J. Am. Chem. Soc.* *In press*.
7. Chung, L. W., Li, X., Sugimoto, H., Shiro, Y., and Morokuma, K. (2008) Density Functional Theory Study on a Missing Piece in Understanding of Heme Chemistry: The Reaction Mechanism for Indoleamine 2,3-Dioxygenase and Tryptophan 2,3-Dioxygenase, *J. Am. Chem. Soc.*, 12299-12309.

8. Poljak, A., Grant, R., Austin, C. J., Jamie, J. F., Willows, R. D., Takikawa, O., Littlejohn, T. K., Truscott, R. J., Walker, M. J., Sachdev, P., and Smythe, G. A. (2006) Inhibition of indoleamine 2,3 dioxygenase activity by H<sub>2</sub>O<sub>2</sub>, *Arch. Biochem. Biophys.* 450, 9-19.
9. Skiles, G. L., and Yost, G. S. (1996) Mechanistic studies on the cytochrome P450-catalyzed dehydrogenation of 3-methylindole, *Chem Res Toxicol* 9, 291-297.
10. Meunier, B., de Visser, S. P., and Shaik, S. (2004) Mechanism of oxidation reactions catalyzed by cytochrome P450 enzymes, *Chem. Rev.* 104, 3947-3980.

# **Chapter 8**

---

## **Experimental**

This Chapter describes the experimental methods and techniques used throughout this thesis.

## 8.1 Materials and stock solutions

All chemicals were obtained from commercial sources and used without further purification unless otherwise stated. All glycerol was sterilised. All buffers and solutions were made using deionised water and are listed in Appendix B. Water was of high quality, doubly deionised and was drawn from an Elga PureLab Option (DV35) water purifier, which itself was fed with deionised water. Hydrogen peroxide solutions were freshly prepared by dilution of a 30% (v/v) solution (BDH): exact concentrations were determined using the published absorption coefficient ( $\epsilon_{240} = 39.4 \text{ M}^{-1} \text{ cm}^{-1}$ ) (1). All molecular biology kits and enzymes were used according to manufacturer's protocols.

## 8.2 Recombinant DNA techniques

### 8.2.1 Oligonucleotides

Complementary oligonucleotides (27 - 35 bases in length) were designed to have ~15 bases either side of the residue to be mutated and end in the base G or C. The complementary pairs of oligonucleotides, synthesised and desalted by Invitrogen, contained the appropriate mismatch bases. Sterile water (300  $\mu\text{l}$ ) was added to the lyophilized oligonucleotides, followed by centrifugation using a microcentrifuge (3,000 rpm for 2 minutes) and stored at  $-20 \text{ }^\circ\text{C}$ . The melting temperatures ( $T_m$ ) of primers were calculated according to Equation [8.1],

$$T_m = 81.5 - 16.6 + (0.41(\% \text{ GC}) - (600/L)) \quad \dots[8.1]$$

where % GC is the percentage of the bases G and C in the designed oligonucleotide and L is the length of the oligonucleotide in base pairs.

The complementary pairs of oligonucleotides containing the appropriate mismatch bases (Table II, Appendix C) were used to prepare the variants of rhIDO studied in this thesis.

The S167H, F163A, F164A, F227A and R231K variants of rhIDO were kindly prepared by Dr. Jaswir Basran.

### 8.2.2 Site-directed mutagenesis

Site-directed mutagenesis was carried out using the Quickchange™ mutagenesis kit (Stratagene). Two complementary oligonucleotides (Table II, Appendix C) encoding the desired mutation were synthesised and purified (Invitrogen). Reactions were prepared in thin-walled PCR tubes on ice and in the order listed in Table 8.1 - with the exception of the DNA polymerase (*KOD Hot Start™*), which was added last. Evaporation from the mixture was prevented by addition of 1 drop of PCR Mineral oil (Sigma). The DNA polymerase was supplied in the kit along with 10 × reaction buffer and the dNTP mix and the reaction contained 125 µg of each primer.

**Table 8.1:** Reaction volumes used in site-directed mutagenesis PCR (µl).

	S167A	F226A	F226Y
10× Buffer	5	2.5	5
Template	2.5	1.5	2.5
Primer F	4	0.5	4
Primer R	4	0.5	4
dNTPs	5	0.5	5
MgSO <sub>4</sub>	2	2	2
Water	26.5	14.5	26.5
KOD Hot Start Polymerase	1	0.5	1
Total volume	50	22	50

The PCR tubes were then centrifuged (13,000 rpm, ~10 seconds) and the PCR block (Perkin Elmer, 480 DNA Thermocycler) turned on with the programs set as in Table III, Appendix C. The successful conditions for each PCR experiment are described in Table III, Appendix C. Samples were placed on ice for 2 minutes to cool when the reaction had finished. The methylated and hemimethylated parental DNA were then digested by the addition of *Dpn1* (1  $\mu$ l). Mixtures were then centrifuged (1 minute) and immediately incubated at 37 °C for at least 1 hour to digest the parental DNA. Agarose gel electrophoresis was performed to determine successful reaction samples.

### 8.2.3 Isolation of DNA

An overnight cell culture (5 ml) was harvested using a microcentrifuge (3,000 rpm for 5 minutes). DNA was extracted from this cell culture using a QIAprep® Spin Miniprep kit (Qiagen catalogue number 27104) and the protocol from the kit was followed. The pellet was then resuspended in buffer P1 (250  $\mu$ l, with RNase added, and stored at 4 °C, see Appendix B). Buffer P2 (250  $\mu$ l, see Appendix B) was added and the tube was gently inverted 4-6 times, after which N3 buffer (350  $\mu$ l, see Appendix B) was added and the tube inverted 4-6 times. The tube was centrifuged (13,000 rpm) for 10 minutes. The supernatant was added to a QIAprep spin column and centrifuged for 1 minute at 13,000 rpm and the flow through was discarded. The column was washed with PB buffer (500  $\mu$ l, see Appendix B) and centrifuged at 13,000 rpm for 1 minute discarding the flow through. The column was then washed with PE buffer (750  $\mu$ l, with ethanol added, see Appendix B) and centrifuged for 1 minute at 13,000 rpm discarding the flow through. The column was centrifuged for 1 minute at 13,000 rpm to remove residual ethanol. The column was placed in a clean 1.5 ml microcentrifuge tube with EB buffer (50  $\mu$ l, see Appendix B) in the centre of the column and left standing for 1 minute before centrifuging at 13,000 rpm for 1 minute. The DNA sample obtained was stored at -20 °C. The isolated DNA concentration was calculated using Equation [8.2].

$$A_{260} \times 50 \times \text{Dilution factor} = \text{DNA concentration (ng/\mu l)} \quad \dots [8.2]$$

#### **8.2.4 Agarose gel electrophoresis**

Agarose gels (1.0% w/v) containing ethidium bromide (20  $\mu$ l of 10 mg/ml) were cast on a horizontal bed. Electrophoresis was performed in TAE buffer (see Appendix B) at 80 V and samples (10  $\mu$ l) were mixed with 2  $\mu$ l sample loading buffer prior to being loaded onto the gel. DNA ladder (2  $\mu$ l, Generuler™, 1 kb DNA ladder, Fermentas, catalogue number SM03111) was also loaded onto the gel to aid location of the desired bands. Nucleic acids were visualised by exposing the gel to long wavelength UV radiation on a transilluminator.

#### **8.2.5 DNA sequencing**

DNA sequencing was performed to the entire gene of rhIDO variants to ensure that no spurious mutations had arisen during the mutagenic reactions. All sequencing was carried out by the Protein and Nucleic Acid Chemistry Laboratory (PNAAC), using an Applied Biosystems 3730 automated fluorescent sequencer. The sequencing primers used are listed in Table I in Appendix C.

#### **8.2.6 Transformation of the recombinant DNA into competent *E. coli* cells**

The *DpnI*-treated DNA (15  $\mu$ l) was placed into a prechilled Falcon® 2059 polypropylene tube. Competent cells (XL1-Blue supercompetent/SG cells) (70  $\mu$ l) were gently thawed on ice and, once thawed, were added to the Falcon tube. Immediately after the addition of competent cells, the tube was swirled to mix the solutions and then placed on ice for 30 minutes. A heat shock of the solution at 42 °C, for 45 seconds, was followed by incubation on ice for 2 minutes. Psi broth (500  $\mu$ l) was added to the Falcon tube and the reaction was incubated for 90 minutes at 37 °C, 225 rpm. The cell culture was then pelleted using a bench centrifuge (1,500 rpm for 15 minutes), 400  $\mu$ l of the supernatant media was removed and the cell pellet was resuspended in the remaining supernatant. The cultures were then plated on LB Amp agar plates (for XL1-Blue supercompetent cells) or LB Amp/Kan agar plates (for SG cells). A single colony from the overnight plate was selected and incubated into LB media (10 ml) containing 100  $\mu$ g/ml ampicillin (for XL1-Blue

supercompetent cells) or 100 µg/ml ampicillin/30 µg/ml kanamycin (for SG cells), at 37 °C with vigorous shaking (225 rpm). DNA was isolated from the overnight cultures using the QIAprep® Spin Miniprep kit (Qiagen) and analysed as above using agarose electrophoresis and the DNA was re-sequenced to confirm the mutation.

Glycerol stocks were prepared by placing the overnight cultures (600 µl) into an eppendorf with sterile glycerol (600 µl); after addition of glycerol the eppendorf was vortexed and immediately stored at -80 °C.

### 8.3 Protein expression of rhIDO and variants

Expression of rhIDO was carried out in *E.coli* SG1300 cells (Qiagen, containing pREP4 vector) incorporating pQE30 expression plasmid (Qiagen), (see Appendix D). The *E. coli* cells, sourced from frozen glycerol stocks, were streaked onto LB agar plates which contained ampicillin (100 µg/ml) and kanamycin (30 µg/ml). The plates were kept inverted, overnight at 37 °C. After ~18 hours, the LB agar plates were removed from the incubator and stored at 4 °C until further use. A single colony was used to inoculate 2x YT media (250 ml) containing ampicillin (100 µg/ml) and kanamycin (30 µg/ml), the flask was incubated overnight at 37 °C with shaking at 225 rpm. This formed the starter culture. An aliquot of this starter culture (600 µl) was added to sterile glycerol (600 µl) to form the new glycerol stock, which was then frozen on dry ice and stored at -80 °C. The starter culture (20 ml) was used to inoculate 1 L of 2 x YT medium, which contained the same quantity of antibiotics as the starter culture. These flasks were incubated as before, until the absorbance at 600 nm (OD<sub>600</sub>) reached approximately 0.7 (~2.5 hours). The temperature was adjusted to 27 °C and protein expression was induced with IPTG (100 µl, 1 M), hemin (2 ml, 3.5 mM) (made in 10 mM NaOH) and PMSF (1 ml, 200 mM) (made in isopropanol). The flasks were incubated overnight at 27 °C with shaking at 225 rpm. The cells were pelleted by centrifugation (12 minutes, 6,000 rpm, 4 °C) and the pellets were stored at -80 °C until needed.

## 8.4 Isolation and purification of rhIDO and variants

### 8.4.1 Preparation of *E. coli* lysate

Sonication buffer (50 ml) was added to the frozen cell pellets, followed by the addition of two EDTA-free Complete™ tablets (Roche). The pellets were allowed to thaw in the solution for 15 minutes at room temperature.

Lysozyme (5 mg), DNase I (5 mg) and MgCl<sub>2</sub> (final concentration 20 mM) were added to the cell suspension, which was stirred for 20 minutes at room temperature until the liquid became viscous. The mixture was then sonicated, on ice, on medium power, for 6×1 minute bursts, followed by a cooling period of approximately 1 minute. Lysozyme, DNase I and MgCl<sub>2</sub> (quantities same as above) were added to the suspension for a second time to ensure lysis of all the cells in solution. This solution was stirred for a further 10 minutes. The cell-free extract was obtained through pelleting of the cell debris by centrifugation (16,000 rpm for 60 minutes, 4 °C). The supernatant containing the cell-free extract was decanted and kept at 4 °C for protein purification.

### 8.4.2 Ni-NTA metal-affinity chromatography

A nickel - nitrilotracetic acid (Ni-NTA) agarose column (Qiagen) was used to isolate the hexa-histidine tagged proteins from the supernatant. Ni-NTA resin (10 ml) was packed and flushed through with water (250 ml). The resin was regenerated with 50 ml of regeneration buffer (see Appendix B) and was equilibrated with sonication buffer (300 ml). The cell-free extract was loaded on at a steady flow rate. The column was flushed with sonication buffer to ensure that all cell-free extract had loaded onto the column. The column was then washed with wash buffer (1 L), (see Appendix B). The protein was eluted from the column by the addition of elution buffer (~200 ml) (see Appendix B) and the protein was collected in fractions of ~10 ml. The fractions were pooled together and the protein solution was dialysed overnight, with stirring, against 50 mM Tris/HCl buffer (pH 8.0, 5 L) to remove EDTA from the protein.

### **8.4.3 Reconstitution of rhIDO variants**

Hemin (1.5 equivalents) (in 10 mM NaOH) was mixed with the rhIDO variant protein (100  $\mu$ M) and incubated on ice in the dark for 1-2 hours. Free hemin was removed from the protein by passage through a small pre-packed gel filtration (Bio-Rad 10 DG) column. The eluted protein was concentrated to a minimum volume (~1 ml) using a Centricon (YM30 membrane, Millipore) before FPLC purification.

### **8.4.4 Fast Performance Liquid Chromatography**

Fast Performance Liquid Chromatography (FPLC) was used to obtain ultra pure samples of rhIDO protein. The column was initially flushed with water (double deionised, filtered, 500 ml) followed by equilibration of the column with Tris/HCl buffer (pH 8.0, filtered, 500 ml). The protein had been previously concentrated to a minimum volume (~1 ml). Precipitated protein in the sample was collected by centrifugation using a microcentrifuge (13,000 rpm, 10 minutes). The protein in solution was then transferred into a clean eppendorf and the precipitated protein was discarded. After injection of the protein sample onto the column, the protein was monitored at the wavelength of 280 nm using the Unicorn software (version 4.0, Amersham Pharmacia Biotech). The purified protein was eluted using 50 mM Tris/HCl buffer pH 8.0 with retention time of 240 minutes (at a flow rate of 0.25 ml/min). The purified protein samples were then concentrated using a Centricon (YM30 membrane, Millipore) and were then stored at -80 °C until required.

### **8.4.5 Polyacrylamide gel electrophoresis (SDS-PAGE)**

In order to confirm the purity of the protein, SDS-PAGE was carried out on all protein samples (Figure 8.1). Discontinuous polyacrylamide gels (15%) containing 0.1% SDS and 4% polyacrylamide stacking gel and a mini-Protean II gel system (Bio-Rad) at 0.75 mm thickness were used. Protein samples were prepared for electrophoresis by adding an equal volume of reducing sample application buffer (see Appendix B) and boiling for 6 minutes. The gels were run in SDS running buffer at 180 V until the dye-front reached the end of the gel. The gels were stained by soaking in Coomassie Brilliant Blue R250 (Appendix B) for 1 hour and then

destained by soaking in destaining buffer overnight (Appendix B). Protein markers (Low Molecular Weight Protein Marker) were from Sigma, band sizes were 77.0, 66.0, 45.0, 30.0, 20.1 and 14.4 kDa.

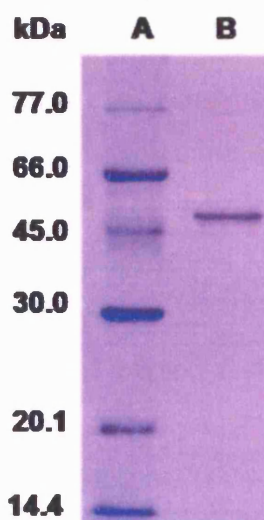


**Figure 8.1:** SDS-page gel of a purified sample of rhIDO after FPLC anion exchange analysis.

## 8.5 Protein expression and purification of rhTDO

The rhTDO construct was transformed into XL1-Blue Super competent cells (Stratagene) and an overnight culture (5 ml) was grown and used for a DNA prep. The rhTDO coding region was sequenced using a standard T7 sequencing primer to check the integrity of the gene.

BL21 (DE3) pLysS cells were freshly transformed with the sequenced DNA and colonies grown on a LB plate containing kanamycin (30  $\mu\text{g/ml}$ ) at 37  $^{\circ}\text{C}$  for 12 hours. A single colony was used to inoculate 100 ml of 2x YT media containing kanamycin (30  $\mu\text{g/ml}$ ) and was grown at 37  $^{\circ}\text{C}$ , overnight, with shaking at 225 rpm. Flasks (10  $\times$  0.5 L) of 2x YT media containing kanamycin (30  $\mu\text{g/ml}$ ) were inoculated with 10 ml of the overnight culture and were left to incubate at 37  $^{\circ}\text{C}$ , with shaking, until the optical density at 600 nm reached a value of  $\sim 0.8$ . After this, they were induced with IPTG (200  $\mu\text{M}$ , final concentration) and 0.5 mL of 3 mM hemin (in 10 mM NaOH) was added. The cell cultures were left to incubate at 25  $^{\circ}\text{C}$ , overnight, with shaking. The cells were pelleted by centrifugation (15 minutes, 6,000 rpm, 4  $^{\circ}\text{C}$ ) and the pellets were stored at -80  $^{\circ}\text{C}$  to aid lysis.

The cell pellets were resuspended in sonication buffer (50 mM sodium phosphate, 300 mM NaCl, 10 mM imidazole, pH 8.0) supplemented with two EDTA-free Complete™ tablets and lysed by the addition of 5 mg of lysozyme and by sonication (6×30 s pulses with 30 s intervals). After sonication, DNase I (5 mg) was added and the suspension stirred for 30 minutes at 4 °C. The lysate was centrifuged at 18 000 rpm for 50 minutes, and the cell-free extract loaded onto a 20 mL column of Ni-NTA Superflow resin (Qiagen) equilibrated in sonication buffer. The resin was washed with 300 mL of wash buffer (50 mM sodium phosphate, 300 mM NaCl, 20 mM imidazole, pH 8.0), and the protein was eluted using a linear gradient ranging from 20 to 250 mM imidazole in 50 mM sodium phosphate, 300 mM NaCl, pH 8.0. Fractions containing rhTDO were pooled and dialysed against 50 mM Tris/HCl buffer, pH 8.0.

Reconstitution of rhTDO was carried out using the same method as rhIDO variants (Section 8.4.3). Enzyme concentrations for rhTDO and H76S were determined using absorption coefficients of  $\epsilon_{408} = 196 \text{ mM}^{-1}\text{cm}^{-1}$  and  $\epsilon_{409} = 105 \text{ mM}^{-1}\text{cm}^{-1}$  respectively. rhTDO and H76S protein samples used for this work were kindly prepared and provided by Dr. Jaswir Basran and Miss Sara Rafice, respectively.

## 8.6 UV-visible spectroscopy

Routine absorbance measurements and spectra were conducted using variable-slit Perkin-Elmer Lambda 14, Lambda 25, Lambda 35 or Lambda 40 (1 mm slit width) UV-visible spectrometers. Temperature control ( $25 \pm 0.1$  °C) was achieved using an internal thermally-jacketed cell holder that was connected to a circulating water bath (NESLAB RTE-200) or Peltier device (Perkin-Elmer, Peltier thermostatted reference holder, BS0510412). A typical 270-700 nm scan was obtained using a scan speed of 960 nm/minute, acquiring at 0.5 nm intervals, using a 0.5 ml, 1 ml or 3 ml (10 mm pathlength) quartz cuvette. Baseline corrections were made against the buffers and solvents used.

## 8.7 Determination of heme absorption coefficients

The absorption coefficient of rhIDO and its variants were determined using the pyridine hemochromagen method according to the protocol of Antonini and Brunori (2). An alkaline pyridine solution was prepared from the addition of pyridine (2 ml), 1 M NaOH (600  $\mu$ l) and distilled water to a final volume of 6 ml. A protein sample with an absorbance of 0.3 – 0.9 in the visible region was required to provide the most reliable data. Pyridine solution (600  $\mu$ l) was added to the protein solution (200  $\mu$ l of known concentration) to form the pyridine-heme complex. After 5 minutes (to allow complete conversion to hemochromagen), the absorption spectrum of the resulting solution (800  $\mu$ l) of oxidised hemochromagen (yellow in colour) was recorded. A single crystal of dithionite was added to the oxidised pyridine hemochromagen solution and the spectrum of the unstable reduced hemochromagen was recorded immediately over the wavelength range 450 – 650 nm. The complete transfer of heme from the protein to the pyridine was checked by determining the absorbance at maximum ( $\lambda = 557$  nm) and minimum ( $\lambda = 540$  nm) wavelengths; a ratio of  $A_{557}/A_{540} = 3.5$  is found for protoheme. Absorption coefficients were calculated knowing the absorption coefficient for the pyridine-protoheme complex ( $\epsilon = 32 \text{ mM}^{-1} \text{ cm}^{-1}$ ) using Equation [8.3]: where A is the absorbance of the stock solution, c is the concentration of the protein,  $\epsilon$  is the molar absorption coefficient and l is the pathlength of the cuvette.

$$A = \epsilon cl \quad \dots[8.3]$$

## 8.8 Ligand-bound derivative spectra

Potassium cyanide, sodium fluoride and sodium azide (Sigma, analytical grade) were used without any further purification and were dissolved in 50 mM Tris/HCl buffer, pH 8.0. Small additions of excess ligand (1 M NaF, KCN or NaN<sub>3</sub> stock solutions) were made to a solution of ferric rhIDO (50 mM Tris/HCl buffer, pH 8.0). The ferrous form of rhIDO and variants were prepared by the addition of microlitre volumes of fresh sodium dithionite solution to ferric enzyme. All solutions were prepared in a glove box (Belle Technology) using anaerobic buffer. The

concentration of the sodium dithionite stock was not determined directly, but was used to provide qualitative reduction of the protein samples.

## 8.9 Ligand binding equilibria

Equilibrium binding parameters were determined by adding microlitre volumes of the appropriately diluted ligand (cyanide or L-Trp) solutions (made up in 50 mM Tris/HCl buffer, pH 8.0) using a Hamilton syringe to a cuvette containing ferric protein (~2-5  $\mu\text{M}$ ), which was mixed by inversion and allowed to equilibrate. The UV-visible spectra were recorded after each addition of ligand. The ligand binding affinity was monitored spectroscopically using absorption at 419 nm (rhIDO and various mutants) and 418 nm (S167H, F163A, F226A, F227A) for cyanide binding and 404 nm (rhIDO and various mutants) and 408 nm (S167H) for L-Trp binding. Binding of L-Trp to ferric rhIDO and S167A in the presence of cyanide was carried out on samples of ferric rhIDO and S167A saturated with 80  $\mu\text{M}$  and 20  $\mu\text{M}$  cyanide, respectively, and absorbance changes were monitored at 416 nm. Equilibrium dissociation constants for binding of cyanide and L-Trp to ferric enzyme, were calculated using Equation [8.4] in the Grafit 5 software package (Grafit version 5.0.3, Erithacus Software Ltd.):

$$\Delta A = \frac{\Delta A_{\infty} [\text{Free}]}{K_D + [\text{Free}]} \quad \dots[8.4]$$

where  $\Delta A$  and  $\Delta A_{\infty}$  are the absorbance changes corresponding to the intermediate and saturating ligand concentrations,  $[\text{Free}]$  is total concentration of unbound ligand and  $K_D$  is the equilibrium dissociation constant.

## 8.10 Xanthine/xanthine oxidase method for determination of Fe<sup>III</sup>/Fe<sup>II</sup> reduction potential

Fe<sup>III</sup>/Fe<sup>II</sup> reduction potentials for rhIDO, S167A and S167H were determined by simultaneous reduction with a dye of known potential (3) according to previous methodology (4). The assay contained xanthine (300  $\mu$ M), xanthine oxidase (50 nM), and enzyme (3-4  $\mu$ M). The buffer (50 mM potassium phosphate buffer, pH 7.0) was made oxygen free using glucose (5 mM), glucose oxidase (50  $\mu$ g/mL) and catalase (5  $\mu$ g/mL). Various dyes were used: nile blue chloride ( $E_{m,7} = -116$  mV), phenosafranin ( $E_{m,7} = -252$  mV), methylene blue ( $E_{m,7} = 11$  mV) and toluidene blue O ( $E_{m,7} = 34$  mV). Absorbance changes corresponding to reduction of heme were measured at the isosbestic points for the dyes: nile blue chloride (406 nm), phenosafranin (407 nm), methylene blue (404 nm) and toluidene blue O (400 nm). Reduction of the dye (at the wavelength at which the absorption change due to heme reduction was negligible) was measured at 635 nm for nile blue chloride, 520 nm for phenosafranin, 664 nm for methylene blue and 637 nm for toluidene blue O.

In all cases, linear Nernst plots for one electron reduction of heme ( $25$  mV  $\ln(E_{ox}/E_{red})$ ) (where  $E_{ox}$  = concentration of oxidized enzyme,  $E_{red}$  = concentration of reduced enzyme) and two-electron reduction of dye ( $12.5$  mV  $\ln(D_{ox}/D_{red})$ ) (where  $D_{ox}$  = concentration of oxidized dye,  $D_{red}$  = concentration of reduced dye) produced the expected slope of 1 across a wide range of potentials, and the intercept gives a reliable value for  $\Delta E_{m,7}$  with an error of  $\pm 2$  mV. UV-visible spectra obtained in all experiments were analyzed using SPECFIT (5) for singular value decomposition based on factor analysis. All potentials reported in this thesis are given versus the normal hydrogen electrode (NHE).

## 8.11 Steady-state kinetics

Reduction of heme iron is required to facilitate the observation of catalytic activity. L-ascorbate (20 mM, Sigma), catalase (10  $\mu$ g, bovine liver, Sigma), and methylene blue (10  $\mu$ M Sigma) are employed in the assay to achieve this. Ascorbate and methylene blue are reducing agents, but also react with dioxygen to form superoxide and peroxide by-products, which can bleach the heme and destroy catalytic activity.

Catalase is therefore present to remove any superoxide or peroxide in solution and hence allows an efficient turnover of substrate (variable concentration). All steady-state assays were carried out in 50 mM Tris/HCl buffer, pH 8.0 (1 ml total volume) (6).

The reaction was initiated by addition of rhIDO (0.3  $\mu\text{M}$ ). The rate of activity was determined by dividing the change in absorbance at 321 nm by the extinction coefficient of *N*-formyl-kynurenine ( $\epsilon_{321} = 3.75 \text{ mM}^{-1} \text{ cm}^{-1}$  (7)). Values for  $k_{\text{cat}}$  were obtained directly from rate ( $\mu\text{M s}^{-1}$ )/[enzyme concentration used in the assay] ( $\mu\text{M}$ ) versus substrate concentration plots of the assay data. All kinetic parameters reported are averages of at least three separate experiments, unless stated otherwise. All kinetic profiles were fitted to the Michaelis-Menten Equation [8.5].

$$V = V_{\text{max}} \frac{[S]}{[S] + K_M} \quad \dots [8.5]$$

Where,  $V_{\text{max}}$  ( $k_{\text{cat}}$ ) is the maximal rate,  $K_M$ , the Michaelis constant is the concentration at which the reaction rate is half its maximal value and  $[S]$  is the substrate concentration.

## 8.12 Transient-state kinetics

Transient-state kinetics were performed using a SX.18 MV microvolume stopped flow spectrophotometer (Applied Photophysics) housed in an anaerobic glove box (Belle Technology,  $[\text{O}_2] < 5 \text{ ppm}$ ) fitted with a Neslab RTE200 circulating water bath. Reported values of  $k_{\text{obs}}$  were an average of at least four measurements (50 mM Tris/HCl buffer, pH 8.0, 25.0  $^\circ\text{C}$ ).

### 8.12.1 Kinetics of binding of L-Trp, cyanide and $\text{O}_2$ to rhIDO and its variants

All reactions were carried out under pseudo-first-order conditions; final (reaction cell) protein concentrations used were 0.5-1  $\mu\text{M}$ . Absorbance changes accompanying L-Trp and cyanide binding were monitored at 404 nm for rhIDO and

S167A, and 408 nm for S167H. For each enzyme-ligand complex the apparent association rate constant ( $k_{\text{on}}$ ) was obtained from the slope of the linear dependence of the observed rate constant,  $k_{\text{obs}}$ , against ligand concentration; the dissociation rate constant ( $k_{\text{off}}$ ) was obtained from the ordinate intercept of this plot (Equation [8.6]).

$$k_{\text{obs}} = k_{\text{on}}[\text{L}] + k_{\text{off}} \quad \dots[8.6]$$

For O<sub>2</sub> binding experiments, anaerobic conditions were obtained by extensive N<sub>2</sub>-equilibration of the buffer and reactions initiated by mixing anaerobic solutions of enzyme (typically 2 μM, pre-reduced with dithionite) with an equal volume of buffer containing O<sub>2</sub> at different concentrations (0.12 – 1.2 mM). The ferrous forms of rhIDO and variants were prepared by the addition of microlitre volumes of fresh sodium dithionite solution to ferric enzyme present in anaerobic buffer in an air-tight cuvette until no further change in the spectrum was observed. All solutions were prepared in a glove box (Belle Technology) using anaerobic buffer. The concentration of the sodium dithionite stock was not determined directly, but was used to provide qualitative reduction of the protein samples.

Formation of the ferrous-oxy complex was monitored at 416 nm in single mixing mode. Formation of the ferrous-oxy rhIDO complex was also monitored in the presence of 1-Me-Trp (300 μM) at the same wavelength. The rate constant for the auto-oxidation of the ferrous rhIDO-oxygen complex ( $k_{\text{auto}}$ ) was monitored at 576 nm over a longer timescale in order to monitor the complete conversion of the ferrous-oxy complex to the ferric rhIDO derivative.

### 8.12.2 Detection of intermediate species during reaction of reduced enzyme with L-Trp and O<sub>2</sub>

Time-dependent spectral changes observed during steady-state turnover by rhIDO were examined by stopped-flow spectroscopy using a photodiode array detector and X-SCAN software (Applied Photophysics). The sequential mixing mode of the stopped-flow apparatus was used for these experiments. This involved first mixing a solution of ferrous enzyme (1.5 μM) with O<sub>2</sub> (250 μM) with a 1 s (500 ms for S167H) ageing time to allow for formation of the ferrous-oxy complex, followed by mixing of the second substrate, L-Trp (50 μM and 100 μM, respectively for rhIDO

and S167H) (Figure 8.2(A)). The reaction was then monitored for 50 s for rhIDO and 200 s for S167H and the spectral changes recorded. The sequential mixing experiment was also carried out where ferrous enzyme was incubated with L-Trp first and then mixed with O<sub>2</sub> (Figure 8.2(B)) and the spectral changes accompanying the reaction monitored again.

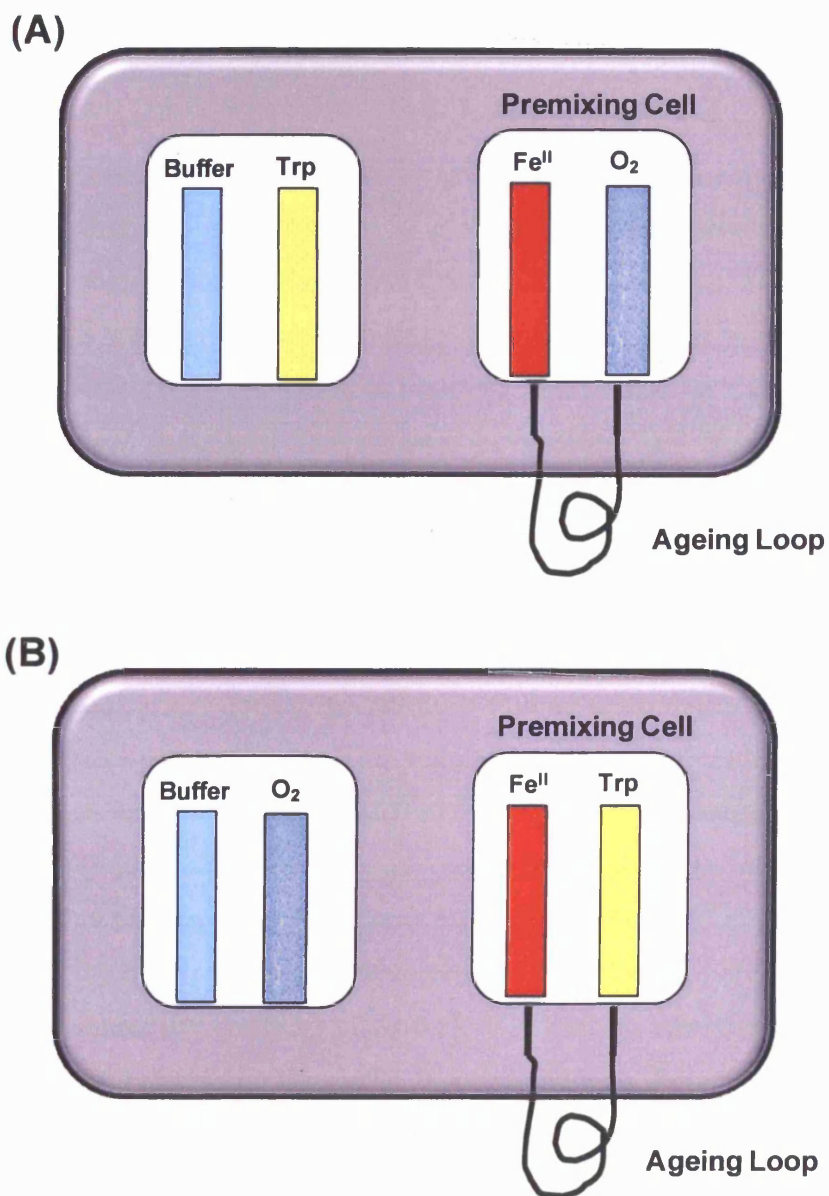


**Figure 8.2:** Set-up of the sequential mixing mode of the stopped-flow apparatus.

### 8.12.3 Preparation of O<sub>2</sub>-saturated solutions

Anaerobic solutions of Tris/HCl buffer (50 mM) containing various concentrations of O<sub>2</sub> were prepared by mixing different volumes of buffer saturated with O<sub>2</sub> gas at 25.0 °C with anaerobic buffer. Saturation was achieved by bubbling O<sub>2</sub> for 1 hour in a septum sealed flask at 25 °C. Final O<sub>2</sub> concentrations were calculated on the basis of a saturating concentration of O<sub>2</sub> of ~ 1.2 mM at 25 °C and 1 atm pressure.

## 8.13 Liquid Chromatography Mass Spectrometry

LC-MS of the reaction products produced by rhIDO, rhTDO and its mutants were carried out by Dr. Graham Eaton (Department of Chemistry, University of Leicester) using selected ion monitoring. A Micromass Quatro LC spectrometer was used and the sample was run with acetonitrile/H<sub>2</sub>O (0.1% formic acid) as the solvent (in the ratio of 10:90 or 20:80) at a flow rate of 0.3 ml/min. A C18 aqua (2 × 250 mm × 5 μM) column was used to separate the reactants and products and the UV detector monitored all reactions at 321 nm.

### 8.13.1 Reaction of rhIDO, rhTDO and its variants with 1-Me-Trp

LC-MS analysis was carried out on the products formed upon reaction of rhIDO, rhTDO and its variants with 1-Me-Trp. This was carried out by performing a steady-state reaction, which would allow accumulation of the product. Ascorbate (20 mM), methylene blue (10 μM), catalase (10 μg), 1-Me-Trp (1.5 mM), and enzyme (typically 1-5 μM) were employed to achieve this. After addition of all the steady-state components, the reaction was allowed to proceed for ~ 1 hour, although longer timescales were required for rhTDO (~ 3 hours). The reaction was stopped by the addition of 30% (v/v) trichloroacetic acid. The sample was then centrifuged to collect degraded protein and the supernatant was then filtered using a Millipore 0.45 μM filter unit to ensure no protein remained in solution. Samples were then subjected to LC-MS analysis.

### 8.13.2 Reaction of rhIDO and rhTDO with H<sub>2</sub>O<sub>2</sub> and L-Trp

Experiments using ferric enzyme (either rhIDO or rhTDO), H<sub>2</sub>O<sub>2</sub> and L-Trp were all carried out in an anaerobic environment (glove box, [O<sub>2</sub>] < 5 ppm) and all solutions were made oxygen free by extensive N<sub>2</sub>-equilibration. In a typical reaction, ferric enzyme (~2-5 μM), H<sub>2</sub>O<sub>2</sub> (~40 equivalents) and L-Trp (~100 μM) were incubated in a sealed vessel for ~ 1 hour. The reaction was stopped by the addition of 30% (v/v) trichloroacetic acid. The sample was then centrifuged to collect degraded protein and the supernatant was then filtered using a Millipore 0.45 μM filter unit to ensure no protein remained in solution. If necessary, samples were subjected to LC-MS analysis.

### 8.14 EPR and ENDOR spectroscopy

All EPR spectra presented in Chapter 2 were measured using a Bruker EMX EPR spectrometer (X-band) at a modulation frequency of 100 kHz and were collected by Dr. Dimitri Svistunenko (Department of Chemistry, University of Essex). Accurate *g*-values were obtained using the built-in microwave frequency counter and a 2,2-diphenyl-1-picrylhydrazyl powder standard (*g* = 2.0037 ± 0.0002 (8)). A spherical high quality Bruker resonator SP9703 and an Oxford Instruments liquid helium system were used to measure low temperature EPR spectra. Spectra for blank samples (frozen water) were subtracted from the corresponding protein spectrum to eliminate the base line caused by the resonator's walls, quartz insert, or quartz EPR tube. Ferric rhIDO, S167A and S167H (80 μM) samples were prepared in 50 mM Tris/HCl buffer, pH 8.0. Tubes containing protein solutions or water (blanks) were frozen in cold methanol. Once frozen, samples were transferred to liquid nitrogen (77 K) where they were stored before measurements.

All X-band EPR spectra presented in Chapter 4 were recorded on a Bruker ESP 300 spectrometer equipped with an Oxford Instruments ESR 910 He flow cryostat. EPR/ENDOR (35 GHz) spectra were recorded with a modified Varian E-109 spectrometer and were recorded at 2 K. EPR and <sup>1</sup>H ENDOR spectra of all protein samples presented in Chapter 4 were collected by Dr. Roman Davydov (Department of Chemistry, Northwestern University). All protein samples were concentrated in 50 mM potassium phosphate buffer (pH 8.0) using a centricon concentrator (30000

MW cutoff) to 2 mM and then diluted by the addition of glycerol and substrate. The ferric-Trp complex was prepared by the addition of L-Trp (40 mM stock solution, 20  $\mu$ L) to ferric rhIDO (2 mM, 20  $\mu$ L) followed by the addition glycerol (40% stock, 40  $\mu$ L) to yield a final protein concentration of 0.5 mM. Ferrous-oxy complexes were generated at  $\sim -40$  °C in a chest freezer box and samples were gently bubbled with O<sub>2</sub> to reduced rhIDO (0.5 mM). Reduced rhIDO was prepared by the addition of microlitre volumes of sodium dithionite solution to ferric rhIDO present in anaerobic buffer in an air-tight cuvette until no further change in the spectrum was observed. The concentration of the sodium dithionite stock was not determined directly, but was used to provide qualitative reduction of the protein samples.

For preparation of the ternary complexes, either L-Trp or 1-Me-Trp (16 mM stock solution, 25  $\mu$ L) was added to the protein sample (2 mM, 25  $\mu$ L), followed by the addition of glycerol (90%, 50  $\mu$ L) to yield a final protein concentration of 0.5 mM. Sodium dithionite titrations were then carried out on the ferric-Trp and the ferric-MeTrp complexes until no further spectral changes were observed.

The sample was then immediately frozen in liquid nitrogen and placed in a dalek which was then shipped to Northwestern University. All ferrous protein samples were prepared in an anaerobic glove box (Belle Technology, [O<sub>2</sub>] < 5 ppm). Moments before EPR and ENDOR spectra were collected, O<sub>2</sub> was gently bubbled into the ferrous, ferrous-Trp, and ferrous-MeTrp complexes at  $\sim -40$  °C.

## 8.15 Crystal screens

All screens for the crystallisation of rhIDO were carried out using the sitting drop method (Figure 8.3) and using 24 well plates (4  $\times$  6 Cryschem plates with 1 ml reservoirs, Hampton Research). Screening of crystallisation conditions used the sparse-matrix factorial search method (9) using commercially available kits (Crystal screen (I) and Membfac crystal screens, Hampton Research, Appendix E). The screens were prepared in a temperature controlled room at 15 °C. The protein solution (38 mg/ml in deionised water) was kept on ice throughout. Ferric and ferrous protein was used with the commercially available kits. Ferrous protein was prepared by the addition of sodium dithionite and all steps were performed in a Belle

Technology anaerobic glove box ( $[O_2] < 5$  ppm). Excess sodium dithionite was removed by gel filtration (Sephadex G25 column) before crystallization.

Screens were set up using the crystallisation conditions that have been published for ferric rhIDO (10). The screens were initially set up using ferrous protein (in 10 mM Mes pH 6.5, 25 mM NaCl, 2 mM L-Trp), 200 mM ammonium acetate, 100 mM bis-tris propane pH 8.0 to 9.3, 4-26% polyethylene glycol and 2 mM L-Trp (Tables 8.2 and 8.3). Screens were also set up using 100 mM CHES pH 8.6 to 10 which was used in replacement for bis-tris propane (Tables 8.2 and 8.3).

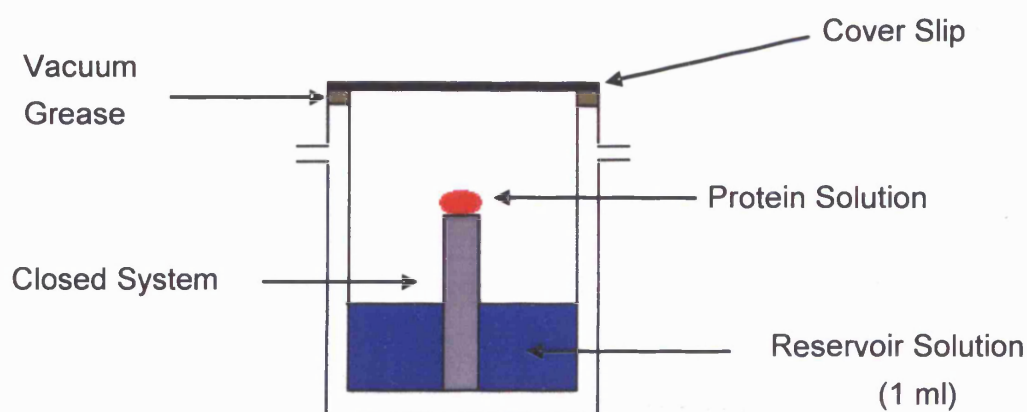


**Figure 8.3:** Diagrammatic representation of the sitting drop method.

Unfortunately, all crystallisation attempts using ferrous enzyme were unsuccessful. As a result, additional screens were set up using ferric rhIDO based around those used for ferrous rhIDO. Screens were set up using ferric protein (in 10 mM Mes pH 6.5, 25 mM NaCl, 2 mM L-Trp), 200 mM ammonium acetate, 100 mM bis-tris propane pH 8.0 to 9.0 or 100 mM CHES pH 9.0 to 9.5, 10-32% polyethylene glycol and 2 mM L-Trp (Tables 8.4 and 8.5). All the well solutions were prepared from the same stock solutions and all the buffer pHs were checked as 1 M stock solutions.

Protein solution (2  $\mu$ l) was added to the first twelve of the small drop wells (6 x 2). Well solution (2  $\mu$ l) was added to the drop of protein solution, and the first twelve wells sealed with clear postal tape making sure there were no air bubbles. The process was then repeated to complete the plate. The wells contained 1 ml of

reservoir solution. The screens were left in temperature controlled rooms with no vibrations. The above conditions gave no crystals.

**Table 8.2:** Screen conditions using ferrous rhIDO.

Bis-tris propane/CHES 100 mM pH	Polyethylene glycol (%)					
	4	6	8	10	12	14
8.0/8.6						
8.5/9.0						
9.0/9.5						
9.3/10.0						

**Table 8.3:** Screen conditions using ferrous rhIDO.

Bis-tris propane/CHES 100 mM pH	Polyethylene glycol (%)					
	16	18	20	22	24	26
8.0/8.6						
8.5/9.0						
9.0/9.5						
9.3/10.0						

**Table 8.4:** Screen conditions using ferric rhIDO.

Bis-tris propane/CHES	Polyethylene glycol (%)					
	10	12	14	16	18	20
100 mM						
pH						
8.0/9.0						
8.0/9.0						
8.5/9.5						
9.0/9.5						

**Table 8.5:** Screen conditions using ferric rhIDO.

Bis-tris propane/CHES	Polyethylene glycol (%)					
	22	24	26	28	30	32
100 mM						
pH						
8.0/9.0						
8.0/9.0						
8.5/9.5						
9.0/9.5						

## 8.16 References

---

1. Nelson, D. P., and Kiesow, L. A. (1972) Enthalpy of decomposition of hydrogen peroxide by catalase at 25 degrees C (with molar extinction coefficients of H<sub>2</sub>O<sub>2</sub> solutions in the UV), *Anal. Biochem.* 49, 474-478.
2. Antonini, M., and Brunori, E. (1971) *Hemoglobin and Myoglobin and their reactions with ligands*, North Holland Publishers, Amsterdam.
3. Massey, V. (1991) Flavins and Flavoproteins (Curti, B., Ronchi, S., and Zanetti, G., Eds.) pp 59-66, *Walter de Gruyter & Co., New York*.
4. Efimov, I., Papadopoulou, N. D., McLean, K. J., Badyal, S. K., Macdonald, I. K., Munro, A. W., Moody, P. C., and Raven, E. L. (2007) The Redox Properties of Ascorbate Peroxidase, *Biochemistry* 46, 8017-8023.
5. Binstead, R. A., and Zuberbuehler, A. D. Spectrum Software Associates, Chapel Hill, NC.
6. Takikawa, O., Kuroiwa, T., Yamazaki, F., and Kido, R. (1988) Mechanism of interferon-gamma action. Characterization of indoleamine 2,3-dioxygenase in cultured human cells induced by interferon-gamma and evaluation of the enzyme-mediated tryptophan degradation in its anticellular activity, *J. Biol. Chem.* 263, 2041-2048.
7. Shimizu, T., Nomiya, S., Hirata, F., and Hayaishi, O. (1978) Indoleamine 2,3-dioxygenase. Purification and some properties, *J. Biol. Chem.* 253, 4700-4706.
8. Weil, J. A., Bolton, J. R., and Wertz, J. E. (1994) *Electron paramagnetic resonance: Elementary theory and practical applications.*, Wiley. xxi, New York.
9. Collaborative Computational Project, N. (1994) The CCP4 suite: programs for protein crystallography, *Acta Cryst. D* 50, 760-763.
10. Sugimoto, H., Oda, S., Otsuki, T., Hino, T., Yoshida, T., and Shiro, Y. (2006) Crystal structure of human indoleamine 2,3-dioxygenase: catalytic mechanism of O<sub>2</sub> incorporation by a heme-containing dioxygenase, *Proc. Natl. Acad. Sci. USA* 103, 2611-2616.

# **Appendix A**

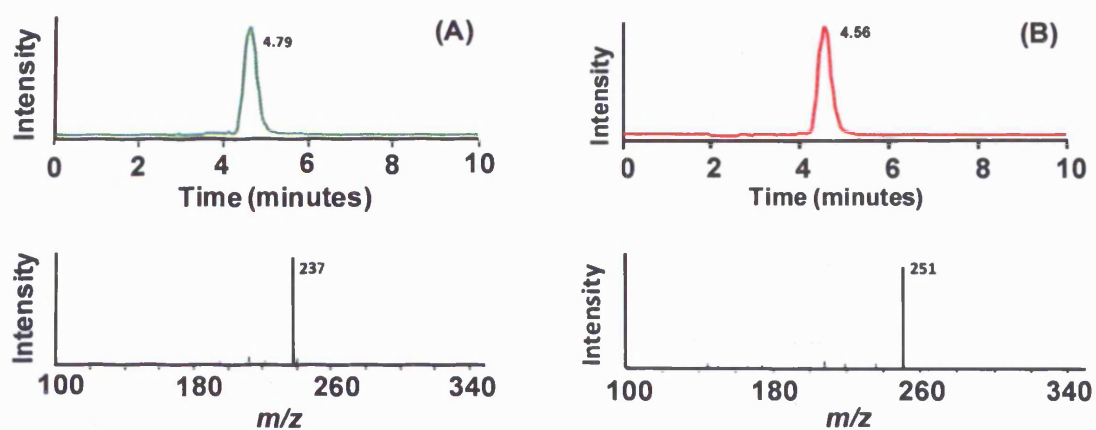


**Figure 1:** LC-MS analysis of products obtained on reaction of S167A with L-Trp (Panel A) and 1-Me-Trp (Panel B). Panel A: (top) elution profile for selected ion chromatogram with  $m/z$  of 237 and (bottom) the corresponding positive ESI mass spectrum for the product eluted at 4.79. Panel B: (top) elution profile for selected ion chromatogram with  $m/z$  of 251 and (bottom) the corresponding positive ESI mass spectrum for the product eluted at 4.56.

# Appendix B

**Destain (SDS-PAGE)**

7.5% acetic acid, 5% methanol

**DNA gel mix**

1.4 g agarose, 200 ml TAE, 20 µl ethidium bromide

**EB Buffer (Qiagen)**

10 mM Tris-HCl, pH 8.5

**Elution Buffer**

50 mM potassium phosphate, pH 8.0

300 mM potassium chloride

100 mM EDTA

made up to 1 L with water

**FPLC grade**

50 mM Tris/HCl, pH 8

**LB-Amp/Kan agar plates**

20 g LB-Broth, 2 g glucose and water to 500 ml. 15 g agar and water to 500 ml

Both solutions sterilised, mixed and supplemented with 100 mg/ml ampicillin and 30 mg/ml kanamycin

**LB Media**

Per 10 L: 210 g LB-Broth, 2.10 g glucose

**N3 Buffer (Qiagen)**

Contains guanidine hydrochloride and acetic acid

**P1 Buffer (Qiagen)**

Alkaline buffer that contains RNase

**P2 Buffer (Qiagen)**

Contains sodium hydroxide

**PB Buffer (Qiagen)**

Contains guanidine hydrochloride and isopropanol

**PE Buffer (Qiagen)**

Contains ethanol

**Pyridine base solution**

1.2 ml 1 M NaOH, 4 ml pyridine, 6.8 ml water

**Regeneration buffer**

114.6 g guanidine hydrochloride

40 ml acetic acid

160 ml water

**Resolve buffer**

(1.5 M Tris with 0.4 % SDS, pH 8.8)

30.3 g Tris base in 100 ml water, adjusted to pH 8.8, plus 0.66 g SDS and made up to 166 ml with water

**Resolving gel mix**

3.25 ml acrylamide solution, 1.9 ml resolve buffer, 2.4 ml water, 25  $\mu$ l 10 % APS, 12.5  $\mu$ l TEMED (add TEMED last and proceed immediately)

**SDS Running buffer (SDS-PAGE)**

25 mM Tris-HCl

192 mM glycine

0.1% w/v SDS

**Sonication Buffer**

50 mM potassium phosphate buffer pH 8.0

300 mM potassium chloride

2 EDTA-free Complete™ tablets (Roche)

**Stacking buffer**

(0.5 M Tris with 0.4 % SDS, pH 6.8)

6.05 g Tris base in 40 ml water, adjusted to pH 6.8, plus 0.4 g SDS and made up to 100 ml with water

**Stacking gel mix**

325  $\mu$ l acrylamide solution, 625  $\mu$ l stacking buffer, 1.525 ml water, 2  $\mu$ l saturated bromophenol blue, 12.5  $\mu$ l 10% APS, 6.5  $\mu$ l TEMED (add TEMED last and proceed immediately)

**Staining Buffer (SDS-PAGE)**

30% v/v methanol, 12% w/v trichloroacetic acid, 0.01% w/v Coomassie Blue R250, 10% w/v sulphosalicylic acid

**Storing Buffer**

50 mM Tris/HCl pH 7.4

**2 x YT media**

Per 10 L: 310g 2 x YT media

**50× TAE Buffer (Agarose gel electrophoresis)**

242 g Tris base, 37.1 g glacial acetic acid, 100 ml of 0.5 M EDTA, made up to 1 L with deionised water

**Wash Buffer**

50 mM potassium phosphate pH 6.0

300 mM potassium chloride

# Appendix C

**Table I.** The forward and reverse oligonucleotides used for sequencing.

Sequencing Primer	T <sub>m</sub> (°C)	% GC
PQEF 5' CGG ATA ACA ATT TCA CAC AG 3'	48	40
PQER 5' GTT CTG AGG TCA TTA CTG G 3'	49	47

**Table II.** The forward and reverse oligonucleotides used to generate the variants of rhIDO. The mismatched codons are highlighted in red.

Variant	T <sub>m</sub> (°C)	% GC
<b>S167A rhIDO</b> Forward: 5' GGATTCTTCCTGGTC <b>GCT</b> CTATTGGTG 3' Reverse: 5' CACCAATAG <b>AGCG</b> ACCAGGAAGAATCC 3'	68	51
<b>F226A rhIDO</b> Forward: 5' GTGAACCCAAAAGCA <b>GCT</b> TTTCAGTGTTCCTTCGC 3' Reverse: 5' GCGAAGAACACTGAA <b>AGCT</b> GTCTTTTGGGTTCCAC 3'	66	48
<b>F226Y rhIDO</b> Forward: 5' GTGAACCCAAAAGCA <b>TACT</b> TTTCAGTGTTCCTTCGC 3' Reverse: 5' GCGAAGAACACTGAA <b>GTAT</b> GTCTTTTGGGTTCCAC 3'	65	45

**Table III.** Temperature cycler program for site directed mutagenesis.**(A) S167A rhIDO**

Number of Cycles	Temperature (°C)	Time (s)
1	95	30
16	95	30
	63	60
	72	300
1	72	420

**(B) F226A rhIDO**

Number of Cycles	Temperature (°C)	Time (s)
1	95	30
16	95	30
	61	60
	72	300
1	72	600

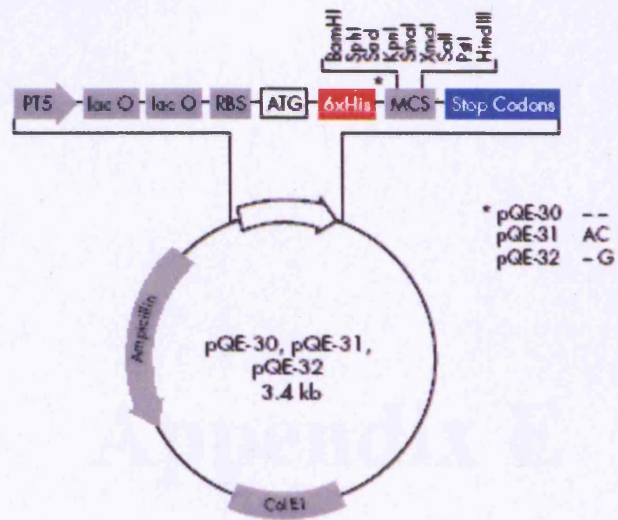
---

**(C) F226Y rhIDO**

<b>Number of Cycles</b>	<b>Temperature (°C)</b>	<b>Time (s)</b>
1	95	30
16	95	30
	60	60
	72	300
1	72	420

# **Appendix D**

## Vector pQE-30:



# **Appendix E**

---

**Crystal screen I (Hampton Research)**

1	0.02 M Calcium chloride dihydrate	0.1 M Sodium acetate trihydrate pH 5.0	30 % v/v (+/-)-2-Methyl-2,4-pentanediol
2	None	None	0.4 M Potassium sodium tartrate tetrahydrate
3	None	None	0.4 M Ammonium phosphate monobasic
4	None	0.1 M Tris hydrochloride pH 9.0	2 M Ammonium sulfate
5	0.2 M Sodium citrate tribasic dihydrate	0.1 M HEPES sodium pH 8.0	30 % v/v (+/-)-2-Methyl-2,4-pentanediol
6	0.2 M Magnesium chloride hexahydrate	0.1 M Tris hydrochloride pH 9.0	30 % w/v Polyethylene glycol 4,000
7	None	0.1 M Sodium cacodylate trihydrate pH 7.0	1.4 M Sodium acetate trihydrate
8	0.2 M Sodium citrate tribasic dihydrate	0.1 M Sodium cacodylate trihydrate pH 7.0	30 % v/v 2-Propanol
9	0.2 M Ammonium acetate	0.1 M Sodium citrate tribasic dihydrate pH 6.0	30 % w/v Polyethylene glycol 4,000
10	0.2 M Ammonium acetate	0.1 M Sodium acetate trihydrate pH 5.0	30 % w/v Polyethylene glycol 4,000
11	None	0.1 M Sodium citrate tribasic dihydrate pH 6.0	1 M Ammonium phosphate monobasic
12	0.2 M Magnesium chloride hexahydrate	0.1 M HEPES sodium pH 8.0	30 % v/v 2-Propanol
13	0.2 M Sodium citrate tribasic dihydrate	0.1 M Tris hydrochloride pH 9.0	30 % v/v Polyethylene glycol 400
14	0.2 M Calcium chloride dihydrate	0.1 M HEPES sodium pH 8.0	28 % v/v Polyethylene glycol 400
15	0.2 M Ammonium sulfate	0.1 M Sodium cacodylate trihydrate pH 7.0	30 % w/v Polyethylene glycol 8,000
16	None	0.1 M HEPES sodium pH 8.0	1.5 M Lithium sulfate monohydrate
17	0.2 M Lithium sulfate monohydrate	0.1 M Tris hydrochloride pH 9.0	30 % w/v Polyethylene glycol 4,000
18	0.2 M Magnesium acetate tetrahydrate	0.1 M Sodium cacodylate trihydrate pH 7.0	20 % w/v Polyethylene glycol 8,000
19	0.2 M Ammonium acetate	0.1 M Tris hydrochloride pH 9.0	30 % v/v 2-Propanol

## Appendix E

20	0.2 M Ammonium sulfate	0.1 M Sodium acetate trihydrate pH 5.0	25 % w/v Polyethylene glycol 4,000
21	0.2 M Magnesium acetate tetrahydrate	0.1 M Sodium cacodylate trihydrate pH 7.0	30 % v/v (+/-)-2-Methyl-2,4-pentanediol
22	0.2 M Sodium acetate trihydrate	0.1 M Tris hydrochloride pH 9.0	30 % w/v Polyethylene glycol 4,000
23	0.2 M Magnesium chloride hexahydrate	0.1 M HEPES sodium pH 8.0	30 % v/v Polyethylene glycol 400
24	0.2 M Calcium chloride dihydrate	0.1 M Sodium acetate trihydrate pH 5.0	30 % v/v 2-Propanol
25	None	0.1 M Imidazole pH 7.0	1 M Sodium acetate trihydrate
26	0.2 M Ammonium acetate	0.1 M Sodium citrate tribasic dihydrate pH 6.0	30 % v/v (+/-)-2-Methyl-2,4-pentanediol
27	0.2 M Sodium citrate tribasic dihydrate	0.1 M HEPES sodium pH 8.0	20 % v/v 2-Propanol
28	0.2 M Sodium acetate trihydrate	0.1 M Sodium cacodylate trihydrate pH 7.0	30 % w/v Polyethylene glycol 8,000
29	None	0.1 M HEPES sodium pH 8.0	0.8 M Potassium sodium tartrate tetrahydrate
30	0.2 M Ammonium sulfate	None	30 % w/v Polyethylene glycol 8,000
31	0.2 M Ammonium sulfate	None	30 % w/v Polyethylene glycol 4,000
32	None	None	2 M Ammonium sulfate
33	None	None	4 M Sodium formate
34	None	0.1 M Sodium acetate trihydrate pH 5.0	2 M Sodium formate
35	None	0.1 M HEPES sodium pH 8.0	0.8 M Sodium phosphate monobasic monohydrate
36	None	0.1 M Tris hydrochloride pH 9.0	8 % w/v Polyethylene glycol 8,000
37	None	0.1 M Sodium acetate trihydrate pH 5.0	8 % w/v Polyethylene glycol 4,000
38	None	0.1 M HEPES sodium pH 8.0	1.4 M Sodium citrate tribasic dihydrate
39	None	0.1 M HEPES sodium pH 8.0	2 % v/v Polyethylene glycol 400

40	None	0.1 M Sodium citrate tribasic dihydrate pH 8.0	20 % v/v 2-Propanol
41	None	0.1 M HEPES sodium pH 8.0	10 % v/v 2-Propanol
42	0.05 M Potassium phosphate monobasic	None	20 %w/v polyethylene glycol
43	None	None	30 % w/v polyethylene glycol 1500
44	None	None	0.2 M magnesium formate dihydrate
45	0.2 M Zinc acetate dihydrate	0.1 M Sodium cacodylate trihydrate pH 7.0	18 % w/v Polyethylene glycol 8,000
46	0.2 M Calcium acetate hydrate	0.1 M Sodium cacodylate trihydrate pH 7.0	18 % w/v Polyethylene glycol 8,000
47	None	0.1 M Sodium acetate trihydrate pH 5.0	2 M Ammonium sulfate
48	None	0.1 M Tris hydrochloride pH 9.0	2 M Ammonium phosphate monobasic
49	1 M Lithium sulfate monohydrate	None	2 % w/v Polyethylene glycol 8,000
50	0.5 M Lithium sulfate monohydrate		15 % w/v Polyethylene glycol 8,000

## Crystal screen I (Hampton Research)

1	0.1 M sodium chloride	0.1 M sodium acetate trihydrate pH 4.6	12% v/v MPD
2	0.1 M zinc acetate dihydrate	0.1 M sodium acetate trihydrate pH 4.6	12% w/v polyethylene glycol 4000
3	0.2 M ammonium sulfate	0.1 M sodium acetate trihydrate pH 4.6	10% w/v polyethylene glycol 4000
5	None	0.1 M sodium acetate trihydrate pH 4.6	12% w/v polyethylene glycol 4000
6	None	0.1 M sodium acetate trihydrate pH 4.6	1 M ammonium sulfate
7	None	0.1 M sodium acetate trihydrate pH 4.6	1 M magnesium sulfate heptahydrate
8	0.1 M magnesium chloride hexahydrate	0.1 M sodium acetate trihydrate pH 4.6	18% v/v polyethylene glycol 400
10	0.1 M sodium chloride	0.1 M sodium acetate trihydrate pH 4.6	12% w/v polyethylene glycol 6000
11	0.1 M magnesium chloride hexahydrate	0.1 M sodium acetate trihydrate pH 4.6	12% w/v polyethylene glycol 6000
13	0.1 M lithium sulfate monohydrate	0.1 M tri-sodium citrate dihydrate pH 5.6	12% w/v polyethylene glycol 4000
15	0.1 M sodium chloride	0.1 M tri-sodium citrate dihydrate pH 5.6	12% v/v MPD
16	None	0.1 M tri-sodium citrate dihydrate pH 5.6	1 M magnesium sulfate heptahydrate
17	0.1 M sodium chloride	0.1 M tri-sodium citrate dihydrate pH 5.6	12% w/v polyethylene glycol 4000
18	0.1 M lithium sulfate monohydrate	0.1 M tri-sodium citrate dihydrate pH 5.6	12% w/v polyethylene glycol 6000
19	0.1 M magnesium chloride hexahydrate	0.1 M tri-sodium citrate dihydrate pH 5.6	4% v/v MPD
20	None	0.1 M tri-sodium citrate dihydrate pH 5.6	0.1 M sodium chloride
21	0.1 M lithium sulfate monohydrate	0.1 M tri-sodium citrate dihydrate pH 5.6	4% v/v polyethylene glycol 400
22	None	0.1 M ADA pH 6.5	1 M ammonium sulfate
23	0.1 M lithium sulfate monohydrate	0.1 M ADA pH 6.5	12% w/v polyethylene glycol 4000
24	None	0.1 M ADA pH 6.5	1 M di-ammonium

			hydrogen phosphate
25	0.1 M magnesium chloride hexahydrate	0.1 M ADA pH 6.5	12% w/v polyethylene glycol 6000
26	None	0.1 M ADA pH 6.5	12% v/v MPD
27	0.1 M lithium sulfate monohydrate	0.1 M ADA pH 6.5	1 M magnesium sulfate hydrate
28	0.3 M lithium sulfate monohydrate	0.1 M ADA pH 6.5	4% v/v polyethylene glycol 400
29	0.1 M ammonium sulfate	0.1 M HEPES-Na pH 7.5	0.5 M di-sodium hydrogen phosphate
30	0.1 M sodium chloride	0.1 M HEPES-Na pH 7.5	10% w/v polyethylene glycol 4000
31	0.1 M magnesium chloride hexahydrate	0.1 M HEPES-Na pH 7.5	18% v/v polyethylene glycol 400
32	None	0.1 M HEPES-Na pH 7.5	1 M potassium sodium tartrate tetrahydrate
33	0.1 M ammonium sulfate	0.1 M HEPES-Na pH 7.5	18% v/v polyethylene glycol 400
34	0.1 M ammonium sulfate	0.1 M HEPES-Na pH 7.5	10% w/v polyethylene glycol 4000
35	0.1 M tri-sodium citrate dihydrate	0.1 M HEPES-Na pH 7.5	12% v/v MPD
36	None	0.1 M HEPES-Na pH 7.5	1 M tri-sodium citrate dihydrate
37	0.6 M magnesium sulfate hydrate	0.1 M HEPES-Na pH 7.5	4% v/v polyethylene glycol 400
38	0.6 M magnesium sulfate hydrate	0.1 M HEPES-Na pH 7.5	4% v/v MPD
39	0.1 M lithium sulfate monohydrate	0.1 M HEPES-Na pH 7.5	0.1 M potassium sodium tartrate tetrahydrate
40	0.1 M lithium sulfate monohydrate	0.1 M tris hydrochloride pH 8.5	12% v/v MPD
41	0.1 M di-ammonium hydrogen phosphate	0.1 M tris hydrochloride pH 8.5	0.5 M di-sodium hydrogen phosphate
42	None	0.1 M tris hydrochloride pH 8.5	0.1 M sodium acetate trihydrate
43	None	0.1 M tris hydrochloride pH 8.5	0.1 M sodium chloride
44	0.1 M di-ammonium	0.1 M tris hydrochloride pH 8.5	12% w/v polyethylene

	hydrogen phosphate		glycol 6000
45	0.1 M potassium sodium tartrate tetrahydrate	0.1 M tris hydrochloride pH 8.5	0.4 M magnesium sulfate hydrate
46	None	0.1 M tris hydrochloride pH 8.5	0.2 M lithium sulfate monohydrate
47	None	0.1 M tris hydrochloride pH 8.5	0.5 M ammonium sulfate
48	0.1 M tri-sodium citrate dihydrate	0.1 M tris hydrochloride pH 8.5	5% v/v polyethylene glycol 400

# **Publications**

## The Role of Serine 167 in Human Indoleamine 2,3-Dioxygenase: A Comparison with Tryptophan 2,3-Dioxygenase<sup>†</sup>

Nishma Chauhan,<sup>‡</sup> Jaswir Basran,<sup>§</sup> Igor Efimov,<sup>‡</sup> Dimitri A. Svistunenko,<sup>||</sup> Harriet E. Seward,<sup>§</sup> Peter C. E. Moody,<sup>§</sup> and Emma Lloyd Raven<sup>\*‡</sup>

Department of Chemistry, University of Leicester, University Road, Leicester LE1 7RH, England, Department of Biochemistry, University of Leicester, Lancaster Road, Leicester LE1 9HN, England, and Department of Biological Sciences, University of Essex, Wivenhoe Park, Colchester CO4 3SQ, England

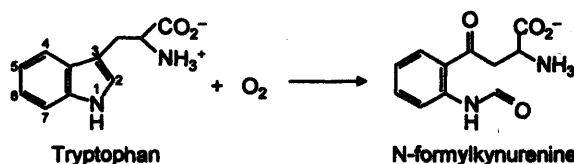
Received December 8, 2007; Revised Manuscript Received February 7, 2008

**ABSTRACT:** The initial step in the L-kynurenine pathway is oxidation of L-tryptophan to *N*-formylkynurenine and is catalyzed by one of two heme enzymes, tryptophan 2,3-dioxygenase (TDO) or indoleamine 2,3-dioxygenase (IDO). Here, we address the role of the conserved active site Ser167 residue in human IDO (S167A and S167H variants), which is replaced with a histidine in other mammalian and bacterial TDO enzymes. Our kinetic and spectroscopic data for S167A indicate that this residue is not essential for O<sub>2</sub> or substrate binding, and we propose that hydrogen bond stabilization of the catalytic ferrous–oxy complex involves active site water molecules in IDO. The data for S167H show that the ferrous–oxy complex is dramatically destabilized in this variant, which is similar to the behavior observed in human TDO [Basran et al. (2008) *Biochemistry* 47, 4752–4760], and that this destabilization essentially destroys catalytic activity. New kinetic data for the wild-type enzyme also identify the ternary [enzyme–O<sub>2</sub>–substrate] complex. The data reveal significant differences between the IDO and TDO enzymes, and the implications of these results are discussed in terms of our current understanding of IDO and TDO catalysis.

The initial, rate-limiting step in the L-kynurenine pathway is the oxidative cleavage of L-tryptophan to *N*-formylkynurenine (Scheme 1) and is catalyzed by one of two heme dioxygenase enzymes, indoleamine 2,3-dioxygenase (IDO)<sup>1</sup> or tryptophan 2,3-dioxygenase (TDO). Although they catalyze the same reaction, TDO and IDO are otherwise distinct, and we know little about their structure and mechanism.

The first detailed structural and functional information that appeared was for human indoleamine 2,3-dioxygenase. A recent crystal structure for ferric human IDO (1) reveals an active site that is much more hydrophobic than for other, well-characterized O<sub>2</sub>-dependent heme enzymes (Figure 1A) and which is presumably configured to encourage binding of the hydrophobic substrate. Subsequently, a structure for the bacterial *Xanthomonas campestris* TDO (xTDO) in complex with L-Trp (2) was published (Figure 1B,C) and indicated that an active site histidine, His55, hydrogen bonds

Scheme 1: Reaction Catalyzed by IDO, with IUPAC Numbering Indicated



to the indole nitrogen of the substrate in the substrate-bound complex (Figure 1C).

Although these structures have provided critical insight into the molecular details of the active site architecture and the substrate binding interactions, they also raise a number of important questions for which there are currently no satisfactory answers. To begin with, the most striking feature of the IDO active site is that, with the notable exception of Ser167, it is almost devoid of polar residues (Figure 1A). This marks IDO as distinct from some other heme proteins (e.g., the globins and peroxidases), which often have an active site histidine residue in the distal pocket that provides hydrogen-bonding stabilization to ligands bound at the heme iron. The first questions that arise, therefore, are whether similar hydrogen-bonding stabilization of the ferrous–oxy species is required during IDO catalysis, how is this provided, and whether this applies universally across the heme dioxygenase family. A second notable difference between xTDO and IDO is that the critical His55 residue is missing in IDO, replaced by a serine residue at position 167 that is conserved across all IDOs (Figure 1). Sequence alignments indicate that this active site histidine is similarly conserved among all

<sup>†</sup> This work was supported by grants from The Leverhulme Trust (fellowship to E.L.R.), BBSRC (grants BB/C00602X/1 and IIP0206/009), and EPSRC (studentship to N.C.).

\* To whom correspondence should be addressed. Telephone: +44 (0)116 229 7047. Fax: +44 (0)116 252 3789. E-mail: emma.raven@le.ac.uk.

<sup>‡</sup> Department of Chemistry, University of Leicester.

<sup>§</sup> Department of Biochemistry, University of Leicester.

<sup>||</sup> Department of Biological Sciences, University of Essex.

<sup>1</sup> Abbreviations: IDO, indoleamine 2,3-dioxygenase; rhIDO, recombinant human indoleamine 2,3-dioxygenase; L-Trp, L-tryptophan; TDO, tryptophan 2,3-dioxygenase; rhTDO, recombinant human tryptophan 2,3-dioxygenase; xTDO, *Xanthomonas campestris* tryptophan 2,3-dioxygenase.

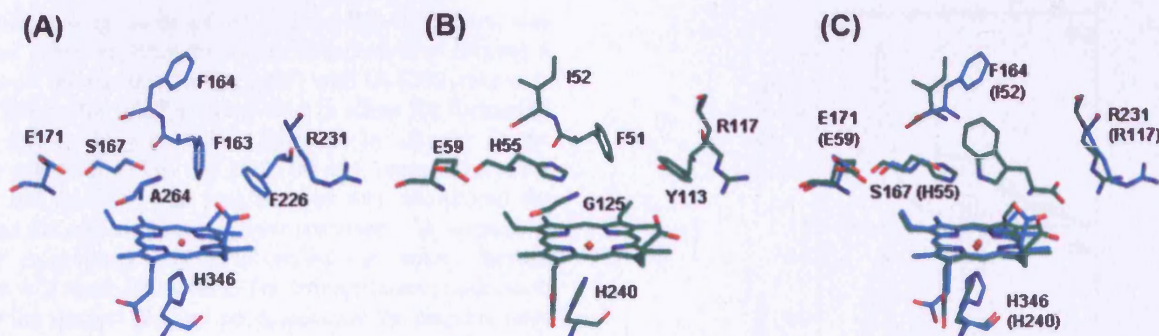


FIGURE 1: Comparison of the active sites of IDO and TDO. (A) The active site of rhIDO [in cyan (1)]. (B) The active site of xTDO [in green (2)] in the same orientation as that shown for rhIDO. Active site residues for rhIDO are H346, R231, F226, F163, S167, A264, F164, and E171 which correspond to H240, R117, Y113, F51, H55, G125, I52, and E59 in xTDO. (C) An overlay of rhIDO (cyan) and the xTDO-Trp (green) complex with the residues for rhIDO indicated and those for xTDO in parentheses.

TDOs isolated to date (3) (including human TDO), raising the question as to its specific role in the reaction mechanism.

In this paper, we sought answers to these questions in recombinant human IDO (rhIDO) by means of a direct comparison with the TDO enzymes (S167A and S167H variants in rhIDO). Together with the data presented for human tryptophan 2,3-dioxygenase in the preceding paper (4), the results reveal important differences in reactivity between different dioxygenases, and the data are discussed in terms of our wider understanding of the reaction mechanism in this family of enzymes.

## EXPERIMENTAL PROCEDURES

**Materials.** L-Tryptophan and all of the chemicals used for buffers (Sigma-Aldrich) were of the highest analytical grade (more than 99% purity) and were used without further purification. Aqueous solutions were prepared using water purified through an Elgastat option 2 water purifier, which itself was fed with deionized water. All pH measurements were made using a Russell pH electrode attached to a digital pH meter (Radiometer Copenhagen, model PHM 93).

**Mutagenesis and Protein Purification.** Site-directed mutagenesis on rhIDO was performed according to the QuikChange protocol (Stratagene Ltd., Cambridge, U.K.). Bacterial fermentation of cells and purification of rhIDO, S167A, and S167H mutants were carried out according to published procedures (5) with the exception that, after sonication, 5 mg of DNase I and 20 mM MgCl<sub>2</sub> were added and the suspension was stirred for a further 30 min at 4 °C. Absorption coefficients for S167A ( $\epsilon_{404} = 144 \text{ mM}^{-1} \text{ cm}^{-1}$ ) and S167H ( $\epsilon_{408} = 166 \text{ mM}^{-1} \text{ cm}^{-1}$ ) were determined using the pyridine hemochromagen method (6); for rhIDO,  $\epsilon_{404} = 172 \text{ mM}^{-1} \text{ cm}^{-1}$  (5). Ligand-bound derivatives (azide, cyanide, and fluoride) were obtained by the addition (typically 2–10  $\mu\text{L}$ ) of a concentrated (1 M) solution of ligand to the ferric enzyme. The ferrous-oxy derivative was generated by direct bubbling of O<sub>2</sub> gas through a dithionite-reduced sample of enzyme.

**Equilibrium Binding Constants.** Equilibrium dissociation constants (50 mM Tris-HCl, pH 8.0, 25.0  $\pm$  0.1 °C),  $K_D$ , for binding of both L-Trp and cyanide were determined according to published procedures (7). Binding of L-Trp to ferric rhIDO and S167A in the presence of cyanide was carried out on samples of ferric rhIDO and S167A saturated with 80 and 20  $\mu\text{M}$  cyanide, respectively, and absorbance changes were monitored at 416 nm.

**EPR Spectroscopy.** EPR spectra were recorded using a Bruker EMX EPR spectrometer (X-band) equipped with a spherical high-quality Bruker resonator SP9703 and an Oxford Instruments liquid helium system. The  $g$ -values were obtained by using the built-in microwave frequency counter and a 2,2-diphenyl-1-picrylhydrazyl standard, the  $g$ -value for which is  $2.0037 \pm 0.0002$ .

**Steady-State Measurements.** Steady-state oxidation of L-Trp (50 mM Tris-HCl, pH 8.0, 25.0 °C) was carried out using a Perkin-Elmer Lambda 35 UV-visible spectrophotometer according to published protocols (5). Initial reaction rates were monitored by following formation of *N*-formylkynurenine as an increase in absorbance at 321 nm ( $\epsilon_{321} = 3.75 \text{ mM}^{-1} \text{ cm}^{-1}$ ). The  $K_M$  value for O<sub>2</sub> was determined by varying the O<sub>2</sub> concentration (0–300  $\mu\text{M}$ ) while keeping the concentration of L-Trp constant and saturating at 200  $\mu\text{M}$ .

**Kinetic Measurements.** The kinetics of binding of L-Trp, cyanide, and O<sub>2</sub> to rhIDO were determined using an SX.18MV stopped-flow spectrometer housed in an anaerobic glovebox (Belle Technology, [O<sub>2</sub>] < 5 ppm) and fitted with a Neslab RTE-200 circulating water bath ( $\pm 0.1$  °C). Reported values of  $k_{\text{obs}}$  are an average of at least four measurements (50 mM Tris-HCl, pH 8.0, 25.0 °C). All reactions were carried out under pseudo-first-order conditions; final (reaction cell) protein concentrations used were 0.5  $\mu\text{M}$ . Absorbance changes accompanying L-Trp and cyanide binding were monitored at 404 nm for rhIDO and S167A and at 408 nm for S167H. For each enzyme-ligand complex the apparent association rate constant ( $k_{\text{on}}$ ) was obtained from the slope of the linear dependence of the observed rate constant,  $k_{\text{obs}}$ , against ligand concentration; the dissociation rate constant ( $k_{\text{off}}$ ) was obtained from the ordinate intercept of this plot. For O<sub>2</sub> binding experiments, anaerobic conditions were obtained by extensive N<sub>2</sub> equilibration of the buffer and reactions initiated by mixing anaerobic solutions of enzyme (typically 2  $\mu\text{M}$ , prerduced with dithionite) with an equal volume of buffer containing O<sub>2</sub> at different concentrations (0.12–1.2 mM). Formation of the ferrous-oxy complex was monitored at 416 nm. Formation of the ferrous-oxy rhIDO complex was also monitored in the presence of 1-methyl-Trp (300  $\mu\text{M}$ ) at the same wavelength.

**Detection of Intermediate Species during Reaction of Fe<sup>2+</sup> with L-Trp and O<sub>2</sub>.** Time-dependent spectral changes observed during steady-state turnover by IDO were examined by stopped-flow spectroscopy using a photodiode array detector and X-SCAN software (Applied Photophysics). The

sequential mixing mode of the stopped-flow apparatus was used for these experiments. This involved first mixing a solution of ferrous enzyme (1.5  $\mu\text{M}$ ) with  $\text{O}_2$  (250  $\mu\text{M}$ ) with a 1 s (500 ms for S167H) aging time to allow for formation of the ferrous–oxy complex, followed by mixing of the second substrate, L-Trp (50 and 100  $\mu\text{M}$ , respectively, for rhIDO and S167H). The reaction was then monitored for 50 s, and the spectral changes were recorded. The sequential mixing experiment was also carried out where ferrous enzyme was incubated with L-Trp first and then mixed with  $\text{O}_2$ , and the spectral changes accompanying the reaction were monitored again.

**Determination of  $\text{Fe}^{3+}/\text{Fe}^{2+}$  Reduction Potentials.**  $\text{Fe}^{3+}/\text{Fe}^{2+}$  reduction potentials for rhIDO, S167A, and S167H were determined by simultaneous reduction with a dye of known potential (8) according to previous methodology (9). Various dyes were used: Nile blue chloride ( $E_{m,7} = -116$  mV), phenosafranin ( $E_{m,7} = -252$  mV), methylene blue ( $E_{m,7} = 11$  mV), and toluidene blue O ( $E_{m,7} = 34$  mV). Absorbance changes corresponding to reduction of heme were measured at the isosbestic points for the dyes; Nile blue chloride (406 nm), phenosafranin (407 nm), methylene blue (404 nm), and toluidene blue O (400 nm). Reduction of the dye (at the wavelength at which the absorption change due to heme reduction was negligible) was measured at 635 nm for Nile blue chloride, 520 nm for phenosafranin, 664 nm for methylene blue, and 637 nm for toluidene blue O. In all cases, linear Nernst plots for one-electron reduction of heme produced the expected slope of 1 across a wide range of potentials, and the intercept gives a reliable value for  $\Delta E_{m,7}$  with an error of  $\pm 2$  mV (9). UV–visible spectra obtained in all experiments were analyzed using Specfit (10) for singular value decomposition based on factor analysis. All potentials are given versus the normal hydrogen electrode (NHE).

## RESULTS

**Characterization of S167A and S167H Variants.** Analysis of the electronic spectrum of ferric S167A reveals that the wavelength maxima ( $\lambda_{\text{max}} = 404, 500, 537, 575,$  and  $628$  nm, Figure 2B) are very similar to those for rhIDO ( $\lambda_{\text{max}} = 404, 500, 533,$  and  $635$  nm, Figure 2A); rhIDO is known to exist as a mixed population of high- and low-spin heme (5). For S167H (Figure 2C), the Soret band is red shifted to 408 nm ( $\lambda_{\text{max}} = 408, 499, 536, 570,$  and  $628$  nm), which is indicative of an increased proportion of low-spin heme, possibly as a result of coordination of His167 to the heme iron.

The spectra of the ferric derivatives of both S167A and S167H did not show any significant dependence on pH over the range examined (pH 6–8); no substantial changes in peak positions or intensities were observed (data not shown). Similar observations have been reported for rhIDO (5) and have been attributed to the lack of a proton acceptor in the distal cavity capable of hydrogen bonding to a bound hydroxide in the ferric derivative. A similar arrangement presumably applies for both S167A and S167H.

The electronic spectra of the ferrous derivatives of S167A and S167H are similar to those of rhIDO. This is consistent with the presence of a 5-coordinate heme species in all cases and indicates that the low-spin component in ferric S167H is converted to a high-spin, 5-coordinate heme on reduction.

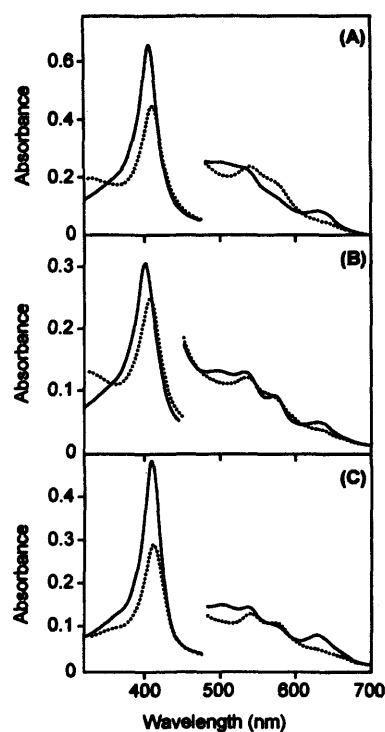


FIGURE 2: UV–visible spectra of (A) rhIDO, (B) S167A, and (C) S167H in the absence (solid line) and presence (dotted line) of L-Trp (20 mM for rhIDO and 40 mM for S167H and S167A). Absorbance values in the visible region have been multiplied by a factor of 5. Reaction conditions: 50 mM Tris-HCl, pH 8.0, 25.0  $^{\circ}\text{C}$ .

Wavelength maxima for other ferric and ferrous derivatives of S167A and S167H in the presence of various exogenous ligands are given in Table 1.

**EPR Spectroscopy.** EPR spectroscopy was used as a means of providing further information on the heme coordination geometry in S167A and S167H. The EPR spectrum of ferric rhIDO is shown for reference in Figure 3A; axial and rhombic high-spin ( $g = 5.82, 1.99$  and  $6.17, 5.52, 1.99$ , respectively) and low-spin ( $g = 2.85, 2.27, 1.62$ ) species have been previously assigned (5). The EPR spectrum of S167A (Figure 3B) has an increased proportion of high-spin heme compared to rhIDO, which consists mainly of an axial ( $g = 5.85, 1.99$ ) form.

In contrast, the spectrum of S167H (Figure 3C) contains a major low-spin species ( $g = 2.88, 2.28,$  and  $1.63$ ) which is likely to arise from bis-histidine axial ligation in which the imidazole planes are aligned approximately parallel to each other (11, 12).

**Cyanide Binding.** The binding of various noncatalytic ligands to the ferric enzymes is informative because it provides further information on the different coordination environments of the heme. Addition of cyanide gives changes in the visible region that are indicative of the formation of a 6-coordinate low-spin species for both S167A [ $\lambda_{\text{max}} = 419, 540, 570$  (sh) nm] and S167H [ $\lambda_{\text{max}} = 418, 540, 568$  (sh) nm] (Table 1). The corresponding binding constants,  $K_D$ , are given in Table 2, with spectra shown in Figure 4A. Values of  $K_D$  for rhIDO and S167A are broadly similar, but that for S167H is increased by a factor of  $\approx 170$ , which is in agreement with the spectroscopic data above and consistent with binding of His167 to the iron. Binding of cyanide was also determined kinetically. Second-order rate constants,  $k_{\text{on}}$ , were derived from a plot of  $k_{\text{obs}}$  against [cyanide] (Figure

Table 1: Absorption Maxima for rhIDO, S167A, and S167H (50 mM Tris-HCl, pH 8.0, 25.0 °C)

derivative	rhIDO	S167A	S167H
ferric	404, 500, 533, 635	404, 500, 537, 575, 628	408, 500, 536, 570, 628
ferrous	425, 527 sh, <sup>a</sup> 558	426, 529 sh, 557	426, 535 sh, 558
ferrous-oxy	416, 539, 576	416, 539, 576	416, 538, 575
ferric + L-Trp	410, 540, 576	409, 539, 572	409, 539, 573
ferric-azide	413, 535, 572, 643	410, 540, 576, 627	nd <sup>b</sup>
ferric-fluoride	404, 502, 532, 635	405, 500, 537, 575, 628	nd <sup>b</sup>
ferric-cyanide	419, 538, 569 sh	419, 540, 570 sh	418, 540, 568 sh

<sup>a</sup> sh = shoulder. <sup>b</sup> No spectroscopic changes were observed on binding of either azide or fluoride to S167H.

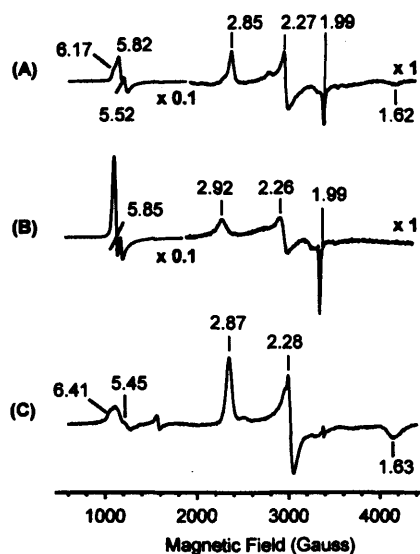


FIGURE 3: EPR spectra of (A) ferric rhIDO, (B) ferric S167A, and (C) ferric S167H. Spectra were measured at 10 K. Experimental conditions: modulation frequency, 100 kHz; microwave frequency, 9.67 GHz; microwave power, 2 mW; modulation amplitude, 10 G. Reaction conditions: 50 mM Tris-HCl, pH 8.0.

4B), and values are given in Table 2. As for the binding data above, the  $k_{on}$  value for S167H was  $\sim 50$  times smaller than for rhIDO. This is informative because it tells us that the weaker  $K_D$  for S167H is due to a decreased  $k_{on}$ , which is consistent with the bis-histidine ligated heme detected by EPR. The  $k_{on}$  value obtained for S167A is  $\approx 8$ -fold faster than for rhIDO.

**Substrate Binding.** Both S167A and S167H exhibited characteristic spectroscopic changes upon binding of L-Trp at pH 8.0 (Figure 2B,C): the Soret band shifts to 409 nm in both cases. Similar changes in absorbance are observed for rhIDO (Figure 2A) and are consistent with the loss of high-spin heme and the formation of a low-spin, hydroxide-bound species on binding of L-Trp, most likely as a consequence of deprotonation of a water molecule in the active site (5). The similarity of the spectroscopic changes for S167A and S167H indicates that binding of substrate occurs in a similar manner and that the corresponding deprotonation of the distal water molecule to form a hydroxide-bound species occurs by a similar mechanism.

Binding constants,  $K_D$ , for binding of L-Trp to S167A and S167H were determined from the above data as  $8000 \pm 1000$  and  $6900 \pm 1100 \mu\text{M}$  (pH 8.0), respectively (Table 2). Both of these values are significantly larger than the corresponding value for rhIDO ( $285 \pm 6 \mu\text{M}$ ), although we note that binding of substrate to the ferrous form of both variants (as evidenced by the  $K_M$  values, *vide infra*) is similar

in all three cases. Pseudo-first-order rate constants,  $k_{obs}$ , for binding of L-Trp were fitted to eq 1:

$$k_{obs} = k_{on}[L] + k_{off} \quad (1)$$

Derived rate constants are given in Table 2 and show a marked increase in  $k_{off}$  for S167H. Values for  $K_D$  ( $=k_{off}/k_{on}$ ) derived from these data were within error of those determined under equilibrium conditions (data not shown).

Binding constants for binding of L-Trp to the ferric-cyanide complexes were also determined under equilibrium conditions, and derived values of  $16.4 \pm 1.5 \mu\text{M}$  for rhIDO and  $992 \pm 200 \mu\text{M}$  for S167A were obtained (Table 2). These values are significantly lower than those for the ferric enzyme alone (Table 2) and are indicative of enhanced affinity for L-Trp in the presence of cyanide. The same experiment on the ferric-cyanide complex of S167H gave spectral changes that were much smaller than those for either rhIDO or S167A (both in terms of shift of the Soret band and total change in absorbance). We have interpreted this to mean that binding of L-Trp probably occurs, but the spectroscopic changes were too small to extract a meaningful  $K_D$ .

**Redox Measurements.** The  $\text{Fe}^{3+/2+}$  reduction potential for S167A was found to be  $-12$  mV (Figure 5A); this compares to a value of  $-63$  mV for rhIDO which was determined using the same method.<sup>2</sup> The  $\text{Fe}^{3+/2+}$  reduction potential for S167H ( $-203$  mV, Figure 5B) was significantly lower than that for both rhIDO and S167A.

**Steady-State Kinetics.** Steady-state oxidation of L-Trp at pH 8.0 gave values for  $k_{cat} = 1.56 \pm 0.04 \text{ s}^{-1}$  and  $K_M = 21 \pm 1.9 \mu\text{M}$  for S167A,<sup>3</sup> which is similar to that for rhIDO ( $k_{cat} = 1.4 \pm 0.05 \text{ s}^{-1}$ ,  $K_M = 7 \pm 0.8 \mu\text{M}$ ). The corresponding values for S167H were  $k_{cat} = 0.006 \pm 0.28 \times 10^{-5} \text{ s}^{-1}$  and  $K_M = 26 \pm 1.3 \mu\text{M}$ , showing that S167H is effectively inactive for oxidation of L-Trp. A steady-state analysis at fixed concentration of substrate and varying concentration of  $\text{O}_2$  was carried out to extract a  $K_M$  for  $\text{O}_2$  binding to

<sup>2</sup> The xanthine/xanthine oxidase method produces a slightly different value than that obtained by potentiometric titration [ $-30$  mV (5)]. We have observed slightly different values for reduction potentials of other heme proteins determined by the xanthine/xanthine oxidase method and other electrochemical methods (9). The discrepancy probably arises from the use of dithionite as a reductant in the potentiometric technique. Dithionite, a strong reducing agent, transfers all electron equivalents immediately to the protein, with subsequent equilibration assisted by mediators after equilibration at each potential; the next addition of dithionite corresponding to another potential requires a new equilibration. In the xanthine/xanthine oxidase method, xanthine oxidase feeds electrons slowly to the protein and the dye, so that equilibrium is reached at any point during the experiment. As an important control, experiments on rhIDO using different dyes gave the same value for the reduction potential [ $E^\circ(\text{Fe}^{3+}/\text{Fe}^{2+}) = -63$  mV using methylene blue;  $E^\circ(\text{Fe}^{3+}/\text{Fe}^{2+}) = -68$  mV using Nile blue chloride].

<sup>3</sup> A  $k_{cat}$  of  $1.95 \pm 0.08 \text{ s}^{-1}$  has been reported for S167A (1), but no  $K_M$  was reported.

Table 2: Kinetic and Thermodynamic Parameters for Binding of L-Trp and Cyanide to Ferric and of O<sub>2</sub> to Ferrous rhIDO, S167A, and S167H (50 mM Tris-HCl, pH 8.0, 25.0 °C)

variant	parameter	rhIDO	S167A	S167H
tryptophan	$K_D$ ( $\mu\text{M}$ )	$285 \pm 6$	$8000 \pm 1000^c$	$6900 \pm 1100^d$
	$K_D$ ( $\mu\text{M}$ ) (with CN)	$16.4 \pm 1.5^e$	$992 \pm 200^e$	ND <sup>f</sup>
	$k_{\text{on}}$ ( $\mu\text{M}^{-1} \text{s}^{-1}$ )	$15500 \pm 350$	$15000 \pm 16700$	$5930 \pm 150$
	$k_{\text{off}}$ ( $\text{s}^{-1}$ )	$9.1 \pm 0.6$	$61 \pm 2.7$	$41.6 \pm 4$
cyanide	$K_D$ ( $\mu\text{M}$ )	$3.57 \pm 0.37^b$	$1.92 \pm 0.17$	$594 \pm 30$
	$k_{\text{on}}$ ( $\mu\text{M}^{-1} \text{s}^{-1}$ )	$0.0214 \pm 0.0006$	$0.1708 \pm 0.0032$	$0.0004 \pm 1.2 \times 10^{-5}$
oxygen	$k_{\text{on}}$ ( $\mu\text{M}^{-1} \text{s}^{-1}$ )	$0.53 \pm 0.006^g$	$0.25 \pm 0.002$	$0.11 \pm 0.02$
	$k_{\text{off}}$ ( $\text{s}^{-1}$ )	$6.8 \pm 1.8^g$	$6.96 \pm 8.2$	$3.03 \pm 3.7$
	$k_{\text{off}}/k_{\text{on}}$ ( $=K_D$ ) <sup>g</sup>	$12.8 \pm 3.53$	$27.8 \pm 33$	$27.5 \pm 38.5$

<sup>a</sup> rhIDO was fully saturated with cyanide (80  $\mu\text{M}$ ) before addition of L-Trp. <sup>b</sup> There are no reported binding constants for cyanide binding to rhIDO, although Sono et al. have reported binding of cyanide to rabbit IDO [ $K_D = 11 \mu\text{M}$  (19)]. <sup>c</sup> Rate constants for binding of O<sub>2</sub> to rhIDO have not been reported previously. <sup>d</sup> Errors on these values are larger because the limited solubility of L-Trp in solution (maximum concentration  $\approx 50 \text{ mM}$ ) means that larger volumes are needed during the titration and corrections for this dilution were necessary. <sup>e</sup> S167A was fully saturated with cyanide (20  $\mu\text{M}$  cyanide) before addition of L-Trp. <sup>f</sup> ND,  $K_D$  could not be measured because the spectral changes upon addition of L-Trp were too small to monitor. <sup>g</sup> These are calculated values and have higher errors because they use the  $k_{\text{off}}$  values which have large errors themselves (since they derive from an intercept on the  $k_{\text{obs}}$  versus concentration plot).

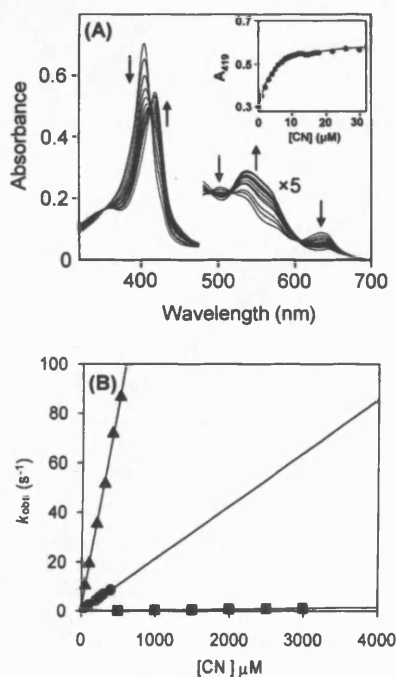


FIGURE 4: (A) Representative data set for the determination of  $K_D$  for binding of CN to rhIDO at pH 8.0. The arrows indicate the direction of change in absorbance upon successive additions of CN. Absorbance values in the visible region have been multiplied by a factor of 5. (Inset) Fit of binding data at 419 nm (according to eq 1 in ref 4). (B) Concentration dependence of the observed rate constants of cyanide binding to ferric rhIDO ( $\bullet$ ), S167A ( $\blacktriangle$ ), and S167H ( $\blacksquare$ ). Linear regression analysis of the data yielded an apparent association constant ( $k_{\text{on}}$ ) from the slope and a dissociation rate constant ( $k_{\text{off}}$ ) from the ordinate intercept.

rhIDO. This yielded a plot of reaction rate against O<sub>2</sub> concentration that was sigmoidal and did not follow typical Michaelis–Menten kinetics (data not shown). This may be a consequence of the complex nature of the assay mixture (an ascorbate/methylene blue reducing system, plus catalase). However, the rate of formation of *N*-formylkynurenine was independent of O<sub>2</sub> concentration above 150  $\mu\text{M}$ , which suggests that at this concentration enzyme is saturated with O<sub>2</sub>; we estimate therefore that the  $K_M$  for O<sub>2</sub> is  $<50 \mu\text{M}$ .

**Formation and Decay of the Catalytic Ferrous–Oxy Intermediate.** Spectroscopic changes observed on reaction of rhIDO, S167A, and S167H with O<sub>2</sub> were monitored using

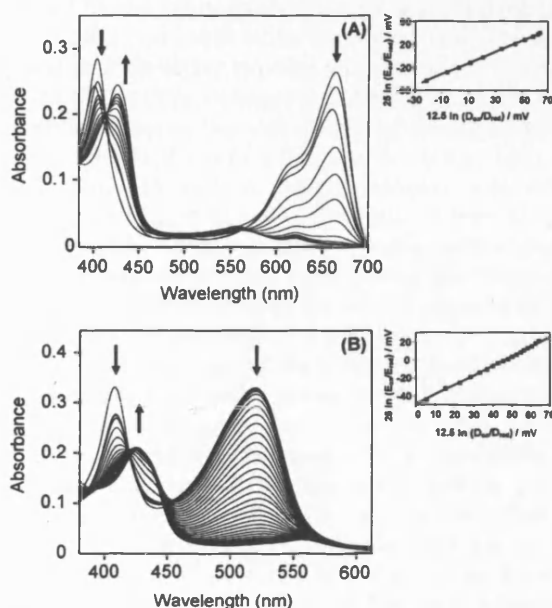


FIGURE 5: Family of spectra collected during determination of Fe<sup>3+</sup>/Fe<sup>2+</sup> reduction potential for (A) S167A with methylene blue and (B) S167H with phenosafranin. Conditions: 50 mM potassium phosphate, pH 7.0. Arrows indicate the direction of absorption changes at various parts of the spectrum during the reductive titration. (Inset) The corresponding linear Nernst plot.

stopped-flow photodiode array spectroscopy. For rhIDO, the data were collected over a period of 1 s from the mixing event and were best fitted to a one-step model ( $A \rightarrow B$ , Figure 6A and inset) in which species A (solid line) clearly represents the ferrous form of rhIDO ( $\lambda_{\text{max}} = 425, 527, 558 \text{ nm}$ ) and species B (dotted line) has spectral properties characteristic of the ferrous–oxy rhIDO complex ( $\lambda_{\text{max}} = 416, 539, 576 \text{ nm}$ ). The ferrous–oxy complex was also observed for S167A and S167H, and both variants exhibited similar wavelength maxima to that seen for rhIDO (Table 1).

The concentration dependence of the rate constant ( $k_{\text{obs}}$ ) for ferrous–oxy complex formation in rhIDO and the Ser 167 mutants was monitored at 416 nm using the single-wavelength mode of the stopped-flow apparatus. The corresponding rate constants for O<sub>2</sub> binding ( $k_{\text{on}}$ ,  $k_{\text{off}}$ , eq 1) to rhIDO, S167A, and S167H are given in Table 2, and data are shown in Figure 6B. Similar values for  $k_{\text{on}}$  and  $k_{\text{off}}$  and the derived  $K_D$  were found for rhIDO and S167A (Table 2).

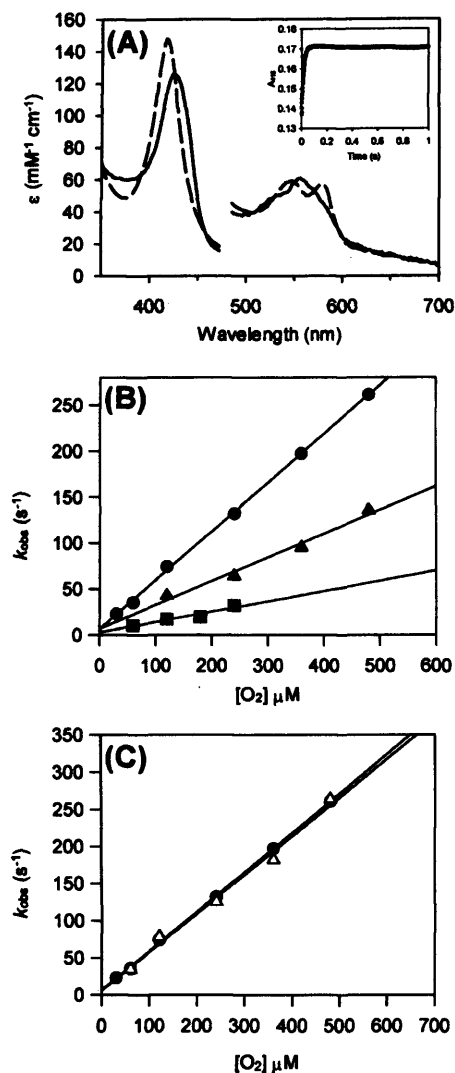


FIGURE 6: Reaction of rhIDO with  $\text{O}_2$  monitored by stopped-flow spectroscopy. (A) Deconvoluted spectra for the time-dependent spectral changes on mixing 1  $\mu\text{M}$  ferrous rhIDO with 130  $\mu\text{M}$   $\text{O}_2$  (time base of 1 s). The data were fitted to a single-step model,  $\text{A} \rightarrow \text{B}$ , with a rate constant (obtained from global fitting) of  $75.4 \pm 0.3 \text{ s}^{-1}$ . (Inset) Absorption transient at 416 nm observed upon mixing of 1  $\mu\text{M}$  ferrous rhIDO with 130  $\mu\text{M}$   $\text{O}_2$ . (B) Concentration dependence of the observed rate constant ( $k_{\text{obs}}$ ) of  $\text{O}_2$  binding to ferrous rhIDO ( $\bullet$ ), S167A ( $\blacktriangle$ ), and S167H ( $\blacksquare$ ). (C) Concentration dependence of the observed rate constant ( $k_{\text{obs}}$ ) of  $\text{O}_2$  binding to ferrous rhIDO in the absence ( $\bullet$ ) and presence of 300  $\mu\text{M}$  1-methyl-Trp ( $\blacktriangle$ ).

These ferrous–oxy complexes spontaneously decompose to ferric enzyme for all three proteins under anaerobic conditions (monitored at 576 nm). For S167H, the ferrous–oxy complex was particularly unstable, as evidenced by the half-life for this variant ( $t_{1/2} = 0.7 \text{ s}$ ), which is much faster than the corresponding half-lives of both rhIDO and S167A ( $t_{1/2} = 36$  and  $47 \text{ s}$ , respectively).

It is not possible to determine a rate constant for reaction of  $\text{O}_2$  with rhIDO in the presence of L-Trp under pre-steady-state conditions, because turnover occurs during the experiment. Instead, the rate constant was determined in the presence of excess 1-methyl-Trp (as a substrate analogue), which is a potent inhibitor of IDO (13). The data are shown in Figure 6C, which yields values for  $k_{\text{on}}$  and  $k_{\text{off}}$  of  $0.52 \pm 0.03 \mu\text{M}^{-1} \text{ s}^{-1}$  and  $6 \pm 9 \text{ s}^{-1}$ , respectively, and were very

similar to the values calculated for  $\text{O}_2$  binding to the ferrous enzyme alone (Table 2).

**Detection of Intermediate Species during Reaction of  $\text{Fe}^{2+}$  with L-Trp and  $\text{O}_2$ .** The above data clearly show that the S167H variant is unable to form a ferrous–oxy complex that is as stable as that observed for both rhIDO and S167A. We therefore sought to establish whether this instability was the source of the poor catalytic activity of S167H in the steady state. This was achieved by monitoring spectroscopic changes (by stopped flow) during the course of the catalytic reaction of S167H and comparing them to those observed for rhIDO.

rhIDO was incubated with  $\text{O}_2$  for a period of 1 s (to allow for formation of the ferrous–oxy complex) and then mixed with excess L-Trp, and the spectral changes were monitored for 50 s. The first spectrum (collected at 1.28 ms after mixing of L-Trp) clearly represents the enzyme in the ferrous–oxy form [Figure 7A (solid line),  $\lambda_{\text{max}} = 416, 539, 576 \text{ nm}$ ]. For the next 0.75 s no major spectral change was observed [apart from a small (2 nm) shift in the Soret peak from 416 to 414 nm], and no *N*-formylkynurenine was detected as evidenced by a lack of absorbance change at 321 nm (Figure 7A, inset). We therefore propose that this species represents the ternary [enzyme– $\text{O}_2$ –Trp] complex [Figure 7A (dashed line),  $\lambda_{\text{max}} = 414, 544, 576 \text{ nm}$ ]. A ternary complex with similar characteristics ( $\lambda_{\text{max}} = 413, 541, 576 \text{ nm}$ ) has been observed previously under nonphysiological conditions (low temperature and cryogenic solvent) (14). During the steady-state phase, formation of *N*-formylkynurenine is apparent as there is a linear increase in absorbance at 321 nm over 5 s (Figure 7A, inset). The spectrum of the species present during the steady-state phase is similar to that of the proposed ternary complex [Figure 7A (dotted line),  $\lambda_{\text{max}} = 413, 543, 576 \text{ nm}$ ].

When the experiment was repeated but ferrous rhIDO was incubated with L-Trp first and then mixed with  $\text{O}_2$ , the first spectrum after final mixing was in this case identified as a ferrous–Trp complex [Figure 7B (solid line),  $\lambda_{\text{max}} = 413, 551, 575 \text{ (sh) nm}$ ]. After 0.75 s, the next species identified [Figure 7B (dashed line)] had a spectral form identical to that seen above, and we therefore assign it as arising from the ternary [enzyme– $\text{O}_2$ –Trp] complex. The steady-state intermediate [Figure 7B (dotted line)] that was detected was also identical to that observed in the experiment above. These two experiments indicate that, regardless of the order of mixing, a species is identified in rhIDO that closely resembles a ferrous–oxy intermediate and that we assign as the catalytic ternary complex.

Parallel experiments with S167H were also carried out. In the first experiment, ferrous S167H was mixed first with  $\text{O}_2$ , and after a predetermined period of time (typically 0.8 s) the solution was mixed with excess L-Trp and the spectral changes were monitored over a period of 500 s. The first species observed, 2.56 ms after mixing with L-Trp [Figure 7C (solid line),  $\lambda_{\text{max}} = 416, 543, 581 \text{ nm}$ ], is clearly identified as the ferrous–oxy form of the enzyme. Within 0.5 s, this ferrous–oxy species has decayed, and a second species with a blue-shifted Soret band and a broad band in the visible region [ $\lambda_{\text{max}} = 412, 433 \text{ (sh), 553 \text{ nm}}$ ] was detected [Figure 7C (dashed line)]; no product formation had occurred at this point (as shown by the absence of an absorbance change at 321 nm; Figure 7C, inset). This species is different from the corresponding species in rhIDO that was assigned as arising from the ternary complex [Figure 7A (dashed line)]. The

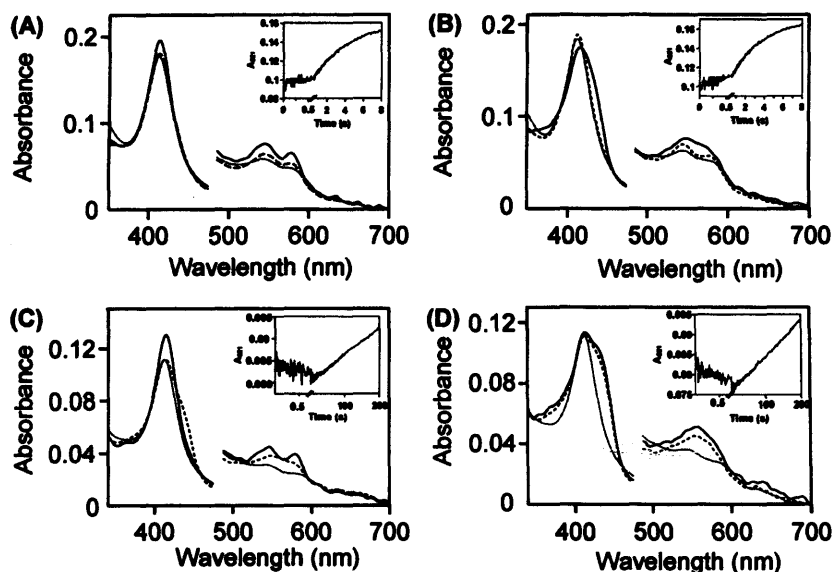
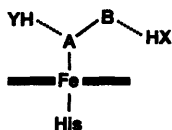


FIGURE 7: Detection of steady-state intermediates. (A) rhIDO premixed with  $O_2$  followed by mixing with L-Trp. (B) rhIDO premixed with L-Trp followed by mixing with  $O_2$ . (C) S167H premixed with  $O_2$  followed by mixing with L-Trp. (D) S167H premixed with L-Trp followed by mixing with  $O_2$ . (Inset) Time dependence of absorbance changes at 321 nm, which report on *N*-formylkynurenine formation. Absorbance values in the visible region have been multiplied by a factor of 3. For (A) and (B), the solid line shows the spectrum at 1.28 ms, the dashed line at 0.75 s, and the dotted line at 5 s; for (C) and (D), the solid line shows the spectrum at 2.56 ms, the dashed line at 0.5 s, and the dotted line at 100 s.

Scheme 2: Schematic Diagram of the Possible Hydrogen-Bonding Interactions (Dashed Lines) to a Bound Diatomic Ligand (either  $O_2$  or CN, Represented by AB) in IDO (2)<sup>a</sup>



<sup>a</sup> Hydrogen bond donors are indicated as XH and YH and are envisaged as being provided by either active site water molecules or substrate. Although water molecules are not present in the crystal structure of rhIDO (1), the actual hydration structure is likely to be different since the crystal structure contained two CHES molecules and the inhibitor 4-phenylimidazole in the active site, neither of which would be present physiologically.

final spectrum [Figure 7C (dotted line)] is typical of the species observed during the steady-state phase of the reaction ( $\lambda_{\max} = 412, 543, 577$  nm), but the intensities are reduced when compared to the corresponding steady-state intermediate in rhIDO [Figure 7A (dotted line)]. During this steady-state phase, *N*-formylkynurenine formation is observed as a linear increase in absorbance at 321 nm (Figure 7C, inset). Note the differences in time scales for product formation in rhIDO (5 s) and S167H (200 s) (insets to panels A and C of Figure 7, respectively).

In the second experiment, ferrous S167H was incubated first with L-Trp, and then this complex was mixed with  $O_2$ . The first species observed 2.56 ms after mixing with  $O_2$  [ $\lambda_{\max} = 414, 549$  nm, Figure 7D (solid line)], by comparison with rhIDO above (Figure 7B solid line), we assign as arising from the ferrous-Trp complex. After 0.5 s (when *N*-formylkynurenine has not yet been formed) a second species was identified [ $\lambda_{\max} = 412, 425$  (sh), 553 nm, Figure 7D (dashed line)] which is similar to that observed at the same time point in Figure 7C. During the steady-state phase, *N*-formylkynurenine formation is observed as a linear increase in absorbance at 321 nm (Figure 7D, inset), and

the intermediate that is detected at this point [Figure 7D (dotted line)] is identical to that in Figure 7C (dotted line). At no stage is clear formation of a ferrous-oxy species observed.

These experiments for S167H indicate (i) that the proposed ternary complex identified for rhIDO above is not observed in S167H and (ii) that the species present in the steady state for S167H is not the same as that for rhIDO nor does it resemble a ferrous-oxy species (as for rhIDO), regardless of the order of mixing.

## DISCUSSION

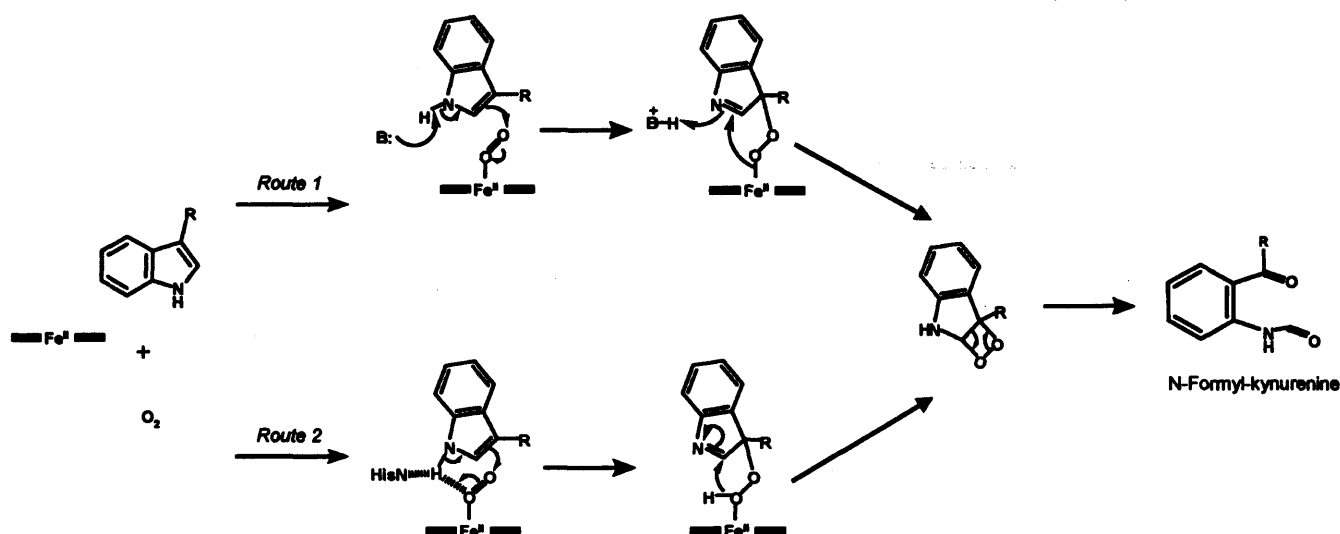
Our intention in this paper was to make comparisons between the active site structures of different mammalian and bacterial heme dioxygenases and to use this as a basis for developing our ideas on the reaction mechanism in these enzymes. Below we discuss the implications of these data in terms of our broader understanding of substrate binding and catalysis across the heme dioxygenase family; we include direct comparisons with human TDO (4).

### Hydrogen-Bonding Interactions in the Active Site of IDO.

Electronic spectra for the ferrous form of S167A are similar to the those of wild-type protein and indicate that this variant is 5-coordinate (as for rhIDO). In accordance with this, the ferrous-oxy derivative forms normally (as evidenced by  $k_{\text{on}}$ ,  $k_{\text{off}}$ ) and decays with a half-life ( $t_{1/2} = 47$  s) that is essentially the same as that for rhIDO ( $t_{1/2} = 37$  s). Since the steady-state data indicate that S167A binds (as evidenced by  $K_M$ ) and turns over ( $k_{\text{cat}}$ ) substrate essentially as normal, the immediate conclusion is that Ser167, which is the only polar residue in the IDO active site (Figure 1), is not important either for binding of  $O_2$ , for stabilization of the ferrous-oxy complex, or for conversion of the substrate to *N*-formylkynurenine.

There are no other potential hydrogen-bonding residues in the active site of IDO (Figure 1). This is in contrast to the globins, in which a distal histidine residue is located

Scheme 3: Possible Reaction Mechanisms for the Conversion of L-Trp to N-Formylkynurenine Catalyzed by IDO and TDO



directly above the iron and is poised to hydrogen bond to the bound  $O_2$ . We therefore interpret these data to mean that any hydrogen-bonding stabilization of the bound  $O_2$  ligand in IDO is most likely through an active site water molecule(s), as occurs in some other catalytic  $O_2$  binding proteins (e.g., heme oxygenase and cytochrome P450). In this context, we note that  $k_{on(O_2)}(\text{rhIDO}) \approx 2k_{on(O_2)}(\text{S167A})$ : if binding of  $O_2$  involves electron transfer and formation of a ferric-superoxide species, then  $k_{on(O_2)}(\text{rhIDO})/k_{on(O_2)}(\text{S167A}) = \exp[(E^{\circ}_{\text{rhIDO}} - E^{\circ}_{\text{S167A}})/2RT] = 2.7$ , which is close to the observed value of 2. The similarity in values suggests that differences in  $k_{on}$  can be accounted for by the differences in potential, assuming that the binding event involves electron transfer. In other words, the kinetic and thermodynamic data support the idea of a hydrogen-bonding network involving water molecules since movement of electron density onto  $O_2$  would be expected to involve hydrogen bonding from  $O_2$  to a hydrogen bond donor.

The precise mode of substrate binding in IDO is not yet known, but we envisage that in the presence of L-Trp these hydrogen-bonding interactions to  $O_2$  are replaced with hydrogen bonds to the substrate (Scheme 2). This would also account for the fact that the affinity of L-Trp for both ferric rhIDO and ferric S167A is considerably enhanced in the presence of cyanide (Table 2), where these hydrogen-bonding interactions to the substrate are also presumably possible (Scheme 2).

**Comparisons with Bacterial and Human TDOs: S167H Variant.** In xTDO, Ser167 is replaced with a histidine residue (His55, Figure 1). Sequence alignments with human TDO indicate that it also has a His at this position (His76). In the following sections, we compare the properties of the S167H variant with these other two dioxygenases.

The spectroscopic and ligand binding data indicate that the ferric derivative of the S167H variant most likely has His167 bound to the iron but that this is displaceable on binding of other strong ligands (e.g., cyanide) or on reduction. Hence, although the new ligand is not located directly "above" the heme (as in other bishistidine ligated heme proteins such as cytochrome  $b_5$ ), it appears that His167 is within bonding distance of the heme. This is in contrast to the presumed coordination geometry in human TDO, which contains a histidine (His76) at the position equivalent to

Ser167, for which spectroscopic data indicate mainly a high-spin, water-bound heme species in the ferric form (4). We conclude that there are differences in the precise orientation of the histidine residue between the two enzymes, such that coordination to the heme occurs in one case but not the other.

**Comparisons with Bacterial and Human TDOs: Stability of the Ferrous-Oxy Complex.** The ferrous-oxy complex of S167H is very greatly destabilized compared to rhIDO. This behavior for S167H replicates that in *Pseudomonas* TDO (15) and in recombinant human TDO (4), where the ferrous-oxy complex is similarly unstable. The very low reduction potential for S167H ( $-203$  mV) is certainly likely to be influential in destabilizing the ferrous-oxy complex but does not provide a complete explanation because the reduction potential of recombinant human TDO ( $-92$  mV) is higher and in this enzyme the ferrous-oxy species is not detected at all (4). By way of comparison, reduction potentials for myoglobin, in which the ferrous-oxy complex is much more stable, are typically in the range of  $\approx +50$  mV (16). The absence of potential hydrogen-bonding residues within the active site of IDO and the presumed failure of IDO to duplicate the stabilizing hydrogen-bonding interactions observed in the globins (*vide supra*) might also be influential, however.

The poor stability of the ferrous-oxy complex in S167H is reflected in the fact that the enzyme has lost  $>99\%$  of its activity (as evidenced by  $k_{\text{cat}}$ ), although we note that it binds L-Trp normally (as evidenced by  $K_M$ ). The formation of the ferrous-oxy complex is an important junction in the overall dioxygenase mechanism: this intermediate needs to be stable enough to interact with the substrate so that effective conversion to product can occur. Our stopped-flow kinetic data for rhIDO in the steady state indicate that significant amounts of the ferrous-oxy complex are present under turnover conditions. For S167H this is not the case, however; this presumably reflects the rapid and unproductive decay of the ferrous-oxy species, which then competes with the slower (productive) conversion of substrate to product.

**Mechanistic Implications.** Our kinetic data for rhIDO reveal that the enzyme shows no substantial preference for binding of  $O_2$  over L-Trp because the steady-state  $K_M$  for  $O_2$  (which is consistent with the  $K_D$  determined under pre-

steady-state conditions) is in a similar range to the  $K_M$  for L-Trp binding. Also, the kinetic data with 1-methyl-Trp show no enhancement of affinity for  $O_2$  in the presence of this substrate analogue. By implication we conclude that substrate binding does not preferentially favor  $O_2$  binding in rhIDO. This is consistent with our pre-steady-state data in which we observe a catalytic intermediate, proposed as the ternary enzyme- $O_2$ -Trp complex, at the same point in the reaction mechanism regardless of whether  $O_2$  or L-Trp is mixed with the enzyme first.

There are two possible mechanisms for initial reaction of the ferrous-oxy complex with bound substrate (Scheme 3). One mechanism involves base-catalyzed abstraction of the indole NH (route 1); the other does not (route 2). Early suggestions (13) favored the base-catalyzed mechanism. However, there is no evidence from our data that the only polar residue present in the active site of rhIDO, Ser167, plays any role in controlling the reaction mechanism. The alternative route (route 2) does not involve base-catalyzed proton abstraction (17). However, in xTDO the  $N^\epsilon$  of His55 is hydrogen bonded to the indole nitrogen of the bound substrate (Scheme 3), and although removal of this residue (H55A) lowers activity ( $k_{\text{cat(H55A)}} = 0.1k_{\text{cat(wild type)}}$  (2)), some activity remains, indicating that catalysis still occurs even in the absence of His55. This would be consistent with the fact that His55 is not needed in IDO and is replaced with Ser167. Further, it would mean that the most likely role for His55 is not in base-catalyzed abstraction but in orienting the indole proton, through hydrogen bonding, in a suitable position for deprotonation (although we note that the  $pK_a$  for the indole nitrogen of L-Trp in solution ( $pK_a = 16.9$  (18)) is out of range and would need to decrease substantially in the enzyme-substrate complex). Presumably, the same interaction exists in human TDO (through His76).

#### ACKNOWLEDGMENT

We thank Dr. P. Jenkins, Dr. B. Rawlings, and Dr. I. K. Macdonald for helpful discussions.

#### REFERENCES

- Sugimoto, H., Oda, S., Otsuki, T., Hino, T., Yoshida, T., and Shiro, Y. (2006) Crystal structure of human indoleamine 2,3-dioxygenase: catalytic mechanism of  $O_2$  incorporation by a heme-containing dioxygenase. *Proc. Natl. Acad. Sci. U.S.A.* **103**, 2611–2616.
- Forouhar, F., Anderson, J. L., Mowat, C. G., Vorobiev, S. M., Hussain, A., Abashidze, M., Bruckmann, C., Thackray, S. J., Seetharaman, J., Tucker, T., Xiao, R., Ma, L. C., Zhao, L., Acton, T. B., Montelione, G. T., Chapman, S. K., and Tong, L. (2007) Molecular insights into substrate recognition and catalysis by tryptophan 2,3-dioxygenase. *Proc. Natl. Acad. Sci. U.S.A.* **104**, 473–478.
- Dick, R., Murray, B. P., Reid, M. J., and Correia, M. A. (2001) Structure-function relationships of rat hepatic tryptophan 2,3-dioxygenase: identification of the putative heme-ligating histidine residues. *Arch. Biochem. Biophys.* **392**, 71–78.
- Basran, J., Rafice, S., Chauhan, N., Efimov, I., Cheesman, M. R., Ghamsari, L., and Raven, E. L. (2008) A kinetic, spectroscopic, and redox study of human tryptophan 2,3-dioxygenase. *Biochemistry* **47**, 4752–4760.
- Papadopoulou, N. D., Mewies, M., McLean, K. J., Seward, H. E., Svistunenko, D. A., Munro, A. W., and Raven, E. L. (2005) Redox and spectroscopic properties of human indoleamine 2,3-dioxygenase and a His303Ala variant: implications for catalysis. *Biochemistry* **44**, 14318–14328.
- Antonini, M., and Brunori, E. (1971) *Hemoglobin and Myoglobin and their Reactions with Ligands*, North Holland Publishers, Amsterdam.
- Patel, N., Jones, D. K., and Raven, E. L. (2000) Investigation of the haem-nicotinate interaction in leghaemoglobin. Role of hydrogen bonding. *Eur. J. Biochem.* **267**, 2581–2587.
- Massey, V. (1991) *Flavins and Flavoproteins* (Curti, B., Ronchi, S., and Zanetti, G., Eds.) pp 59–66, Walter de Gruyter, New York.
- Efimov, I., Papadopoulou, N. D., McLean, K. J., Badyal, S. K., Macdonald, I. K., Munro, A. W., Moody, P. C., and Raven, E. L. (2007) The Redox Properties of Ascorbate Peroxidase. *Biochemistry* **46**, 8017–8023.
- Binstead, R. A., and Zuberbuehler, A. D., Specfit, Chapel Hill, NC.
- Gadsby, P. M., and Thomson, A. J. (1990) Assignment of the axial ligands of ferric ion in low-spin hemoproteins by near-infrared magnetic circular dichroism and electron paramagnetic resonance spectroscopy. *J. Am. Chem. Soc.* **112**, 5003–5011.
- More, C., Belle, V., Asso, M., Fournel, A., Roger, G., Guigliarelli, B., and Bertrand, P. (1999) *Biospectroscopy* **55**, S3–S18.
- Sono, M., Roach, M. P., Coulter, E. D., and Dawson, J. H. (1996) Heme-containing oxygenases. *Chem. Rev.* **96**, 2841–2888.
- Sono, M. (1986) Spectroscopic and equilibrium properties of the indoleamine 2,3-dioxygenase-tryptophan-oxygen ternary complex and of analogous enzyme derivatives. Tryptophan binding to ferrous enzyme adducts with dioxygen, nitric oxide, and carbon monoxide. *Biochemistry* **25**, 6089–6097.
- Ishimura, Y., Nozaki, M., and Hayaishi, O. (1970) The oxygenated form of L-tryptophan 2,3-dioxygenase as reaction intermediate. *J. Biol. Chem.* **245**, 3593–3602.
- Raven, E. L., and Mauk, A. G. (2001) Chemical reactivity of the active site of myoglobin. *Adv. Inorg. Chem.* **51**, 1–49.
- Terentis, A. C., Thomas, S. R., Takikawa, O., Littlejohn, T. K., Truscott, R. J., Armstrong, R. S., Yeh, S. R., and Stocker, R. (2002) The heme environment of recombinant human indoleamine 2,3-dioxygenase. Structural properties and substrate-ligand interactions. *J. Biol. Chem.* **277**, 15788–15794.
- Yagil, G. (1967) The proton dissociation constant of pyrrole, indole, and related compounds. *Tetrahedron* **23**, 2855–2861.
- Sono, M. (1989) Enzyme kinetic and spectroscopic studies of inhibitor and effector interactions with indoleamine 2,3-dioxygenase. 2. Evidence for the existence of another binding site in the enzyme for indole derivative effectors. *Biochemistry* **28**, 5400–5407.

BI702405A

## Reassessment of the Reaction Mechanism in the Heme Dioxygenases

Nishma Chauhan,<sup>†</sup> Sarah J. Thackray,<sup>‡</sup> Sara A. Rafice,<sup>†</sup> Graham Eaton,<sup>†</sup> Michael Lee,<sup>†</sup> Igor Efimov,<sup>†</sup> Jaswir Basran,<sup>§</sup> Paul R. Jenkins,<sup>†</sup> Christopher G Mowat,<sup>‡</sup> Stephen K. Chapman,<sup>\*,†</sup> and Emma Lloyd Raven<sup>\*,†</sup>

Department of Chemistry, University of Leicester, University Road, Leicester, LE1 7RH, U.K., EaStCHEM, School of Chemistry, University of Edinburgh, West Mains Road, Edinburgh EH9 3JJ, U.K., and Department of Biochemistry, University of Leicester, Lancaster Road, Leicester, LE1 9HN, U.K.

Received October 23, 2008; E-mail: s.k.chapman@ed.ac.uk; emma.raven@le.ac.uk

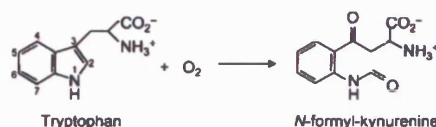
Indoleamine 2,3-dioxygenase (IDO) and tryptophan 2,3-dioxygenase (TDO) are heme enzymes that catalyze oxidation of L-tryptophan to *N*-formyl-kynurenine (Scheme 1),<sup>1–3</sup> in a mechanism that involves binding of dioxygen to reduced iron. The mechanistic details of this oxidation are not yet known, but early studies<sup>3</sup> suggested base-catalyzed deprotonation of the indole NH group (Scheme 2A). This was based largely on the observation that 1-methyl-L-tryptophan (1-Me-L-Trp) is an inhibitor of dioxygenase activity and was plausible since base-catalyzed abstraction is not possible with the methylated compound. There are problems with this mechanism, however. To begin with, it is inconsistent with the chemistry of indoles,<sup>4</sup> which typically react by electrophilic addition across the C<sub>3</sub> position and subsequent formation of a cation at N<sub>1</sub>. In addition, the structure of human IDO (hIDO)<sup>5</sup> reveals that there is no active-site base close enough for proton abstraction at N<sub>1</sub>. The only polar active-site residue is Ser167, but this is not essential for activity.<sup>5,6</sup> Although *X. campestris* TDO (XcTDO) does contain an active-site histidine (His55, equivalent to Ser167 in hIDO)<sup>7</sup> which hydrogen bonds to the indole N<sub>1</sub>, it is not essential for activity.<sup>7,8</sup> Together, this led to the hypothesis<sup>5,7</sup> that the bound dioxygen might act as the active-site base (Scheme 2B), with no involvement from active-site residues.

Here, we examine the activity of three heme dioxygenases (hIDO, human TDO (hTDO) and XcTDO<sup>9</sup>) with 1-Me-L-Trp, including a number of site-directed variants focused on the His55/Ser167 location. In contrast to previous work,<sup>10</sup> we find that 1-Me-L-Trp is a slow substrate. These observations are inconsistent with current proposals for the mechanism of substrate oxidation, and we propose an alternative.

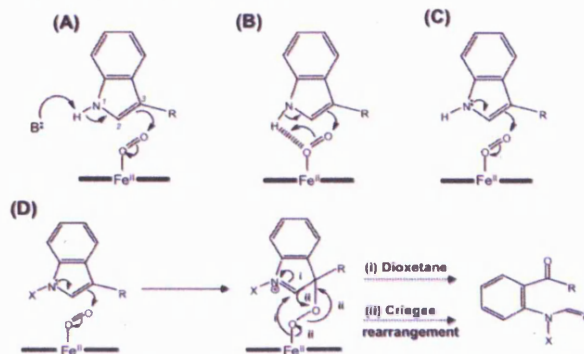
To determine if the purified enzymes could utilize 1-Me-L-Trp as a substrate, identification of the methylated product was essential.<sup>11,12</sup> Formation of *N*-formyl-kynurenine and *N*-formyl-methylkynurenine was confirmed at 321 nm (Figure S2, solid and dashed line, respectively). The reaction with 1-Me-L-Trp was repeated in the absence of enzyme (Figure S2, dotted line) and no absorbance change at 321 nm was observed, confirming that product formation is from enzymatic oxidation. LC-MS analysis using selected ion monitoring (shown for hIDO, Figure 1A) was then carried out. For the reaction with L-Trp, this gave an ion with *m/z* = 237 (Figure 1B, top) which corresponds to the mass of *N*-formyl-kynurenine (*m/z* = 236); for the reaction with 1-Me-L-Trp, an equivalent ion is detected at *m/z* = 251 (Figure 1B, bottom) as expected for *N*-formyl-methylkynurenine (*m/z* = 250).

Steady-state kinetic parameters for the oxidation of 1-Me-L-Trp were also determined<sup>6,7</sup> (Figure S3 and Table 1).<sup>13</sup> Clear increases

### Scheme 1. Reaction Catalyzed by IDO and TDO



### Scheme 2. Possible Mechanisms for Oxidation of Trp (C<sub>2</sub>, C<sub>3</sub>, and N<sub>1</sub> of the Substrate Are Labeled)<sup>a</sup>



<sup>a</sup> (A) Abstraction of the indole proton by an active-site base.<sup>3,15</sup> (B) Abstraction of the indole proton by the heme-bound dioxygen.<sup>5,16</sup> (C) Direct electrophilic addition. (D) A revised mechanism for product formation in heme dioxygenases, where X = H or Me. The conversion to product is proposed to occur by either a Criegee or dioxetane mechanism.<sup>3</sup>

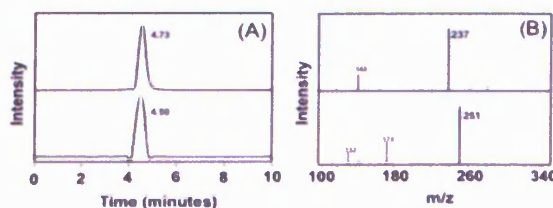


**Figure 1.** LC-MS analyses of products obtained on reaction of hIDO with *N*-formyl-kynurenine (top) and *N*-formyl-methylkynurenine (bottom). Panel A: Elution profiles for selected ion chromatograms with *m/z* of (top) 237 and (bottom) 251, corresponding to *N*-formyl-kynurenine and *N*-formyl-methylkynurenine, respectively. Panel B: Corresponding positive ESI mass spectra for the products eluted at 4.73 and 4.50 min (top and bottom, respectively).

in absorbance, corresponding to product formation, are observed for hIDO (Figure S3), as well as for the S167A variant of hIDO and variants of both hTDO and XcTDO (Table 1).<sup>13</sup>

These data clearly indicate that formation of *N*-formyl-methylkynurenine occurs upon reaction of 1-Me-L-Trp with hIDO and variants of hIDO, hTDO, and XcTDO. However, no activity was detected for hTDO and XcTDO with 1-Me-L-Trp in either steady-

<sup>†</sup> Department of Chemistry, University of Leicester.

<sup>‡</sup> University of Edinburgh.

<sup>§</sup> Department of Biochemistry, University of Leicester.

**Table 1.** Steady-State Parameters ( $k_{\text{cat}}$ ,  $K_M$ ) for Oxidation of 1-Me-L-Trp

	variant	$k_{\text{cat}}$ ( $\text{s}^{-1}$ )	$K_M$ ( $\mu\text{M}$ )
hIDO	native	$0.027 \pm 0.001$	$150 \pm 11$
	S167A	$0.032 \pm 0.002$	$31 \pm 5.0$
hTDO	native	—	—
	H76S	$0.023 \pm 0.001$	$2300 \pm 230$
XcTDO	native	—	—
	H55A	$0.048 \pm 0.011$	$59 \pm 16$
	H55S	$0.052 \pm 0.009$	$70 \pm 11$

state or LC-MS analyses. The structure of XcTDO<sup>7</sup> reveals a hydrogen bond (2.6 Å) between the indole NH of L-Trp and His55, which would be expected to lead to a steric clash between His55 and the methyl group of 1-Me-L-Trp. Indeed, a model of 1-Me-L-Trp binding to XcTDO (Figure S4) shows a nonbonding distance of  $\sim 1.5$  Å between the N $\epsilon$  of His55 and the carbon atom of the Me group on 1-Me-L-Trp. We propose that binding of 1-Me-L-Trp to XcTDO is weak as a consequence. Sequence alignments<sup>7</sup> indicate that hTDO also contains a histidine (His76) in the same position (in fact this histidine residue is conserved in all TDOs), so that the same steric restrictions apply and thus explain the observed inactivity. Substitution of histidine in XcTDO (H55A, H55S) and hTDO (H76S) allows accommodation of the additional methyl group, and turnover of 1-Me-L-Trp occurs (Table 1). This hypothesis is further supported by the fact that hIDO and S167A, which are both able to accommodate the bulky Me group in their active sites, are also able to oxidize 1-Me-L-Trp (Table 1).

Overall, turnover numbers for 1-Me-L-Trp are lower than those for L-Trp.<sup>6,8,14</sup> When X = Me (Scheme 2D), the inductive effect of the Me group would presumably stabilize the cation intermediate. This would not be expected to slow down the electrophilic attack but might affect other steps in the mechanism that our experiments do not address. A completely different binding location/orientation for 1-Me-L-Trp (and therefore a different mechanism) is also possible, but this is not supported by inhibition data (Table S1 and ref 10) which show 1-Me-L-Trp as a competitive inhibitor for L-Trp.

Since hIDO and variants of both hTDO and XcTDO can oxidize 1-Me-L-Trp, deprotonation of the indole NH cannot be essential for catalysis. Mechanisms involving abstraction of the indole proton, using either an active-site base<sup>3,15</sup> or dioxygen<sup>5,16</sup> (Scheme 2A, B), are therefore unlikely as they cannot proceed with a methyl group on N<sub>1</sub>.

The chemistry of indoles is very well documented<sup>4</sup> and does not occur by loss of the indole proton. Instead, when an indole reacts with an electrophile (e.g., O<sub>2</sub>), the lone pair on N<sub>1</sub> initiates the process (Scheme 2C) and the electrophile becomes attached preferentially at C<sub>3</sub> (Scheme 2D).<sup>17</sup> We propose this as a more likely mechanism for tryptophan oxidation in the heme dioxygenases, allowing both L-Trp and 1-Me-L-Trp to react (Scheme 2D), with the role of the iron merely as a donor of the required oxygen molecule. This mechanism is compatible with the absence of an active-site base in hIDO and avoids the need to deprotonate an N<sub>1</sub> atom with a  $pK_a$  ( $\approx 17$ )<sup>18</sup> that is out of range.<sup>18</sup> In addition, a recent density functional theory study<sup>19</sup> found that direct electrophilic

addition has a lower activation energy than a base-catalyzed deprotonation mechanism, consistent with our observations.

In conclusion, we report that 1-Me-L-Trp is a substrate for hIDO and variants of hTDO and XcTDO in which the active-site histidine has been replaced. This shows that deprotonation of the indole N<sub>1</sub> is not essential for catalysis, and we propose that direct electrophilic addition to dioxygen, facilitated by the lone pair on the indole N<sub>1</sub>, occurs instead.

**Acknowledgment.** We thank Dr. Sharad Mistry for helpful discussions. This work was supported by The Wellcome Trust (Grants 083636 to S.K.C. and E.R.).

**Supporting Information Available:** HPLC/NMR of 1-Me-L-Trp, spectra of *N*-formyl-kynurenine and *N*-formyl-methylkynurenine, steady-state data, and a model of the XcTDO/Me-Trp complex. This material is available free of charge via the Internet at <http://pubs.acs.org>.

## References

- (1) Yamamoto, S.; Hayaishi, O. *J. Biol. Chem.* **1967**, *242*, 5260.
- (2) Knox, W. E.; Mehler, A. H. *J. Biol. Chem.* **1950**, *187*, 419.
- (3) Sono, M.; Roach, M. P.; Coulter, E. D.; Dawson, J. H. *Chem. Rev.* **1996**, *96*, 2841.
- (4) Joule, J. A.; Mills, K. *Heterocyclic Chemistry* 2000, 4th ed.; Blackwell: Oxford; p 319.
- (5) Sugimoto, H.; Oda, S.; Otsuki, T.; Hino, T.; Yoshida, T.; Shiro, Y. *Proc. Natl. Acad. Sci. U.S.A.* **2006**, *103*, 2611.
- (6) Chauhan, N.; Basran, J.; Efimov, I.; Svistunenko, D. A.; Seward, H. E.; Moody, P. C.; Raven, E. L. *Biochemistry* **2008**, *47*, 4761.
- (7) Forouhar, F.; Anderson, J. L.; Mowat, C. G.; Vorobiev, S. M.; Hussain, A.; Abashidze, M.; Bruckmann, C.; Thackray, S. J.; Seetharaman, J.; Tucker, T.; Xiao, R.; Ma, L. C.; Zhao, L.; Acton, T. B.; Montelione, G. T.; Chapman, S. K.; Tong, L. *Proc. Natl. Acad. Sci. U.S.A.* **2007**, *104*, 473.
- (8) Thackray, S. J.; Bruckmann, C.; Anderson, J. L.; Campbell, L. P.; Xiao, R.; Zhao, L.; Mowat, C. G.; Forouhar, F.; Tong, L.; Chapman, S. K. *Biochemistry* **2008**, *47*, 10677.
- (9) All proteins were isolated as described previously.<sup>6,7,14</sup>
- (10) Cady, S. G.; Sono, M. *Arch. Biochem. Biophys.* **1991**, *291*, 326.
- (11) Commercially available 1-Me-L-Trp (95% purity) was purified by HPLC to remove contaminating species which could act as substrate (Figure S1A), and the purity was confirmed by further HPLC and <sup>1</sup>H NMR (Figure S1B, C).
- (12) Steady-state assays contained sodium ascorbate (20 mM), methylene blue (10  $\mu\text{M}$ ), catalase (10  $\mu\text{g}$ ), 1-Me-L-Trp (variable), and enzyme (1–5  $\mu\text{M}$ ),<sup>6,7</sup> in either 50 mM Tris/HCl buffer, pH 8.0 (hIDO and hTDO and respective variants), or 100 mM phosphate buffer, pH 7.5 (XcTDO and variants). Reactions were allowed to proceed for at least 1 h and then quenched by addition of 30% (v/v) trichloroacetic acid, followed by centrifugation to remove the enzyme. Values for  $K_i$  were measured in the same way by varying [L-Trp] as above through differing concentrations of 1-Me-L-Trp. Data were analyzed by plotting  $1/v$  (the observed rate) against  $1/[L-Trp]$ .
- (13) The corresponding LC-MS data for these proteins also showed ions at 251, as for hIDO (data not shown).
- (14) Basran, J.; Rafice, S. A.; Chauhan, N.; Efimov, I.; Cheesman, M. R.; Ghamsari, L.; Raven, E. L. *Biochemistry* **2008**, *47*, 4752.
- (15) Leeds, J. M.; Brown, P. J.; McGeehan, G. M.; Brown, F. K.; Wiseman, J. S. *J. Biol. Chem.* **1993**, *268*, 17781.
- (16) Terentis, A. C.; Thomas, S. R.; Takikawa, O.; Littlejohn, T. K.; Truscott, R. J.; Armstrong, R. S.; Yeh, S. R.; Stocker, R. *J. Biol. Chem.* **2002**, *277*, 15788.
- (17) Attack at C<sub>3</sub> generates a positive charge on C<sub>2</sub> which is resonance stabilized by the lone pair on N<sub>1</sub> (Scheme 2D). Attack at C<sub>2</sub>, as proposed recently,<sup>19</sup> is less favourable and not observed in indole chemistry because this generates a positive charge on C<sub>3</sub>, which is less well stabilized (through the benzene ring). This preference for attack at C<sub>3</sub> would also apply for radical addition.<sup>19</sup>
- (18) Yagil, G. *Tetrahedron* **1967**, *23*, 2855.
- (19) Chung, L. W.; Li, X.; Sugimoto, H.; Shiro, Y.; Morokuma, K. *J. Am. Chem. Soc.* **2008**, *12299*.

JA808326G

## Reassessment of the Reaction Mechanism for the Heme Dioxygenases

Nishma Chauhan,<sup>†</sup> Sarah J. Thackray,<sup>‡</sup> Sara A. Rafice,<sup>†</sup> Graham Eaton,<sup>†</sup> Michael Lee,<sup>†</sup> Igor Efimov,<sup>†</sup> Jaswir Basran,<sup>§</sup> Paul R. Jenkins,<sup>†</sup> Christopher G Mowat,<sup>‡</sup> Stephen K. Chapman,<sup>\*,‡</sup> and Emma Lloyd Raven<sup>\*,†</sup>

<sup>†</sup> Department of Chemistry, University of Leicester, University Road, Leicester, LE1 7RH, U.K., <sup>‡</sup> EaStCHEM, School of Chemistry, University of Edinburgh, West Mains Road, Edinburgh EH9 3JJ, U.K., and <sup>§</sup> Department of Biochemistry, University of Leicester, Lancaster Road, Leicester, LE1 9HN, UK.

### Supporting information

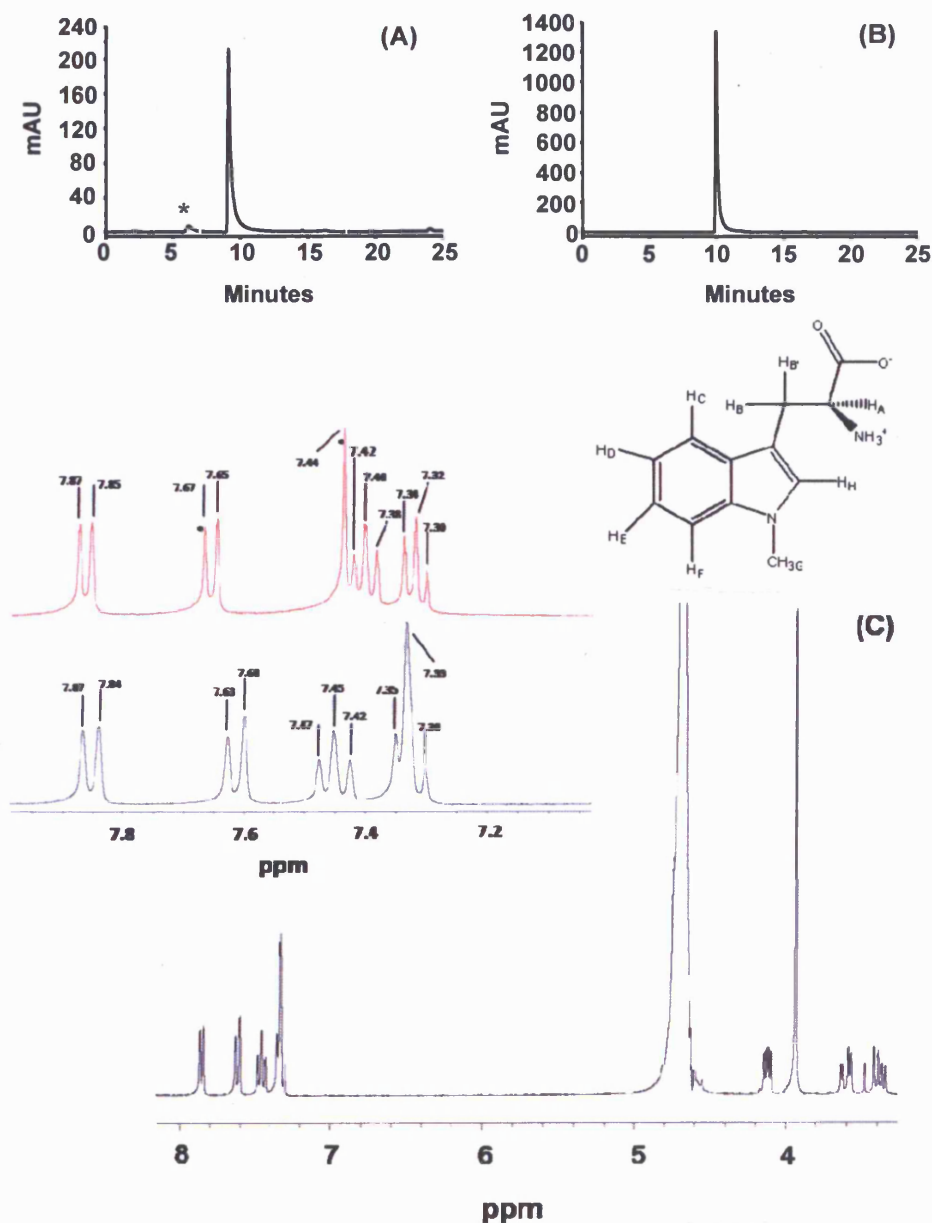


**Figure S1.** Chromatogram of commercially available 1-Me-L-Trp (A) before and (B) after purification by HPLC. The HPLC retention time for L-Trp (data not shown) was found to be identical to the contaminating species labeled \* in (A). (C) NMR spectrum of purified 1-Me-L-Trp from (B). <sup>1</sup>H NMR (300 MHz, D<sub>2</sub>O/CD<sub>3</sub>CN)  $\delta$  3.33-3.65 (m, 2H, H<sub>B</sub> + H<sub>B'</sub>), 3.93 (s, 3H, H<sub>C</sub>), 4.12 (dd, 1H, J = 8.2 Hz, 4.7 Hz, H<sub>A</sub>), 7.33 (s + t, 2H, J = 7.5 Hz, H<sub>H</sub> + H<sub>D/E</sub>), 7.45 (t, 1H, J = 7.5 Hz, H<sub>D/E</sub>), 7.61 (d, 1H, J = 8.5 Hz, H<sub>C/F</sub>), 7.85 (d, 1H, J = 8.1 Hz, H<sub>C/F</sub>). Inset: <sup>1</sup>H NMR spectra of commercially available L-Trp (red) and purified 1-Me-L-Trp (black) expanded between the 7-8 ppm region. \* indicates the peaks that have shifted significantly in respect to the spectrum of 1-Me-L-Trp and therefore confirm the removal of L-Trp from purified 1-Me-L-Trp. HPLC conditions: wavelength - 280 nm; column - RP C18, 250 x 4.6 mm; eluant - H<sub>2</sub>O:MeCN, 90:10 v/v; flow rate - 1 ml/min. NMR conditions: machine - Bruker DPX300; basic frequency - <sup>1</sup>H = 300.03 MHz; spectral width 16 ppm.

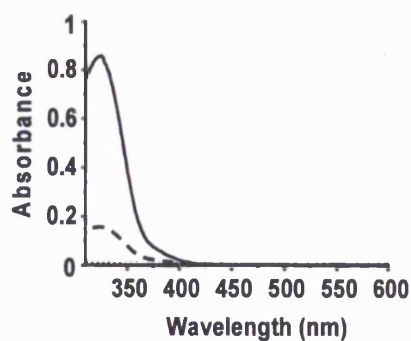


**Figure S2.** UV-visible spectrum of *N*-formyl-kynurenine (solid line) and *N*-formyl-methylkynurenine (dashed line) showing absorption bands at 321 nm. Spectra were obtained after isolation of the compounds from steady state assays with hIDO. Parallel experiments carried out with 1-Me-L-Trp in the absence of enzyme show no product formation at 321 nm (dotted line).

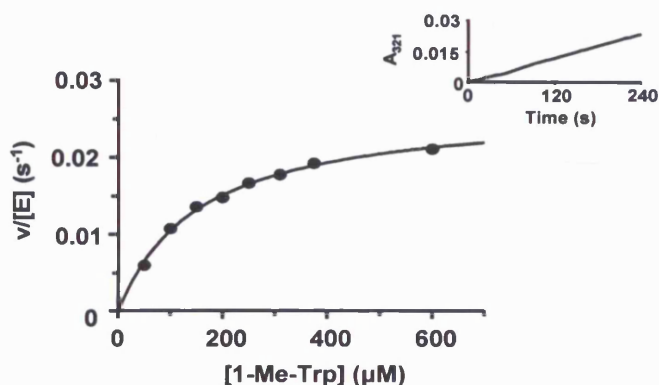


**Figure S3.** Steady state oxidation of 1-Me-L-Trp by hIDO. Solid line shows a fit of the data to the Michaelis-Menten equation. Inset: Time-dependence of absorbance changes at 321 nm, which report on *N*-formyl-methylkynurenine formation. Conditions: Tris/HCl buffer, pH 8.0, 25.0 °C. Reactions in the presence and absence of enzyme (Figure S2) confirm that product formation is due to enzymatic oxidation alone.

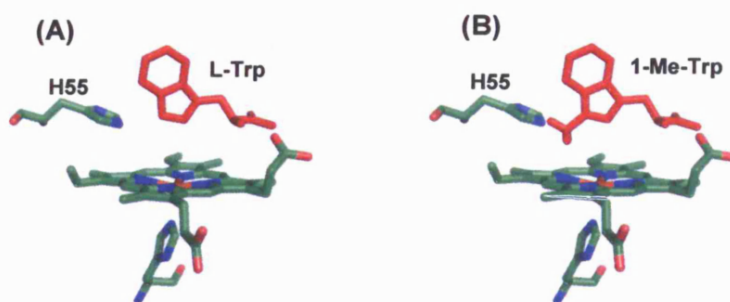


**Figure S4.** (A) Crystal structure of XcTDO in complex with (A) L-Trp<sup>8</sup>; (B) A model of 1-Me-L-Trp binding to XcTDO generated by overlay of 1-Me-L-Trp on the L-Trp coordinates in (A).

**Table S1.** Inhibition data ( $K_i$ ) for inhibition of L-Trp oxidation by 1-Me-L-Trp (dash indicates no measurable activity).

<sup>a</sup> The high  $K_M$  in this case meant that a reliable measure of  $K_i$  was not accessible.

	Variant	$K_i$ ( $\mu\text{M}$ )
hIDO	native	$3.4 \pm 0.4$
	S167A	$2.2 \pm 0.2$
hTDO	native	-
	H76S	<sup>a</sup>
XcTDO	native	-
	H55A	$150 \pm 10$
	H55S	$400 \pm 50$

## A Kinetic, Spectroscopic, and Redox Study of Human Tryptophan 2,3-Dioxygenase<sup>†</sup>

Jaswir Basran,<sup>‡</sup> Sara A. Rafice,<sup>§</sup> Nishma Chauhan,<sup>§</sup> Igor Efimov,<sup>§</sup> Myles R. Cheesman,<sup>||</sup> Lila Ghamsari,<sup>‡</sup> and Emma Lloyd Raven<sup>\*,\*‡</sup>

Department of Biochemistry, Henry Wellcome Building, University of Leicester, University Road, Leicester LE1 7RH, England, Department of Chemistry, University of Leicester, Lancaster Road, Leicester LE1 9HN, England, and School of Chemical Sciences and Pharmacy, University of East Anglia, Norwich NR4 7TJ, England

Received December 8, 2007; Revised Manuscript Received February 7, 2008

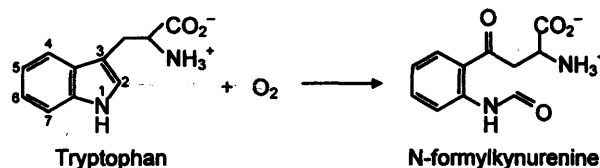
**ABSTRACT:** The family of heme dioxygenases, as exemplified by indoleamine 2,3-dioxygenase and tryptophan 2,3-dioxygenase, catalyzes the oxidative cleavage of L-tryptophan to *N*-formylkynurenine. Here, we describe a bacterial expression system for human tryptophan 2,3-dioxygenase (rhTDO) together with spectroscopic, kinetic, and redox analyses. We find unexpected differences between human tryptophan 2,3-dioxygenase and human indoleamine 2,3-dioxygenase [Chauhan et al. (2008) *Biochemistry* 47, 4761–4769]. Thus, in contrast to indoleamine 2,3-dioxygenase, the catalytic ferrous–oxy complex of rhTDO is not observed, nor does the enzyme discriminate against substrate binding to the ferric derivative. In addition, we show that the rhTDO is also catalytically active in the ferric form. These new findings illustrate that significant mechanistic differences exist across the heme dioxygenase family, and the data are discussed within this broader framework.

The L-kynurenine pathway, which leads to the formation of NAD, is the major catabolic route of L-tryptophan metabolism in biology. The initial step in this pathway is oxidation of L-tryptophan to *N*-formylkynurenine (Scheme 1). In all biological systems examined to date, this is catalyzed by one of two heme enzymes, tryptophan 2,3-dioxygenase (TDO)<sup>1</sup> or indoleamine 2,3-dioxygenase (IDO), in a reaction mechanism that involves binding of O<sub>2</sub> to ferrous heme.

In mammalian systems, IDO is ubiquitously distributed but is not found in the liver; tryptophan 2,3-dioxygenase, on the other hand, is found exclusively in the liver (1). For the mammalian enzymes, the best information that is available so far is for human IDO. In this case, new expression systems (2–4) have allowed the first functional information to emerge. More recently, a crystal structure for human IDO has been published (5).

In this paper, we report an expression system for recombinant human TDO and describe spectroscopic, kinetic, and redox analyses on the purified protein. We find unexpected

Scheme 1: Reaction Catalyzed by TDO, with IUPAC Numbering Indicated



differences between human TDO and human IDO (6) in terms of both substrate binding and the catalytic reaction intermediates. These new data considerably widen the scope of information available on the heme dioxygenase enzymes, and we use it to make functional comparisons both with human IDO and more generally across the heme dioxygenase family.

### EXPERIMENTAL PROCEDURES

**Materials.** L-Ascorbate, bovine liver catalase, DNase I, D-glucose, glucose oxidase, methylene blue, Nile blue chloride, xanthine, xanthine oxidase, L-tryptophan, and substrate analogues were purchased from Sigma-Aldrich Co. Restriction enzymes and DNA-modifying enzymes were from MBI fermentas. *Escherichia coli* strain BL21(DE3) pLysS was from Novagen. Hemin was obtained from Fluka.

**Cloning and Expression of Recombinant Human TDO.** The gene encoding human TDO was isolated by PCR amplification from a cDNA clone (IMAGE clone ID 4071714) obtained from a human liver cDNA library. The primers 5' GCC TTT TCA CCA TGG CGG GGT GCC CAT TTT TAG G 3' (forward primer) and 5' CAT AGA TTT TGC AGA CGC TCG AGA TCT GAT TCA TCA C 3' (reverse primer) were designed with reference to the published

<sup>†</sup> This work was supported by grants from BBSRC (project grants BB/C00602X/1 and IIP0206/009), EPSRC (studentships to S.R. and N.C.), and The Leverhulme Trust (fellowship to E.L.R.).

\* To whom correspondence should be addressed. Telephone: +44 (0)116 229 7047. Fax: +44 (0)116 252 3789. E-mail: emma.raven@le.ac.uk.

<sup>‡</sup> Department of Biochemistry, University of Leicester.

<sup>§</sup> Department of Chemistry, University of Leicester.

<sup>||</sup> School of Chemical Sciences and Pharmacy, University of East Anglia.

<sup>1</sup> Abbreviations: TDO, tryptophan 2,3-dioxygenase; rhTDO, recombinant human tryptophan 2,3-dioxygenase; xTDO, *Xanthomonas campestris* tryptophan 2,3-dioxygenase; IDO, indoleamine 2,3-dioxygenase; rhIDO, recombinant human indoleamine 2,3-dioxygenase; L-Trp, L-tryptophan.

sequence of the gene encoding TDO (GenBank number BC005355) and incorporated 5' *Nco*I and 3' *Xho*I restriction sites (underlined). The *Nco*I–*Xho*I PCR fragment was cloned into pET28a (Novagen) to produce plasmid pEThtDO8, which encodes a C-terminal hexahistidine fusion of TDO cleavable with thrombin. DNA sequencing (Protein and Nucleic Acid Laboratory, University of Leicester) confirmed that no spurious mutations had arisen during the PCR.

For expression of recombinant human TDO (rhTDO), transformed cells of *E. coli* strain BL21(DE3)pLysS harboring the pEThtDO8 expression plasmid were grown overnight at 37 °C in LB media supplemented with 30 µg/mL kanamycin. The overnight culture (10 mL) was used to inoculate 0.5 L of 2× YT media containing 30 µg/mL kanamycin. The cultures were grown at 37 °C until the optical density at 600 nm reached a value of ~0.8, and then isopropyl 1-thio-β-D-galactopyranoside (to a final concentration of 0.2 mM) and 0.5 mL of 3 mM hemin (in 10 mM NaOH) were added. The temperature was reduced to 25.0 °C and the incubation continued overnight. Cells were harvested by centrifugation (15 min, 6000 rpm, 4 °C) and stored at –80 °C.

**Protein Purification and Handling.** Cell pellets were resuspended in lysis buffer (50 mM NaH<sub>2</sub>PO<sub>4</sub>, 300 mM NaCl, 10 mM imidazole, pH 8.0) supplemented with two Complete protease inhibitor tablets (Roche) and lysed by the addition of 5 mg of lysozyme and by sonication (6 × 30 s pulses with 30 s intervals using a MSE Soniprep 150 sonicator). After sonication, DNase I was added and the suspension stirred for 30 min at 4 °C. The lysate was centrifuged at 18000 rpm for 50 min, and the cell-free extract loaded onto a 20 mL column of Ni-NTA Superflow resin (Qiagen) equilibrated in lysis buffer. The resin was washed with 300 mL of wash buffer (50 mM NaH<sub>2</sub>PO<sub>4</sub>, 300 mM NaCl, 20 mM imidazole, pH 8.0), and the protein was eluted using a linear gradient ranging from 20 to 250 mM imidazole in 50 mM NaH<sub>2</sub>PO<sub>4</sub> and 300 mM NaCl, pH 8.0. TDO-containing fractions were pooled and dialyzed against 50 mM Tris-HCl buffer, pH 8.0, and frozen in aliquots at –80 °C.

**Reconstitution of TDO.** rhTDO isolated from *E. coli* exists as a mixture of apo- and holoenzyme forms. For this reason rhTDO was reconstituted with hemin prior to use in biochemical studies. rhTDO (typically 100 µM) was mixed with 1.5 equiv of hemin and incubated on ice in the dark for 1–2 h. Free hemin was removed from the protein by passage through a small gel filtration (Bio-Rad 10 DG) column and the eluant concentrated using a Centricon YM-30 (30 kDa) filtration unit. An absorption coefficient of ε<sub>408</sub> = 196 mM<sup>-1</sup> cm<sup>-1</sup> was determined for ferric rhTDO using the pyridine–hemochromagen procedure (7).

**Steady-State Kinetic Assays.** TDO activity was measured by monitoring the formation of *N*-formylkynurenine at 321 nm. Steady-state kinetic measurements were carried out using a Varian Cary 50 probe UV–visible spectrophotometer with a 1 cm light path. Reactions were performed at 25.0 °C in 50 mM Tris-HCl buffer, pH 8.0, containing 10 µM methylene blue, 100 µg of catalase, 20 mM L-ascorbate, and a fixed concentration of rhTDO. The reaction was initiated by the addition of tryptophan (or tryptophan analogue), and initial rates were calculated from the absorbance increase at 321 nm [ε<sub>321</sub> = 3750 M<sup>-1</sup> cm<sup>-1</sup> (2)]. Apparent *K*<sub>M</sub> and *k*<sub>cat</sub> values were determined by varying the concentration of each

substrate and fitting the data to the Michaelis–Menten equation using the Grafit software package (8).

**Electronic Spectroscopy.** All absorbance spectra and equilibrium ligand binding experiments were measured in 50 mM Tris-HCl buffer, pH 8.0, at 25.0 °C using a Varian Cary 50 probe UV–visible spectrophotometer. Ferrous rhTDO was generated by stoichiometric titration of the ferric enzyme with sodium dithionite. The ferrous–oxy and ferrous–CO derivatives were generated by direct bubbling of O<sub>2</sub> and CO gases, respectively, through dithionite-reduced samples. Absorption spectra for rhTDO ferric–azide, ferric–fluoride, and ferrous–cyanide complexes were recorded in the presence of 5 M, 1 M, and 15 mM ligand, respectively.

Equilibrium binding constants, *K*<sub>D</sub>, for binding of various ligands to ferric and ferrous forms of rhTDO were determined according to published procedures (9) and typically involved the addition of small volumes (0.5–2.0 µL) of ligand (from an appropriate stock solution) to the protein (~1–5 µM) until no further spectral change occurred. Binding constants were determined spectrophotometrically by monitoring the change in absorbance at the appropriate wavelength and fitting to eq 1:

$$\Delta A_{\text{abs}} = (K_D A_i + [L]_{\text{tot}} A_f) / (K_D + [L]_{\text{tot}}) \quad (1)$$

where *A*<sub>i</sub> and *A*<sub>f</sub> are the initial and final absorbance values, respectively, and [L]<sub>tot</sub> is the total concentration of the ligand. The binding of CO to the ferrous enzyme in the presence (4 mM) and absence of L-Trp was followed at 421 nm; the *K*<sub>D</sub> for CO binding to the ferrous–Trp complex was calculated using eq 2, which was used instead of eq 1 because of the tighter binding affinity:

$$\Delta A = \frac{\Delta A_{\infty}}{2[E]} [E + L + K_D - \{(E + L + K_D)^2 - 4[E][L]\}^{1/2}] \quad (2)$$

where [E] and [L] represent the calculated concentrations of total enzyme and total ligand, respectively, after each addition and Δ*A* and Δ*A*<sub>∞</sub> are the absorbance changes corresponding to intermediate and saturating ligand concentrations. Binding constants were also determined kinetically, using stopped flow (*vide infra*).

**EPR Spectroscopy.** EPR spectra were recorded using a Bruker ER300D spectrometer fitted with a dual-mode cavity, type ER4116M, interfaced to an ELEXYS computer control system (Bruker Analytische Messtechnik GmbH) and equipped with a variable temperature cryostat and liquid helium transfer line (Oxford Instruments). EPR simulations were performed using the Bruker program WINEPR Simfonia (v1.25). Determination of low-spin heme concentrations was achieved by simulation and double integration of spectra recorded under nonsaturating conditions at 15 K using 1 mM Cu(II)-EDTA as a spin standard. Enzyme samples were prepared in 50 mM potassium phosphate, pH 8.0. For samples in the presence of L-Trp, the substrate (10 mM stock solution in buffer) was added to a final concentration of 3 mM and then frozen immediately to prevent oxidation of the substrate. Final concentrations of enzyme were 60 µM in both cases.

**Stopped-Flow Kinetics.** Stopped-flow experiments were carried out using an Applied Photophysics SX.18 MV

Table 1: Absorption Maxima (nm) for rhTDO (50 mM Tris-HCl Buffer, pH 8.0, 25.0 °C)

derivative	rhTDO	rat liver <sup>a</sup>	<i>B. brevis</i> <sup>b</sup>	<i>P. fluorescens</i> <sup>c</sup>
ferric	408, 533, 621	406, 498, 632	407, 500, 630	405, 500, 635
ferric + L-Trp	410, 536, 565 sh <sup>d</sup>	407, 498, 632 <sup>d</sup>		
ferrous	428, 533, 560	430, 557	432, 555, 585	432, 553, 588
ferrous + L-Trp	426, 533, 560	421, 557 <sup>d</sup>		
ferrous-cyanide	430, 534, 564			
ferrous-oxy	413 <sup>e</sup>			
ferrous-CO	421, 540, 564	420, 538, 569		
ferrous-CO + L-Trp	421, 540, 564	420, 538, 569		
ferric-azide	415, 540 <sup>f</sup>			
ferric-cyanide	419, 538, 566 sh			
ferric-fluoride	406, 527, 633 <sup>g</sup>			

<sup>a</sup> Taken from ref 15. <sup>b</sup> Taken from ref 16. Only the ferric and ferrous derivatives have been reported. <sup>c</sup> Taken from ref 14. Only the ferric and ferrous derivatives have been reported. <sup>d</sup> Assumed (i.e., authors have stated there is no spectral change upon addition of substrate). <sup>e</sup> This derivative shows only a broad, featureless spectrum in the visible region, with no evidence of the characteristic oxy peaks. There is a broad peak with a maximum at  $\approx 526$  nm. <sup>f</sup> Binding of these ligands to rhTDO is substantially weaker than for cyanide, meaning that dissociation constants could not be calculated accurately for these complexes. <sup>g</sup> sh = shoulder.

stopped-flow spectrophotometer. Unless otherwise stated, measurements were carried out at 25.0 °C in 50 mM Tris-HCl buffer, pH 8.0. For experiments performed under anaerobic conditions, the sample-handling unit of the stopped-flow instrument was contained within a Belle Technology glovebox. Buffers were made anaerobic by bubbling oxygen-free nitrogen gas through solutions for  $\sim 2$  h. Buffers were then placed in the glovebox overnight to remove any residual traces of oxygen. Solutions of dithionite and substrate were made by adding the appropriate solid to anaerobic buffer. Stopped-flow, multiple-wavelength absorption studies were carried out using a photodiode array detector and X-SCAN software (Applied Photophysics Ltd.). In single wavelength studies, changes in absorbance were monitored at 408 nm. Transients were either monophasic or biphasic and were fitted using the standard single or double exponential equations, respectively.

**Mass Spectrometry.** Protein bands of interest were excised from an SDS gel and subjected to in-gel trypsin digestion (10). Proteolytic peptide fragments were analyzed by MALDI-ToF mass spectrometry: the sample was mixed 1:1 with  $\alpha$ -cyano-4-hydroxycinnamic acid (5 mg/mL in 0.1% TFA/50% acetonitrile), spotted onto a stainless steel MALDI target plate, and analyzed using a Voyager DE-STR MALDI-ToF mass spectrometer (Applied Biosystems). The resulting peptide masses were analyzed against the NCBI protein database using the MASCOT search algorithm (Matrix Science, London, U.K.). A 95% significance threshold was used for validating statistically significant identifications.

**Redox Potentiometry.** Reduction potentials for  $\text{Fe}^{3+}/\text{Fe}^{2+}$  of rhTDO were determined by the reduction of a dye with a known potential (11). The assay solution contained potassium phosphate buffer (0.1 M, pH 7.0), glucose (5 mM), xanthine (300  $\mu\text{M}$ ), xanthine oxidase (50 nM), glucose oxidase (50  $\mu\text{g}/\text{mL}$ ), catalase (5  $\mu\text{g}/\text{mL}$ ), enzyme (2  $\mu\text{M}$ ), and either the dye nile blue chloride [ $E^{\circ} = -116$  mV (12)] or the dye methylene blue [ $E^{\circ} = +11$  mV (12)]. The components glucose, glucose oxidase, and catalase generated an oxygen-free environment. The absorbance change for the heme peak was measured at the isosbestic point for the dye at 410 nm, and the absorbance change for the dye was measured at the isosbestic point for the heme peak at 635 nm using a Perkin-Elmer Lambda 40 spectrophotometer; at these wavelengths there is no absorption from the other components of the reaction solution.

The results were analyzed using the Nernst equations [ $25$  mV  $\ln(E_{\text{ox}}/E_{\text{red}})$ ] and [ $12.5$  mV  $\ln(D_{\text{ox}}/D_{\text{red}})$ ], where  $E_{\text{ox}}/E_{\text{red}}$  and  $D_{\text{ox}}/D_{\text{red}}$  are the oxidized and reduced forms of the enzyme and dye, respectively, thus producing a linear graph, with a slope of 1 across a wide potential range (6). Determination of the relationship between equilibrium binding constants for oxidized,  $K_{\text{ox}}$ , and reduced,  $K_{\text{red}}$ , proteins and the reduction potential was according to the thermodynamic cycle in eq 3:

$$K_{\text{ox}}/K_{\text{red}} = \exp[F(E^{\text{bound}} - E^{\text{free}})/RT] \quad (3)$$

where  $K_{\text{ox}}$  and  $K_{\text{red}}$  are equilibrium binding constants for oxidized and reduced rhTDO, respectively,  $E^{\text{bound}}$  and  $E^{\text{free}}$  are the redox potentials of rhTDO bound to L-tryptophan and free protein, respectively,  $R$  is the gas constant,  $F$  is the Faraday constant, and  $T$  is the temperature.

## RESULTS

**Protein Expression and Purification.** Recombinant human TDO was expressed in *E. coli* as a full-length, C-terminal hexahistidine fusion protein. An expression system for rat TDO has been previously reported (13). Our expression system for rhTDO gave yields of purified protein of  $\approx 15$  mg/L. Trypsin digestion of a sample of enzyme followed by MALDI-ToF mass spectrometry gave clear indication that the protein band is indeed rhTDO (Supporting Information, Figure S1).

**Electronic Spectroscopy.** The absorption maxima for various ferric and ferrous derivatives of rhTDO are given in Table 1. Maxima for a few derivatives have been published for the rat liver enzyme and for the bacterial *Bacillus brevis* and *Pseudomonas fluorescens* enzymes (14–16);<sup>2</sup> these are compared with rhTDO in Table 1. The spectrum of the ferric form of rhTDO has maxima at 408, 533, and 621 nm (Table 1 and Figure 1A), consistent with there being a mixture of high- and low-spin heme species. As observed previously for human IDO (3), the binding of L-Trp to ferric rhTDO leads to a red shift of the Soret band (to 410 nm), increases in the low-spin signatures at 536 and 565 nm, and decreases

<sup>2</sup> For these other TDOs, there is very limited information available. The majority of the published information is summarized in Table 1, but  $k_{\text{cat}}$  and  $K_{\text{M}}$  values have also been reported, as discussed in the text below.

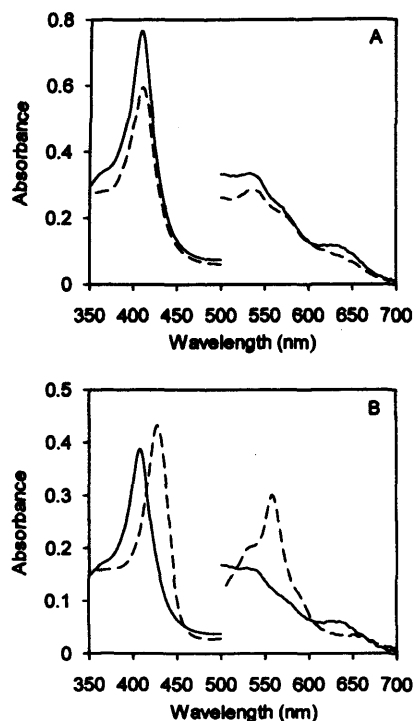


FIGURE 1: Electronic absorption spectra of rhTDO. (A) Ferric rhTDO in the absence (solid line) and presence (dashed line) of L-Trp. (B) Ferric rhTDO (solid line) and ferrous rhTDO (dashed line). Absorbance values in the visible region have been multiplied by a factor of 4. Reaction conditions: 50 mM Tris-HCl, pH 8.0, 25.0 °C.

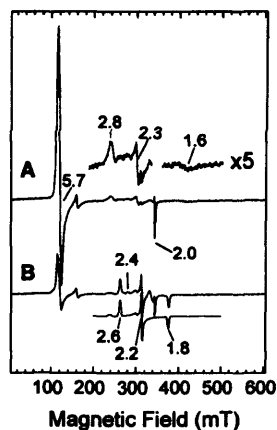


FIGURE 2: X-band EPR spectra of rhTDO in the absence (A) and presence (B) of L-Trp. Spectra were recorded at a temperature of 10 K using 2.01 mW microwave power at a frequency of 9.67 GHz and a modulation amplitude of 1 mT. Spectra are adjusted to account for differences in receiver gain. The trace below the experimental spectrum in (B) is a simulation of the contributions from two low-spin hemes with  $g_{\text{xy}}$ -values and line widths ( $W_{\text{yx}}$ ) as follows: species a, 2.632, 2.202, 1.835 (4.1, 2.3, 3.6 mT); species b, 2.892, 2.297, 1.620 (8.0, 5.7, 20.0 mT).

in absorbance at 621 nm (Figure 1A), all of which are consistent with the formation of a low-spin heme species on addition of substrate.

Reduction of ferric rhTDO results in a red shift in the Soret band (from 408 to 428 nm) and the formation of a sharp peak in the visible region (560 nm) (Figure 1B).

**EPR Spectroscopy.** Figure 2A shows the low-temperature X-band EPR spectrum of rhTDO and is dominated by an axial spectrum ( $g_{\text{xy}} = 5.71$ ,  $g_z = 2.01$ ) typical of high-spin ferric heme. The presence of a minority low-spin form

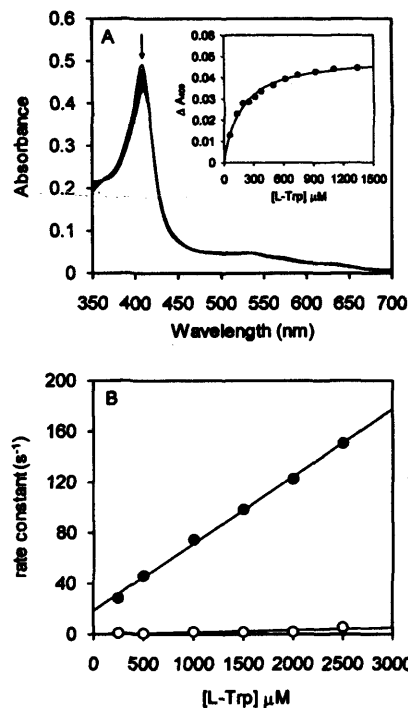


FIGURE 3: Reaction of ferric rhTDO (2.5 μM) with L-Trp. (A) Representative data set for the determination of  $K_D$  for binding of L-Trp to rhTDO. The arrow indicates the direction of change in absorbance upon successive additions of L-Trp. Inset: Absorbance change at 409 nm upon successive additions of L-Trp and fit of the data to eq 1. (B) Dependence of the rate constant on concentration for the fast (closed circles) and slow (open circles) phases of the biphasic reaction of rhTDO with substrate (monitored at 408 nm). Reaction conditions: 50 mM Tris-HCl, pH 8.0, 25.0 °C.

(species b) is evident ( $g = 2.89, 2.30, 1.62$ ) and is shown in the expansion in Figure 2A. These high- and low-spin species correlate with those observed for rhIDO [ $g = 5.82, 1.99$  and  $g = 2.85, 2.27, 1.62$ , respectively (6)], although there is a higher proportion of high-spin heme for ferric rhTDO than in the corresponding spectrum for rhIDO.

On addition of substrate (Figure 2B), there is a substantial decrease in the level of the high-spin species coupled with the emergence of a new low-spin form (species a) with  $g$ -values of 2.63, 2.20, 1.84. These  $g$ -values correspond with those previously observed for ferric rhIDO in the presence of L-Trp [ $g = 2.52, 2.19, 1.86$  (3)] and have been assigned as arising from hydroxide-bound heme. A similar assignment is proposed here for rhTDO, which is in agreement with the UV-visible data presented above. Underneath the spectrum shown in Figure 2B is a simulation of the spectrum of both this new low-spin species a plus a residual amount of species b.

**Binding of L-Trp to Ferric rhTDO.** Absorbance changes observed upon binding of L-Trp to ferric rhTDO (under anaerobic conditions, Figure 3A) give a dissociation constant,  $K_D$ , of  $170 \pm 11 \mu\text{M}$  (Figure 3A, inset). The binding of L-Trp was also measured kinetically under pseudo-first-order conditions ( $[\text{L-Trp}] \gg [\text{rhTDO}]$ ). Absorption changes at 408 nm were biphasic with the first phase contributing the majority (60–70%) of the total amplitude change. The observed pseudo-first-order rate constant for the fast phase ( $k_{\text{obs1}}$ ) was linearly dependent on L-Trp concentration (Figure 3B) and gives a slope ( $=k_{\text{on}}$ ) of  $0.053 \pm 0.001 \mu\text{M}^{-1} \text{s}^{-1}$  and intercept ( $=k_{\text{off}}$ ) of  $18.5 \pm 2 \text{s}^{-1}$ . The calculated  $K_D$

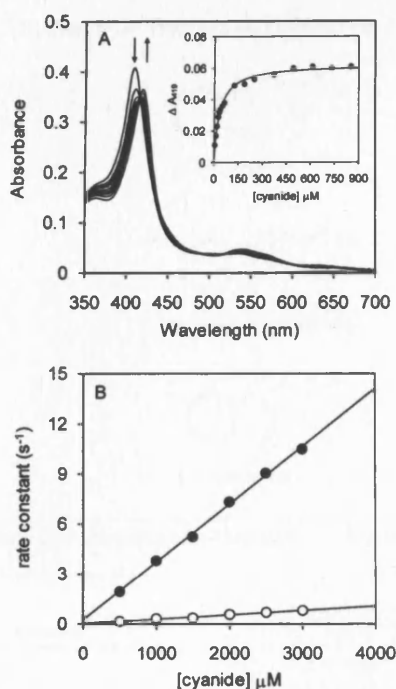


FIGURE 4: Reaction of ferric rhTDO (2.0  $\mu\text{M}$ ) with cyanide. (A) Representative data set for the determination of  $K_D$  for binding of cyanide to rhTDO. The arrows indicate the direction of changes in absorbance upon successive additions of cyanide. Inset: Absorbance change at 419 nm upon successive additions of cyanide and fit of the data to eq 1. (B) Dependence of the rate constant on concentration for the fast (closed circles) and slow (open circles) phases of the biphasic reaction of rhTDO with cyanide (monitored at 419 nm). Reaction conditions: 50 mM Tris-HCl, pH 8.0, 25.0  $^{\circ}\text{C}$ .

( $=k_{\text{off}}/k_{\text{on}}$ ) is thus  $349 \pm 44 \mu\text{M}$ , similar to that obtained by equilibrium titration (*vide supra*). The observed rate constant for the second phase ( $k_{\text{obs},2}$ ) was weakly dependent on L-Trp concentration (Figure 3B). We assign this biphasic behavior as arising from the existence of multiple heme conformers that are in slow equilibrium.

**Binding of Cyanide to Ferric rhTDO.** The equilibrium dissociation constant for the rhTDO–cyanide complex was calculated to be  $33 \pm 1.7 \mu\text{M}$  (Figure 4A and inset). In stopped-flow experiments, binding of cyanide to ferric rhTDO also occurred in two phases (as for L-Trp, above) with the first phase contributing  $\approx 60\%$  to the total absorption change. Each phase was linearly dependent on cyanide concentration with second-order rate constants of  $0.0035 \mu\text{M}^{-1} \text{s}^{-1}$  and  $0.0003 \mu\text{M}^{-1} \text{s}^{-1}$  for the fast and slow phases, respectively (Figure 4B). In this case, however, the intercepts are very close to zero and have large errors, making it difficult to calculate a  $K_D$  value with confidence.

**Steady-State Oxidation of L- and D-Trp.** Steady-state kinetic parameters for rhTDO with L-Trp and a number of substrate analogues (Scheme 2) are shown in Table 2. For comparison, data for rhIDO are also given. For rhTDO with L-Trp,  $k_{\text{cat}} = 1.4 \pm 0.02 \text{ s}^{-1}$  and  $K_M = 222 \pm 15 \mu\text{M}$ . The steady-state turnover rate ( $k_{\text{cat}}$ ) for both dioxygenases is the same ( $1.4 \text{ s}^{-1}$ ), although substrate binding for L-Trp is at least 20-fold weaker for rhTDO ( $K_M \approx 220 \mu\text{M}$  compared with  $\approx 10 \mu\text{M}$  for rhIDO). Similar values for  $k_{\text{cat}}$  and  $K_M$  have very recently been reported for a truncated form of rhTDO (17).

IDO from a number of different sources has been shown to be capable of catalytic turnover with the D-stereoisomer of Trp (1, 18–20). This is also true for the human enzyme ( $k_{\text{cat}} = 3.93 \text{ s}^{-1}$ , Table 2), although the  $K_M$  value is  $>100$ -fold higher than for L-Trp, suggesting much weaker binding for D-Trp. For rhTDO, there is evidence for oxidation of D-Trp, but the activity is very low (Table 2). Given the relative binding affinities of the two enzymes for L-Trp (rhIDO  $>$  rhTDO) and of the two substrates for the two enzymes (L-Trp  $>$  D-Trp), this poor activity is probably a result of very weak binding of D-Trp to rhTDO.

**Steady-State Oxidation of Other Trp Analogues.** The heme dioxygenases can support insertion of  $\text{O}_2$  into a number of ring-substituted tryptophan analogues. For rhIDO, substitutions at the 5-position of the indole ring (Scheme 1) are tolerated, and there is little effect on the affinity of these substituted analogues for the enzyme (Table 2). On the other hand, no detectable activity was observed with analogues in which either the amino group or the carboxylate group of the aliphatic side chain has been modified or is absent (Table 2).

For rhTDO, the only L-Trp analogues which could be oxidized were 5-fluoro-L-Trp and 5-methyl-L-Trp (although the latter very slowly, Table 2); all other derivatives tested gave no observable catalytic activity.

**Oxidation of L-Trp by Ferric rhTDO.** The steady-state assays above use ferrous rhTDO as the catalytically reactive form of the enzyme. However, we also observed activity with the ferric form of rhTDO. Incubation of ferric rhTDO with 2 mM L-Trp (50 mM Tris-HCl, pH 8.0) at atmospheric concentrations of  $\text{O}_2$  results in an increase in absorption at 300–350 nm indicative of product formation (Figure 5A). In parallel experiments with ferric rhIDO under identical conditions, no increase in absorbance was observed on prolonged incubation (Figure 5B). When the experiments with rhTDO were repeated under anaerobic conditions, there was no significant increase in absorption at 321 nm (Figure 5C). The ratio of the absorbance changes measured at 321 nm was 150:7:1 for rhTDO (aerobic), rhTDO (anaerobic), and rhIDO, respectively, which gives an indication of the relative rates of the reactions. A truncated form of human TDO has also very recently been shown to have activity in the ferric form (17).

**Binding of  $\text{O}_2$  to Ferrous rhTDO.** Bubbling of  $\text{O}_2$  gas directly into a solution of ferrous rhTDO results in the formation of a species that has a Soret band at 413 nm, but there are no sharp peaks in the visible region (expected at  $\approx 540$  and  $\approx 570$  nm) that characterize this complex as a ferrous–oxy species (Table 1 and Figure 6A). To examine whether formation of a ferrous–oxy species was occurring over shorter time scales, the reaction was monitored using photodiode array spectroscopy (Figure 6B). In this experiment, data were collected over a period of 10 s from the mixing event. When mixed with  $\text{O}_2$ , ferrous rhTDO shows an overall decrease in absorbance in the visible region, and the Soret band decreases in intensity and is blue shifted (to 417 nm). There is no evidence for formation of the characteristic ferrous–oxy peaks (expected at  $\approx 540$  and  $\approx 580$  nm) even if the reaction is observed over an extended period (e.g., 200 s). The spectrum of the final species at 200 s is essentially identical to that obtained under equilibrium conditions when a solution of ferrous rhTDO was purged

Scheme 2: Structures of Tryptophan Derivatives Used in This Work

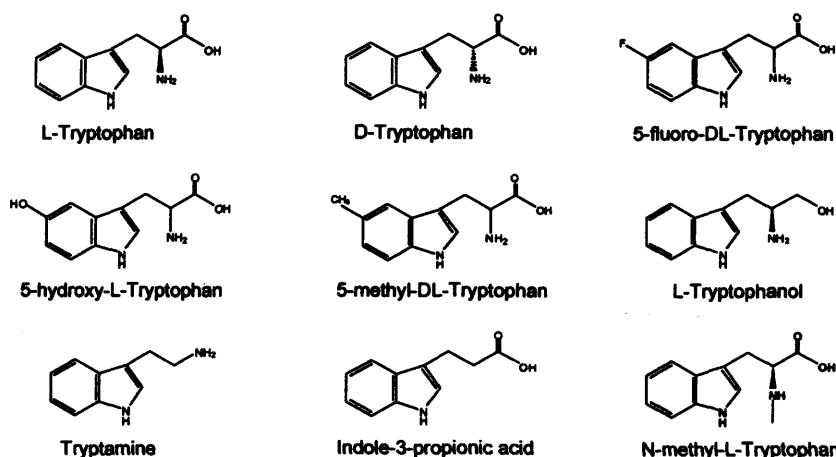


Table 2: Steady-State Parameters for Oxidation of L-Trp and Other Substrate Analogues by rhTDO and rhIDO (50 mM Tris-HCl Buffer, pH 8.0, 25.0 °C)

substrate	rhIDO		rhTDO	
	$k_{\text{cat}}$ ( $\text{s}^{-1}$ )	$K_M$ ( $\mu\text{M}$ )	$k_{\text{cat}}$ ( $\text{s}^{-1}$ )	$K_M$ ( $\mu\text{M}$ )
L-Trp	$1.4 \pm 0.05$	$7 \pm 0.8$	$1.4 \pm 0.019$	$222 \pm 15$
D-Trp	$3.93 \pm 0.07$	$1570 \pm 100$	<i>a</i>	<i>a</i>
5-fluoro-Trp	$0.76 \pm 0.01$	$6 \pm 0.8$	$0.18 \pm 0.004$	$360 \pm 28$
5-methyl-Trp	$3.78 \pm 0.16$	$98 \pm 14$	<i>b</i>	<i>b</i>
5-hydroxy-Trp	$0.025 \pm 0.0004$	$17 \pm 1.1$	no activity	
N-methyl-Trp	no activity		no activity	
tryptamine	no activity		no activity	
indole-3-propionic acid	no activity		no activity	
tryptophanol	no activity		no activity	

<sup>a</sup> Catalytic turnover of D-Trp was only measured at one concentration (50 mM) as very little activity was detectable at lower concentrations. At a concentration of 50 mM D-Trp, the measured rate of catalytic turnover for rhTDO was  $0.073 \text{ s}^{-1}$ , i.e., 5% of the  $k_{\text{cat}}$  value calculated for rhTDO with L-Trp. <sup>b</sup> In these assays the initial velocity was linearly dependent on 5-methyl-Trp concentration across the experimental range; the value of  $k_{\text{cat}}/K_M$  determined from the slope of this plot was  $0.0001 \mu\text{M}^{-1} \text{ s}^{-1}$ .

directly with  $\text{O}_2$  gas (compare with Figure 6). By means of comparison, reaction of rhIDO with  $\text{O}_2$  on the stopped-flow time scale leads to clear formation of a ferrous-oxy species ( $\lambda_{\text{max}} = 416, 539, \text{ and } 576 \text{ nm}$ ), and this species is stable (6).

**Binding of Other Ligands to Ferrous rhTDO.** In contrast to the reaction with  $\text{O}_2$ , the ferrous-CO complex of rhTDO is readily isolated ( $\lambda_{\text{max}} = 421, 540 \text{ and } 564 \text{ nm}$ ; Table 1 and Figure 6A). Addition of L-Trp (1 mM) to the ferrous-CO complex did not result in any further spectral change (Table 1). Binding constants,  $K_D$ , for binding of CO to ferrous rhTDO and the [ferrous rhTDO-Trp] complex were  $5.1 \pm 0.3$  and  $1.4 \pm 0.15 \mu\text{M}$ , respectively. In addition, ferrous rhTDO also binds cyanide, as evidenced by the formation of sharp peaks at 534 and 564 nm in the visible region (Figure 6A).

**Redox Potentiometry.** Reduction potentials for the  $\text{Fe}^{3+}/\text{Fe}^{2+}$  couple of rhTDO in the absence,  $E^{\text{free}}$ , and presence,  $E^{\text{bound}}$ , of L-Trp were found to be  $-92 \pm 3$  and  $-76 \pm 3 \text{ mV}$ , respectively (Figure 7). This similarity in the two values was unexpected since in other heme dioxygenases a shift in reduction potential is observed on binding of substrate (3, 21). In separate experiments (data not shown), these reduction potentials were confirmed using methylene blue instead of Nile blue chloride as the redox dye. As an independent check on whether the values were correct, these reduction potentials ( $E^{\text{bound}} = -76 \text{ mV}$  and  $E^{\text{free}} = -92 \text{ mV}$ ) were correlated with the binding constants determined above for binding of L-Trp to the oxidized ( $K_{\text{ox}} = 170 \mu\text{M}$ ) and reduced ( $K_{\text{red}} =$

$222 \mu\text{M}$ ) states<sup>3</sup> according to eq 3 (where  $RT/F = 25 \text{ mV}$ ). In this case, a value for  $K_{\text{ox}}/K_{\text{red}}$  of 0.77 is calculated, which is similar to the value of 1.89 calculated for  $\exp[F(E^{\text{bound}} - E^{\text{free}})/RT]$ . The fact that these reduction potentials correlate with the experimentally determined values for the binding constants in this way is evidence that the measured reduction potentials in the absence and presence of substrate are indeed correct and are a true reflection of the binding thermodynamics.

## DISCUSSION

In this work, we report a bacterial expression system for human TDO that produces milligram quantities of enzyme. This has allowed us to report detailed mechanistic and redox information for this human enzyme.<sup>4</sup> Below, we compare the properties of human TDO with other dioxygenase enzymes and discuss the implications of these data in terms of our current understanding of the heme dioxygenase structure and function.

**Redox Properties.** The  $\text{Fe}^{3+}/\text{Fe}^{2+}$  reduction potential for human TDO has not been reported previously and was determined here as  $-92 \text{ mV}$ , which is in a similar range to that for rhIDO (6). There is no reliable determination of a

<sup>3</sup> In this treatment, we have assumed that  $K_D \approx K_M$  for the reduced form.

<sup>4</sup> rhTDO is available commercially (www.genwaybio.com), although there are no functional data.

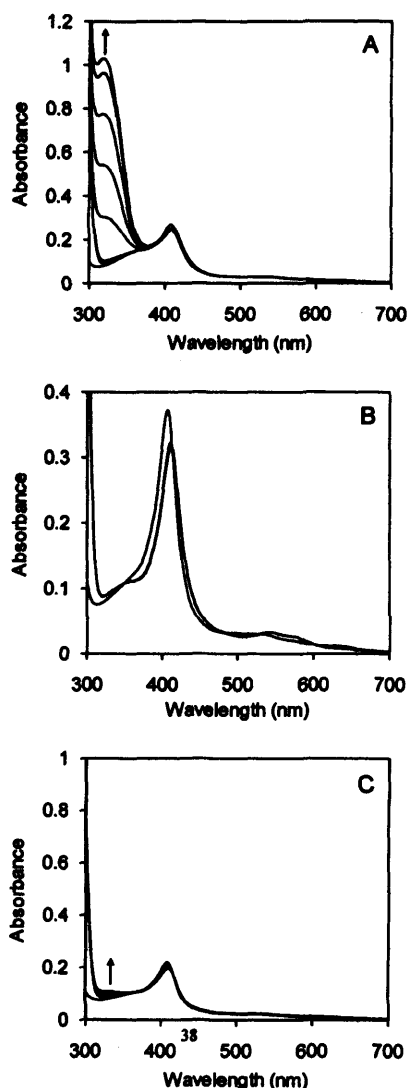


FIGURE 5: Oxidation of L-Trp by ferric rhTDO. (A) Spectral changes observed upon reaction of ferric rhTDO with L-Trp under aerobic conditions. (B) Spectral changes observed upon reaction of ferric rhIDO with L-Trp under aerobic conditions. (C) Spectral changes observed upon reaction of ferric rhTDO with L-Trp under anaerobic conditions. All reactions were monitored for 60 min; arrows indicate the direction of the absorbance change during the course of the reaction. Reaction conditions: 50 mM Tris-HCl, pH 8.0, 25.0 °C.

reduction potential for a mammalian TDO.<sup>5</sup> The reduction potential for rhTDO does not shift significantly on addition of substrate. This has functional implications, since the reduction potentials of the substrate-bound and substrate-free forms of the enzyme report indirectly on the relative binding affinity of the substrate. Thus, with rhTDO the redox data show that there is no stabilization of the ferrous derivative upon binding of the substrate. This is in contrast to rhIDO and *Xanthomonas campestris* TDO in which the

<sup>5</sup> The literature is confusing here. An early report (22) cites a value of -110 mV for rat liver TDO at pH 7 taken from ref 23 (which is cited as 1980b in ref 22), but this value of -110 mV is not correct since in ref 23 no actual reduction potential is stated nor do the data that are shown indicate a potential close to this value. In ref 22 two papers by Makino et al. are cited (1980a and 1980b), and we assume that ref 22 incorrectly cites 1980b instead of 1980a. The correct 1980a reference (24) does give a reduction potential and the data are shown: a value of +100 mV is reported here in the absence of L-Trp, which shifts to +160 mV on addition of saturating concentrations of L-Trp.

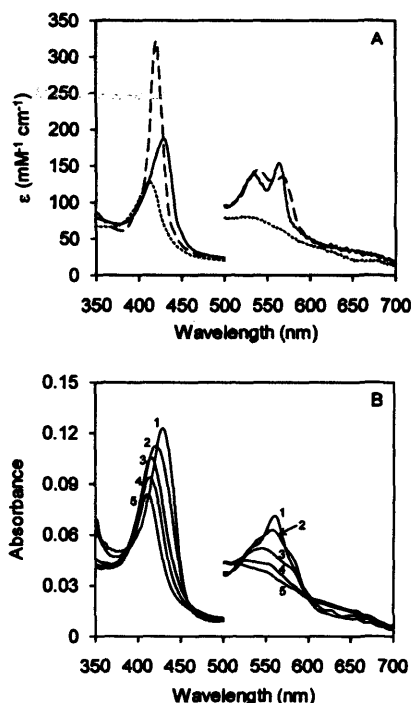


FIGURE 6: Electronic absorption spectra of ferrous derivatives of rhTDO. (A) UV-visible spectra of the ferrous complex in the presence of O<sub>2</sub> (dotted line), CO (dashed line), and CN (solid line) forms of rhTDO; absorbance values in the visible region have been multiplied by a factor of 4. (B) Reaction of rhTDO with O<sub>2</sub> monitored by stopped-flow photodiode array spectroscopy. Time-dependent spectral changes on mixing rhTDO with O<sub>2</sub> (time base of 10 s). For clarity, only selected spectra are shown at (1) 1.28 ms, (2) 100 ms, (3) 1 s, and (4) 10 s after mixing. The spectrum collected 200 s after mixing (5) is also shown. Reaction conditions: 50 mM Tris-HCl, pH 8.0, 25.0 °C.

Fe<sup>3+</sup>/Fe<sup>2+</sup> reduction potentials increase by ≈60–80 mV (3, 6) and ≈140 mV (21), respectively, upon binding of L-Trp. The functional implications of this are discussed in more detail below.

**Substrate Binding.** Our data with the various substrate analogues clearly show that modifications to the α-carboxylate and/or α-ammonium groups of the substrate are not tolerated, which indicates that hydrogen-bonding interactions to these charged groups are important in the substrate-bound complex, as observed in the crystal structure of xTDO in complex with L-Trp (21).<sup>6</sup> An assessment of other TDOs for which binding of substrate analogues has been reported (Table 3) describes a similar picture, which suggests that binding interactions to the substrate across the TDO family are likely to be conserved.

The binding affinity of the substrate to ferric and ferrous rhTDO is in the same range as that to ferric rhIDO [≈200–300 μM in all cases (6)]. In human IDO, however, the substrate discriminates between the ferric and ferrous forms of the enzyme by a factor of ≈40 (3), so that the substrate binds preferentially to the ferrous form ( $K_M \approx 10 \mu\text{M}$ ). As dictated by the reduction potentials (above), human

<sup>6</sup> Binding of D-Trp is clearly much less favorable than that for L-Trp (Table 2). Batabyal et al. (17), however, report similar values of  $K_M$  for the two substrates in a truncated human TDO. We believe that this might arise from the fact that substrate is present during protein purification in ref 17 (which is not the case in our protein preparations) and that L-Trp might therefore be present in the D-Trp assays.

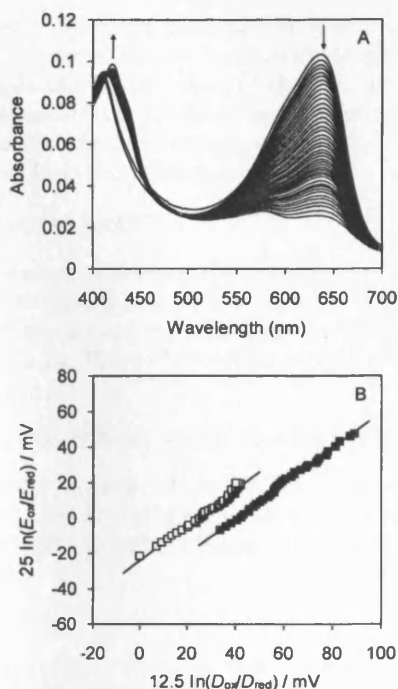


FIGURE 7: Redox potentiometry of rhTDO. (A) Spectral changes observed during determination of  $\text{Fe}^{3+}/\text{Fe}^{2+}$  reduction potential for rhTDO with the dye Nile Blue chloride. For clarity, only certain spectra are shown; arrows indicate the direction of absorption change during the reductive titration. (B) Nernst plots for the data shown in (A) (open squares) and for the data collected in the presence of substrate (filled squares). Reaction conditions: 100 mM potassium phosphate, pH 7.0, 25.0 °C.

Table 3: Activity of TDOs with Different Substrate Analogues<sup>a</sup>

	X. <i>campestris</i> <sup>b</sup>	B. <i>breviss</i> <sup>c,d</sup>	S. <i>parvulus</i> <sup>c</sup>	R. <i>metallidurans</i> <sup>f</sup>	mouse liver <sup>g,h</sup>
D-Trp	—	—	+	—	+
5-fluoro-Trp	+	+	+	nd	nd
5-OH-Trp	nd	+	nd	nd	—
5-methyl	nd	+	+	nd	nd
6-fluoro-Trp	+	+	nd	nd	nd
6-methyl	nd	+	nd	nd	nd
$\alpha$ -methyl	nd	nd	+	nd	nd
tryptamine	—	—	nd	—	—
serotonin	nd	nd	nd	nd	—
indolepropionic acid	—	—	nd	—	nd
indole	nd	—	nd	—	nd

<sup>a</sup> +, activity observed; —, no activity; nd, not determined. <sup>b</sup> Reference 21. <sup>c</sup> Reference 15. <sup>d</sup> Measured at 10 mM concentration of each substrate. <sup>e</sup> Reference 25. <sup>f</sup> Reference 26. <sup>g</sup> Reference 20. <sup>h</sup> Authors demonstrate that rat liver TDO is also active with D-Trp.

TDO shows no such discrimination because in this case  $K_{d(\text{ferric})} \approx K_{M(\text{ferrous})} \approx 200 \mu\text{M}$ .

Why then does IDO need to specifically favor substrate binding to the ferrous form whereas TDO does not? One explanation relates to the physiological location of the two dioxygenases. IDO is always located in the cytoplasm, which is an overall reducing environment. This would mean that only low concentrations of ferric IDO were present so that efficient binding to the ferric enzyme was not necessary *in vivo* (and consequently that the ferrous form binds substrate preferentially). On the other hand, human TDO is located exclusively in the liver, which is a more oxygen-rich (oxidizing) environment: this would mean that significant

amounts of ferric TDO are present physiologically such that binding to the ferric protein needs to be more efficient relative to IDO.

**Oxidation of Substrate.** The value of  $k_{\text{cat}}$  for rhTDO is identical to that for rhIDO ( $1.4 \text{ s}^{-1}$ ). These values for the two mammalian enzymes are lower than those found typically for the bacterial enzymes [ $k_{\text{cat}}$  usually  $\approx 20 \text{ s}^{-1}$ ] (14, 21, 23), although the reason for this difference is not clear at this stage. Most significantly for rhTDO, our data clearly show that oxidation of substrate is not a reaction catalyzed exclusively by the ferrous enzyme since substrate oxidation also occurs (albeit more slowly) with ferric rhTDO under aerobic conditions. Substrate oxidation by ferric rhTDO is most likely a result of trace amounts of either  $\text{H}_2\text{O}_2$  and/or superoxide in solution. This is supported by the fact that substrate oxidation does not occur in the absence of  $\text{O}_2$  and by separate experiments in which incubation of the reaction mix with either catalase or superoxide dismutase resulted in a 90% reduction in the total amount of product formed (data not shown). This characteristic ability of ferric rhTDO to catalyze product formation is not one that rhIDO can duplicate. The difference most likely relates to the fact that rhIDO discriminates against substrate binding to the ferric enzyme ( $K_{M(\text{ferrous})} \ll K_{d(\text{ferric})}$ , as discussed above) whereas TDO does not and the fact that higher concentrations of ferric enzyme are likely present *in vivo* for TDO.

**Formation of the Catalytic Ferrous–Oxy Complex.** In our experiments under equilibrium and pre-steady-state conditions we find no evidence for formation of a stable ferrous–oxy complex of rhTDO. This inability of rhTDO to binding  $\text{O}_2$  does not derive from an intrinsically unreactive ferrous heme group, since reaction of ferrous rhTDO with other diatomics (cyanide, CO) occurs normally. Our complete failure to detect a ferrous–oxy complex, even on the stopped-flow time scale, is all the more surprising when one considers that human IDO has a similar reduction potential to rhTDO and forms a relatively stable ferrous–oxy intermediate (6). We were not able to assess whether binding of substrate to rhTDO stabilizes the ferrous–oxy complex (because this leads to turnover in the stopped-flow experiment), but the data that we have for binding of CO to rhTDO in the presence of substrate (which does not lead to turnover) do not support the idea that binding of L-Trp stabilizes the ferrous–oxy complex (data not shown).

Why is the ferrous–oxy complex of rhTDO so unstable? We do not have a complete answer at this stage, but we note that the S167H variant of rhIDO, in which an active site histidine, analogous to that presumed (from sequence alignments) to be present in rhTDO, has been incorporated, also has a very unstable ferrous–oxy complex (6).

**Summary.** Our data for rhTDO reveal several unexpected differences with other heme dioxygenases. (i) The catalytic ferrous–oxy complex of rhTDO is not detected at all even though the reduction potential for rhTDO is in a similar range to that for rhIDO in which the same complex is stable. This instability of the ferrous–oxy complex is not, however, reflected in the overall activity of the enzyme, which is on a par with other dioxygenases. (ii) rhTDO does not specifically favor substrate binding to the ferrous enzyme, as observed in other heme dioxygenases. (iii) The ferric form of rhTDO is also active toward substrate under aerobic conditions.

Collectively, what these data tell us is that, unlike other categories of heme proteins (e.g., peroxidases, globins) which have fairly consistent patterns of behavior, significant differences in mechanism and functional properties are already emerging across the heme dioxygenase family. The reasons for this remain to be established.

#### ACKNOWLEDGMENT

Peptide mass fingerprinting was carried out by Dr. Andrew R. Bottrill and Shairbanu Ibrahim from the Protein Nucleic Acid Chemistry Laboratory (PNAAC), University of Leicester. We thank Dr. Harriet Seward for helpful discussions on EPR data.

#### SUPPORTING INFORMATION AVAILABLE

Amino acid sequence of rhTDO showing the peptides observed by MALDI-ToF after tryptic digest of rhTDO. This material is available free of charge via the Internet at <http://pubs.acs.org>.

#### REFERENCES

- Sono, M., Roach, M. P., Coulter, E. D., and Dawson, J. H. (1996) Heme-containing dioxygenases. *Chem. Rev.* 96, 2841–2888.
- Littlejohn, T. K., Takikawa, O., Skylas, D., Jamie, J. F., Walker, M. J., and Truscott, R. J. (2000) Expression and purification of recombinant human indoleamine 2,3-dioxygenase. *Protein Expression Purif.* 19, 22–29.
- Papadopoulou, N. D., Mewies, M., McLean, K. J., Seward, H. E., Svistunenko, D. A., Munro, A. W., and Raven, E. L. (2005) Redox and spectroscopic properties of human indoleamine 2,3-dioxygenase and a His303Ala variant: implications for catalysis. *Biochemistry* 44, 14318–14328.
- Vottero, E., Balgi, A., Woods, K., Tugendreich, S., Melese, T., Andersen, R. J., Mauk, A. G., and Roberge, M. (2006) Inhibitors of human indoleamine 2,3-dioxygenase identified with a target-based screen in yeast. *Biotechnol. J.* 1, 282–288.
- Sugimoto, H., Oda, S., Otsuki, T., Hino, T., Yoshida, T., and Shiro, Y. (2006) Crystal structure of human indoleamine 2,3-dioxygenase: catalytic mechanism of O<sub>2</sub> incorporation by a heme-containing dioxygenase. *Proc. Natl. Acad. Sci. U.S.A.* 103, 2611–2616.
- Chauhan, N., Basran, J., Efimov, I., Svistunenko, D. A., Seward, H. E., Moody, P. C. E., and Raven, E. L. (2008) The role of serine 167 in human indoleamine 2,3-dioxygenase: a comparison with tryptophan 2,3-dioxygenase. *Biochemistry* 47, 4761–4769.
- Antonini, M., and Brunori, E. (1971) *Hemoglobin and Myoglobin and their Reactions with Ligands*, North Holland Publishers, Amsterdam.
- Leatherbarrow, R. J. (2001) Grafit version 5, Erithacus Software Ltd., Staines, U.K.
- Patel, N., Jones, D. K., and Raven, E. L. (2000) Investigation of the haem-nicotinate interaction in leghaemoglobin. Role of hydrogen bonding. *Eur. J. Biochem.* 267, 2581–2587.
- Speicher, K. D., Kolbas, O., Harper, S., and Speicher, D. W. (2000) Systematic Analysis of Peptide Recoveries from In-Gel Digestions for Protein Identifications in Proteome Studies. *J. Biomol. Technol.* 11, 74–86.
- Massey, V. (1991) *Flavins and Flavoproteins* (Curti, B., Ronchi, S., and Zanetti, G., Eds.) pp 59–66, Walter de Gruyter, New York.
- Clark, W. M. (1972) *Oxidation-Reduction Potentials of Organic Systems*, Kreiger Publishing, Huntington, NY.
- Ren, S., Liu, H., Licad, E., and Correia, M. A. (1996) Expression of rat liver tryptophan 2,3-dioxygenase in *Escherichia coli*: structural and functional characterization of the purified enzyme. *Arch. Biochem. Biophys.* 333, 96–102.
- Ishimura, Y., Nozaki, M., and Hayaishi, O. (1970) The oxygenated form of L-tryptophan 2,3-dioxygenase as reaction intermediate. *J. Biol. Chem.* 245, 3593–3602.
- Manandhar, S. P., Shimada, H., Nagano, S., Egawa, T., and Ishimura, Y. (2002) Subunit structure of recombinant rat liver L-tryptophan 2,3-dioxygenase. *Int. Congr. Ser.* 1233, 161–169.
- Matsumura, M., Osada, K., and Aiba, S. (1984) L-tryptophan 2,3-dioxygenase of a moderate thermophile, *Bacillus brevis*. Purification, properties and a substrate-mediated stabilization of the quaternary structure. *Biochim. Biophys. Acta* 786, 9–17.
- Batabyal, D., and Yeh, S.-R. (2007) Human Tryptophan Dioxygenase: A Comparison to Indoleamine 2,3-Dioxygenase. *J. Am. Chem. Soc.* 129, 15690–15701.
- Littlejohn, T. K., Takikawa, O., Truscott, R. J., and Walker, M. J. (2003) Asp274 and his346 are essential for heme binding and catalytic function of human indoleamine 2,3-dioxygenase. *J. Biol. Chem.* 278, 29525–29531.
- Kudo, Y., and Boyd, C. A. R. (2000) Human placental indoleamine 2,3-dioxygenase: cellular localization and characterization of an enzyme preventing fetal rejection. *Biochim. Biophys. Acta* 1500, 119–124.
- Watanabe, Y., Fujiwara, M., Yoshida, R., and Hayaishi, O. (1980) Stereospecificity of hepatic L-tryptophan 2,3-dioxygenase. *Biochem. J.* 189, 393–405.
- Forouhar, F., Anderson, J. L., Mowat, C. G., Vorobiev, S. M., Hussain, A., Abashidze, M., Bruckmann, C., Thackray, S. J., Seetharaman, J., Tucker, T., Xiao, R., Ma, L. C., Zhao, L., Acton, T. B., Montelione, G. T., Chapman, S. K., and Tong, L. (2007) Molecular insights into substrate recognition and catalysis by tryptophan 2,3-dioxygenase. *Proc. Natl. Acad. Sci. U.S.A.* 104, 473–478.
- Leeds, J. M., Brown, P. J., McGeehan, G. M., Brown, F. K., and Wiseman, J. S. (1993) Isotope effects and alternative substrate reactivities for tryptophan 2,3-dioxygenase. *J. Biol. Chem.* 268, 17781–17786.
- Makino, R., Sakaguchi, K., Iizuka, T., and Ishimura, Y. (1980) Acid-alkaline transition and thermal spin equilibrium of the heme in ferric L-tryptophan 2,3-dioxygenases. *J. Biol. Chem.* 255, 11883–11891.
- Makino, R., Sakaguchi, K., Iizuka, T., and Ishimura, Y. (1980) L-Tryptophan 2,3-dioxygenase; structure, function and interaction with substrate, in *Biochemical and Medical Aspects of Tryptophan Metabolism* (Hayaishi, O., Ishimura, Y., and Kido, R., Eds.) pp 179–187, Elsevier/North Holland Biomedical Press, Amsterdam.
- Hitchcock, M. J., and Katz, E. (1988) Purification and characterization of tryptophan dioxygenase from *Streptomyces parvulus*. *Arch. Biochem. Biophys.* 261, 148–160.
- Zhang, Y., Kang, S. A., Mukherjee, T., Bale, S., Crane, B. R., Begley, T. P., and Ealick, S. E. (2007) Crystal structure and mechanism of tryptophan 2,3-dioxygenase, a heme enzyme involved in tryptophan catabolism and in quinolinate biosynthesis. *Biochemistry* 46, 145–155.

BI702393B